8-9-2014

# STRUCTURAL HEALTH MONITORING USING LINEAR AND NONLINEAR ULTRASONIC GUIDED WAVES

Yanfeng Shen
*University of South Carolina - Columbia*

Follow this and additional works at: http://scholarcommons.sc.edu/etd

## Recommended Citation

STRUCTURAL HEALTH MONITORING USING LINEAR AND NONLINEAR
ULTRASONIC GUIDED WAVES

By

Yanfeng Shen

Bachelor of Science
Wuhan University, 2010

_____

Submitted in Partial Fulfillment of the Requirements

For the Degree of Doctor of Philosophy in

Mechanical Engineering

College of Engineering and Computing

University of South Carolina

2014

Accepted by:

Victor Giurgiutiu, Major Professor

Yuh J. Chao, Committee Member

Paul Ziehl, Committee Member

Lingyu Yu, Committee Member

Matthieu Gresil, Committee Member

Lacy Ford, Vice Provost and Dean of Graduate Studies

ABSTRACT

The dissertation addresses Structural Health Monitoring (SHM) using linear and nonlinear ultrasonic guided waves, with an emphasis on the development of analytical and numerical models of guided wave propagation and interaction with linear and nonlinear structural damage.

An analytical model was developed based on the exact Lamb wave solution for the simulation of Lamb wave propagation and interaction with damage. The damage effects were inserted into the model using complex valued wave damage interaction coefficients (WDICs). The analytical procedure was coded as a framework into a MATLAB Graphical User Interface (GUI), and the software WaveFormRevealer (WFR) was developed as a general description of wave generation, propagation, interaction with damage, and detection. The WDICs were extracted from the harmonic analysis of small-size local finite element models (FEM) with non-reflective boundaries (NRB). By joining the analytical framework and the local FEM, a Combined Analytical/FEM Approach (CAFA) was developed for efficient simulation of Lamb wave propagation and interaction with damage. To model guided wave propagation in composite structures, the semi-analytical finite element (SAFE) procedure was investigated and coded with MATLAB, and the software SAFE-DISPERSION was developed to generate guided wave dispersion curves, mode shapes, and directivity plots for composites.

Nonlinear ultrasonic SHM techniques were also examined because they have been reported to have remarkable sensitivity to incipient damage. An analytical model

was developed to capture the nonlinear higher harmonic generation phenomena for localized damage. Also investigated was the nonlinear interaction between Lamb waves and breathing cracks using FEM through two specific simulation techniques: element activation/deactivation method and contact analysis. A damage index based on the nonlinear features of the sensing signal was proposed in order to identify the presence and severity of a breathing crack. Nonlinear ultrasonic SHM was also investigated for monitoring bolt tightness status of an aerospace bolted lap joint. The 3-D contact FEM simulation was carried out and compared with experiments using Scanning Laser Doppler Vibrometer (SLDV).

The dissertation finishes with a summary of contributions followed by conclusions, and suggestions for future work.

TABLE OF CONTENTS

# LIST OF TABLES

LIST OF FIGURES

# CHAPTER 1
## INTRODUCTION

Structural Health Monitoring (SHM) is an emerging multi-disciplinary field which aims at detecting/characterizing structural damage and providing diagnosis/prognosis of structural health status in a real-time or on-demand manner. With the advancement of SHM technology, the industry can reduce the maintenance cost, shorten the machine service down time, and improve the safety and reliability of engineering structures. It has shown great potential in both the health management of aging structures and the development of novel self-sensing smart structures. This chapter serves as the introduction to the entire dissertation by addressing the motivation and importance of conducting the research, discussing research goal, scope, and objectives will be discussed, and introducing the organization of the dissertation.

## 1.1 MOTIVATION

The development of computational models for Lamb wave propagation and interaction with damage is of great importance for both SHM system design and signal interpretation purposes. Effective design of SHM systems requires the exploration of a wide range of parameters (transducer size, sensor-damage relative locations, interrogating wave characteristics, etc.) to achieve the best detection and quantification of certain types of damage. On the other hand, active sensing signals using Lamb waves are usually difficult to interpret due to the multi-mode and dispersive nature of Lamb waves. Their interaction with damage involves even more complex scattering and mode conversion

phenomena. Practical applications have imposed three main requirements on computational models: (1) accuracy for high frequency, short wavelength, and long propagation distance waves; (2) efficiency in terms of computational time and computer resources; and (3) versatility with a wide range of parameter exploration capabilities. However, these requirements have not been satisfied with conventional analytical methods or commercially available finite element software. Thus, it is of great importance to develop accurate, efficient, and versatile computational techniques for the simulation of guided wave based active sensing procedures.

In addition to the development of efficient computational models, this dissertation also addresses nonlinear techniques in SHM. Conventional guided wave techniques relying on linear properties such as signal amplitude change, phase shift, scattering, and attenuation are not sensitive to early stage damage. Nonlinear ultrasonic guided waves are found to be more sensitive to incipient changes that are precursors to structural damage. By using the distinctive nonlinear ultrasonic characteristics, we can detect fatigue, micro cracks, and delamination in their early stages to prevent catastrophic failures. There have been intensive studies into nonlinear ultrasonic bulk waves in nondestructive evaluation (NDE), but the studies of nonlinear dispersive guided waves are still limited with unlimited possibilities and new applications in SHM (Jhang 2009). There are also difficulties not solved or answered well in the nonlinear guided wave inspection, such as the nonlinear phenomena threshold conditions and interaction mechanisms between guided waves and nonlinear damage (Broda et al. 2014). Thus, investigations of modeling nonlinear ultrasonic guided waves need to be carried out to better understand and apply nonlinear techniques in SHM.

1.2  RESEARCH GOAL, SCOPE, AND OBJECTIVES

The research goal of the PhD work presented in this dissertation is to develop accurate, efficient, and versatile computational models for guided wave propagation and interaction with damage. The scope of this research covers the analytical modeling, finite element simulation, and experiments for the development of SHM concepts. The modeling techniques were advanced in both linear and nonlinear region. The objectives of the work presented in this dissertation are as follows:

1. To construct a 1-D analytical framework which can describe wave damage interaction phenomena, including transmission, reflection, mode conversion, and nonlinear higher harmonic addition.

2. To extend the concept developed in the 1-D case to the 2-D wave propagation and damage interaction problems.

3. To develop a non-reflective boundary condition for plate guided Lamb waves which is effective for both symmetric and antisymmetric modes, and apply it for the construction of efficient local finite element models (FEM).

4. To develop an accurate, efficient, and versatile hybrid approach for the simulation of 2-D Lamb wave propagation and interaction with damage.

5. To develop user-friendly software to guide/assist effective and efficient design of SHM and active sensing systems.

6. To apply the semi-analytical finite element (SAFE) method to the modeling of ultrasonic guided wave propagation in composite structures, and develop user friendly software for the calculation of dispersion curves, mode shapes, and directivity plots in composite structures.

7. To advance the modeling techniques of nonlinear interaction between guided waves and structural damage.

8. To review the nonlinear SHM techniques and apply nonlinear ultrasonic techniques for the detection of fatigue crack and health monitoring of bolted lap joints.

## 1.3    ORGANIZATION OF THE DISSERTATION

To achieve the objectives set forth in the preceding section, the dissertation is organized in nine chapters. The focus and contents of each chapter is introduced in Chapter 1.

In Chapter 2, guided wave theory is briefly reviewed, guided wave application to SHM was discussed, and the piezoelectric wafer active sensors (PWAS) were introduced.

In Chapter 3, the 1-D analytical framework for 1-D multimode Lamb wave propagation and interaction with damage is developed. The predictive tool WaveFormRevealer 1-D (WFR-1D) is presented.

In Chapter 4, the analytical framework is extended to 2-D wave problems. The development of an effective non-reflective boundary (NRB) condition for plate guided Lamb waves is presented. Also presented is a combined analytical/FEM approach (CAFA) for the accurate, efficient, and versatile simulation of 2-D Lamb wave active sensing.

In Chapter 5, the derivation of the semi-analytical finite element (SAFE) formulation for plate waveguides is discussed. The user-friendly software SAFE-DISPERSION is presented. Case studies conducted to verify the SAFE-DISPERSION results against analytical solutions and global matrix method (GMM) solutions are discussed.

In Chapter 6, nonlinear ultrasonic mechanisms and nonlinear phenomena are discussed. Nonlinear techniques for SHM are introduced.

In Chapter 7, two nonlinear finite element techniques for the simulation of nonlinear interaction between Lamb waves and a breathing crack are investigated. A damage index is proposed to detect the breathing cracks and further estimate the severity of the nonlinear damage.

In Chapter 8, the higher harmonics nonlinear ultrasonic technique for the application on the bolt load monitoring of an aerospace bolted lap joint is investigated.

# CHAPTER 2
## FUNDAMENTALS OF GUIDED WAVES AND PIEZOELECTRIC WAFER ACTIVE SENSORS FOR STRUCTURAL HEALTH MONITORING

This chapter introduces fundamentals of guided wave theory, basic concepts of Structural Health Monitoring (SHM), and piezoelectric wafer active sensors (PWAS) for generating and receiving guided waves. It will also serve as the theoretical prerequisite for the wave modeling and simulation tasks. First, the guided wave theory is briefly reviewed by types, including Rayleigh waves, shear horizontal (SH) plate waves, straight crested Lamb waves, circular crested Lamb waves, and guided waves in rods, pipes, and waveguides with arbitrary cross sections. Next, guided waves based SHM concepts and techniques are introduced. The key points of modeling guided wave based SHM are discussed. Finally, the PWAS transducers are introduced, including their working principle, their coupling with guided waves and tuning effect, and their operation modes.

## 2.1    BRIEF REVIEW OF GUIDED WAVE THEORY

Guided waves are widely used as interrogating field for damage detection, because they can travel long distances without much energy loss, with the wave energy confined and guided within the structures. Besides, guides waves can travel inside curved walls, and across component joints. These aspects make them suitable for inspection of large areas of complicated structures. Ultrasonic guided waves are sensitive to changes in the propagating medium, such as plastic zone, fatigue zone, cracks, and delamination. This sensitivity exists for both surface damage and cross thickness/interior damage,

because guided waves have various mode shapes throughout the cross section of the waveguides.

### 2.1.1 RAYLEIGH WAVES

Rayleigh waves, known as the surface wave, propagate close to the body surface, with the motion amplitude decreasing rapidly with depth. The polarization of Rayleigh wave lies in a plane perpendicular to the surface. The effective depth of penetration is less than a wavelength.

One benefit of using Rayleigh waves for structural health monitoring lies in that Rayleigh wave is not dispersive, i.e. the wave speed is constant. It is found that the Rayleigh wave speed, $c_R$, depends on the shear wave speed, $c_S$, and the Poisson ratio, $v$. A common approximation of the wave speed of Rayleigh wave is given as

$$c_R(v) = c_S \left( \frac{0.87 + 1.12v}{1+v} \right) \tag{2.1}$$

For common Poisson ratio values, the Rayleigh wave speed takes values close to and just below the shear wave speed (Giurgiutiu 2008). The particle motion or the mode shape of the Rayleigh waves across the thickness direction, $y$, is given by

$$\hat{u}_x(y) = Ai \left( \xi e^{-\alpha y} - \frac{\beta^2 + \xi^2}{2\xi} e^{-\beta y} \right)$$
$$\hat{u}_y(y) = A \left( -\alpha e^{-\alpha y} + \frac{\beta^2 + \xi^2}{2\beta} e^{-\beta y} \right) \tag{2.2}$$

where $A$ is the wave amplitude factor, $\xi = \omega/c_R$ is the wavenumber of Rayleigh surface waves, $\alpha$ and $\beta$ are coefficients given in Eq. (2.3). Figure 2.1 shows the Rayleigh wave in a semi-infinite medium.

$$\alpha^2 = \xi^2\left(1 - \frac{c^2}{c_P^2}\right); \quad \beta^2 = \xi^2\left(1 - \frac{c^2}{c_S^2}\right) \tag{2.3}$$
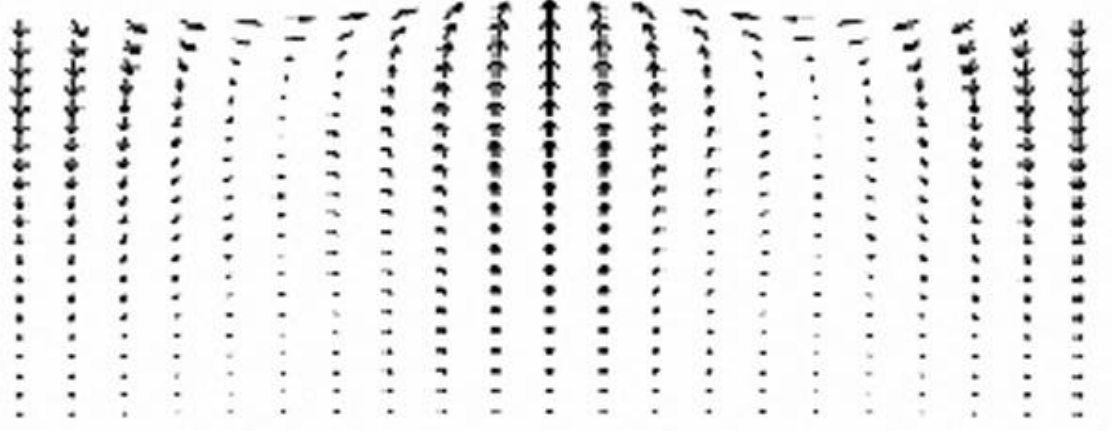


Figure 2.1: Simulation of Rayleigh wave in a semi-infinite medium (Giurgiutiu 2008).

2.1.2    SHEAR HORIZONTAL PLATE WAVES

Shear horizontal (SH) plate waves have a shear-type particle motion contained in the horizontal plane. Figure 2.2 shows the coordinate definition and particle motion of SH plate waves. According to the coordinate defined, an SH wave has the particle motion along the $z$ axis, whereas the wave propagation takes place along the $x$ axis. The particle motion has only the $u_z$ component. Unlike Rayleigh wave which is non-dispersive, SH plate waves are dispersive and may travel with different modes.

The phase velocity dispersion curve of the SH plate wave can be calculated as

$$c(\omega) = \frac{c_S}{\sqrt{1 - (\eta d)^2 \left(\dfrac{c_S}{\omega d}\right)^2}} \tag{2.4}$$

where $\eta$ is given in Eq. (2.5) and $d$ is the half plate thickness.

$$\eta^2 = \frac{\omega^2}{c_S^2} - \frac{\omega^2}{c^2} \tag{2.5}$$

By substituting the appropriate eigenvalue, one gets an analytical expression for the wave-speed dispersion curve of each SH wave mode. For detailed expressions, the readers are referred to Giurgiutiu (2007).
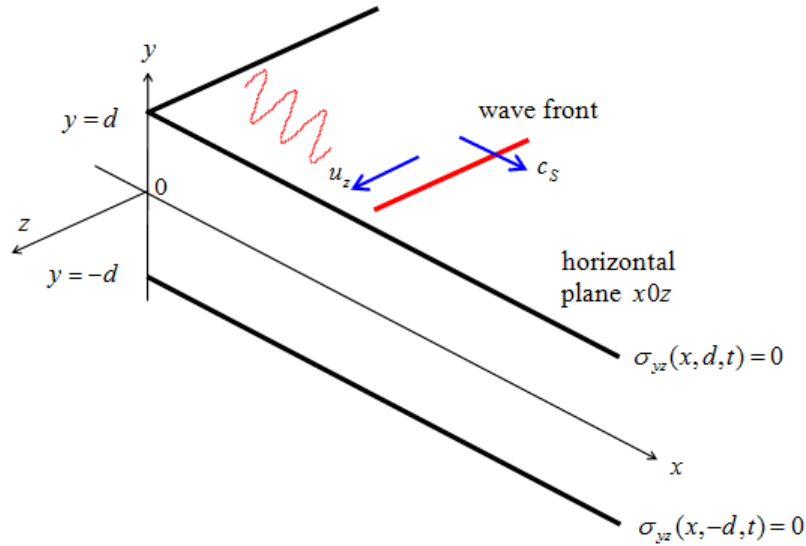


Figure 2.2: Coordinate definition and particle motion of SH plate waves (Giurgiutiu 2008).
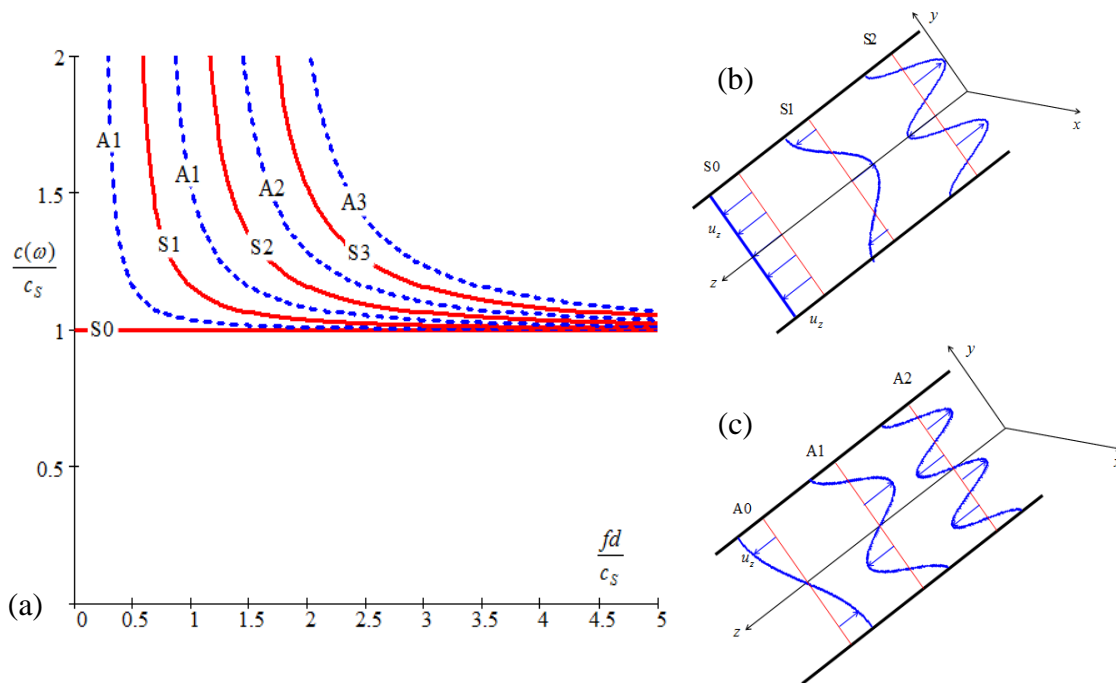


Figure 2.3: (a) SH plate wave-speed dispersion curves; (b) symmetric mode shapes; (c) antisymmetric mode shapes (Giurgiutiu 2008).

9

Figure 2.3 shows the wave-speed dispersion curve of SH plate waves and the mode shapes. It can be noticed that the fundamental symmetric mode (S0) wave is non-dispersive and always exists starting from low frequency-thickness product values. This nice property makes it a good candidate as the interrogating waves in SHM systems. Recently, considerable research has been carried out on the transmission and reception of SH plate wave for SHM (Kamal et al. 2013; Zhou et al. 2014). Higher wave modes only appear beyond the corresponding cut-off frequencies, showing dispersive characteristics, i.e., their phase velocity changes with frequency. For dispersive waves, group velocity is usually used to evaluate the propagation of wave packets. The definition of group velocity is given in Eq. (2.6).

$$c_g = \frac{d\omega}{d\xi} \tag{2.6}$$

### 2.1.3 STRAIGHT CRESTED LAMB WAVES

Lamb waves are a type of ultrasonic waves that are guided between two parallel free surfaces, such as the upper and lower surfaces of a plate. Lamb waves can exist in two basic types, symmetric and antisymmetric. Figure 2.4 shows the particle motion of symmetric and antisymmetric Lamb waves. The Lamb wave motion has asymptotic behavior at low frequency and high frequency. At low frequency, the symmetric mode resembles axial waves, while the antisymmetric mode resembles flexural waves. At high frequency, both symmetric and antisymmetric wave approaches Rayleigh waves, because the particle motion is strong at the surfaces and decays rapidly across the thickness. The axial wave and flexural wave, by their nature, are only low frequency approximations of Lamb waves. The plate structure cannot really sustain pure axial and flexural motion at large frequency-thickness product values.

Symmetric Lamb wave mode

(a)

Antisymmetric Lamb wave mode

(b)
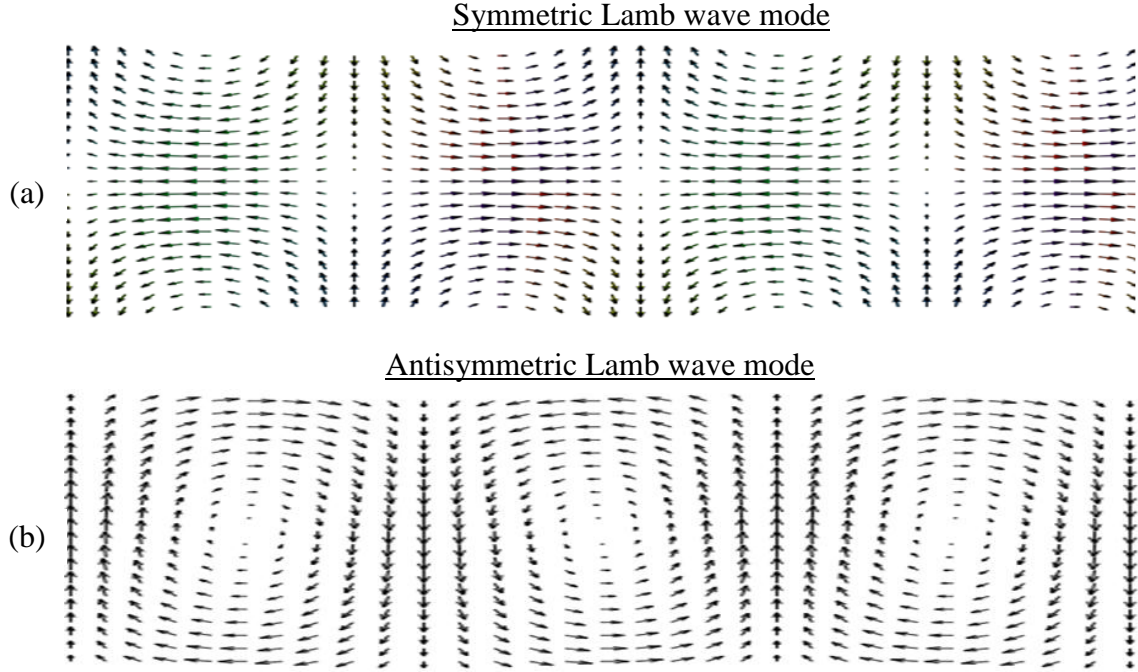
Figure 2.4: Particle motion of Lamb wave modes: (a) symmetric mode and (b) antisymmetric mode (Giurgiutiu 2008).

The straight crested Lamb wave equations are derived under z-invariant assumptions using pressure wave and shear vertical wave (P+SV) waves in a plate. Through multiple reflections on the plate's lower and upper surfaces, and through constructive and destructive interference, the pressure waves and shear vertical waves give rise to the Lamb–waves, which consist of a pattern of standing waves in the thickness *y*–direction (Lamb–wave modes) behaving like traveling waves in the *x*–direction. For detailed derivation of Lamb wave equations, readers are referred to Graff (1991), Rose (1999), and Giurgiutiu (2007). The derivation finally reaches the Rayleigh-Lamb equation:

$$\frac{\tan \eta_S d}{\tan \eta_P d} = \left[ \frac{-4\eta_P \eta_S \xi^2}{\left(\xi^2 - \eta_S^2\right)^2} \right]^{\pm 1} \tag{2.7}$$

11

where +1 exponent corresponds to symmetric Lamb wave modes and -1 exponent corresponds to antisymmetric Lamb wave modes. $d$ is the half plate thickness, and $\xi$ is the frequency dependent wavenumber. $\eta_P$ and $\eta_S$ are given in Eq. (2.8). $\lambda$ and $\mu$ are Lame's constants of the material, and $\rho$ is the material density.

$$\eta_P^2 = \frac{\omega^2}{c_p^2} - \xi^2; \quad \eta_S^2 = \frac{\omega^2}{c_s^2} - \xi^2; \quad c_p = \sqrt{\frac{\lambda + 2\mu}{\rho}}; \quad c_s = \sqrt{\frac{\mu}{\rho}}; \quad (2.8)$$
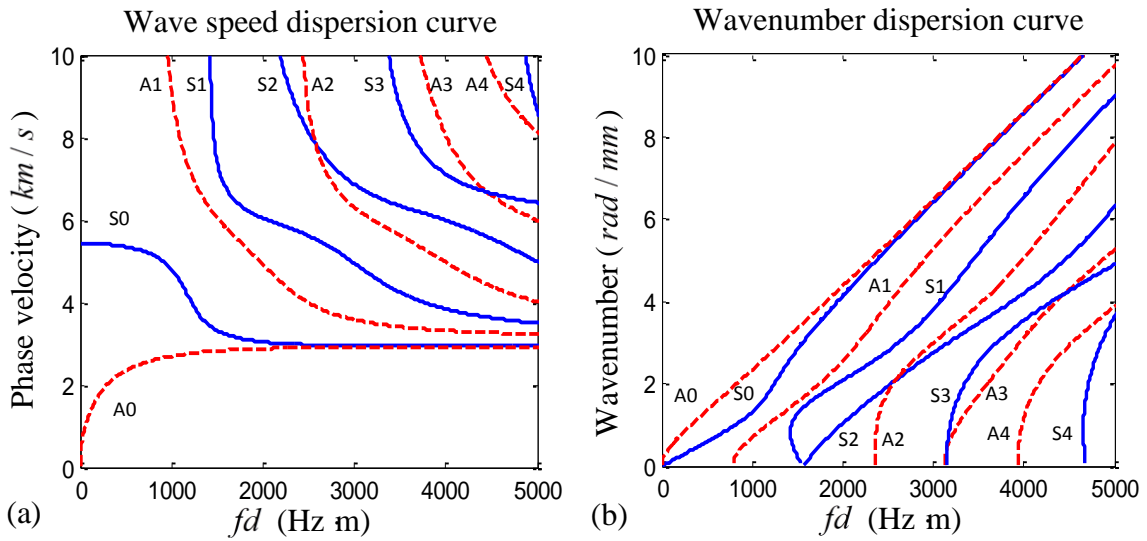


Figure 2.5: (a) Wave speed dispersion curve; (b) wavenumber dispersion curve.

Figure 2.5 shows the dispersion curves of aluminum plates calculated from the Rayleigh-Lamb equations. It can be noticed at least two wave modes (the fundamental symmetric mode: S0; the fundamental antisymmetric mode: A0) exist simultaneously. Beyond the corresponding cut-off frequencies, higher Lamb modes will participate in the propagation. At small frequency-thickness product values, the S0 mode is less dispersive than A0 mode, and all the Lamb wave modes converge to non-dispersive Rayleigh waves at large frequency-thickness product values. The dispersive and multi-mode nature of

Lamb waves adds complexity in both Lamb wave propagation modeling and SHM application.

In their multi-modal and dispersive nature, Lamb waves also have complicated frequency dependent mode shapes associated with particle motion across the plate thickness. Even for certain Lamb modes, the mode shape changes under different frequencies. The displacement mode shapes can be calculated using Eq. (2.9) and Eq. (2.10) (Giurgiutiu 2008).

For symmetric Lamb modes:

$$
\begin{aligned}
u_x^S(x,y,t) &= iC^S\left[-2\xi^2\eta_S\cos\eta_S d\cos\eta_P y + \eta_S(\xi^2-\eta_S^2)\cos\eta_P d\cos\eta_S y\right]e^{i(\xi x-\omega t)} \\
u_y^S(x,y,t) &= C^S\left[2\xi\eta_P\eta_S\cos\eta_S d\sin\eta_P y + \xi(\xi^2-\eta_S^2)\cos\eta_P d\sin\eta_S y\right]e^{i(\xi x-\omega t)}
\end{aligned}
\tag{2.9}
$$

For antisymmetric Lamb modes:

$$
\begin{aligned}
u_x^A(x,y,t) &= iC^A\left[2\xi^2\eta_S\sin\eta_S d\sin\eta_P y - \eta_S(\xi^2-\eta_S^2)\sin\eta_P d\sin\eta_S y\right]e^{i(\xi x-\omega t)} \\
u_y^A(x,y,t) &= C^A\left[2\xi\eta_P\eta_S\sin\eta_S d\cos\eta_P y + \xi(\xi^2-\eta_S^2)\sin\eta_P d\cos\eta_S y\right]e^{i(\xi x-\omega t)}
\end{aligned}
\tag{2.10}
$$

where $C^S$ and $C^A$ determine the mode shape amplitudes; $y$ is the location of interested point across the plate thickness; $i$ is the imaginary unit; $x$ is the coordinate along propagation direction.

Figure 2.6 shows the mode shapes of fundamental S0 and A0 Lamb waves in a 2-mm aluminum plate under various frequencies. It can be observed that for certain Lamb mode, the mode shapes vary a lot with frequency. Within low frequency range, the mode shapes show that S0 and A0 Lamb modes could be approximated by axial and flexural wave motion. However, within high frequency range, the mode shapes become more complicated and deviate from the axial-flexural approximation. And, at even higher frequency, e.g. at 10 MHz, the particle motions are mainly near the top and bottom

surfaces of the plate, while the particles in the middle of the plate undergo very small oscillation. This shows that at high frequency range, Lamb modes converge to Rayleigh waves.
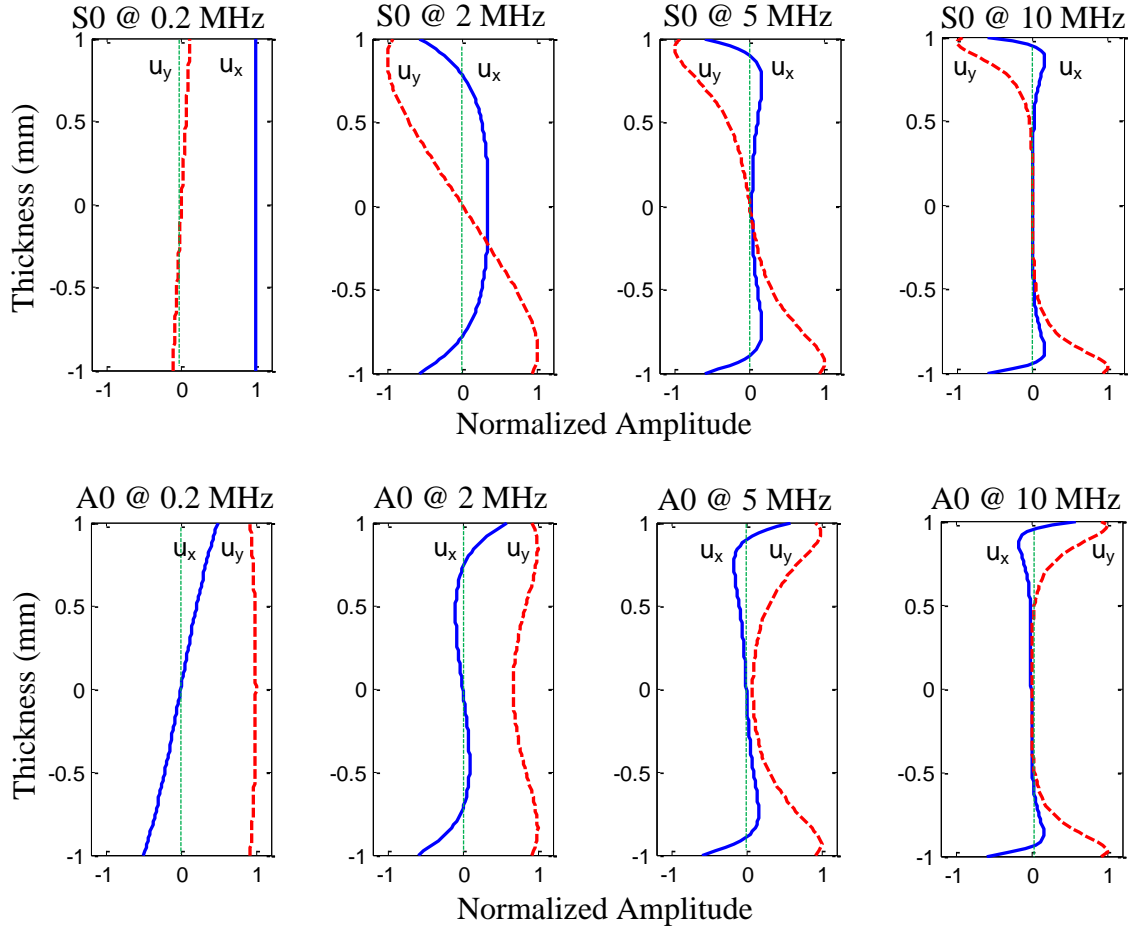


Figure 2.6: Mode shapes of S0 and A0 Lamb waves in a 2-mm thick aluminum plate.

### 2.1.4   CIRCULAR CRESTED LAMB WAVES

In their practical applications, the interrogating Lamb waves generated by a transmitter will propagate out in a circular crested wave front instead of a straight crested wave front, because the transmitter can be considered as a point source compared with the large inspection area. With the wave propagating outward, this amount energy is distributed on a larger area. Thus, the amplitude of the interrogating wave is strong near

the wave source and decays along the propagation direction. The circular crested Lamb wave solution can capture these effects due to outward propagation pattern.

A detailed and rigorous derivation of circular crested Lamb waves is well documented in Giurgiutiu (2014). The derivation of circular crested Lamb waves is found to be more appropriate in a cylindrical coordinate system shown in Figure 2.7a. The derivation arrives at the same Rayleigh-Lamb equation as Eq. (2.7), which means the circular crested Lamb waves propagate with the same wave speed as the straight crested Lamb waves.
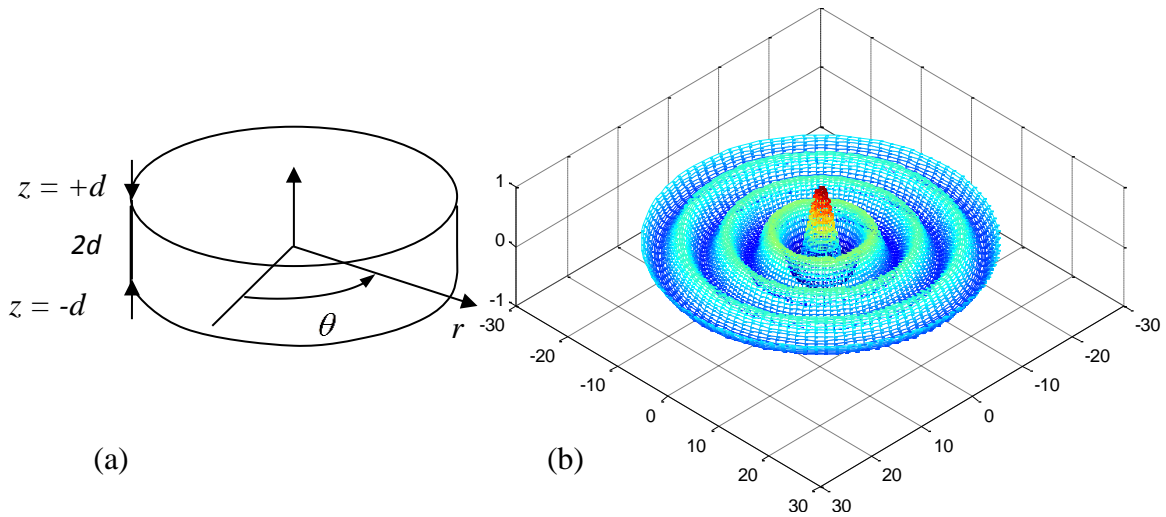


Figure 2.7: (a) Cylindrical coordinate for problem derivation (Giurgiutiu 2014); (b) circular crested wave pattern.

The propagation pattern of circular Lamb waves admits the Bessel and Hankel function family solution. The Bessel functions $J_0$ and $J_1$ is appropriate for standing waves, and the Hankel functions $H_0^{(1)}$ and $H_1^{(1)}$ are appropriate for propagating waves. The first kind Hankel functions ($H_0^{(1)}$ and $H_1^{(1)}$) describes an outward propagating wave field, when $e^{-i\omega t}$ is chosen as the convention for the derivation. While, the second kind

15

Hankel functions ($H_0^{(2)}$ and $H_1^{(2)}$) describes an outward propagating wave field, when $e^{i\omega t}$ is chosen as the convention for the derivation. The mode shape solutions for the circular crested Lamb waves are given below for outward propagating wave fields.

Symmetric Lamb modes:

$$u_r^S(r,z,t) = C^S \left[ 2\xi^2 \zeta_S \cos \zeta_S d \cos \zeta_P z - \zeta_S \left( \xi^2 - \zeta_S^2 \right) \cos \zeta_P d \cos \zeta_S z \right] H_1^{(1)}(\xi r) e^{-i\omega t}$$

$$u_z^S(r,z,t) = C^S \xi \left[ 2\zeta_P \zeta_S \cos \zeta_S d \sin \zeta_P z + \left( \xi^2 - \zeta_S^2 \right) \cos \zeta_P d \sin \zeta_S z \right] H_0^{(1)}(\xi r) e^{-i\omega t}$$

(2.11)

Antisymmetric Lamb modes:

$$u_r^A(r,z,t) = -C^A \zeta_S \left[ 2\xi^2 \sin \zeta_S d \sin \zeta_P z - \left( \xi^2 - \zeta_S^2 \right) \sin \zeta_P d \sin \zeta_S z \right] H_1^{(1)}(\xi r) e^{-i\omega t}$$

$$u_z^A(r,z,t) = C^A \xi \left[ 2\zeta_P \zeta_S \sin \zeta_S d \cos \zeta_P z + \left( \xi^2 - \zeta_S^2 \right) \sin \zeta_P d \cos \zeta_S z \right] H_0^{(1)}(\xi r) e^{-i\omega t}$$

(2.12)

where $C^S$ and $C^A$ are the amplitude factor for symmetric mode and antisymmetric mode, and can be determined from the wave generation calculation. $\zeta_P, \zeta_S$ are defined as

$$\zeta_P^2 = \frac{\omega^2}{c_P^2} - \xi^2; \quad \zeta_S^2 = \frac{\omega^2}{c_S^2} - \xi^2$$

(2.13)

It can be observed from Eq. (2.11) and Eq. (2.12), that the in-plane radian direction motion accepts the solution of the first kind Hankel function of order one ($H_1^{(1)}$), while the out-of-plane direction motion accepts the solution of the first kind Hankel function of order zero ($H_0^{(1)}$). Figure 2.7b shows a typical outward propagation wave pattern calculated using Hankel function $H_0^{(1)}$, describing an out-of-plane wave motion. It can be noticed that the wave amplitude at the wave source (coordinate center) is strong, and it

decays as it propagates out. Figure 2.8 shows the plots of Hankel functions of order zero and order one. It can be noticed that the amplitude is high near the origin of $R$, and beyond certain distance, the amplitude becomes stable and changes more gradually compared with the origin range of R.
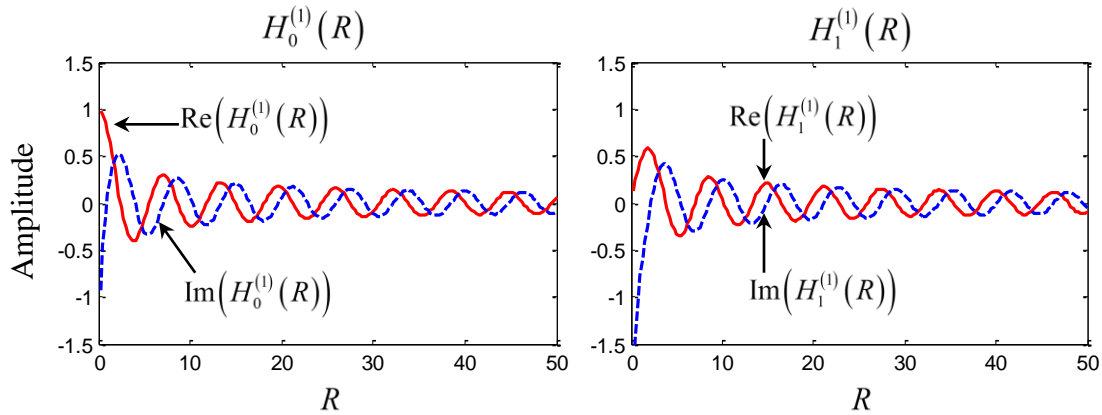


Figure 2.8: Hankel function of order zero ($H_0^{(1)}(R)$) and order one ($H_1^{(1)}(R)$).

### 2.1.5   GUIDED WAVES IN RODS, PIPES, AND ARBITRARY CROSS-SECTION WAVEGUIDES

The guided waves in rods, pipes, and arbitrary cross section waveguides also find great potential in nondestructive evaluation (NDE) and SHM for truss structures, pipelines, and rail tracks. Analytical solutions exist for simple geometry rods and pipes. However, for waveguides with arbitrary cross sections, the semi-analytical finite element (SAFE) method is usually adopted to obtain the numerical solutions of wave propagation problems.

Several investigators have considered the propagation of waves in solid and hollow cylinders. Love (1944) studied wave propagation in an isotropic solid cylinder and showed that three types of solutions are possible: (1) longitudinal; (2) flexural; and (3) torsional. At high frequencies, each of these solutions is multimodal and dispersive.

Meitzler (1961) showed that, under certain conditions, mode coupling could exist between various wave types propagating in solid cylinders such as wires. Extensive numerical simulation and experimental testing of these phenomena was done by Zemenek (1972). Comprehensive work on wave propagation in hollow circular cylinders was done by Gazis (1959). A comprehensive analytical investigation was complemented by numerical studies. The nonlinear algebraic equations and the corresponding numerical solutions of the wave–speed dispersion curves were obtained. These results found important applications in the ultrasonic NDE of tubing and pipes. Silk and Bainton (1979) found equivalences between the ultrasonic in hollow cylinders and the Lamb waves in flat plates and used them to detect cracks in heat exchanger tubing. Rose et al. (1994) used guided pipe waves to find cracks in nuclear steam generator tubing. Alleyne et al. (2001) used guided waves to detect cracks and corrosion in chemical plant pipe work.
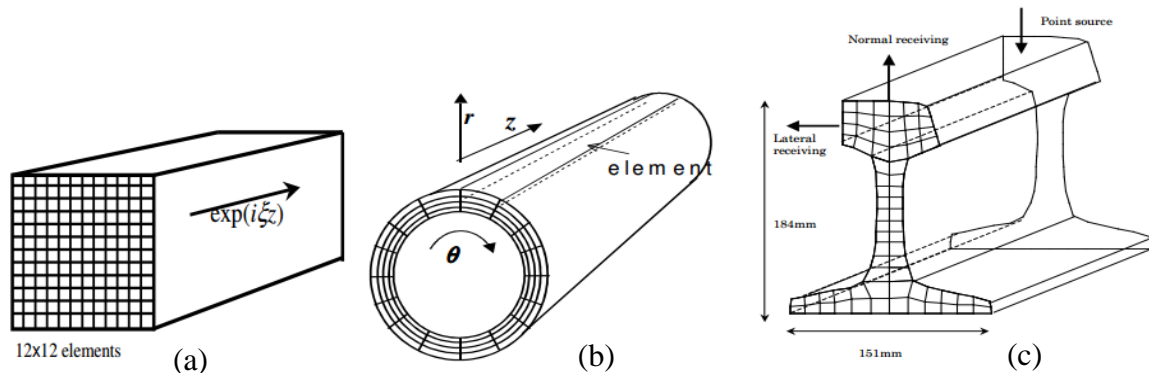


Figure 2.9: Discretization of the cross sections in SAFE: (a) square rod; (b) circular pipe; (c) rail track (Hayashi et al. 2004).

Several researchers have applied the SAFE method to obtain the guided wave solutions in waveguides with arbitrary cross sections. Gavric (1995) calculated the dispersion curves and mode shapes of guided waves in a rail track. Figure 2.9 shows typical discretization of the arbitrary cross sections. A comprehensive case study was

18

presented by Hayashi et al. (2004). Bartoli et al. (2006) further invested the SAFE method and successfully included damping effects into the model.

## 2.2 STRUCTURAL HEALTH MONITORING USING GUIDED WAVES

Structural Health Monitoring (SHM) is an emerging multi-disciplinary field with wide applications. This technology evolves from the conventional nondestructive evaluation (NDE) and conditional based maintenance (CBM), where the damage detection and evaluation are done in a schedule based or conditional based manner. In contrast with NDE and CBM, SHM aims at developing real-time or on-demand damage detection and characterization systems for evaluation of structural health status. Within the scope of SHM, guided wave techniques are favorable for their capability of interrogating large areas of structure from a single location. In this section, fundamental SHM concepts are introduced, prevalent guided wave techniques are covered, and key points in guided wave based SHM are discussed.

### 2.2.1 STRUCTURAL HEALTH MONITORING CONCEPTS

General sensing technology can be cast into two methodological categories: (1) passive sensing and (2) active sensing. Passive sensing systems only passively record events which happened during an interested period of time. By analyzing the recorded signal, diagnosis can be made on the health status of the structure. Examples of passive sensing SHM can be found in the acoustic emission (AE) monitoring and impact detection, where passive sensors are triggered by crack advancing or impact events. By analyzing the AE or impact signal, location of the AE or impact source can be identified (Yu et al 2012; Gresil et al. 2013). In contrast to passive sensing, active sensing methods interrogate the structures with defined excitations, and record the corresponding response.

By analyzing the response, diagnosis can be made. Active sensing procedure has three main advantages for SHM applications: (1) it allows the real-time and on-demand inspection of the structures; (2) the excitation can be optimized for the most sensitive and effective response for damage detection; (3) the active sensing procedure is repeatable, which allows the comparison between two independent interrogations (a baseline data and a current status data).

Figure 2.10 shows a schematic representation of a generic SHM system. The active sensors clusters are implemented on the critical areas of high monitoring interest, such as airplane wines, engine turbines, fuselage, and fuel tank. Permanently bounded on the host structures, the sensors can actively interrogate large areas from local cluster zones in a real-time or on-demand manner, gathering sensing data to the data concentrators. These data concentrators will transmit the data to the SHM processing unit, where the data will be processed and diagnosis will be made.
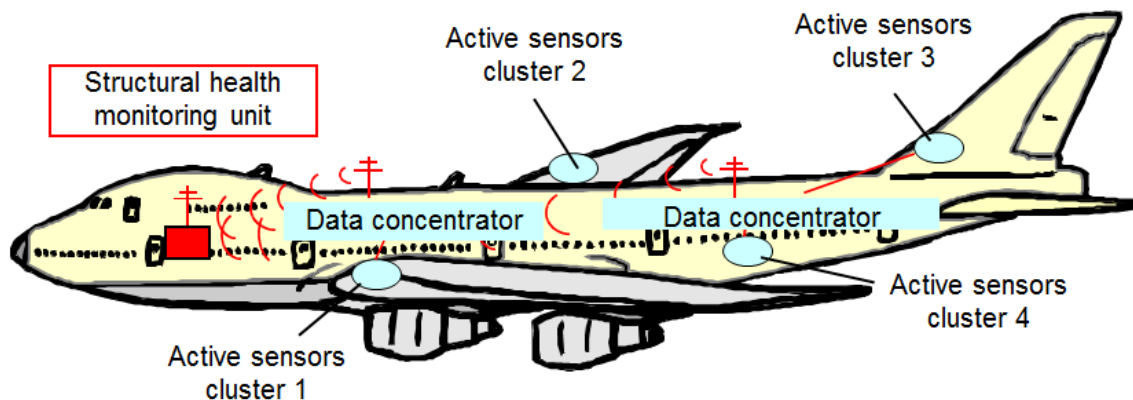


Figure 2.10: Schematic representation of a generic SHM system, consisting of active sensors, data concentrators, wireless communication, and SHM central unit (Giurgiutiu et al. 2002).

SHM is a pattern recognition process. SHM techniques aim at finding deviations of sensing signals or data pattern from the baseline, which are due to the presence of

damage. Farrar and Worden (2012) described SHM from a machine learning perspective and showed how statistical pattern recognition can be achieved for damage detection. The pattern recognition usually requires the comparison of two states of the structures, i.e., the initial or healthy state serving as the baseline and the current state under inspection. This aspect was illustrated by Worden (2007) in the fundamental axioms of SHM. Recent development of SHM technology has pushed the barriers of the axioms. Investigators have proposed baseline-free or reference-free techniques, where on baseline data are required for making diagnosis on the presence and severity of damage, such as the time reversal method and the nonlinear techniques (Wang et al. 2004; Sohn et al. 2013).

### 2.2.2 Guided Wave Techniques

The guided wave techniques can be generally categorized into linear techniques and nonlinear techniques. Many of the interrogating principles stem from conventional NDE. The linear techniques include pitch-catch, pulse-echo, electro-mechanical impedance spectroscopy (EMIS), phased array, and sparse array time-reversal imaging method. The prevalent nonlinear techniques are higher harmonic generation, subharmonic generation, and mixed frequency response (nonlinear modulation).

Figure 2.11 shows the pitch-catch active sensing method in SHM, where one transducer acts as the transmitter and sends out the guided waves, and another transducer acts as the receiver and pick up the sensing signal. In the pristine case (baseline), the interrogating waves are generated by the transmitter, propagate along the structure, and are picked up by the receiver. In the damaged case, the interrogating waves generated by the transmitter, propagate along the structure, interact with the damage, carry the damage information with them, and are finally picked up by the receiver. The subtraction between

these two states reveals the damage scattering response, which may indicate the presence
and severity of the damage.
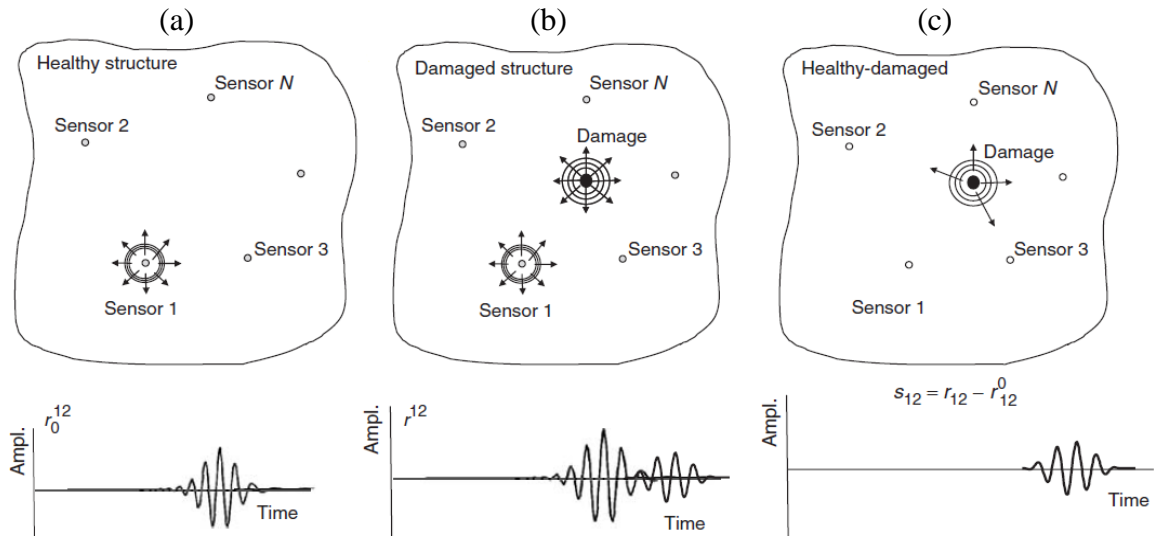


Figure 2.11: Pitch-catch active sensing: (a) baseline response; (b) response with damage;
(c) scattered response. (Ihn and Chang 2008)

Several sensors may work together in a systematically designed manner forming a
sensor network and achieve more complicated diagnostic approaches. Advanced damage
imaging techniques have been developed using phased array and sparse array. Giurgiutiu
and Bao (2004) investigated the embedded-ultrasonics structural radar (EUSR) for in situ
monitoring of thin-wall structures. Figure 2.12a shows the 1-D phased array EUSR and
its imaging result of a crack. Yu and Giurgiutiu (2007) further extended the EUSR
principle to 2-D phased array using 64 sensors. Based on Fink's work (1992), Wang et al.
(2004) proposed the synthetic time-reversal imaging method for structural health
monitoring. Figure 2.12b shows the sparse array with four sensors and its imaging result
using time-reversal method.

(a) Phased array (EUSR)  (b) Sparse array (time-reversal)
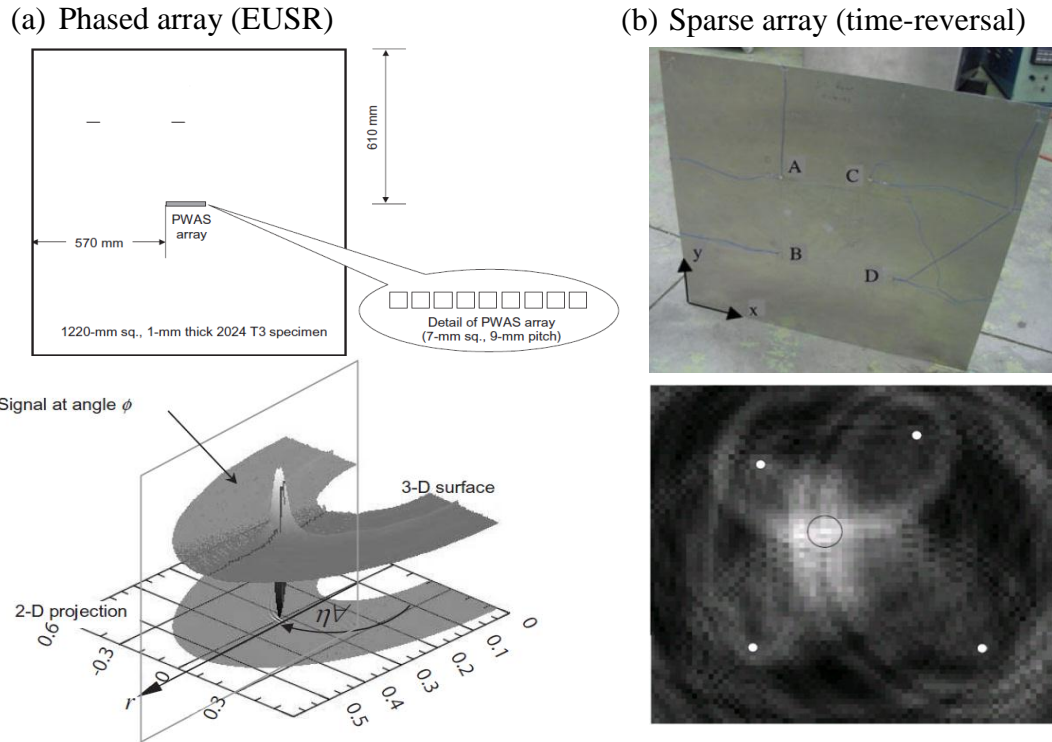
Figure 2.12: (a) Phased array imaging using EUSR (Giurgiutiu and Bao 2004); (b) sparse array imaging using time-reversal method (Wang et al. 2004).
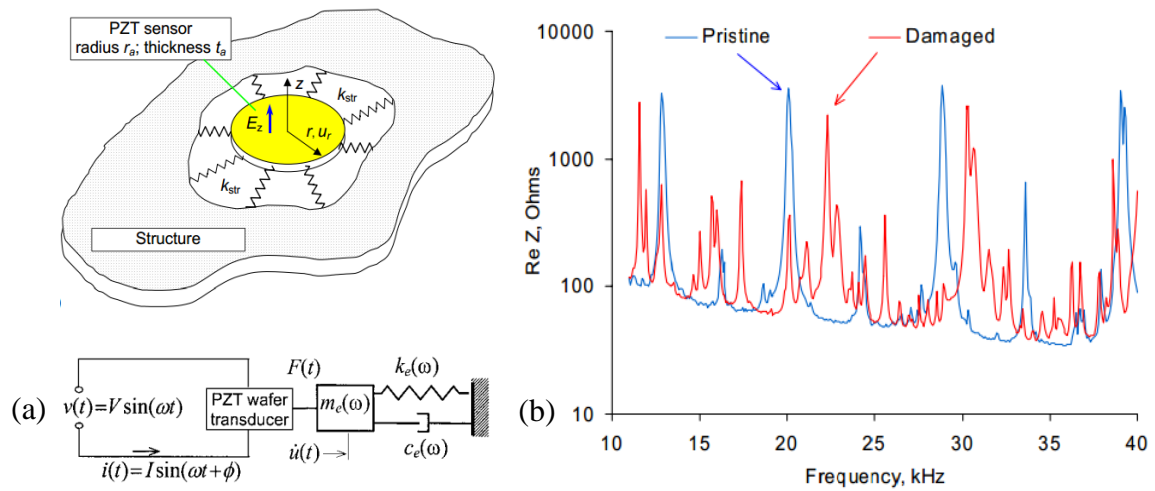


Figure 2.13: (a) Electro-mechanical coupling between the PZT active sensor and the structure (Giurgiutiu et al. 1999); (b) EMIS spectrum (Zagrai and Giurgiutiu 2001).

In addition to traveling wave techniques, the EMIS is a standing guided wave SHM method. The continuous harmonic excitation of a transducer will excite the

23

structure with guided waves, which will be reflected by structural boundaries and damage, forming standing waves between the wave source and the reflectors. This standing wave formation will result in local mechanical resonance, which will be shown in the electrical response through the electro-mechanical coupling. Figure 2.13a shows the electro-mechanical coupling between the transducer and the structure. Figure 2.13b is a typical EMIS spectrum, showing that the damaged case spectrum deviates from the pristine case.

There are other guided wave based SHM techniques, which will not be detailed here. Especially, the nonlinear guided wave techniques will be introduced in a separate chapter later.

### 2.2.3   KEY ASPECTS IN GUIDED WAVE BASED SHM

Several key aspects play important roles in the success and improvement of SHM systems. Each of them by itself is an independent branch of study, and the advancement of each field may bring evolutionary progress to SHM. Figure 2.14 shows the key aspects in guided wave based SHM.
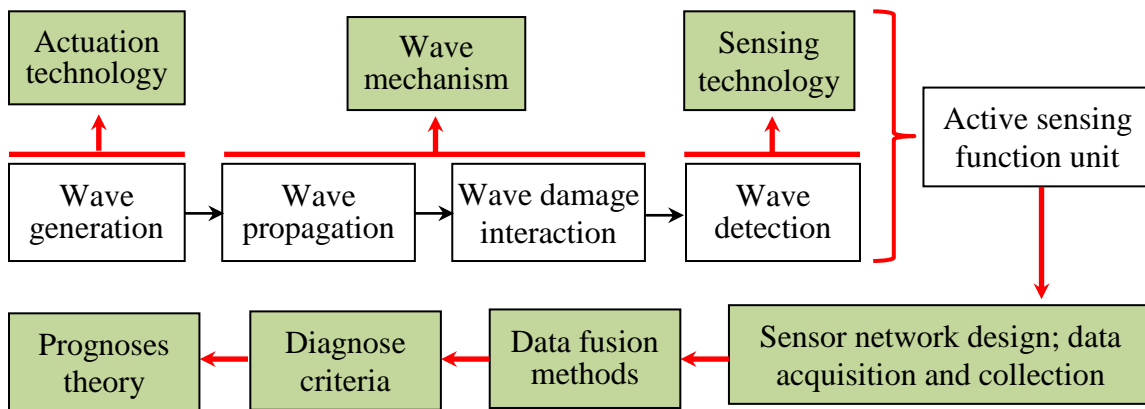


Figure 2.14: Key aspects in guided wave based SHM system.

An active sensing function unit consists of wave generation, propagation, wave-damage interaction, and wave detection. The actuation technology plays the key role in

24

generating the interrogating wave fileds. Conventional ultrasonic transducers can only generate pressure wave across the thickness of the plate, which can be applied to conduct a time consuming point by point inspection. Researchers have used wedge transducers to generate Lamb waves in plate structures by adjusting the incident angle of the pressure waves (Rose 1999). The piezoelectric wafer active sensors (PWAS) were developed to satisfy these requirements on low profile, light weight, and low cost transducers that can be permanently bonded on host structures in large quantities (Giurgiutiu 2008). The shear horizontal PWAS were used to generate this shear wave motion (Kamal et al. 2013; Zhou et al. 2014). Electromagnetic acoustic transducers (EMAT) have been developed to generate torsional mode guided waves in pipelines for detection of axial direction cracks (Bottger et al. 1987). The in-depth understanding of wave mechanism both in wave propagation and wave damage interaction are significant for effective detection of certain damage. It is always found that certain guided wave mode is more sensitive to a specific kind of damage. It can provide more insight in SHM system design by selecting appropriate interrogating wave frequency and mode type, as well as on choosing the sensitive detection location. Sensing technology deals with wave detection. In addition to sensing methods using piezoelectricity, new sensing approaches have been developed, such as fiber bragg grating (FBG) and laser vibrometry (Kabashima et al. 2001; Michaels et al. 2011). Each of them has opened a new field of study in SHM. The sensor network design is of great importance for comprehensively evaluating the interrogating area and collecting sufficient data of structural information for signal processing. The data acquisition, collection, and transmission are associated with hardware implementation and wireless communication between the sensor clusters and the central unit. Since SHM

is a pattern recognition process, the data fusion and processing is among the key aspect. Using different active sensing schemes and data processing methods, various characteristics of the damage may be identified, such as location, severity, and damage type. To diagnose the structural health status, judging criteria need to be developed based on the corresponding SHM method. A statistical technique is always desired to avoid false alarm or failure in detection. The prognoses of the structure residual service life depend on the fatigue theory and models which aims at predicting the material behaviors. Beside the theoretical models, experiments and computational models can also support the prognoses. Recently, a structural life prediction concept is proposed by using a digital twin, i.e., the actual structure collects all the operation data during its service, and the data are updated to a computer model acting as a virtual twin. By observing the behavior of the computer model, the performance of the actual structure can be predicted (Tuegel et al. 2011).

## 2.3    PIEZOELECTRIC WAFER ACTIVE SENSORS

Piezoelectric wafer active sensors (PWAS) are convenient enablers for generating and receiving guided waves. Figure 2.15 shows the comparison between the conventional ultrasonic transducer and PWAS.
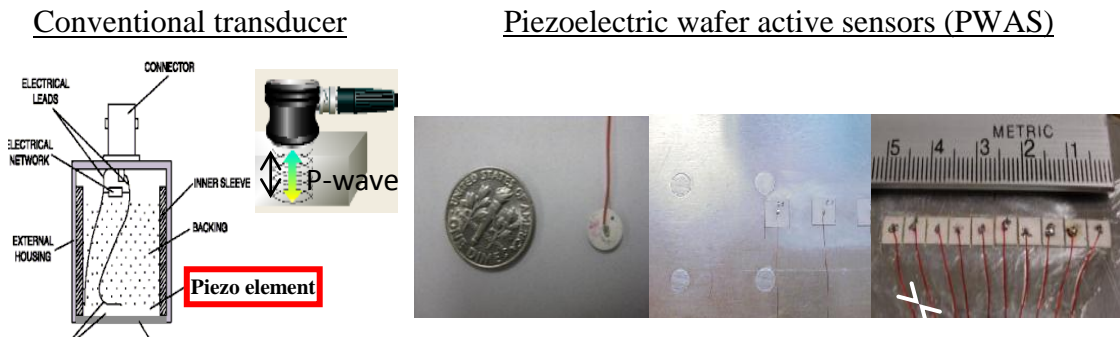


Figure 2.15: Comparison between conventional ultrasonic transducer and PWAS.

26

The conventional ultrasonic transducers are bulky, expensive, and can only generate through thickness pressure wave in the structures, which cannot satisfy the need for inspection of large areas. Compared with conventional transducers, PWAS are low profile, light weight, low cost, and unobtrusive to structures. They can be permanently bonded on host structures in large quantities and achieve real-time monitoring of the structural health status. They couple with the structure through in-plane motion and generate Lamb waves, which makes them suitable for inspection large areas of interest.

2.3.1 PWAS PRINCIPLES AND OPERATION MODES

Piezoelectric wafer active sensors (PWAS) couple the electrical and mechanical effects (mechanical strain, $S_{ij}$, mechanical stress, $T_{kl}$, electrical field, $E_k$, and electrical displacement, $D_j$) through the tensorial piezoelectric constitutive equations

$$
\begin{aligned}
S_{ij} &= s_{ijkl}^E T_{kl} + d_{kij} E_k \\
D_j &= d_{klj} T_{kl} + \varepsilon_{jk}^T E_k
\end{aligned}
\tag{2.14}
$$

where $s_{ijkl}^E$ is the mechanical compliance of the material measured at zero electric field ($E = 0$), $\varepsilon_{jk}^T$ is the dielectric permittivity measured at zero mechanical stress ($T = 0$), and $d_{klj}$ represents the piezoelectric coupling effect. PWAS utilize the $d_{31}$ coupling between in-plane strains, $S_1, S_2$ and transverse electric field $E_3$.

PWAS transducers can be used as both transmitters and receivers. Their modes of operation are shown Figure 2.16. PWAS can serve several purposes (Giurgiutiu 2008): (a) high-bandwidth strain sensors; (b) high-bandwidth wave exciters and receivers; (c) resonators; (d) embedded modal sensors with the electromechanical (E/M) impedance method. By application types, PWAS transducers can be used for (i) active sensing of far-

field damage using pulse-echo, pitch-catch, and phased-array methods, (ii) active sensing of near field damage using high-frequency E/M impedance method and thickness gage mode, and (iii) passive sensing of damage-generating events through detection of low-velocity impacts and acoustic emission at the tip of advancing cracks (Figure 2.16). The main advantage of PWAS over conventional ultrasonic probes is in their lightweight, low profile, and low cost. In spite of their small size, PWAS are able to replicate many of the functions performed by conventional ultrasonic probes.
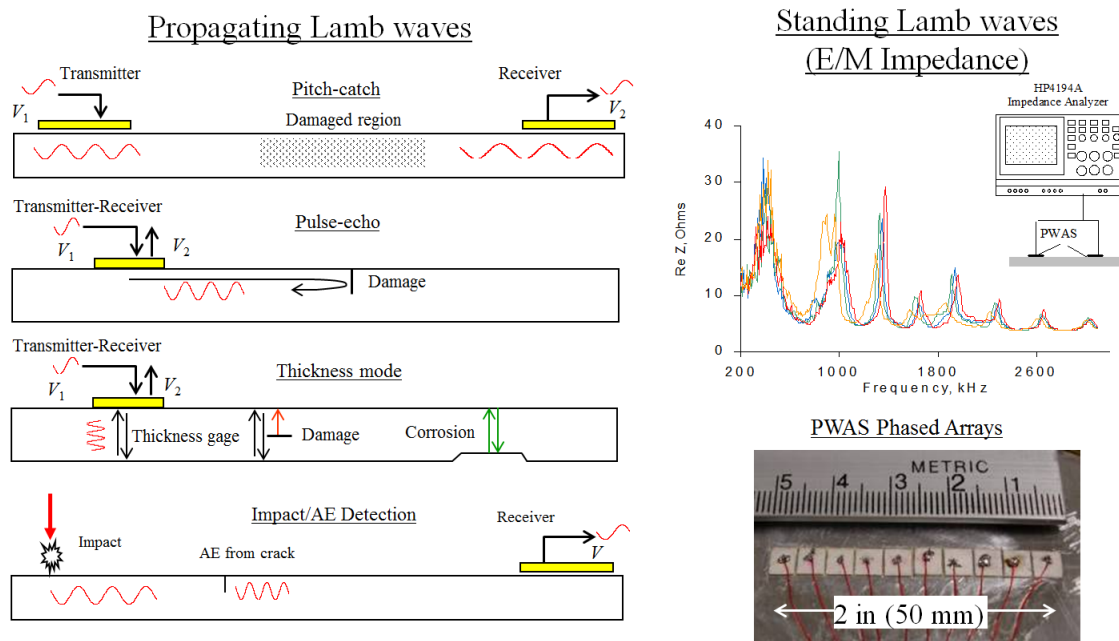


Figure 2.16: Schematic of PWAS application modes (Giurgiutiu 2010).

2.3.2    PWAS COUPLED GUIDED WAVES AND TUNING EFFECT

Figure 2.17 shows the coupling between PWAS and the host structure, and illustrates how PWAS transducers generate Lamb waves. When an oscillatory electric voltage at ultrasonic frequencies is applied on PWAS, due to the piezoelectric effect, a oscillatory strain is induced to the transducer. Since the structure constrains the motion of

PWAS, the reacting force from the bonding layer will act as shear stress on the host structure and generate wave motion.
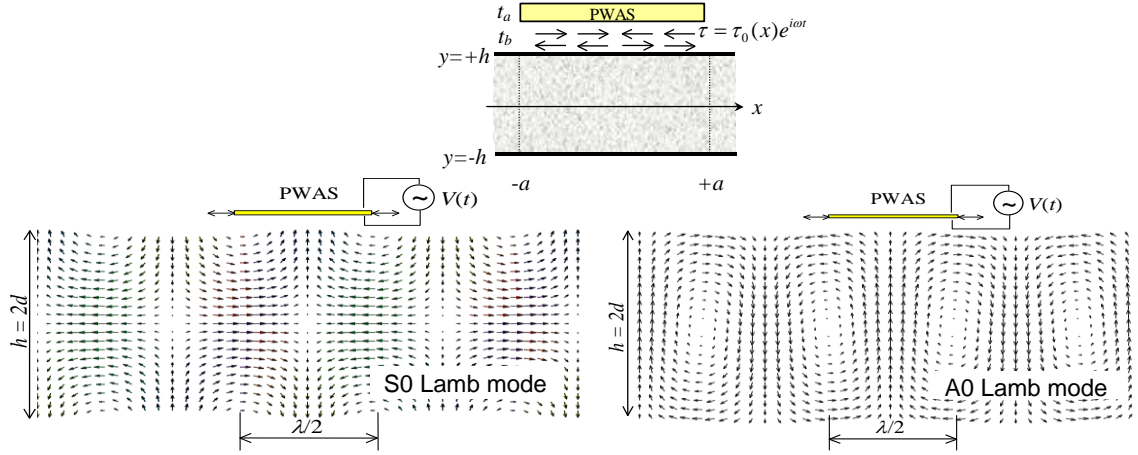


Figure 2.17: Lamb wave generation using PWAS transducers (Giurgiutiu 2008).

The Lamb wave amplitude excited by PWAS depends on the PWAS size, plate thickness, and excitation frequency. For a given PWAS and plate geometry, the amplitudes of Lamb modes changes with frequency. It was found that tuning possibility exists for generating single Lamb mode with PWAS transducers. The tuning effect is important because it overcomes the multimode difficulty for Lamb wave applications. The analytical expression on tuning effect was first developed by Giurgiutiu (2003)

$$\varepsilon_x(x,t) = -i\frac{a\tau_0}{\mu}\left\{\sum_{\xi^S}(\sin\xi^S a)\frac{N_S(\xi^S)}{D_S'(\xi^S)}e^{-i(\xi^S x-\omega t)} + \sum_{\xi^A}(\sin\xi^A a)\frac{N_A(\xi^A)}{D_A'(\xi^A)}e^{-i(\xi^A x-\omega t)}\right\} \quad (2.15)$$

Figure 2.18 shows the tuning curve for 7 mm PWAS and 1.6 mm thick aluminum plate situation. It is apparent that the amplitudes of S0 and A0 Lamb modes excited by the PWAS transducer change with frequency. Around 300 kHz, A0 Lamb mode reaches the rejecting point where no A0 mode Lamb wave will be excited. This is a sweet spot for generating only S0 wave mode for structural inspection.
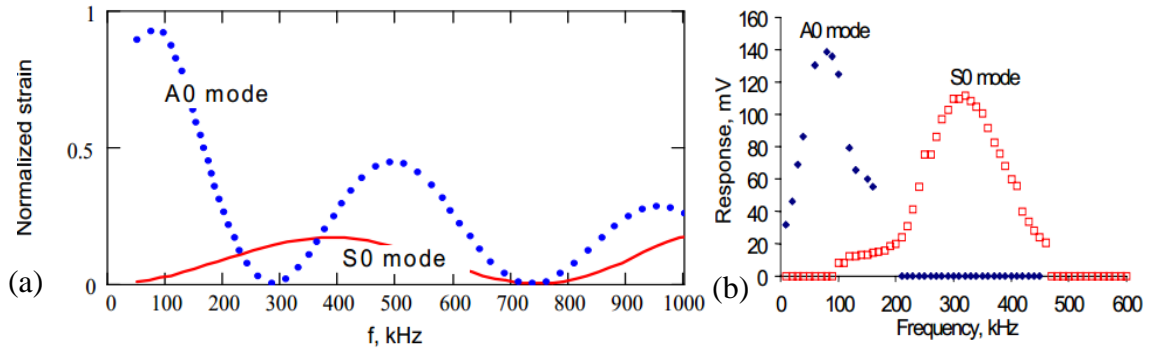
Figure 2.18: (a) Strain Lamb wave tuning results from analytical solution; (b) Experimental results from PWAS response (Giurgiutiu 2003).

CHAPTER 3

MODELING 1-D LAMB WAVE PROPAGATION AND INTERACTION WITH
DAMAGE: WAVEFORMREVEALER 1-D

This chapter presents the theory and an analytical framework for simulating 1-D Lamb

wave propagation and interaction with damage. The method of inserting damage effects

into the analytical model is addressed, including wave transmission, reflection, mode

conversion, and nonlinear higher harmonics. The analytical model is coded into

MATLAB, and a graphical user interface (GUI) WaveFormRevealer 1-D (WFR-1D) is

developed to obtain real-time predictive waveforms for various combinations of sensors,

structural properties, and damage. In this chapter, the theoretical foundation and main

functions of WFR are introduced. Case studies of selective Lamb mode linear and

nonlinear interaction with damage are presented. Experimental and numerical

verifications are carried out.

3.1    INTRODUCTION AND STATE OF THE ART

Guided waves retain a central function in the development of structural health

monitoring (SHM) systems using piezoelectric wafer active sensor (PWAS) principles.

This study focuses on guided plate waves, i.e. Lamb waves, which are guided and

propagate in thin wall structures. The modeling of Lamb waves is challenging, because

Lamb waves propagate in structures with multi-mode dispersive characteristics. At a

certain value of the plate thickness-frequency product, several Lamb modes may exist

simultaneously, and their phase velocities vary with frequency (Graff 1991; Rose 1999;

Giurgiutiu 2008). When Lamb waves interact with damage, they will be transmitted, reflected, scattered and mode converted. Nonlinear interaction with damage may also exist and this will introduce distinctive features like higher harmonics (Jhang 2009; Dutta et al. 2009; Shen and Giurgiutiu 2012). These aspects give rise to the complexity of modeling the interaction between Lamb waves and damage. Typical approaches to solving such complex problems are numerical methods like finite element method (FEM) and boundary element method (BEM). However, to ensure the accuracy of simulating high-frequency waves of short wavelengths, the transient analysis requires considerably small time step and very fine mesh ($\frac{T}{\Delta t}, \frac{\lambda}{l_{FEM}} \geq 20 \sim 30$), which is expensive both in computational time and computer resources (Moser et al. 1999; Gresil et al. 2011). Analytical modeling provides an alternative approach to attack the same problem lower computational costs (Giurgiutiu et al. 2012).

PWAS transducers are a convenient way of transmitting and receiving guided waves in structures for SHM applications (Giurgiutiu 2008). The analytical model of PWAS generated Lamb waves and its tuning effect has been investigated, and a closed-form solution for straight crested guided Lamb wave was derived by Giurgiutiu (2005). Extension of tuning concepts to 2-D analytical models of Lamb waves generated by finite-dimensional piezoelectric transducers was given by Raghavan and Cesnik (2005). These analytical developments facilitate the understanding of PWAS-coupled Lamb waves for SHM applications. However, these analytical solutions only applied to guided wave propagation in pristine structures, whereas the use of Lamb waves in SHM applications requires that their interaction with damage be also studied. After interacting with damage, Lamb waves will carry damage information resulting in waveforms with

special characteristics (phase change, new wave packets generation through mode conversion, and higher-harmonic components, etc.), which need to be investigated for damage detection.

Several researchers have studied the interaction between guided waves and damage analytically using normal-mode expansion and boundary-condition matching (Norris and Venula 1995; Hinders 1996; Vemula and Norris 1997; McKeon and Hinders 1999; Grahn 2002; Moreau et al. 2011; Moreau et al. 2012). Damage interaction coefficients were derived to quantify the guided-wave transmission, reflection, mode conversion, and scatter at the damage site. Due to their mathematical complexity, these analytical solutions are restricted to simple damage geometries: notches, holes, or partial through holes. Extension to more complicated damage geometries has been attempted through series expansion of the rugged damage contour. In the generic case of arbitrary-shape damage, the numerical approaches using space discretization (FEM/BEM) are used due to their convenience, but on the expense of orders of magnitude increase in computational time and/or computer resources.

The design of a SHM system requires computationally-efficient predictive tools that permit the exploration of a wide parameter space to identify the optimal combination between the transducers type, size, number, and guided wave characteristics (mode type, frequency, and wavelength) to achieve best detection and quantification of a certain damage type. Such parameter space exploration desiderate can be best achieved with analytical tools which are fast and efficient.

In this chapter, we describe an analytical approach based on the 1-D (straight crested) guided wave propagation analysis. In our study, we inserted the damage effect

into the analytical model by considering wave transmission, reflection, mode conversion, and higher harmonics components described through damage interaction coefficients at the damage site. We do not attempt to derive these damage interaction coefficients here, but assume that they are available either from literature or from FEM/BEM analysis performed separately in a separate computational module. This analytical approach was coded into MATLAB and the WaveFormRevealer (WFR) graphical user interface was developed. The WFR can generate fast predictions of waveforms resulting from Lamb wave interaction with damage for arbitrary positioning of PWAS transmitters and receivers with respect to damage and with respect to each other. The users may choose their own excitation signal, PWAS size, structural parameters, and damage description. The current chapter focuses WFR-1D for simulation of 1-D (straight crested) guided wave propagation; extension of this approach to 2-D (circular crested) guided wave propagation is introduced in a later chapter where WaveFormRevealer 2-D is coupled with local finite element model forming a highly efficient Combined Analytical/FEM Approach (CAFA).

## 3.2    MODELING OF 1-D LAMB WAVE INTERACTION WITH DAMAGE

This section addresses the analytical modeling of Lamb wave propagation in plate waveguides. The first part introduces the analytical model of multi-mode wave propagation in pristine structures. The second part illustrates the methodology of inserting damage effects into the analytical model.

### 3.2.1    ANALYTICAL MODELING OF LAMB WAVE PROPAGATION IN A PRISTINE PLATE

One aspect of the difficulties in modeling Lamb wave propagation is due to their multi-mode feature. WFR is capable of modeling multi-mode Lamb wave propagation in

structures. From the Rayleigh-Lamb equation, the existence of certain Lamb mode depends on the plate thickness-frequency product. The fundamental S0 and A0 modes will always exist, but the higher modes will only appear beyond their respective cutoff frequencies (Graff 1991).

This section describes how an electrical tone burst applied to a transmitter PWAS transducer (T-PWAS) propagates through a structural waveguide to the receiver PWAS transducer (R-PWAS) in pitch-catch mode (Figure 3.1).

The propagation takes place through ultrasonic guided Lamb waves which are generated at the T-PWAS through piezoelectric transduction and then captured and converted back into electric signal at the R-PWAS. Since several Lamb wave modes traveling with different wave speeds exist simultaneously, the electrical tone-burst applied on the T-PWAS will generate several wave packets. These wave packets will travel independently through the waveguide and will arrive at different times at the R-PWAS where they are converted back into electric signals through piezoelectric transduction.
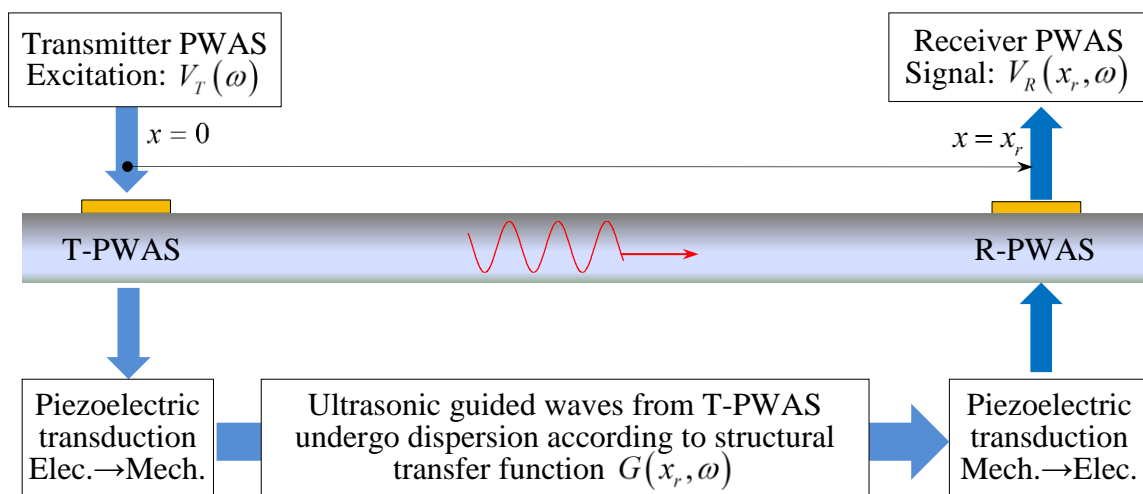


Figure 3.1: A pitch-catch configuration between a T-PWAS and a R-PWAS.

The predictive analytical model for Lamb wave propagation between the T-PWAS and R-PWAS is constructed in frequency domain. The modeling flowchart is shown in Figure 3.2a (Shen and Giurgiutiu 2014).
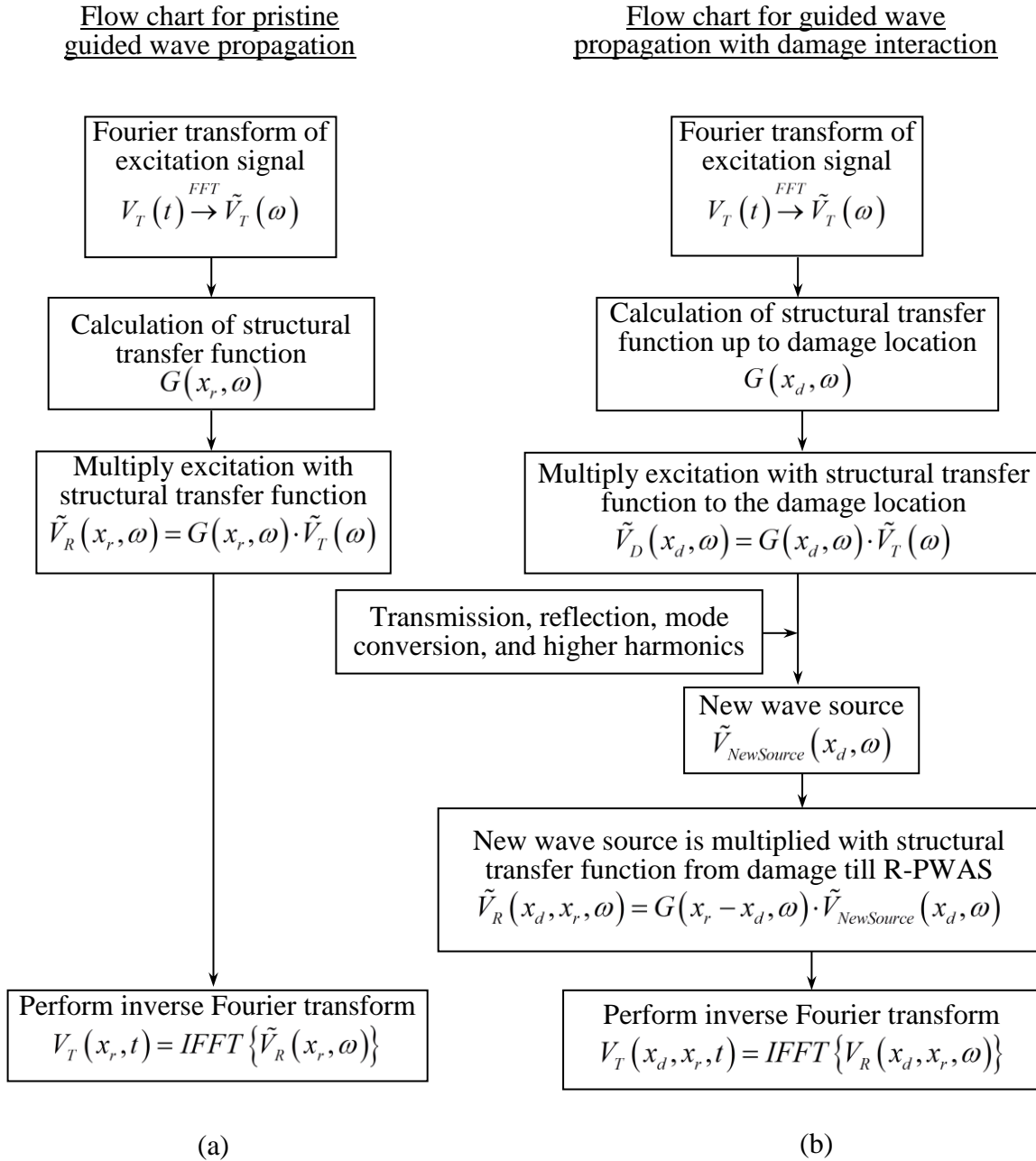


Figure 3.2: WaveFormRevealer flow charts: (a) propagation in a pristine structural waveguide; (b) propagation and interaction with damage at location $x_d$.

The detailed steps of model construction are listed below:

<u>STEP 1</u>: Perform Fourier transform of the time-domain excitation signal $V_T(t)$ to obtain the frequency domain excitation spectrum, $\tilde{V}_T(\omega)$. For a tone burst, the signal $V_T(t)$ and its Fourier transform $\tilde{V}_T(\omega)$ look like in Figure 3.3.

Tone burst of frequency $\omega_c$      Frequency spectrum of tone burst
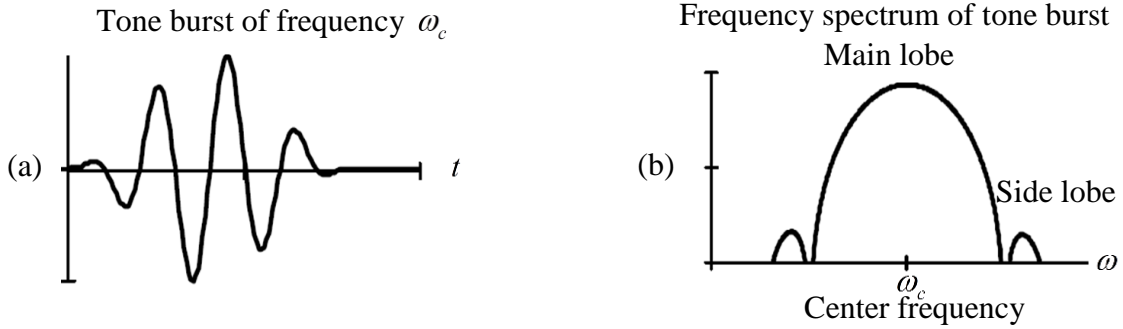


Figure 3.3: Tone burst signal: (a) time domain; (b) frequency domain. (from Giurgiutiu 2008, page 153).

<u>STEP 2</u>: Calculate the frequency-domain structural transfer function $G(x_r,\omega)$ from T-PWAS to R-PWAS. The structure transfer function $G(x_r,\omega)$ is given by Eq. (99) in Giurgiutiu (2007), page 327, which gives the in-plane wave strain at the plate surface as

$$\varepsilon_x(x,t) = -i\frac{a\tau_0}{\mu}\left\{\sum_{\xi^S}(\sin\xi^S a)\frac{N_S(\xi^S)}{D_S'(\xi^S)}e^{-i(\xi^S x-\omega t)} + \sum_{\xi^A}(\sin\xi^A a)\frac{N_A(\xi^A)}{D_A'(\xi^A)}e^{-i(\xi^A x-\omega t)}\right\} \quad (3.1)$$

where $\xi$ is the frequency dependent wave number of each Lamb wave mode and the superscripts S and A refer to symmetric and antisymmetric Lamb wave modes. If only the two fundamental modes, S0 and A0, are present, then $G(x_r,\omega)$ can be written as

$$G(x_r,\omega) = S(\omega)e^{-i\xi^S x_r} + A(\omega)e^{-i\xi^A x_r} \quad (3.2)$$

$$S(\omega) = \kappa_{PWAS}\,\sin\xi^S a\,\frac{N_S(\xi^S)}{D_S'(\xi^S)}, \quad A(\omega) = \kappa_{PWAS}\,\sin\xi^A a\,\frac{N_A(\xi^A)}{D_A'(\xi^A)} \quad (3.3)$$

37

where

$$N_s(\xi) = \xi\beta(\xi^2 + \beta^2)\cos\alpha d \cos\beta d;$$

$$D_s = (\xi^2 - \beta^2)^2 \cos\alpha d \sin\beta d + 4\xi^2\alpha\beta \sin\alpha d \cos\beta d$$

$$N_A(\xi) = -\xi\beta(\xi^2 + \beta^2)\sin\alpha d \sin\beta d; \tag{3.4}$$

$$D_A = (\xi^2 - \beta^2)^2 \sin\alpha d \cos\beta d + 4\xi^2\alpha\beta \cos\alpha d \sin\beta d$$

$$\alpha^2 = \frac{\omega^2}{c_p^2} - \xi^2; \quad \beta^2 = \frac{\omega^2}{c_s^2} - \xi^2; \quad c_p = \sqrt{\frac{\lambda + 2\mu}{\rho}}; \quad c_s = \sqrt{\frac{\mu}{\rho}}; \quad \kappa_{PWAS} = -i\frac{a\tau_0}{\mu}$$

$\kappa_{PWAS}$ is the complex transduction coefficient that converts applied voltage into guided wave strain at the T-PWAS; $a$ is half length of PWAS size; $d$ is plate half thickness. The modal participation functions $S(\omega)$ and $A(\omega)$ determine the amplitudes of the S0 and A0 wave modes. The terms $\sin(\xi^S a)$ and $\sin(\xi^A a)$ control the tuning between the PWAS transducer and the Lamb waves. $\lambda$ and $\mu$ are Lame's constants of the structural material; $\rho$ is the material density. The wavenumber $\xi$ of a specific mode for certain frequency $\omega$ is calculated from Rayleigh-Lamb equation:

$$\frac{\tan\beta d}{\tan\alpha d} = \left[\frac{-4\alpha\beta\xi^2}{(\xi^2 - \beta^2)^2}\right]^{\pm 1} \tag{3.5}$$

where +1 exponent corresponds to symmetric Lamb wave modes and -1 exponent corresponds to antisymmetric Lamb wave modes.

STEP 3: Multiply the structural transfer function by frequency-domain excitation signal (Figure 3.3b) to obtain the frequency domain signal at the R-PWAS, i.e., $\tilde{V}_R(x_r, \omega) = G(x_r, \omega) \cdot \tilde{V}_T(\omega)$. Hence, the wave arriving at the R-PWAS location is

$$\tilde{V}_R(x_r, \omega) = S(\omega)\tilde{V}_T(\omega)e^{-i\xi^S x_r} + A(\omega)\tilde{V}_T(\omega)e^{-i\xi^A x_r} \tag{3.6}$$

38

This signal in Eq. (3.6) can be decomposed into symmetric and antisymmetric components

$$\tilde{V}_R^S(x_r, \omega) = S(\omega)\tilde{V}_T(\omega)e^{-i\xi^S x_r} \tag{3.7}$$

$$\tilde{V}_R^A(x_r, \omega) = A(\omega)\tilde{V}_T(\omega)e^{-i\xi^A x_r} \tag{3.8}$$

STEP 4: Perform the inverse Fourier transform to obtain the time domain wave signal at the R-PWAS, i.e.,

$$V_R(x_r, t) = IFFT\{\tilde{V}_R(x_r, \omega)\} \tag{3.9}$$

Due to the multi-mode character of guided Lamb wave propagation, the received signal has at least two separate wave packets, S0 and A0 (Figure 3.4).
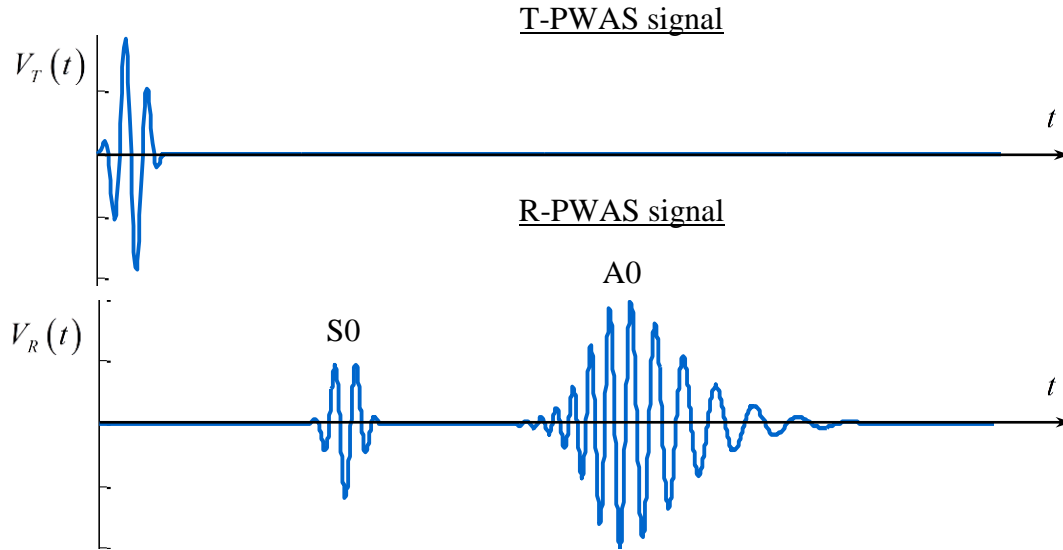


Figure 3.4: T-PWAS signal and R-PWAS signal.

This analysis can be extended to include higher guided wave modes (S1, A1, etc.) , i.e.,

$$\tilde{V}_R(x_r, \omega) = \sum_{\xi^S} S(\omega)\tilde{V}_T(\omega)e^{-i\xi^S x_r} + \sum_{\xi^A} A(\omega)\tilde{V}_T(\omega)e^{-i\xi^A x_r} \tag{3.10}$$

All the wave modes propagate independently in the structure. The final waveform will be the superposition of all the propagating waves and will have the contribution from each Lamb mode.

### 3.2.2 INSERTION OF DAMAGE EFFECTS INTO THE ANALYTICAL MODEL

Figure 3.5 shows the pitch-catch active sensing method for damage detection. The T-PWAS transducer generates ultrasonic guided waves which propagate into the structure, interact with structural damage at $x = x_d$, carry the damage information with them, and are picked up by the R-PWAS transducer at $x = x_r$.



| Transmitter PWAS Excitation: $V_T(\omega)$ | | Receiver PWAS Signal: $V_R(x_d, x_r, \omega)$ |

$x = 0$      $x = x_d$      $x = x_r$

Damage

T-PWAS                                                      R-PWAS

| Piezoelectric transduction Elec.→Mech | Damage: new wave source Transmission, reflection, mode conversion, and higher harmonics | Piezoelectric transduction Mech.→Elec. |

| Ultrasonic guided waves from T-PWAS Transfer function $G(x_d, \omega)$ | Ultrasonic waves with damage information Transfer function $G(x_r - x_d, \omega)$ |

Figure 3.5: A pitch-catch configuration between a T-PWAS and a R-PWAS.

To model the damage effect on Lamb wave propagation, we consider the damage as a new wave source at $x = x_d$ and we add mode conversion and nonlinear sources at the damage location through damage interaction coefficients. The predictive analytical model for Lamb wave interaction with damage is constructed in frequency domain in the following steps:

STEP 1: This step is identical to step 1 of the pristine case. Perform Fourier transform of the time-domain excitation signal $V_T(t)$ to obtain the frequency domain excitation spectrum, $\tilde{V}_T(\omega)$.

STEP 2: Calculate the frequency-domain structural transfer function up to the damage location, $G(x_d, \omega)$. The structure transfer function $G(x_d, \omega)$ is similar to Eq. (3.6) of previous section, only that $x = x_d$, i.e.,

$$\tilde{V}_D(x_d, \omega) = S(\omega)\tilde{V}_T(\omega)e^{-i\xi^S x_d} + A(\omega)\tilde{V}_T(\omega)e^{-i\xi^A x_d} \tag{3.11}$$

STEP 3: Multiply the structural transfer function by frequency-domain excitation signal to obtain the frequency domain signal at the damage location, i.e., $\tilde{V}_D(x_d, \omega) = G(x_d, \omega) \cdot \tilde{V}_T(\omega)$. Hence, the signal at the damage location is

$$\tilde{V}_D(x_d, \omega) = S(\omega)\tilde{V}_T(\omega)e^{-i\xi^S x_d} + A(\omega)\tilde{V}_T(\omega)e^{-i\xi^A x_d} \tag{3.12}$$

This signal could be decomposed into symmetric and antisymmetric components

$$\tilde{V}_D^S(x_d, \omega) = S(\omega)\tilde{V}_T(\omega)e^{-i\xi^S x_d} \tag{3.13}$$

$$\tilde{V}_D^A(x_d, \omega) = A(\omega)\tilde{V}_T(\omega)e^{-i\xi^A x_d} \tag{3.14}$$

STEP 4: The wave signal at the damage location takes the damage information by considering transmission, reflection, mode conversion, and higher harmonics. Each of these addition phenomena is modeled as a new wave source at the damage location using damage interaction coefficients (Figure 3.6). We distinguish two damage interaction types: (a) linear, and (b) nonlinear, as discussed next.

3.2.2.1 Linear damage interaction

Wave transmission, reflection, and mode conversion are realized by using complex-amplitude damage interaction coefficients. Our notations are as follows: we use three letters to describe the interaction phenomena, with the first letter denoting the incident wave type, the second letter standing for resulting wave type, and the third letter meaning propagation direction (transmission/reflection). For instance, SST (symmetric-symmetric-transmission) means the incident symmetric waves transmitted as symmetric waves, while SAT (symmetric-antisymmetric-transmission) means incident symmetric waves transmitted and mode converted to antisymmetric waves. Thus the complex-amplitude damage interaction coefficient $C_{SST}e^{-i\varphi_{SST}}$ denotes the transmitted symmetric mode generated by incident symmetric mode with magnitude $C_{SST}$ and phase $\varphi_{SST}$. Similarly, $C_{SAT}e^{-i\varphi_{SAT}}$ represents the transmitted antisymmetric mode generated by incident symmetric mode with magnitude $C_{SAT}$ and phase $\varphi_{SAT}$. These coefficients are determined by the features of the damage and are to be imported into the WFR model.

3.2.2.2 Nonlinear damage interaction

The center frequency of waves arriving at the damage location can be obtained from Eq. (3.13) and (3.14) as $\omega_c$. The 2nd and 3rd higher harmonics act as wave sources with center frequencies of $2\omega_c$ and $3\omega_c$ respectively. Modeling of higher harmonics is achieved by moving the frequency domain signal at the damage location to the right hand side of the frequency axis by $\omega_c$ and $2\omega_c$, i.e., $\tilde{V}_{2D}(x_d,\omega)=\tilde{V}_D(x_d,\omega-\omega_c)$ and $\tilde{V}_{3D}(x_d,\omega)=\tilde{V}_D(x_d,\omega-2\omega_c)$ represent the 2nd and 3rd higher harmonics nonlinear wave source.

The nonlinear damage interaction coefficients are defined in the same way as the linear ones. For instance, the complex-amplitude damage interaction coefficient $C_{SST}^{M} \cdot e^{-i\varphi_{SST}^{M}}$ denotes the $M$th higher harmonics transmitted symmetric mode generated by incident symmetric mode with magnitude $C_{SST}^{M}$ and phase $\varphi_{SST}^{M}$.
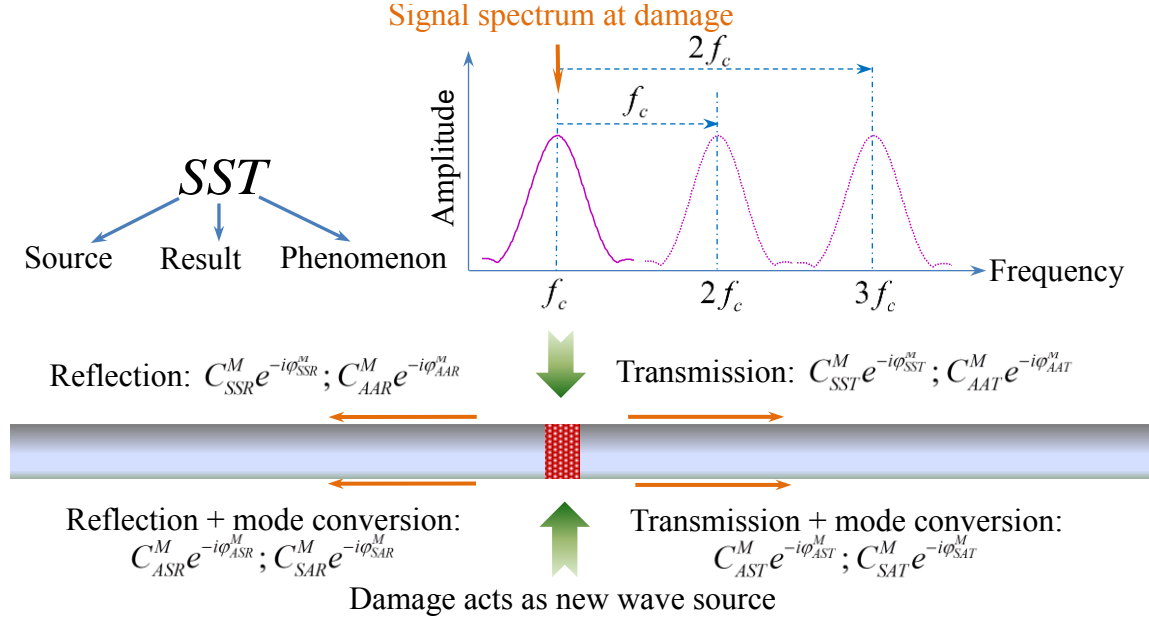


Figure 3.6: Modeling wave transmission, reflection, mode conversion, higher harmonics components ( $f_c$ is the center frequency of wave signal arriving at the damage).

STEP 5: The guided waves from the new wave sources at the damage location propagate through the rest of the structure and arrive at the R-PWAS. The received wave signal is calculated in frequency domain as

$$\tilde{V}_R\left(x_d, x_r, \omega\right) = \sum_{M=1}^{m}\left[C_{SST}^{M} e^{-i\varphi_{SST}^{M}} \cdot \tilde{V}_{MD}^{S}\left(x_d, \omega\right) + C_{AST}^{M} e^{-i\varphi_{AST}^{M}} \cdot \tilde{V}_{MD}^{A}\left(x_d, \omega\right)\right] e^{-i\xi^{S}\left(x_r - x_d\right)}$$
$$+ \sum_{M=1}^{m}\left[C_{AAT}^{M} e^{-i\varphi_{AAT}^{M}} \cdot \tilde{V}_{MD}^{A}\left(x_d, \omega\right) + C_{SAT}^{M} e^{-i\varphi_{SAT}^{M}} \cdot \tilde{V}_{MD}^{S}\left(x_d, \omega\right)\right] e^{-i\xi^{A}\left(x_r - x_d\right)}$$

(3.15)

where $m$ is the number of higher harmonics considered. For linear interaction with damage, $m$ equals to one.

43

STEP 6: Perform inverse Fourier transform to obtain the time domain receiver sensing signal

$$V_R(x_d, x_r, t) = IFFT\{\tilde{V}_R(x_d, x_r, \omega)\} \tag{3.16}$$

It should be noted that the above analysis only considers S0 and A0 modes. But the principle could be easily extended to higher modes (S1, A1, etc.). The difficulty with extending to higher modes will be on defining the increasing number of transmission, reflection, mode conversion coefficients. For each excited Lamb mode, the interaction with damage may result in more mode conversion possibilities. In this study, the WFR has been designed to simulate: (a) multimode (S0, A0, S1, A1) Lamb waves propagation in pristine plates; (b) fundamental modes (S0 and A0) Lamb waves interaction with damage.

## 3.3    WAVEFORMREVEALER INTERFACE AND MAIN FUNCTIONS

The analytical representation of this process was coded in MATLAB and resulted in the WFR GUI shown in Figure 3.7.

WFR allows users to control several parameters: structure material properties, PWAS size, location of sensors, location of damage, damage type (linear/nonlinear damage), and excitation signal (frequencies, count numbers, signal mode excitation, arbitrary waveform type, etc.). Dual display of waveforms allows for the sensing signals to be shown at two different sensor locations. For instance, Figure 3.7 shows two receiver waveforms at locations $x_1 = 0\,\mathrm{mm}$ and $x_2 = 500\,\mathrm{mm}$ as measured from the transmitter (in this case $x_1 = 0\,\mathrm{mm}$ means that receiver PWAS-1 collocated with the transmitter PWAS). Thus, PWAS-1 shows the reflections from damage, and PWAS-2 shows the signal modified after passing through the damage. Users are able to conduct rapid

parametric studies with WFR. It may take several hours for commercial finite element software to obtain an acceptably-accurate solution for high frequency, long distance propagating waves; but it takes only several seconds to obtain the same solution with WFR. Besides analytical waveform solutions, the WFR can also provide users with wave speed dispersion curves, tuning curves, frequency components of received wave packets, structure transfer function, etc. All the calculated results are fully available to the user, and can be exported as Excel. Figure 3.8 shows a case study for Lamb wave propagation of a 100 kHz tone burst in a 1-mm thick aluminum plate, presenting: (1) the dispersion curves; (2) the excitation spectrum overlap with the S0 and A0 tuning curves; (3) the spectra of the S0 and A0 packets displaying frequency shifts; (4) the structure transfer function $G(x, \omega)$.
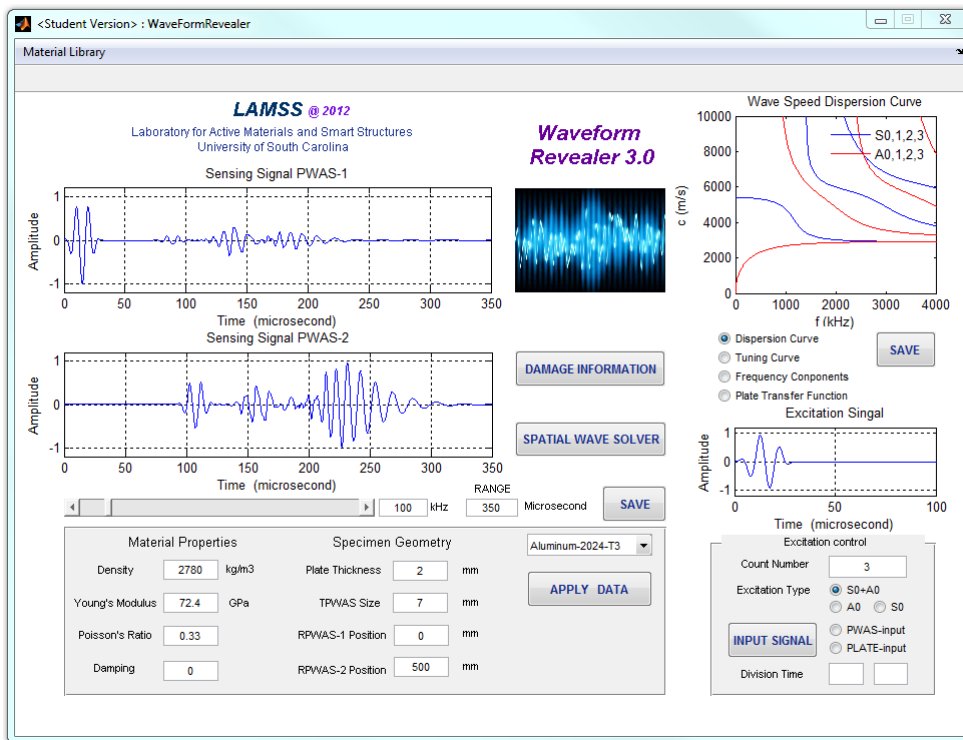


Figure 3.7: Main GUI of WaveFormRevealer.

45
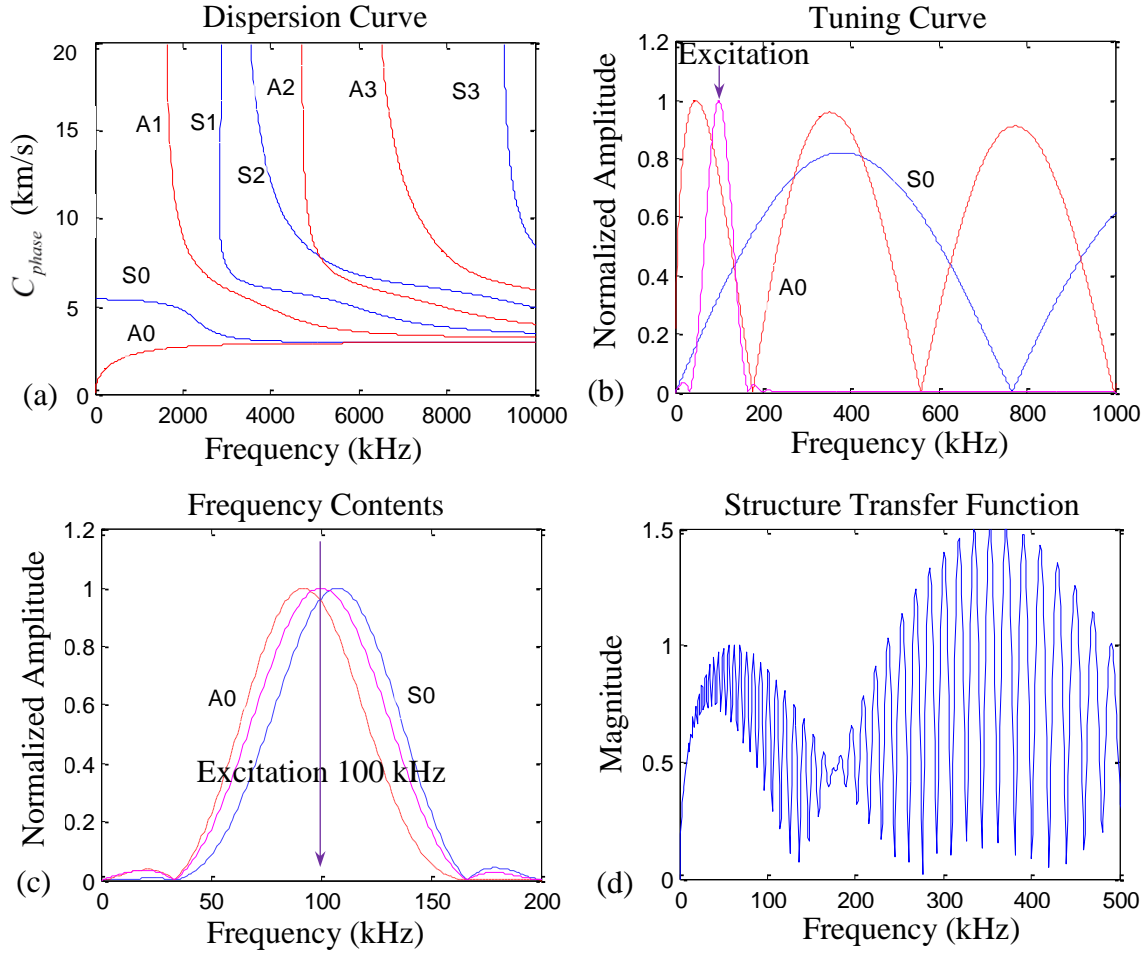
Figure 3.8: Calculation of various quantities in Lamb wave propagation: (a) wave speed dispersion curve; (b) tuning curve; (c) frequency contents of received wave packets; (d) structure transfer function.

Besides the main interface, WFR has two sub-interfaces shown in Figure 3.9: (1) damage information platform; (2) guided wave spatial propagation solver. The damage information platform allows users to input the damage location and damage interaction coefficients. For example, SST represents the magnitude of transmitted S0 mode generated by an incoming S0 mode; whereas, SAT and phi-SAT represent the magnitude and phase of the transmitted A0 mode resulting from the mode-conversion of an incoming S0 mode. The values of these damage interaction coefficients are not calculated

by the WFR. This gives the users the freedom to define their own specific problem. For instance, a particular type of damage (plastic zone, corrosion, or fatigue cracks) with certain degree of severity will have different interaction characteristics with the interrogating guided waves. These coefficients may be determined experimentally or calculated through other methods (analytical, FEM, BEM, etc.). Among all the above methods, FEM approach shows good results for obtaining the interaction coefficients of arbitrary shaped damage. Successful examples and details are given by Velichko and Wilcox (2011; 2012) and Moreau et al. (2012). In an example presented later in this study, we used a trial-and-error approach to tune the WFR coefficients to the data obtained from experiments and finite element simulations.



(a)             (b)
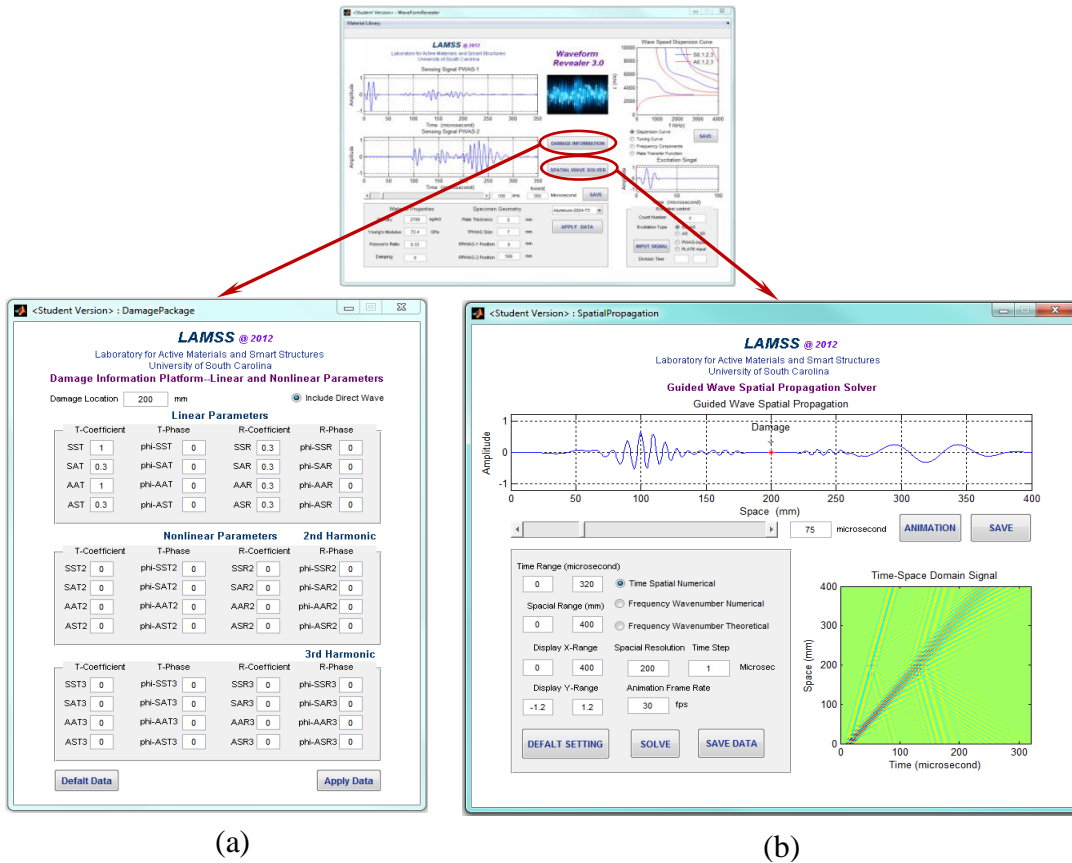
Figure 3.9: User interfaces: (a) damage information platform; (b) guided wave spatial propagation solver.

The spatial propagation solver is like a B-scan. Using the analytical procedure, we obtain the time domain waveform solution at various locations along the structure. Thus, the time domain waveform solutions of a sequence of points along the wave propagation path are obtained. If we select the sequence of solution points fine enough, a time-spatial domain solution of the wave field is obtained. The spatial solution of wave field at a particular time instance is available as shown in Figure 3.9b. After the time-spatial solution of wave field is obtained, we can do the frequency-wavenumber analysis (Ruzzene 2007) to see the wave components of the signal (Figure 3.10). These will be illustrated in the case studies discussed later in this chapter.
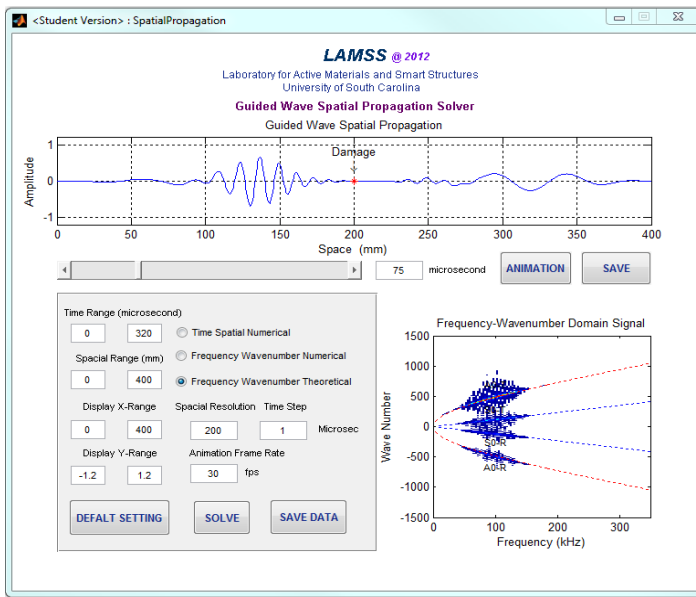


Figure 3.10: Frequency-wavenumber display window.

## 3.4    CASE STUDIES

### 3.4.1    LINEAR INTERACTION WITH DAMAGE OF SELECTIVE LAMB WAVE MODES

WFR allows users to select single mode (S0/A0) or multimode (S0 and A0) to be excited into the structure. Three test cases were conducted: (a) incident S0 wave linear interaction with damage, (b) incident A0 wave linear interaction with damage, and (c)

combined S0 and A0 waves linear interaction with damage. The test case setup is shown in Figure 3.11. The transmitter PWAS (T-PWAS) and receiver PWAS (R-PWAS) are placed 600 mm away from each other on a 1-mm thick aluminum 2024-T3 plate. The damage is placed 200 mm from the T-PWAS. A 5-count Hanning window modulated tone burst centered at 100 kHz is used as the excitation. The time domain and the time-frequency domain signals of the test cases are shown in Figure 3.12 (single S0 mode excitation), Figure 3.13 (single A0 mode excitation), and Figure 3.14 (S0 and A0 multi-mode excitation).
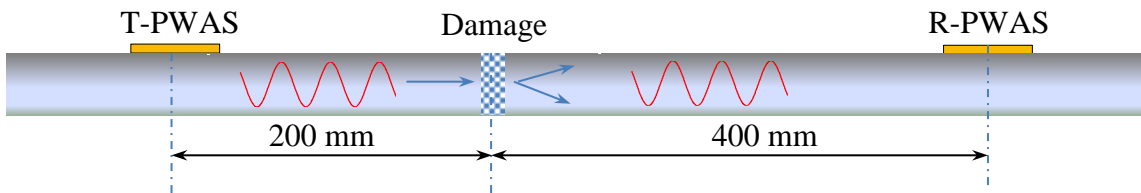


Figure 3.11: Test case setup for pitch-catch Lamb wave interaction with damage.
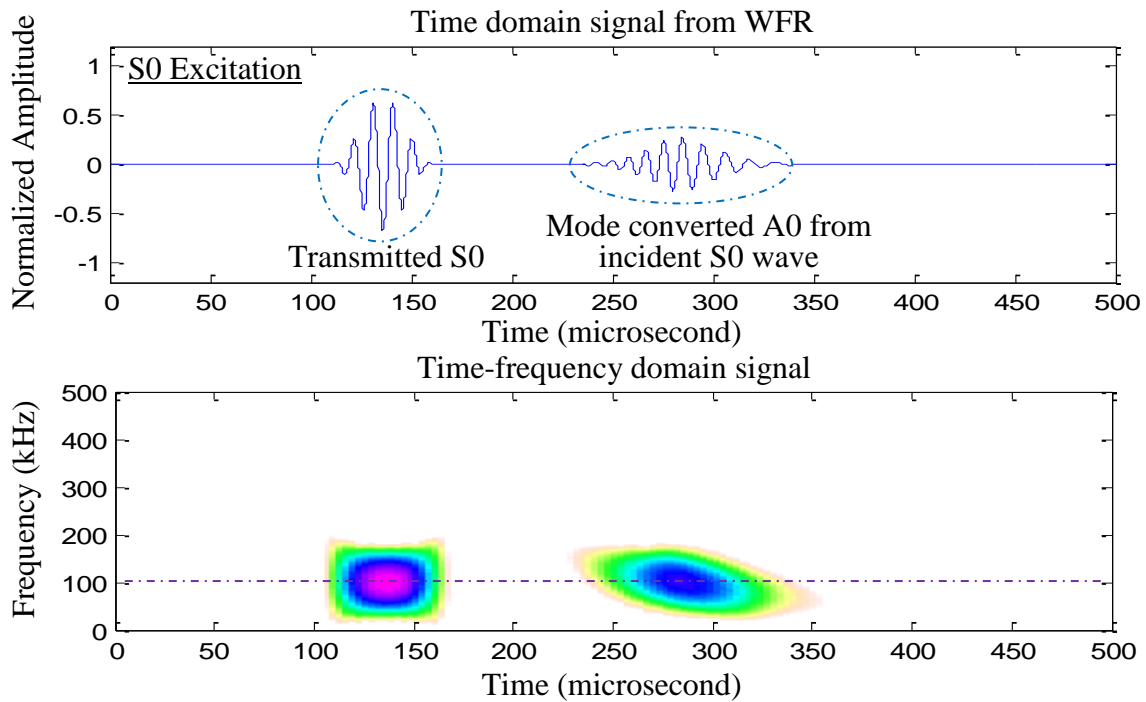


Figure 3.12: Simulation of linear interaction between Lamb waves and damage: S0 mode excitation. It should be noted that no higher harmonics are observed.
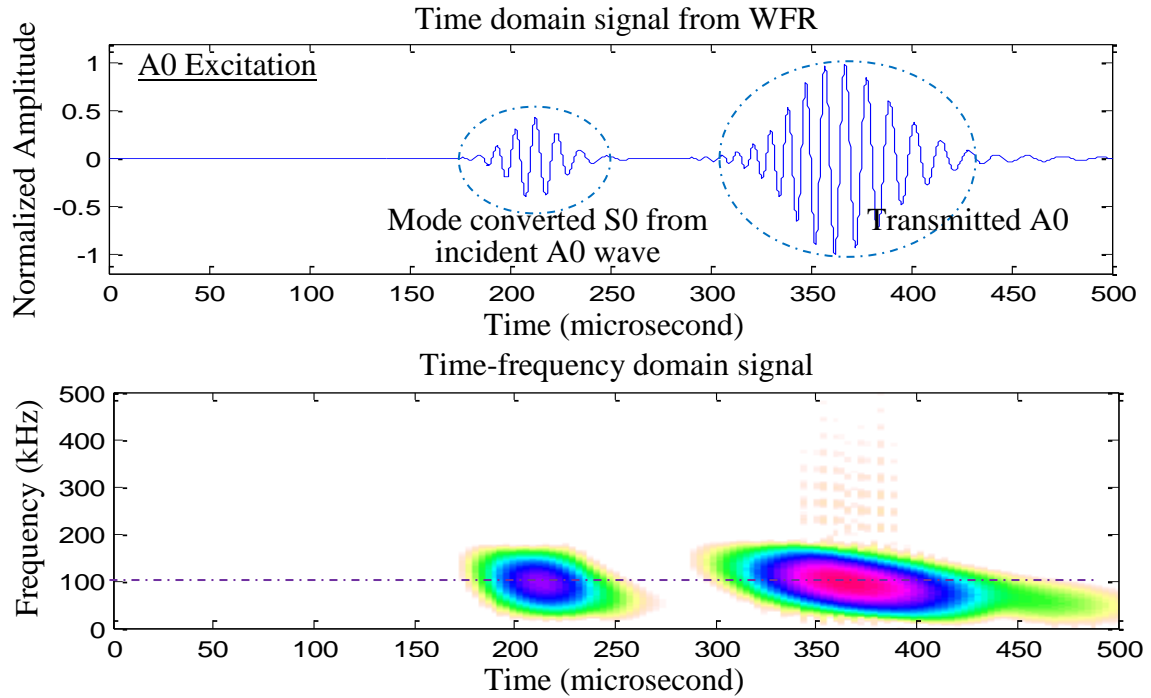
Figure 3.13: Simulation of linear interaction between Lamb waves and damage: A0 mode excitation. It should be noted that no higher harmonics are observed.
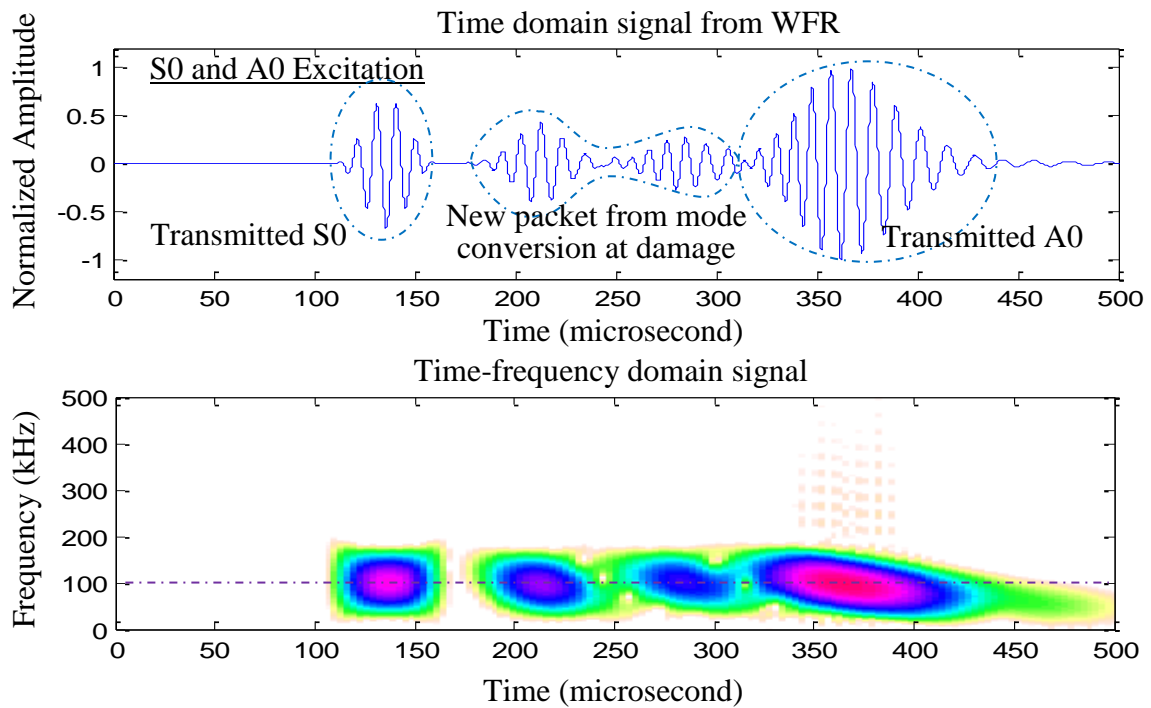


Figure 3.14: Simulation of linear interaction between Lamb waves and damage: S0 and A0 mode excitation. It should be noted that no higher harmonics are observed.

Figure 3.12 through Figure 3.14 show that new wave packets appear due to the interaction between interrogation Lamb waves and damage. The incident S0 wave will generate A0 wave component from mode conversion at the damage; whereas the incident A0 wave will generate S0 wave component from mode conversion at the damage. However, from the time-frequency analysis, it could be observed that after linear interaction, the frequency spectrum of the waves still center around the excitation frequency 100 kHz. No higher harmonic frequency components are observed.

3.4.2 NONLINEAR INTERACTION WITH DAMAGE OF SELECTIVE LAMB WAVE MODES

To investigate nonlinear interaction between Lamb waves and damage, three simulations were carried out: (a) incident S0 wave nonlinear interaction with damage; (b) incident A0 wave nonlinear interaction with damage; (c) combined S0 and A0 waves nonlinear interaction with damage. The test case setup is the same as shown in Figure 3.11, only the interaction with damage is nonlinear. The time signals and the time-frequency analysis of the test cases are shown in Figure 3.15 (single S0 mode excitation), Figure 3.16 (single A0 mode excitation), and Figure 3.17 (S0 and A0 multi-mode excitation).

Figure 3.15 through Figure 3.17 show that after nonlinear interaction with the damage, the waveforms become distorted and contain distinctive nonlinear higher harmonics. For S0 waves which are less dispersive at the given frequency range, the nonlinear higher harmonics stay inside the wave packet. However, for A0 waves which are dispersive at the given frequency range, the higher harmonic components travel faster, leading the way and may escape from the fundamental wave packet.
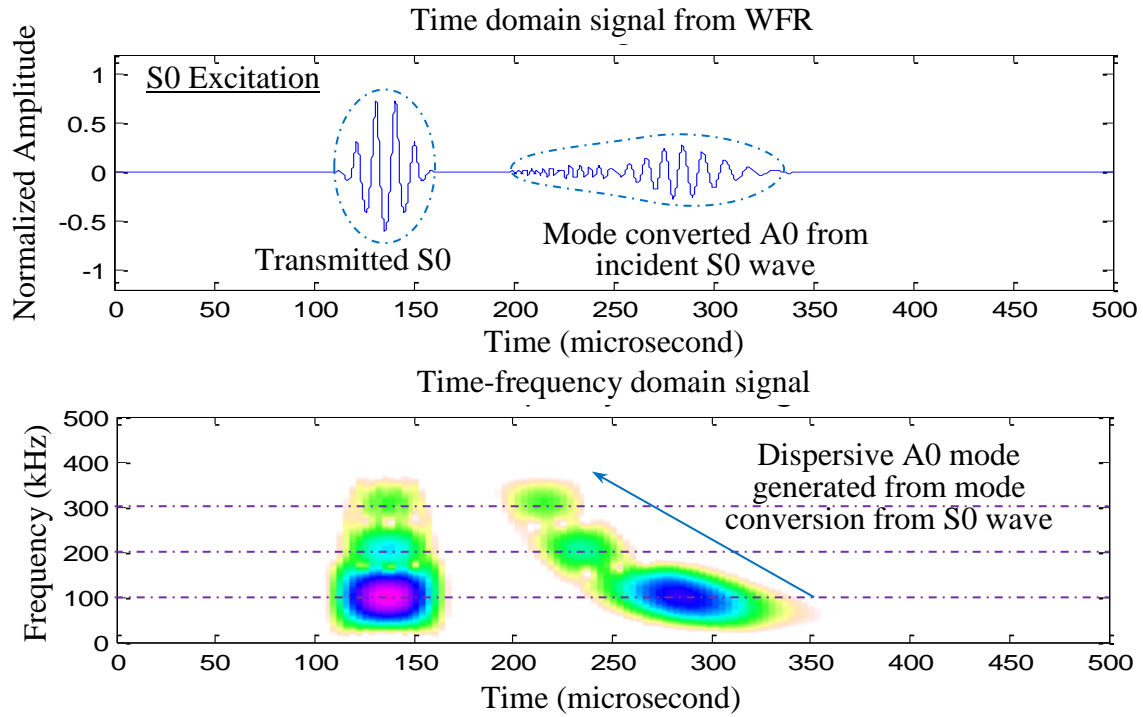
Figure 3.15: Simulation of nonlinear interaction between Lamb waves and damage: S0 mode excitation. It should be noted that distinctive higher harmonics are observed.
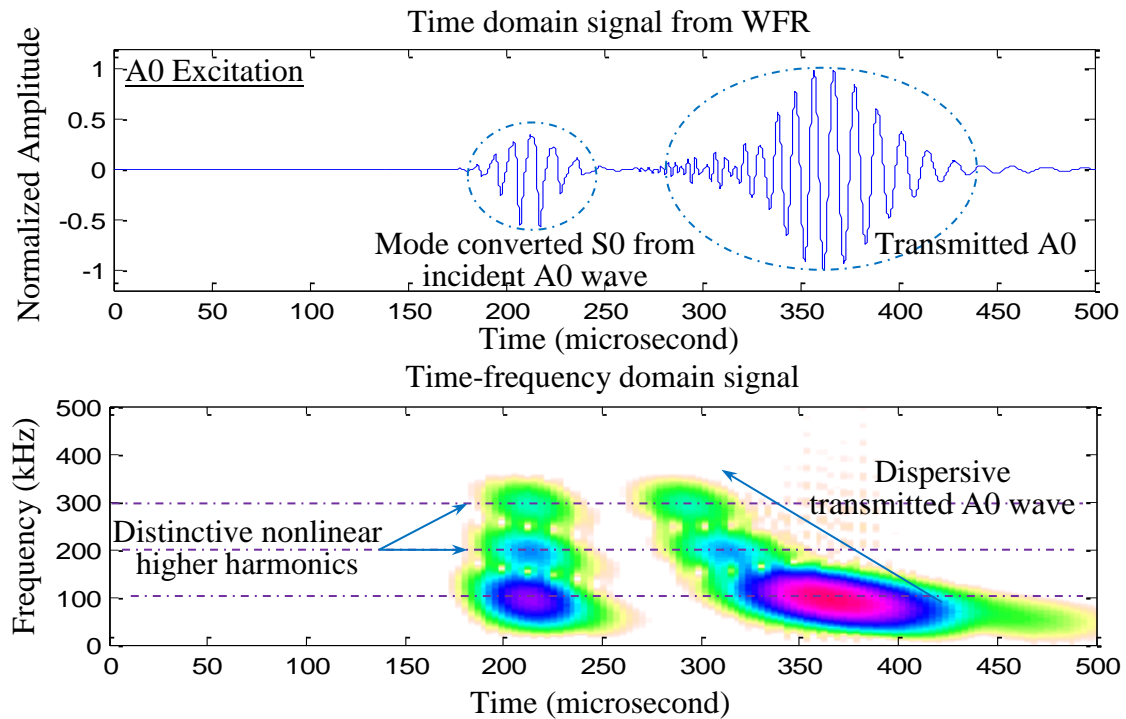


Figure 3.16: Simulation of nonlinear interaction between Lamb waves and damage: A0 mode excitation. It should be noted that distinctive higher harmonics are observed.
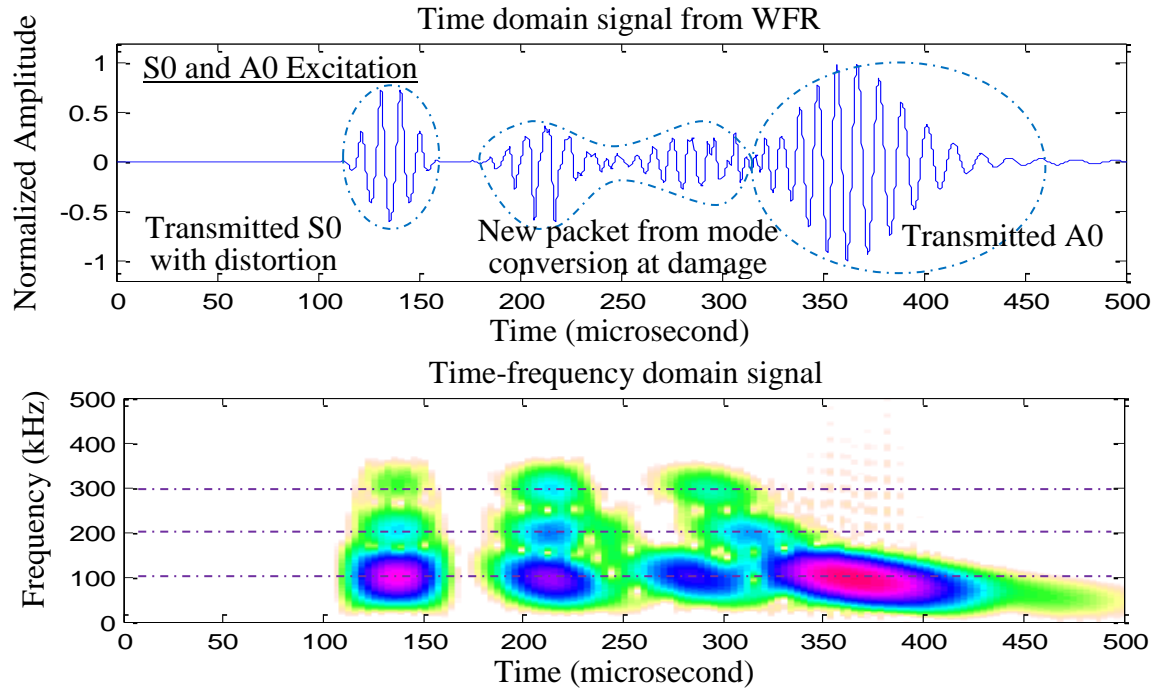
Figure 3.17: Simulation of nonlinear interaction between Lamb waves and damage: S0 and A0 mode excitation. It should be noted that distinctive higher harmonics are observed.

## 3.5  EXPERIMENTAL AND NUMERICAL VERIFICATIONS

### 3.5.1  MULTI-MODE LAMB WAVE PROPAGATION IN A PRISTINE PLATE

In our study, two PWAS transducers were mounted on a 3.17-mm thick aluminum 7075-T6 plate. Figure 3.18 shows the experiment setup. The transmitter PWAS (T-PWAS) sent out ultrasonic guided waves into the structure. The guided waves i.e., Lamb waves propagated in the plate, undergoing dispersion and were picked up by the receiver PWAS (R-PWAS). The Lamb waves are multi-modal, hence several wave packets appeared in the received signal. An Agilent 33120A Arbitrary Waveform Generator was used to generate 3-count Hanning window modulated tone burst excitations. A Tektronix Digital Oscilloscope is used to record the experimental waveforms. The excitation frequency was swept from 300 kHz to 600 kHz.

53
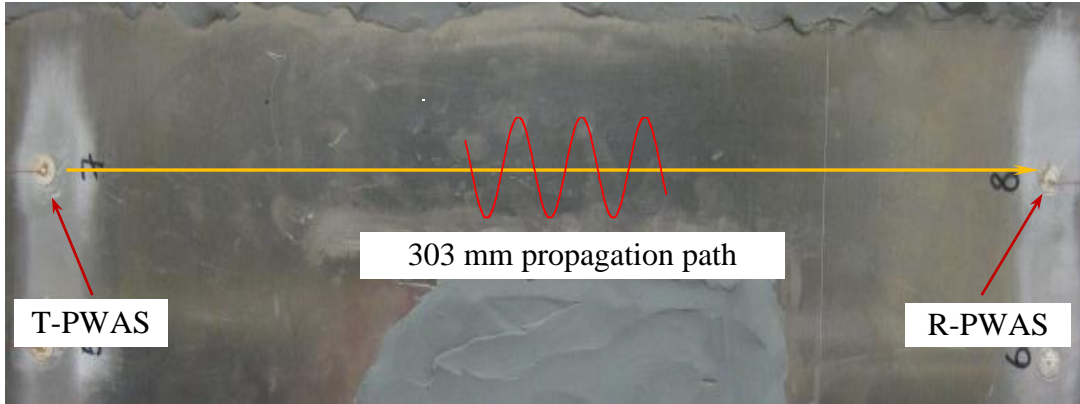
Figure 3.18: Experiment setup for multi-mode Lamb wave propagation.

Corresponding plate material, thickness, PWAS size, and sensing location information is input into WFR. The analytical waveforms of various frequencies are obtained. Figure 3.19 shows the comparison between analytical solution from WFR and experimental data.

It can be observed that at 300 kHz, only S0 and A0 modes exist. The WFR solution matches well with experimental data. At 450 kHz, S0 mode become more dispersive; besides S0 and A0 modes, A1 mode starts to pick up with highly dispersive feature. At 600 kHz, S0, A0, and A1 modes exist simultaneously. The simulation results and the experimental data have slight differences due to the fact that 1-D analytical formulas and pin force excitation assumptions are used in this study.

To further validate WFR predictions, we also conducted 1-D wave propagation FEM simulations with pin force excitation. Figure 3.20 shows the comparison between WFR and 1-D wave propagation FEM simulations. It can be observed that the 300 kHz and 450 kHz waveforms match very well between WFR and 1-D FEM. 600 kHz signals also have reasonably good agreement. It should be noted, even for 1-D wave propagation FEM simulation, the 600 kHz wave computation requires considerably small element size

and time marching step. The FEM simulation for such high frequency, short wavelength situation is becoming prohibitive due to the heavy consumption of computation time and computer resources. On the contrast, WFR only requires several seconds to obtain the same results due to its highly efficient analytical formulation.
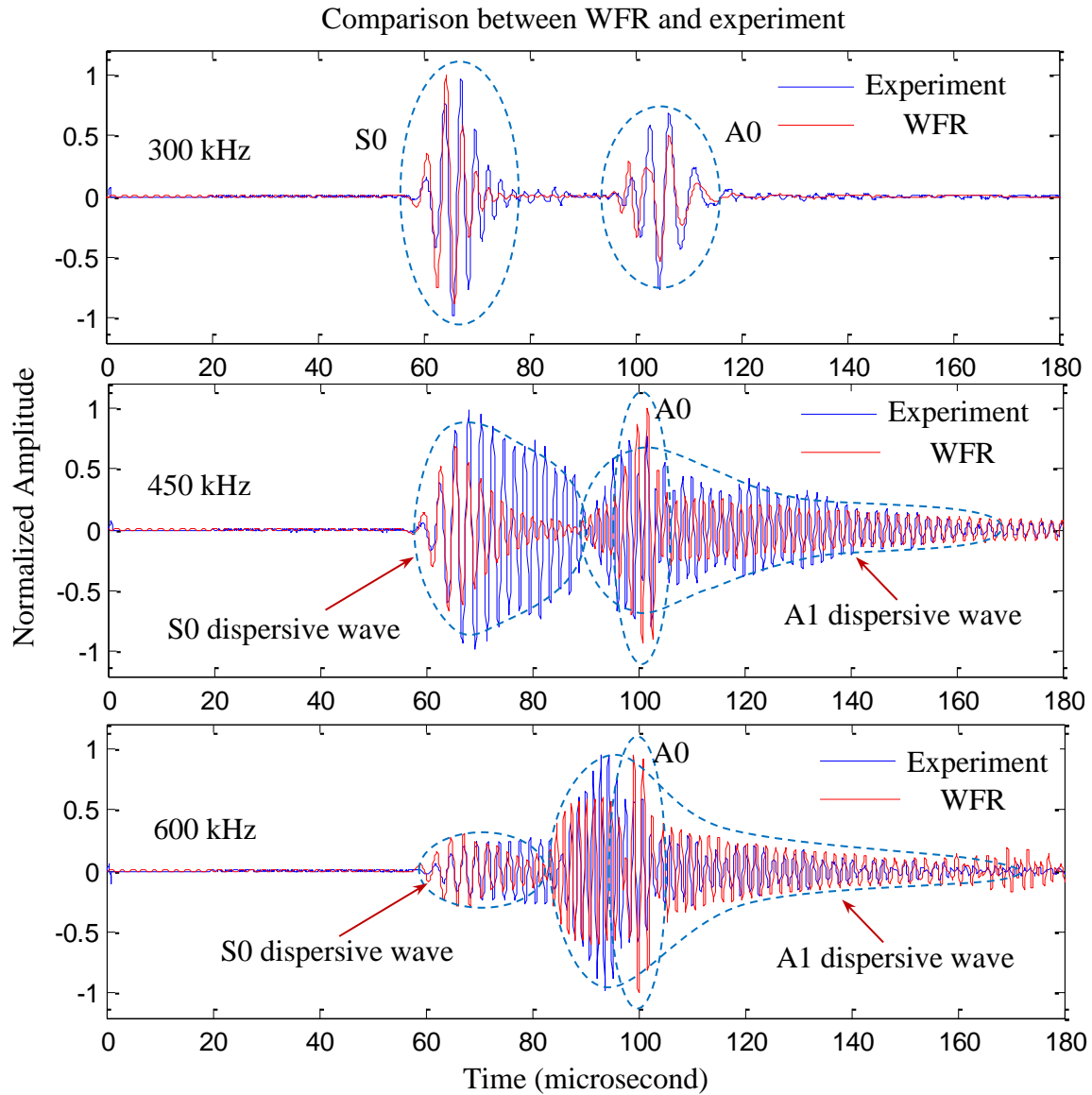
Figure 3.19: Comparison between WFR and experiment for multi-mode Lamb wave propagation in a pristine 3.17-mm aluminum plate.
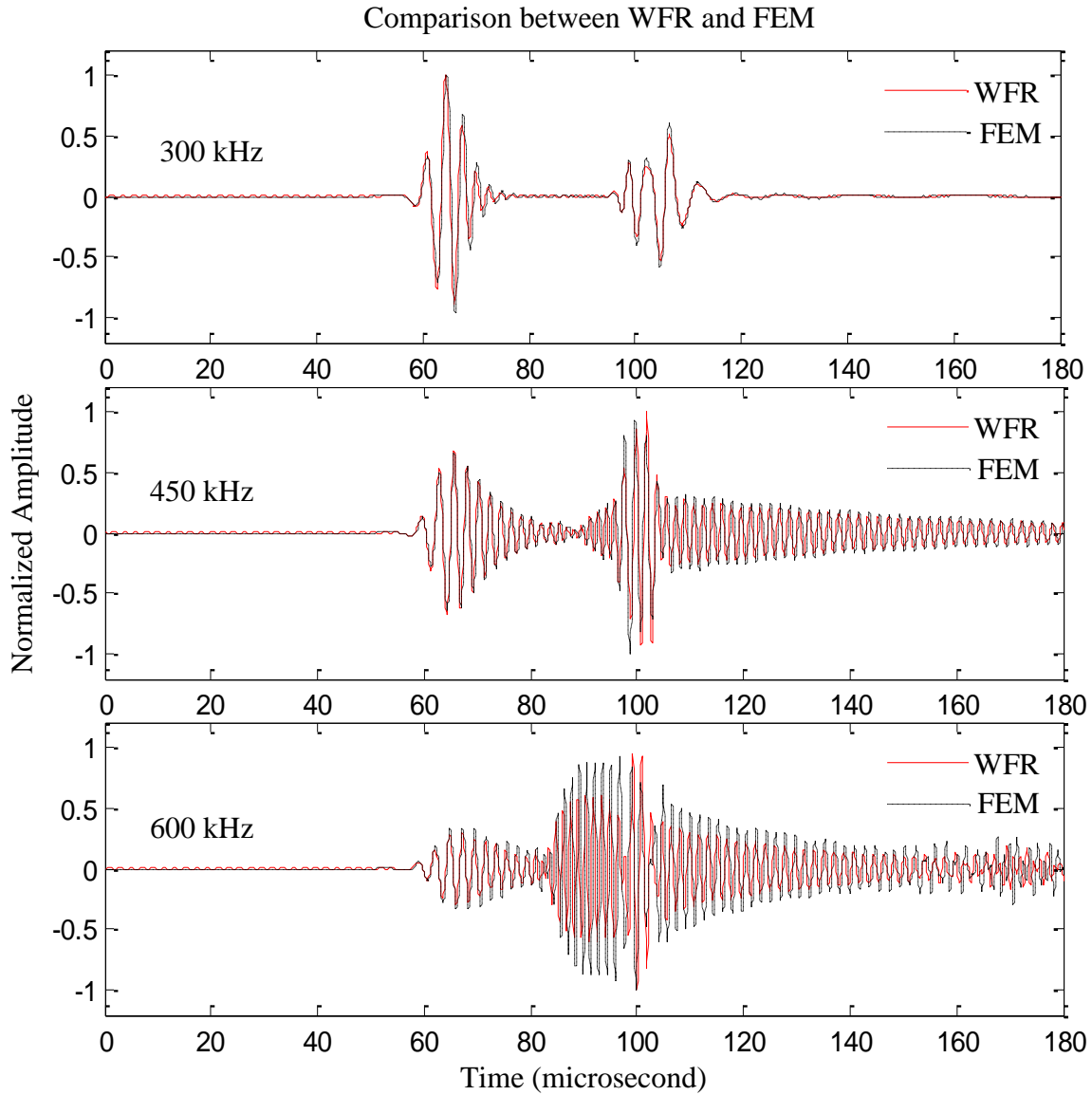
Figure 3.20: Comparison between WFR and FEM for multi-mode Lamb wave propagation in a pristine 3.17-mm aluminum plate.

The guided wave spatial propagation solver in WFR is used to obtain the time space wave field (B-scan) as shown in Figure 3.21a. The frequency-wavenumber analysis is conducted next, as shown in Figure 3.21b. The 600 kHz case is used as an example. From the B-scan, S0, A0, and A1 wave components can be observed. Frequency-wavenumber analysis gives very clear information on the wave mode components of the

wave field. Transmitted S0 wave (S0-T), A0 wave (A0-T), and A1 wave (A1-T) are clearly noticed in Figure 3.21b.
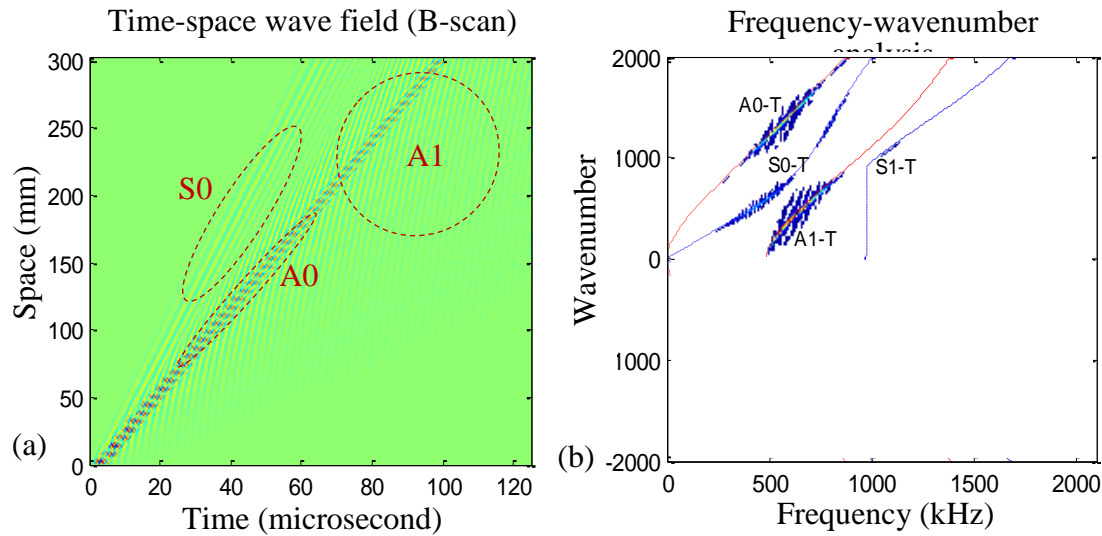


Figure 3.21: (a) Time-space wave field (B-scan); (b) Frequency-wavenumber analysis from WFR.

### 3.5.2    LINEAR INTERACTION BETWEEN LAMB WAVES AND DAMAGE

3.5.2.1 Pitch-catch mode

Figure 3.22 shows the experimental specimen (3.17 mm thick Aluminum-7075-T6 plate), with PWAS #3 used as the transmitter (T-PWAS) and PWAS #4 used as the receiver (R-PWAS). A notch ($h_1 = 2.5\ mm$, $d_1 = 0.25\ mm$) was machined onto the plate, 143.5 mm from the T-PWAS. The wave propagation path from T-PWAS to R-PWAS is 303 mm. 3-count Hanning window modulated tone burst signals were used as the excitation. The center frequency was swept from 150 kHz to 300 kHz.

S0 and A0 waves are transmitted by the T-PWAS. At the notch, S0 waves will be transmitted as S0 waves and also will be mode converted to transmitted A0 waves. A0 waves will be transmitted as A0 waves and also will be mode converted to transmitted S0 waves. All these transmitted waves will propagate along the rest of the structure and be

57

picked up by the R-PWAS. The damage interaction coefficients are physically determined by the size, severity, type of the damage. In this study, we used a trial-and-error approach to tune the WFR damage interaction coefficients to the data obtained from the experiments.
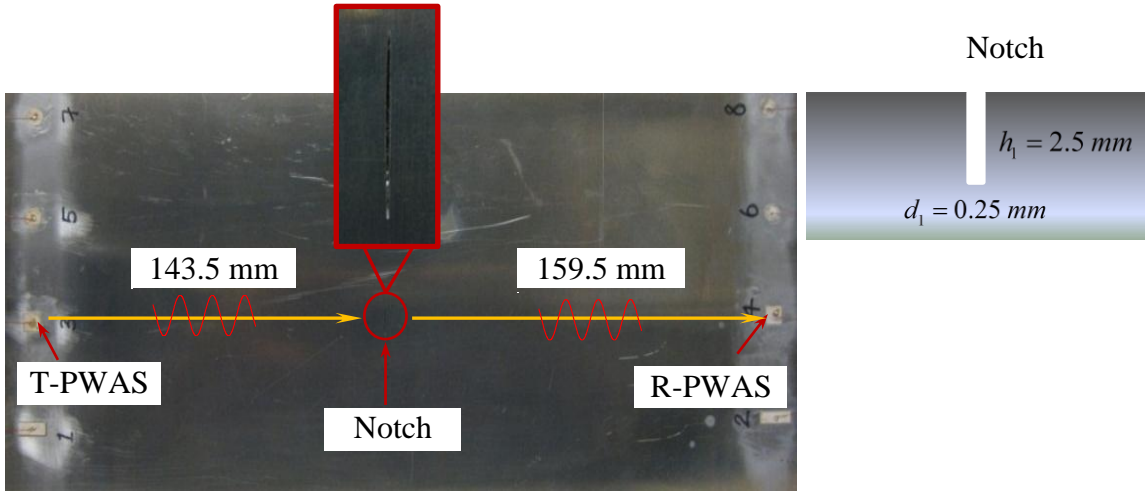


Figure 3.22: Experiment for Lamb waves' linear interaction with a notch (pitch-catch mode).

The adjusted damage interaction coefficients which gave best match with experiments for 150 kHz excitation case are shown in Table 3.1.

Table 3.1: Damage interaction coefficients for pitch-catch mode

| Magnitude coefficient | $C_{SST}^1$ | $C_{SAT}^1$ | $C_{AAT}^1$ | $C_{AST}^1$ |
|---|---|---|---|---|
| Value (normalized) | 0.55 | 0.11 | 0.8 | 0.06 |
| Phase coefficient | $\varphi_{SST}^1$ | $\varphi_{SAT}^1$ | $\varphi_{AAT}^1$ | $\varphi_{AST}^1$ |
| Value (degree) | -30 | 30 | 0 | 30 |

Figure 3.23 shows the WFR simulation results compared with experiments. It can be noticed that the analytical waveforms agree well with experimental data. A new wave packet is generated due to mode conversion at the notch.
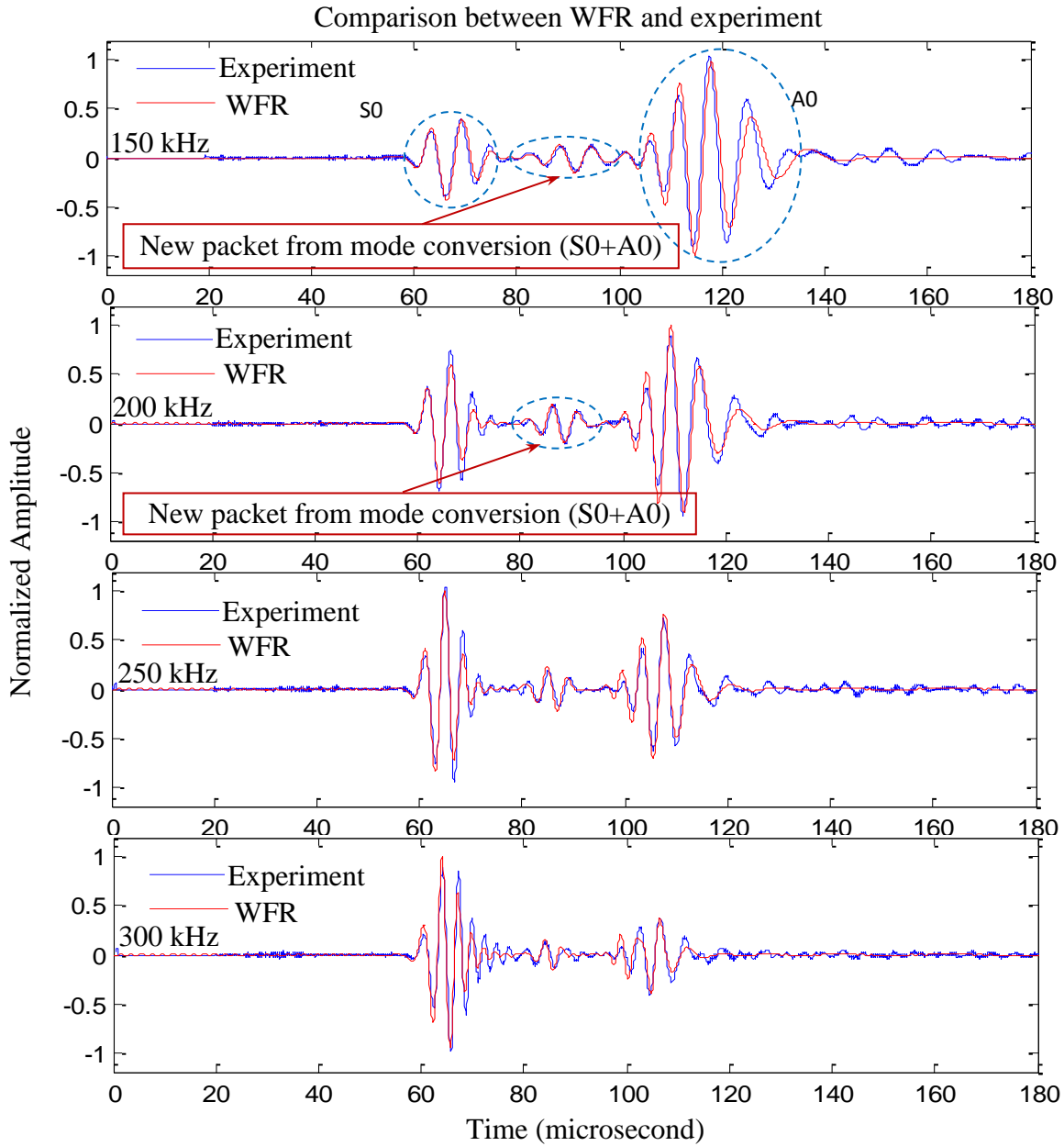
Figure 3.23: Comparison between WFR simulations and experiments for Lamb waves' interaction with a notch in pitch-catch mode.

3.5.2.2 Pulse-echo mode

Figure 3.24 shows the experiment setup for pulse-echo active sensing method. The same specimen is used, with an R-PWAS bounded side by side to the T-PWAS. 3-count Hanning window modulated tone burst signals with the center frequency of 95.5

kHz is used as the excitation. Guided Lamb waves generated by the T-PWAS will propagate into the structure, reach the notch, and be reflected back as echoes. At the notch, S0 waves will be reflected as S0 waves and also will be mode converted to reflected A0 waves. A0 waves will be reflected as A0 waves and also will be mode converted to reflected S0 waves. All the echoes will reach the R-PWAS and be picked up.
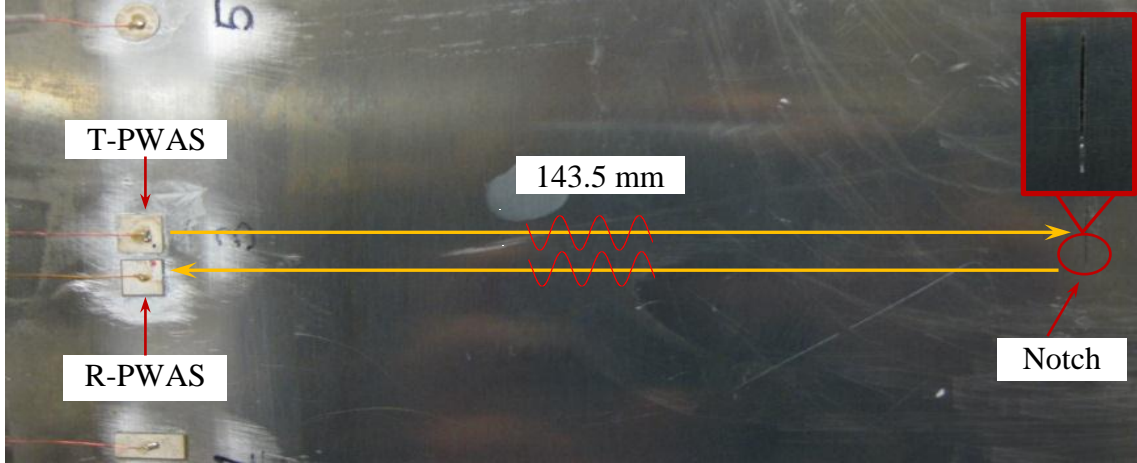


Figure 3.24: Experiment for Lamb waves' linear interaction with a notch (pulse-echo mode).

The adjusted damage interaction coefficients which gave best match with the experiment are shown in Table 3.2.

Table 3.2: Damage interaction coefficients for pulse-echo mode

| Magnitude coefficient | $C^1_{SSR}$ | $C^1_{SAR}$ | $C^1_{AAR}$ | $C^1_{ASR}$ |
|---|---|---|---|---|
| Value (normalized) | 0.2 | 0.04 | 0.12 | 0.04 |
| Phase coefficient | $\varphi^1_{SSR}$ | $\varphi^1_{SAR}$ | $\varphi^1_{AAR}$ | $\varphi^1_{ASR}$ |
| Value (degree) | 60 | 60 | -60 | 60 |

Figure 3.25 shows the WFR simulation result compared with the experiment. The reflected S0 and A0 wave packets could be observed. The new waves between S0 and A0 wave packets are from mode conversion at the notch. The analytical simulation matches

the experiment data. Differences are noticed: first, the direct waves have a phase shift due to the fact that the R-PWAS and T-PWAS are some distance away from each other, while in our analytical model, we consider them to be at the same location; second, the boundary reflections are present and mixed with the weak echoes from the notch in the experiment, but in our model, the boundary reflections are not considered.
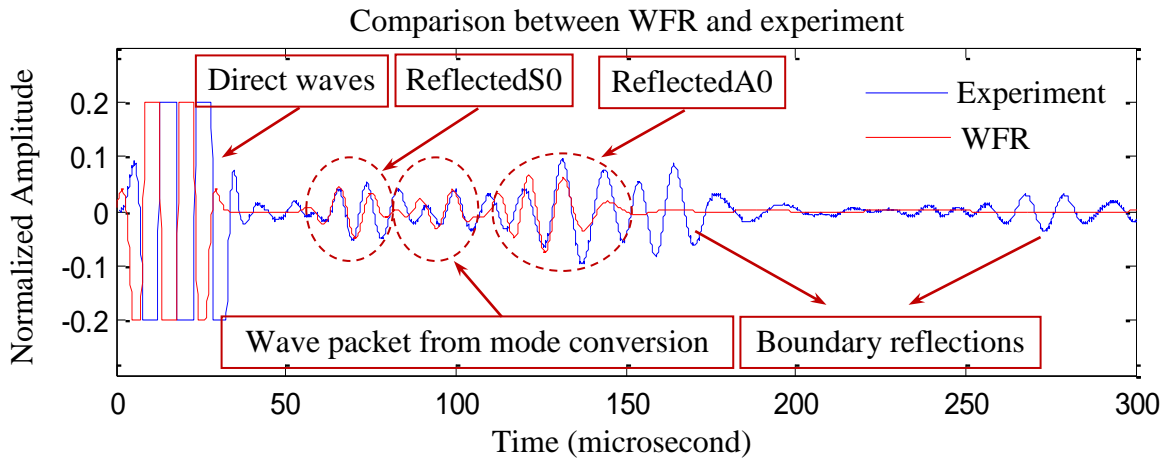


Figure 3.25: Comparison between WFR simulations and experiments for Lamb waves interaction with a notch in pulse-echo mode.
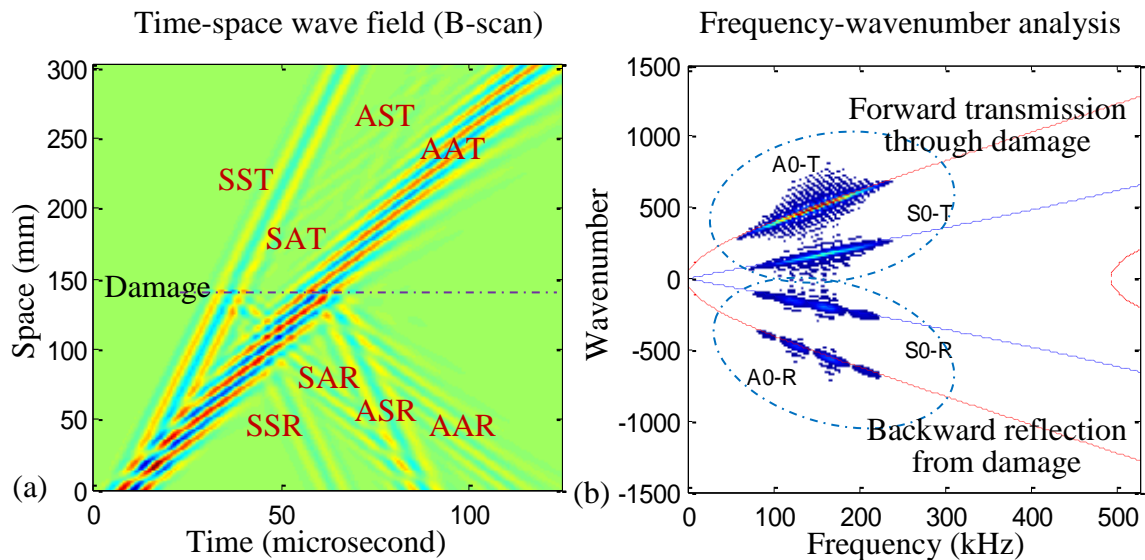


Figure 3.26: (a) Time-space domain solution (B-scan); (b) frequency-wavenumber analysis from WFR. Wave transmission, reflection, and mode conversion damage effects can be clearly noticed.

Figure 3.26 shows the results from WFR spatial propagation solver. The wave transmission, reflection, mode conversion can be clearly noticed in both the B-scan and frequency-wavenumber analysis. It is apparent that the wave field contains transmitted S0 and A0 modes, and reflected S0 and A0 modes.

### 3.5.3 Nonlinear Interaction between Lamb Waves and Damage

A guided wave pitch-catch method may be used to interrogate a plate with a breathing crack which opens and closes under tension and compression (Shen and Giurgiutiu 2012; 2013). The ultrasonic waves generated by the transmitter PWAS (T-PWAS) propagate into the structure, interact with the breathing crack, acquire nonlinear features, and are picked up by the receiver PWAS (R-PWAS). This process is shown in Figure 3.27. The nonlinear interaction between Lamb waves and the breathing crack will introduce nonlinear higher harmonics into the interrogation waves. A multi-physics transient finite element model was used to simulate the Lamb waves' interaction with a nonlinear breathing crack. The damage interaction coefficients obtained from fitting the FEM solution (Table 3.3 shows the nonlinear interaction coefficients for fundamental frequency; Table 3.4 shows the coefficients for second and third higher harmonics) were input into the WFR simulator. Details of the nonlinear finite element model can be found in Chapter 6.

Figure 3.28 shows the comparison between FEM and the WFR analytical solution. It is noticed that the FEM results and the analytical solution agree very well because the damage interaction coefficients were fitted to the FEM solution. The time domain waveforms show nonlinear characteristics of noticeable nonlinear distortion in S0 packet and zigzags in the new packet. The frequency spectrums show distinctive nonlinear

higher harmonics (200 kHz and 300 kHz). Since we only consider up to the 3$^{rd}$ higher

harmonic in this case study, the frequency domain of analytical solution shows only the

first three peaks, while the finite element solution have even higher harmonics. But the

solution up to the third higher harmonics is accurate enough to render an acceptable

waveform in time domain.
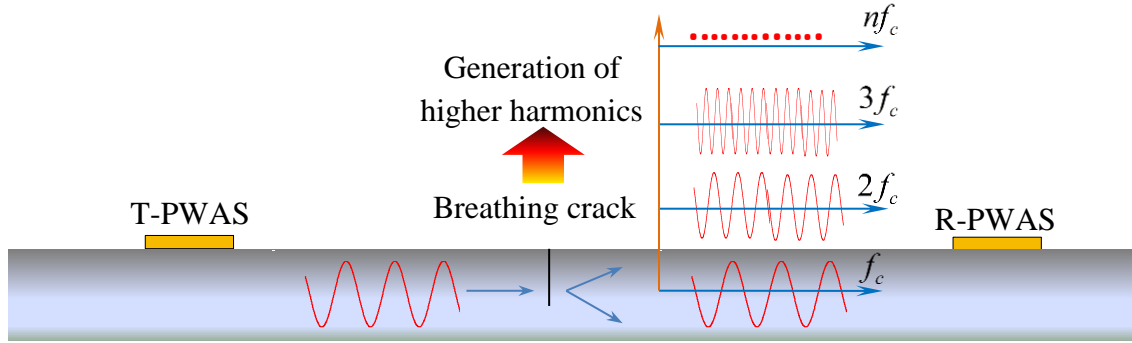


Figure 3.27: Pitch-catch method for the detection of breathing crack; the mode
conversion at the crack is illustrated by the two arrows.

Table 3.3: Nonlinear interaction coefficients of fundamental frequency

| Magnitude coefficient | $C_{SST}^1$ | $C_{SAT}^1$ | $C_{AAT}^1$ | $C_{AST}^1$ |
|---|---|---|---|---|
| Value (normalized) | 0.900 | 0.420 | 0.820 | 0.100 |
| Phase coefficient | $\varphi_{SST}^1$ | $\varphi_{SAT}^1$ | $\varphi_{AAT}^1$ | $\varphi_{AST}^1$ |
| Value (degree) | 0 | 100 | -35 | 90 |

Table 3.4:Nonlinear interaction coefficients of second and third higher harmonics

| Magnitude coefficient | $C_{SST}^2$ | $C_{SAT}^2$ | $C_{AAT}^2$ | $C_{AST}^2$ | $C_{SST}^3$ | $C_{SAT}^3$ | $C_{AAT}^3$ | $C_{AST}^3$ |
|---|---|---|---|---|---|---|---|---|
| Value (normalized) | 0.082 | 0.100 | 0.050 | 0.110 | 0.032 | 0.038 | 0.005 | 0.025 |
| Phase coefficient | $\varphi_{SST}^2$ | $\varphi_{SAT}^2$ | $\varphi_{AAT}^2$ | $\varphi_{AST}^2$ | $\varphi_{SST}^3$ | $\varphi_{SAT}^3$ | $\varphi_{AAT}^3$ | $\varphi_{AST}^3$ |
| Value (degree) | 0 | 0 | 120 | 90 | 0 | 0 | 0 | 0 |
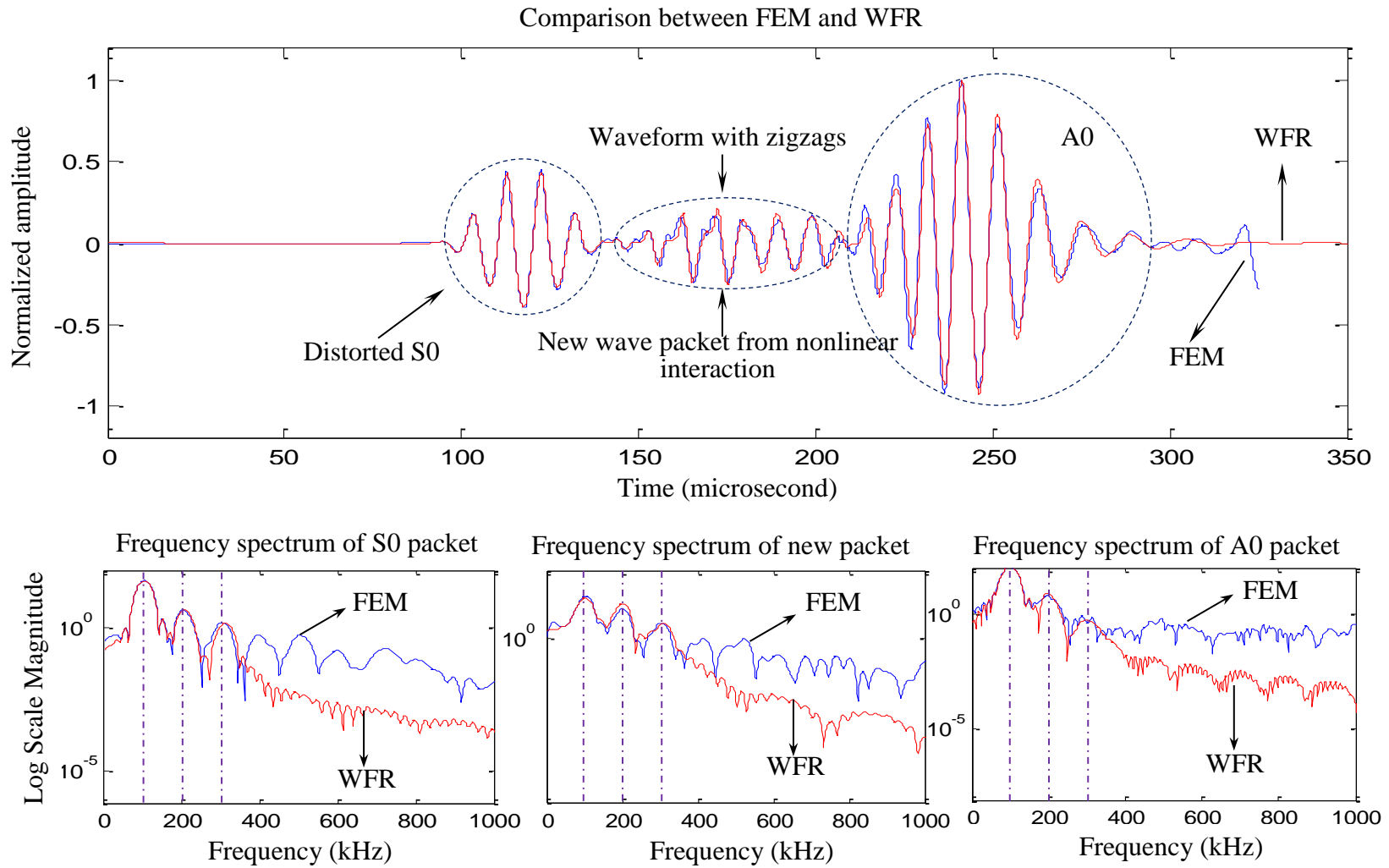
Figure 3.28: Comparison between finite element simulation (FEM) and analytical simulation (WFR).

The guided wave spatial propagation solver in WFR was used to obtain the time-space wave field. Figure 3.29 shows the time-space wave field and frequency-wavenumber analysis of Lamb waves interaction with nonlinear breathing crack.
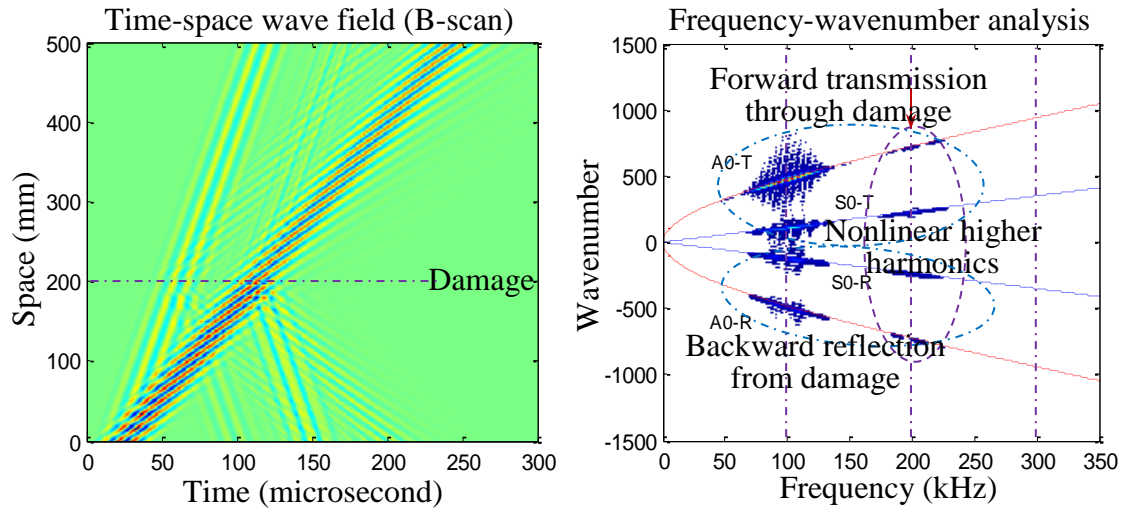


Figure 3.29: Time-space wave field and frequency-wavenumber analysis from WFR.

Transmission, reflection and mode conversion phenomena at the damage can be clearly noticed. The frequency-wavenumber analysis reveals the wave components during the interaction process. The wave field contains transmitted S0, A0 waves and reflected S0, A0 waves. Nonlinear higher harmonics can be observed at 200 kHz.

The WFR guided wave spatial propagation solver can provide the spatial wave pattern at any instance of time. The spatial waveforms at 25, 50, 75, 100, 125, 150, 175, 200 μs are displayed in Figure 3.30. The spatial waveforms shows: (1) Lamb waves propagating into the structure at $T = 25\mu s$; (2) Lamb modes separating into distinctive packets and their interaction with damage at $T = 50\mu s$; (4) Wave transmission, reflection, mode conversion, nonlinear distortion of waveforms at various instances ($T = 75,100,125,150,200\mu s$).
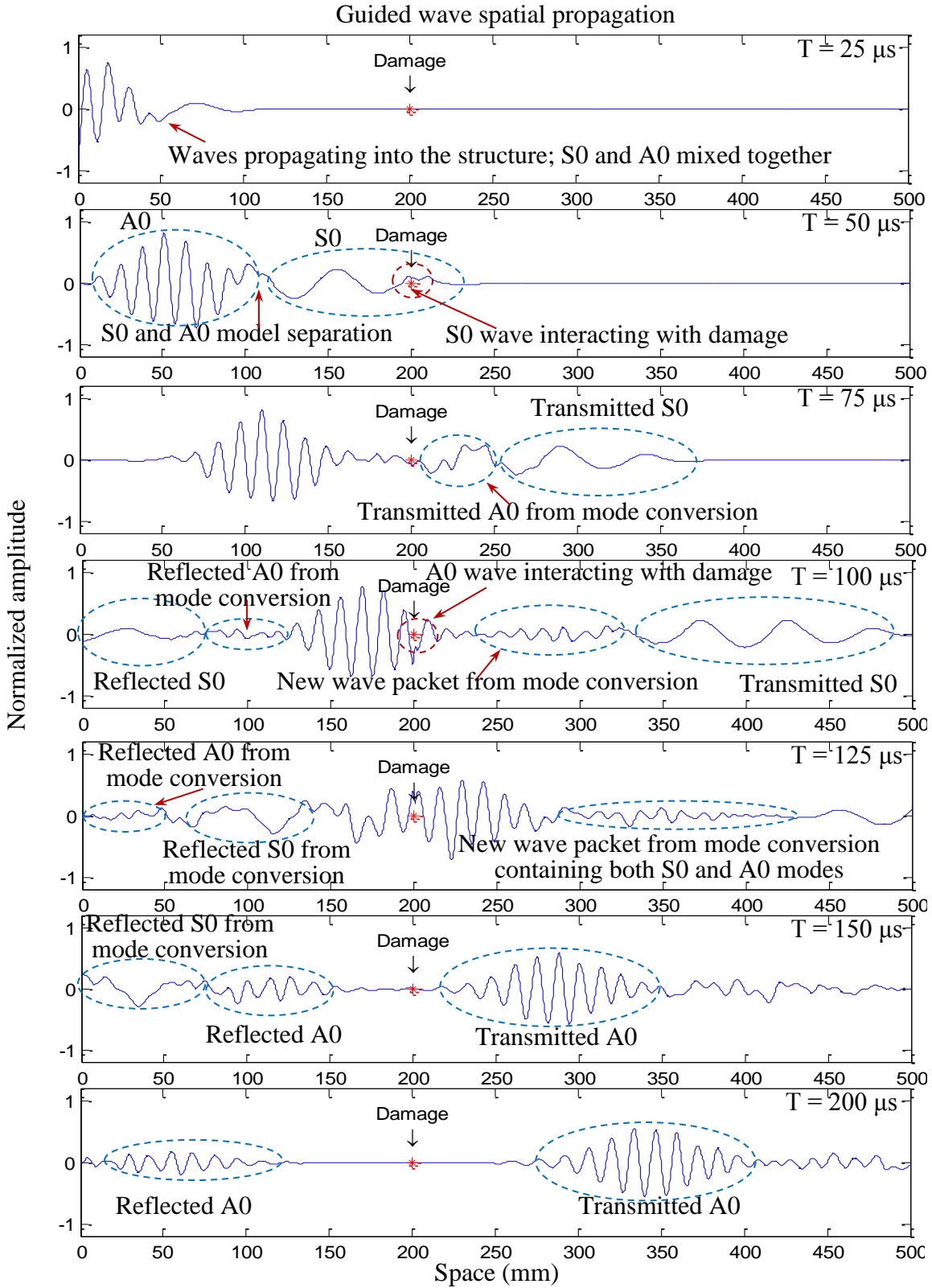
Figure 3.30: Spatial wave propagation of Lamb wave interaction with breathing crack (calculated using WFR).

# CHAPTER 4
## COMBINED ANALYTICAL/FEM APPROACH FOR EFFICIENT SIMULATION OF 2-D GUIDED WAVE PROPAGATION

This chapter presents the Combined Analytical/Finite Element Method (FEM) Approach (CAFA) for efficient simulation of guided Lamb wave propagation and interaction with damage. The development of computation models for Lamb wave propagation and interaction with damage is of great importance for both Structural Health Monitoring (SHM) system design and signal interpretation. Effective design of SHM systems requires the exploration of a wide range of parameters (transducer size, sensor-damage relative locations, interrogating wave characteristics, etc.) to achieve best detection and quantification of certain types of damage. On the other hand, active sensing signals using Lamb waves are usually difficult to interpret due to the multi-mode, dispersive nature of Lamb waves, and their interaction with damage, which involves complicated scattering and mode conversion phenomena. Practical applications have imposed three main requirements on the computation models: (1) accuracy for high frequency, short wavelength, and long propagation distance waves; (2) efficiency in terms of computation time and computer resources; (3) versatility, the capability of exploring a wide range of parameters.

## 4.1 STATE OF THE ART

Research has been conducted on analytical models of PWAS generated Lamb waves and the tuning effect between PWAS transducers and host structures (Giurgiutiu

2005; Raghavan and Cesnik 2005). These models only consider the wave propagation in pristine structures, whereas the design of SHM systems requires research into wave-damage interaction.

Regarding the aspect of wave-damage interaction, many researchers have developed analytical models using Kirchhoff, Mindlin, Kane-Mindlin plate theory, and 3-D elasticity solution or exact Lamb mode solutions (Norris and Vemula 1995; Vemula and Norris 1997; Wang and Chang 2005; Moreau 2012; McKeon and Hinders 1999; Grahn 2002), while others have adopted numerical methods such as finite element method (FEM) (Alleyne and Cawley 1992; Moreau et al. 2012; Shen and Giurgiutiu 2014), boundary element method (BEM) (Cho et al. 2000), spectral element method (SEM) (Ostachowicz et al. 2012), and finite difference method (LISA) (Lee and Staszewski 2007; Nadella and Cesnik 2013). The advantage of analytical models is that they are fast, efficient, and capable of providing parametric studies, but the drawback is that they only apply to simple damage geometries such as circular holes, partial-through circular holes, or flat-bottom cavities. The advantage of numerical methods is that they can simulate wave damage interaction phenomena in very complicated structures; however, these methods usually require the discretization of the analyzed domain and the time marching procedure. For such high frequency, short wavelength, and long propagation wave simulations, considerably small time marching step and dense discretization are are required to obtain an accurate solution, which can make the target problem computationally prohibitive.

Recently, semi-analytical method and small-size numerical methods, such as semi-analytical finite element (SAFE) method and distributed point source method

(DPSM) have been developed to make the computation load manageable (Rahani and Kundu 2011; Srivastava 2009; Benmeddour et al. 2011; Ahmad and Gabbert 2012). The SAFE method has been used to combine with local finite element models to simulate wave interaction with damage in 1-D wave propagation problems, but 2-D wave propagation models have not been achieved. For DPSM method, 1-D wave propagation and mode conversion at damage have been reported. 2-D wave propagation interaction with through thickness damage has been simulated, but 2-D wave interaction with partial through thickness types of damage (i.e. corrosion) has not been reported using DPSM. Hybrid modeling techniques have been proposed to develop efficient simulation schemes. Promising results have been achieved for bulk wave scattering from an axisymmetric inclusion and Lamb wave interaction with cracks in rivet holes (Goetschel et al. 1982; Chang and Mal 1999). However, these studies considered bulk wave or single Lamb mode interaction with damage, and used conventional wedge transmitters and bulky accelerometers as receivers. Terrien et al. (2007) investigated the optimization of hidden corrosion detection in aircraft structures using Lamb waves. In their study, they adopted a 1-D wave propagation hybrid model to predictive the structural response, combining a local 2-D FEM with global 1-D wave modal decomposition. Moreau and Castaings (2008) have used orthogonally relation to reduce the size of FEM to obtain 3-D guided wave scattering features. Gresil and Giurgiutiu (2013a; 2013b) investigated the hybrid modeling concept in time domain, and achieved promising results. But this model requires interface matching between analytical and local FEM, and time domain hybrid model has to be re-run for each test frequency. Obenchain et al. (2014) used a hybrid global matrix/local interaction simulation approach for modeling wave propagation in

69

composites. The formulation uses a finite difference technique and requires time marching procedure. In our study, we developed a Combined Analytical/FEM Approach (CAFA) for efficient simulation of 2-D guided wave propagation and interaction with damage. We are not trying to compare with other methods such as DPSM, LISA and SAFE; instead we are putting forward a new approach for the efficient simulation of guided wave active sensing and SHM system design. Our study advances the state of the art with the following aspects: (1) we incorporated the analytical solution of PWAS-generated Lamb waves, making our model capable of simulating SHM systems with permanently bonded PWAS transducers; (2) our model can selectively generate symmetric, anti-symmetric, or both interrogating wave modes, instead of only the symmetric wave mode; (3) we used the wave-damage interaction coefficients (WDICs) for coupling the analytical expression with small-size local FEM models. These WDICs can describe complicated 3-D interaction between interrogating waves and damage, i.e., scattering and mode conversion. The 3-D wave-damage interaction case study (involving mode conversions among S0, A0, and SH0 wave modes) has not been reported elsewhere using DPSM, SAFE, or other hybrid approaches; (4) CAFA was constructed in the frequency domain and consists of a transfer function method analytical model and harmonic analysis of the local FEM. The frequency domain formulation facilitated a high computation efficiency and wide parameter space exploration capability; (5) to obtain WDICs, we have improved the modeling technique for artificial non-reflective boundaries using spring-damper elements; (6) we have developed an analytical predictive tool, WaveFormRevealer 2-D, as a user-friendly interface for realization of CAFA.

## 4.2    OVERVIEW OF CAFA

Figure 4.1 shows the schematic for CAFA.
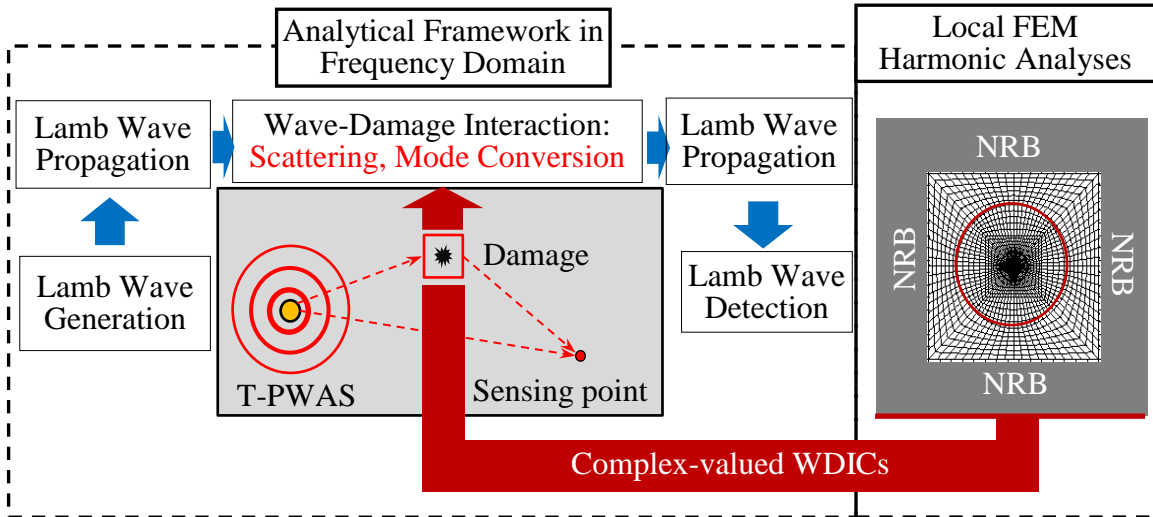


Figure 4.1: Overview of Combined Analytical/FEM Approach (CAFA).

Lamb wave generation, propagation, damage interaction (scattering, mode conversion), and detection are modeled using the exact analytical expressions, while the WDICs are extracted from the harmonic analysis of small-size local FEM models with non-reflective boundaries (NRB).

CAFA couples the global analytical wave expression with the local FEM solution through WDICs. CAFA combines the virtues of both analytical and numerical methods: the analytical formulation provides high calculation efficiency, a wide parameter exploration capability, and excellent accuracy, while FEM models have the ability to simulate damage with complicated geometries.

## 4.3    ANALYTICAL FRAMEWORK FOR GUIDED WAVE ACTIVE SENSING

In this section, we will present the methodology for modeling damage effects, and the steps required to construct the analytical framework for PWAS-generated 2-D Lamb wave propagation and interaction with damage.

71

### 4.3.1 MODELING OF DAMAGE EFFECTS USING COMPLEX-VALUED WDICS

Figure 4.2 shows a typical active sensing procedure via the PWAS and scanning laser vibrometer approach. Under electrical excitation, the transmitter PWAS (T-PWAS) generates Lamb waves into the host structure. They propagate along the structure, interact with damage, undergo scattering and mode conversion, and are finally picked up by the scanning laser vibrometer, which measures the out-of-plane particle velocity at the surface of the structure.

In our analytical framework, the received signal is comprised of two parts: (1) direct incident waves from the T-PWAS; (2) scattered waves from damage. Thus, damage can be modeled as a secondary wave source. The total wave field $W_{TOTAL}$ is the superposition of the incident wave field $W_{IN}$ and the scattered wave field $W_{SC}$ from the damage.

$$W_{TOTAL} = W_{IN} + W_{SC} \qquad (4.1)$$
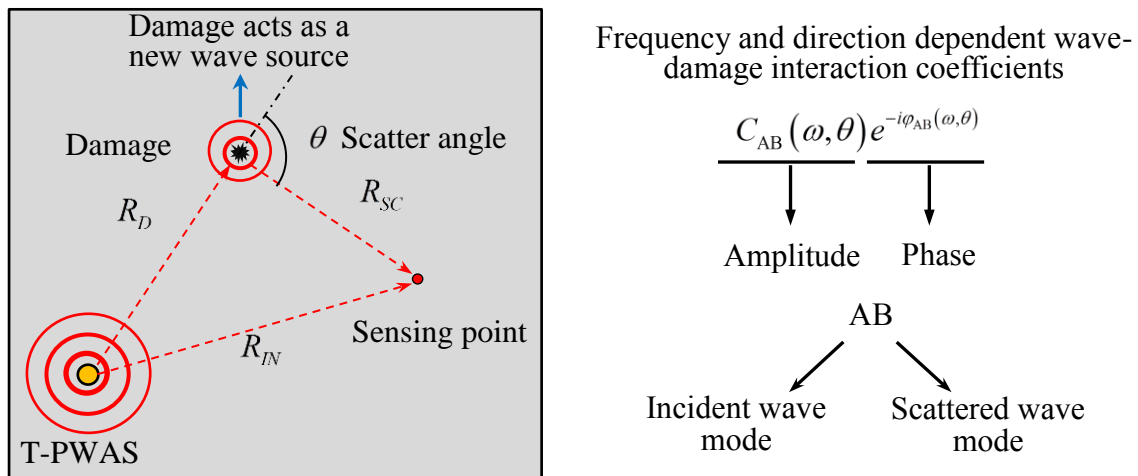


Figure 4.2: Schematic of guided wave active sensing; Frequency dependent complex valued wave-damage interaction coefficients (WDICs).

We used frequency and direction dependent complex-valued WDICs to model the scattering and mode conversion phenomena of wave-damage interaction. These WDICs are capable of describing the scattered waves amplitude and phase as a function of frequency and direction.

Our notations are as follows: two letters are used to describe the interaction phenomena, with the first letter denoting the incident wave type, and the second letter standing for the resulting wave type. For instance, SS (symmetric-symmetric) means the incident symmetric waves are scattered as symmetric waves, while SA (symmetric-antisymmetric) means incident symmetric waves are scattered and mode converted into antisymmetric waves. Thus WDIC $C_{SS}(\omega,\theta)e^{-i\varphi_{SS}(\omega,\theta)}$ denotes the scattered symmetric mode generated by incident symmetric mode with amplitude ratio $C_{SS}(\omega,\theta)$ and phase shift $\varphi_{SS}(\omega,\theta)$. Similarly, $C_{SA}(\omega,\theta)e^{-i\varphi_{SA}(\omega,\theta)}$ represents the scattered antisymmetric mode generated by incident symmetric mode with amplitude ratio $C_{SA}(\omega,\theta)$ and phase shift $\varphi_{SA}(\omega,\theta)$. $\omega$ is the wave component frequency and $\theta$ represents the scattering angle with respect to the incident wave direction. These coefficients are determined by damage features and are calculated from the small-size local FEM harmonic analysis, which will be introduced later.

### 4.3.2   2-D ANALYTICAL FRAMEWORK CONSTRUCTION

Figure 4.3 shows the analytical framework flowchart. The analytical model was constructed in frequency domain based on the exact 2-D Lamb wave solution in the following steps:
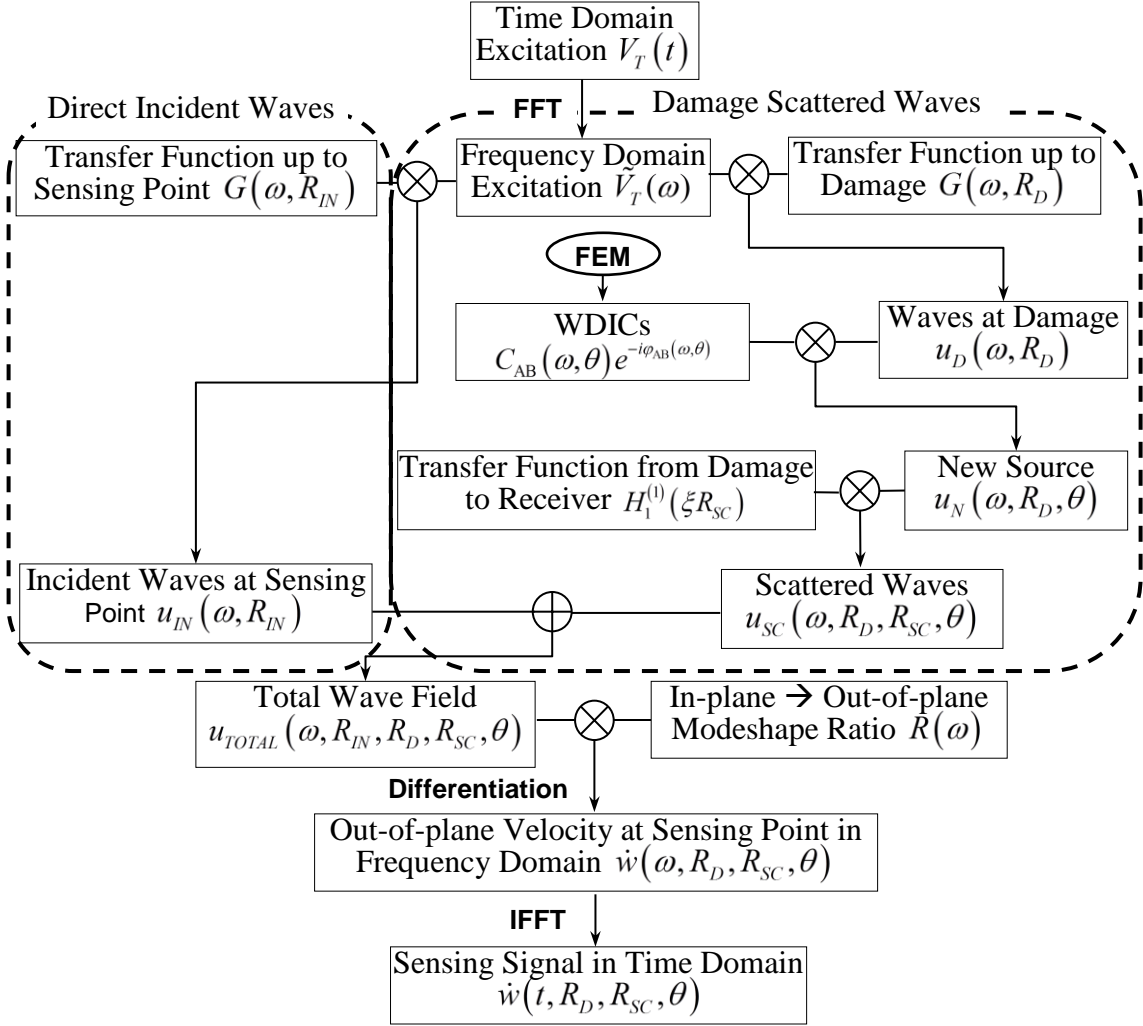
Figure 4.3: Analytical framework flowchart.

<u>STEP 1</u>: Perform Fourier transform of the time-domain excitation signal $V_T(t)$ to obtain

the frequency domain excitation spectrum, $\tilde{V}_T(\omega)$.

<u>STEP 2</u>: Calculate structure transfer function. Detailed analytical derivation of 2-D Lamb

waves generated by a circular transmitter PWAS is given in by Giurgiutiu (2014),

$$
\begin{aligned}
u_r(r)\big|_{z=d} = &-\pi i \frac{a^2 \tau_a}{2\mu} \sum_{\xi^S} \frac{J_1(\xi^S a) N_S(\xi^S)}{D_S'(\xi^S)} H_1^{(1)}(\xi^S r) e^{-i\omega t} \\
&-\pi i \frac{a^2 \tau_a}{2\mu} \sum_{\xi^A} \frac{J_1(\xi^A a) N_A(\xi^A)}{D_A'(\xi^A)} H_1^{(1)}(\xi^A r) e^{-i\omega t}
\end{aligned}
\tag{4.2}
$$

74

$$N_S(\xi) = \xi\eta_S\left(\xi^2 + \eta_S^2\right)\cos\eta_P d \cos\eta_S d$$

$$N_A(\xi) = -\xi\eta_S\left(\xi^2 + \eta_S^2\right)\sin\eta_P d \sin\eta_S d$$

$$D_S = \left(\xi^2 - \eta_S^2\right)^2 \cos\eta_P d \sin\eta_S d + 4\xi^2\eta_P\eta_S \sin\eta_P d \cos\eta_S d \tag{4.3}$$

$$D_A = \left(\xi^2 - \eta_S^2\right)^2 \sin\eta_P d \cos\eta_S d + 4\xi^2\eta_P\eta_S \cos\eta_P d \sin\eta_S d$$

where $a$ is the radius of the circular PWAS, $d$ is half plate thickness, and $r$ is the distance between the point of interest and T-PWAS. $\tau_a$ represents shear stress between the transducer and host structure and $\mu$ denotes the shear modulus of the structure. $J_1$ is Bessel function of order one, which captures the tuning effect between PWAS and the host structure. $H_1^{(1)}$ is the first kind Hankel function of order one, which represents an outward propagating 2-D wave field. $\xi$ is the frequency dependent wavenumber calculated from the Rayleigh-Lamb equation (Graff 1991):

$$\frac{\tan\eta_S d}{\tan\eta_P d} = \left[\frac{-4\eta_P\eta_S\xi^2}{\left(\xi^2 - \eta_S^2\right)^2}\right]^{\pm 1} \tag{4.4}$$

$$\eta_P^2 = \frac{\omega^2}{c_P^2} - \xi^2; \quad \eta_S^2 = \frac{\omega^2}{c_S^2} - \xi^2; \quad c_P = \sqrt{\frac{\lambda + 2\mu}{\rho}}; \quad c_S = \sqrt{\frac{\mu}{\rho}}$$

where +1 exponent corresponds to symmetric Lamb wave modes and -1 exponent corresponds to antisymmetric Lamb wave modes. $c_P$ and $c_S$ represent the pressure wave speed and shear wave speed; $\lambda$ is Lame's constant of the structural material; $\rho$ is the material density. The transfer function $\kappa_{PWAS}(\omega)$ in Eq. (4.5) converts the applied voltage $\tilde{V}_T(\omega)$ into the shear stress $\tau_a$, where $r(\omega)$ is the stiffness ratio between host structure and T-PWAS (Lin et al. 2012).

$$\kappa_{PWAS}(\omega) = \frac{d_{31}}{s_{11}^E} \frac{r(\omega)}{1 - r(\omega)} \tag{4.5}$$

Taking Fourier transform of Eq. (4.2), one can obtain the frequency domain structure transfer function for both symmetric and anti-symmetric modes. For each wave mode, the corresponding wavenumber $\xi$ should be chosen.

$$G(\omega,r) = -\pi i \frac{a^2 \kappa_{PWAS}(\omega)}{2\mu} \sum_{\xi} \frac{J_1(\xi a) N_S(\xi)}{D_S'(\xi)} H_1^{(1)}(\xi r) \tag{4.6}$$

STEP 3: Multiply the structure transfer function by the frequency-domain excitation signal to obtain the direct incident waves at the sensing location, where the distance $R_{IN}$ from T-PWAS up to sensing location is used. Similarly, multiply the structure transfer function up to the damage location by the frequency-domain excitation signal to obtain the interrogating waves arriving at the damage, where the distance $R_D$ from T-PWAS up to the damage location is used.

$$u_{IN}(\omega, R_{IN}) = \tilde{V}_T(\omega) \left[ G^S(\omega, R_{IN}) + G^A(\omega, R_{IN}) \right] \tag{4.7}$$

$$u_D(\omega, R_D) = \tilde{V}_T(\omega) \left[ G^S(\omega, R_D) + G^A(\omega, R_D) \right] \tag{4.8}$$

It can be noticed that the direct incident wave field is the superposition of symmetric and antisymmetric wave modes.

STEP 4: Scattered wave source at the damage location is obtained by modifying incident waves at the damage with WDICs.

$$u_N^S = C_{SS}(\omega, \theta) e^{-i\varphi_{SS}(\omega,\theta)} u_D^S + C_{AS}(\omega, \theta) e^{-i\varphi_{AS}(\omega,\theta)} u_D^A \tag{4.9}$$

$$u_N^A = C_{SA}(\omega, \theta) e^{-i\varphi_{SA}(\omega,\theta)} u_D^S + C_{AA}(\omega, \theta) e^{-i\varphi_{AA}(\omega,\theta)} u_D^A \tag{4.10}$$

where $u_N^S$ and $u_N^A$ represent the S0 and A0 damage generated wave sources respectively. These scattered waves are transferred from damage up to the sensing point. The 2-D

Lamb wave field eradiating from a point source takes the following solution (Glushkov et al. 2011; Giurgiutiu 2014):

$$u_r = \sum_{n=1}^{\infty} a_n(z) H_1^{(1)}(\xi_n r) e^{-i\omega t} \tag{4.11}$$

where $a_n(z)$ is the thickness dependent modeshape of wave mode number $n$. Since the amplitude relationship between the interrogating waves and the scattered waves is enclosed in the WDICs, the transfer function from the damage up to the sensing point is simply $H_1^{(1)}(\xi R_{SC})$, where $R_{SC}$ is the distance from the damage up to the sensing location. Thus, the scattered waves arriving at the sensing point can be calculated.

$$u_{SC}^S = u_N^S H_1^{(1)}(\xi^S R_{SC}); \quad u_{SC}^A = u_N^A H_1^{(1)}(\xi^A R_{SC}) \tag{4.12}$$

STEP 5: The total wave field at the sensing location is the superposition of the direct incident waves calculated from Eq. (4.7) and the scattered waves calculated from Eq. (4.12).

$$u_{TOTAL} = u_{IN} + u_{SC} \tag{4.13}$$

It should be noted that the total wave field obtained in Eq. (4.13) is the in-plane wave displacement. Since laser vibrometer measures out-of-plane particle velocity, we need to convert this in-plane wave motion into out-of-plane wave motion.

STEP 6: The out-of-plane displacement wave field can be obtained by the modeshape component ratio.

$$u_z^S = u_r^S \frac{U_z^S(\omega,d)}{U_r^S(\omega,d)}; \quad u_z^A = u_r^A \frac{U_z^A(\omega,d)}{U_r^A(\omega,d)} \tag{4.14}$$

where $U_r^S, U_z^S, U_r^A, U_z^A$ are Lamb wave modeshape displacement components evaluated at the top surface of the structure. The modeshape solutions can be found in Giurgiutiu

(2008). The out-of-plane velocity was calculated by differentiating the out-of-plane displacement with respect to time. Through this differentiation, the wave amplitude will be modified by a factor of $-i\omega$ as shown in Eq.(4.15).

$$U = ue^{-i\omega t}; \quad \frac{\partial U}{\partial t} = \frac{\partial\left(ue^{-i\omega t}\right)}{\partial t} = -i\omega U \tag{4.15}$$

Thus, the solution for out-of-plane velocity in frequency domain can be obtained in the following form.

$$\dot{u}_z\left(\omega, R_D, R_{SC}, \theta\right) = -i\omega u_z \tag{4.16}$$

STEP 7: Perform inverse Fourier transform to obtain the time domain sensing signal.

$$\dot{u}_z\left(t, R_D, R_{SC}, \theta\right) = IFFT\left[\dot{u}_z\left(\omega, R_D, R_{SC}, \theta\right)\right] \tag{4.17}$$

In this study, we focused our attention on fundamental modes of Lamb waves (S0 and A0), which find the widest application in Lamb wave based SHM. However, higher orders of Lamb modes (S1, A1, S2, A2, etc.) as well as shear horizontal (SH) modes from wave-damage interaction may also exist. The analytical framework can be easily extended to consider these aspects under the same principle; however, difficulty may be found in the extraction of WDICs. The small-size FEM technique developed in this study can solve the WDICs for S0, A0, SH0 wave modes. It should also be pointed out that, for model validation purpose, we used scanning laser vibrometer which measures the out-of-plane velocity of the wave field. Thus, the scattered SH waves, which do not have out-of-plane motion, cannot be captured.

## 4.4 ANALYTICAL SIMULATION TOOL: WAVEFORMREVEALER 2-D

The analytical model is a general description of wave generation, propagation, damage interaction, and detection. Parameter exploration is made possible for T-PWAS

size, structure material and thickness, sensor-damage locations, and arbitrary excitations, etc. This analytical framework was coded with MATLAB, and a graphical user interface (GUI) called WaveFormRevealer 2-D (WFR-2D) was developed (Shen and Giurgiutiu 2014). Figure 4.4 shows the WFR-2D interfaces.

Figure 4.4a shows the WFR-2D main interface which calculates the real time sensing signals as well as dispersion curves and tuning curves. The parameter control panel allows users to modify host structure material properties, thickness, and transmitter-damage-sensing locations. The excitation control panel provides excitation waveform, frequency, and arbitrary excitation loading options. Users can also selectively choose the excited wave mode of interest. Figure 4.4b shows the scatter information platform for inputting wave-damage interaction coefficients (WDICs). Figure 4.4c and Figure 4.4d show the sub-interfaces for loading S0 and A0 WDICs. The T-PWAS properties module allows users to define T-PWAS geometric and material properties (Figure 4.4e). The spatial propagation solver, shown in Figure 4.4f, is like a C-scan, which calculates the transient time-space domain wave field. Thus, the transient spatial wave field can be obtained at any instance during wave propagation.

Users can visualize wave propagation and interaction with damage easily with the animation functions offered by WFR. Additionally, all the calculation data is available for user analysis with the data saving functions. With this analytical tool, an increase in computation efficiency for large parameter space exploration can be achieved. It may take tens of hours for commercial finite element software to run a full scale 3-D simulation for an accuracy solution of a high frequency, short wavelength, and long

distance wave propagation problem, but it takes only several seconds to obtain the same solution with the WFR coupling along with two or three hours local FEM calculation.

(a) WFR Main Interface     (b) Scatter Information Platform     (c) S0 WDICs Module



(f) Spatial Propagation Solver

(e) T-PWAS Properties Module                 (d) A0 WDICs Module
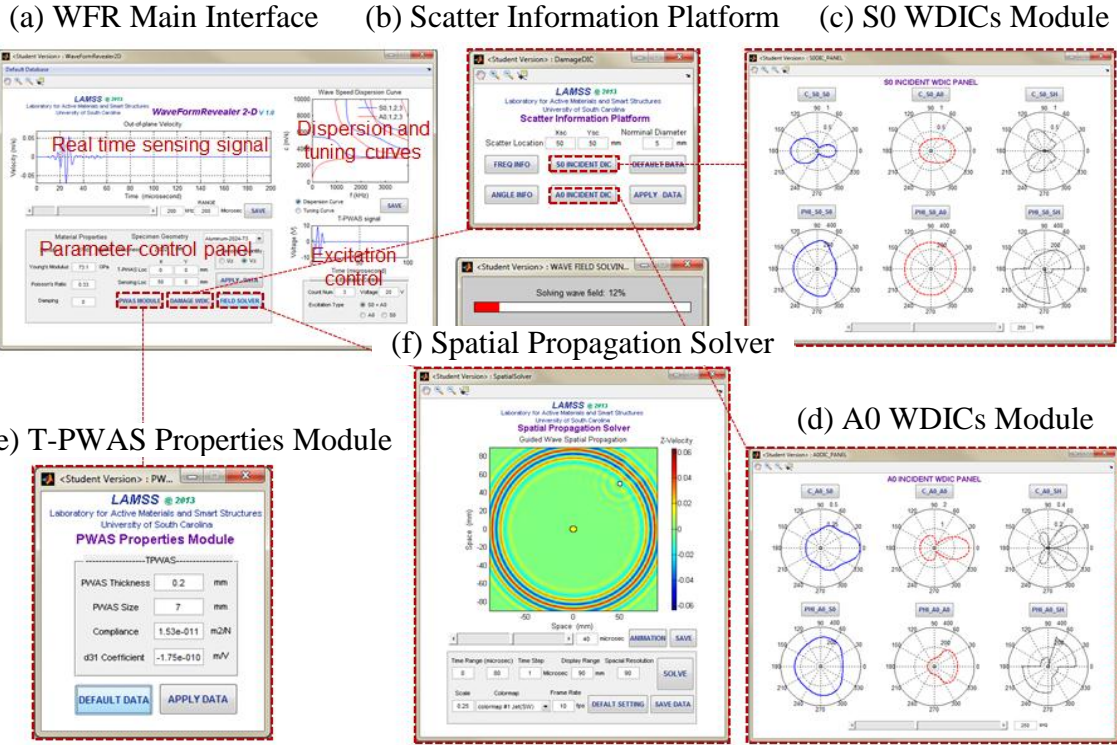
Figure 4.4: GUI of WFR-2D: (a) WFR-2D main interface; (b) damage information platform; (c) S0 WDICs module; (d) A0 WDICs module; (e) T-PWAS properties module; (f) spatial propagation solver.

The extraction of WDICs is the key for CAFA. To obtain these frequency and direction dependent complex-valued coefficients, harmonic analysis of local FEM were carried out. To minimize the model size, we adopted the non-reflective boundary (NRB) technique. The next section will illustrate how we realized and improved the NRB condition in FEM using spring-damper elements.

4.5     NON-REFLECTIVE BOUNDARY CONDITION FOR WAVE PROPAGATION

Non-reflective boundaries (NRB) can eliminate boundary reflections, and thus allow for simulation of wave propagation in infinite medium with small-size models. In commercial FEM codes, such as ANSYS LS-DYNA solver with NRB option and

80

ABAQUS using "solid infinite elements", non-reflective viscous boundary condition has been realized by matching reacting forces at the defined NRB. Lysmer and Kuhlemeryer (1969) found that the matching normal and shear stresses should satisfy

$$\sigma = \rho c_P \frac{\partial u}{\partial t} \tag{4.18}$$

$$\tau = \rho c_S \frac{\partial v}{\partial t} \tag{4.19}$$

where the reacting stresses on the artificial boundary depends on the normal and tangential velocities $\frac{\partial u}{\partial t}$ and $\frac{\partial v}{\partial t}$. COMBIN14 spring-damper elements have been used to construct a viscoelastic boundary condition for wave propagation problems in seismic engineering, and a viscous boundary condition for wave propagation in honeycomb plates (Liu 2005; Wang and Liu 2012; Hosseini et al. 2013). This NRB works well for bulk waves, and in the case of plate guided Lamb waves, it works well for S0 mode, but noticeable reflections occur when A0 mode interacts with the NRB.



(a)                    (b)                    (c)
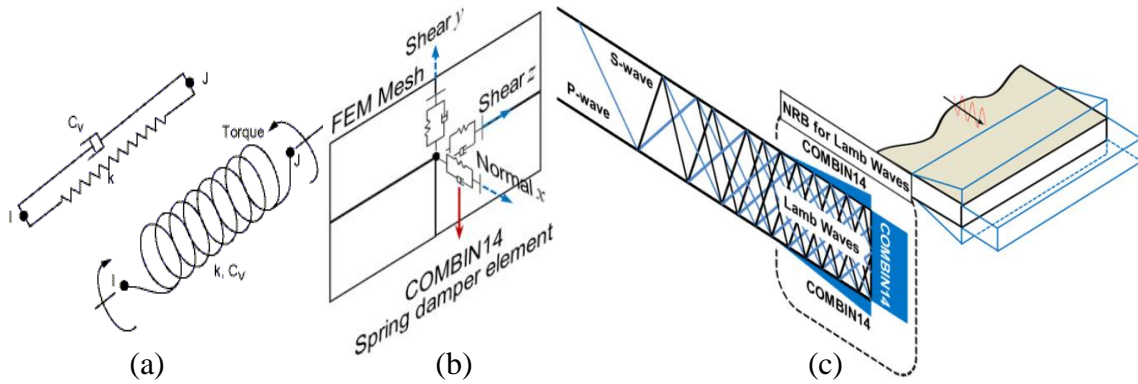
Figure 4.5: (a) COMBIN14 spring-damper element (ANSYS); (b) 3-D NRB construction using COMBIN14; (c) COMBIN14 parameter distribution of NRB for Lamb waves.

In this study, we improved the NRB, making it effective for both symmetric and antisymmetric Lamb modes, in 3-D FEM using COMBIN14 spring-damper elements.

Figure 4.5a shows the schematic of COMBIN14 in ANSYS, and Figure 4.5b illustrates the method of constructing NRB in a 3-D FEM mesh, where each node is connected with three COMBIN14 elements in three directions: one normal direction, and two tangential directions.

According to Eqs. (4.18) and (4.19), the spring damper coefficients can be found

$$
\begin{aligned}
K_N = 0; & \quad C_N = \rho c_P L_Y L_Z \\
K_T = 0; & \quad C_T = \rho c_S L_Y L_Z
\end{aligned}
\tag{4.20}
$$

In conventional practice for constructing NRB, COMBIN14 are only defined at the target boundary. Numerical experiments have found noticeable A0 reflections. In our design of NRB for Lamb waves, we consider the nature of Lamb waves, which is the superposition of multi-reflections of pressure wave and shear vertical wave between top and bottom plate surfaces as shown in Figure 4.5c. Thus, to better absorb out-of-plane wave motion, we distribute COMBIN14 elements not only along the target vertical plate surface, but also along the top and bottom surfaces in the vicinity of the target boundary. Besides, when waves interact with the NRB, the sudden change in FEM matrices will cause reflections. After a series of numerical experiments, a linear transition distribution from zero up to 20% of the full coefficients (given in Eq. (4.20)) was chosen for top and bottom surface COMBIN14 element parameters. This transient distribution should cover at least two A0 wavelengths along the propagation direction. The vertical plate end was implemented with COMBIN14 elements with full parameters calculated from Eq.(4.20).

To evaluate the effectiveness of the NRB for Lamb waves, transient finite element analyses were conducted. Figure 4.6shows the comparison between wave fields and signals from reflective boundaries (RB) and NRB. It can be observed, in Figure 4.6a, that the RB wave field has obvious reflections, however, in Figure 4.6b, the incident waves

are absorbed by NRB and no reflections occurred. Figure 4.7 shows that RB simulation signal contains reflected S0 and A0 waves, while the signal from NRB simulation shows neither reflected S0 nor A0 waves. It is remarkable that the proposed NRB for Lamb waves works well for both S0 mode and A0 mode waves.
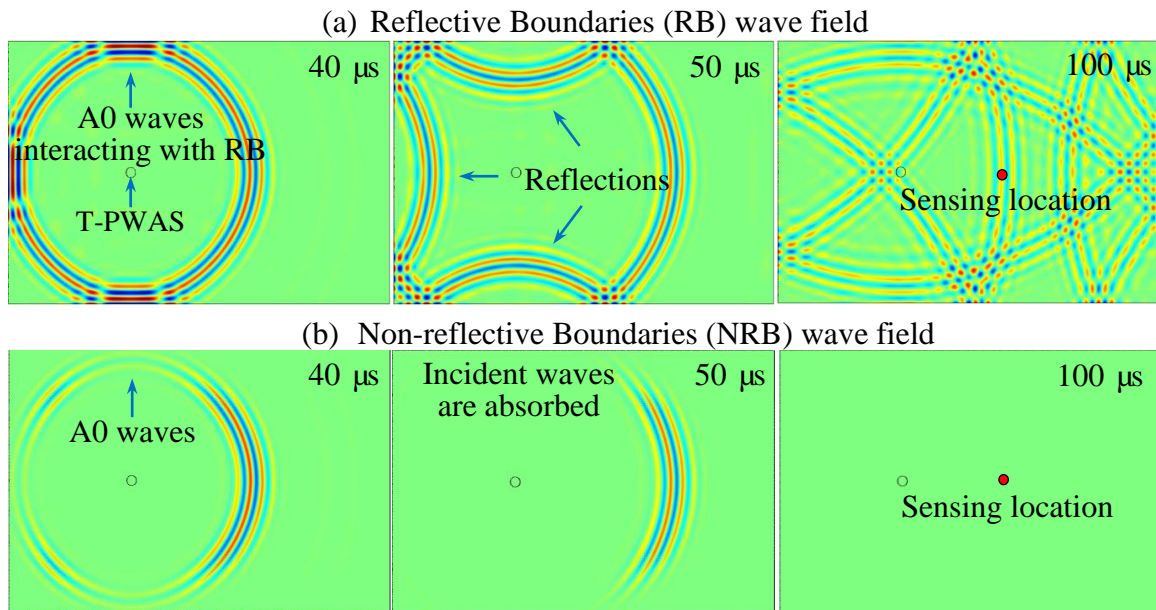


Figure 4.6: (a) Reflective boundaries (RB) wave field; (b) Non-reflective boundaries (NRB) wave field.
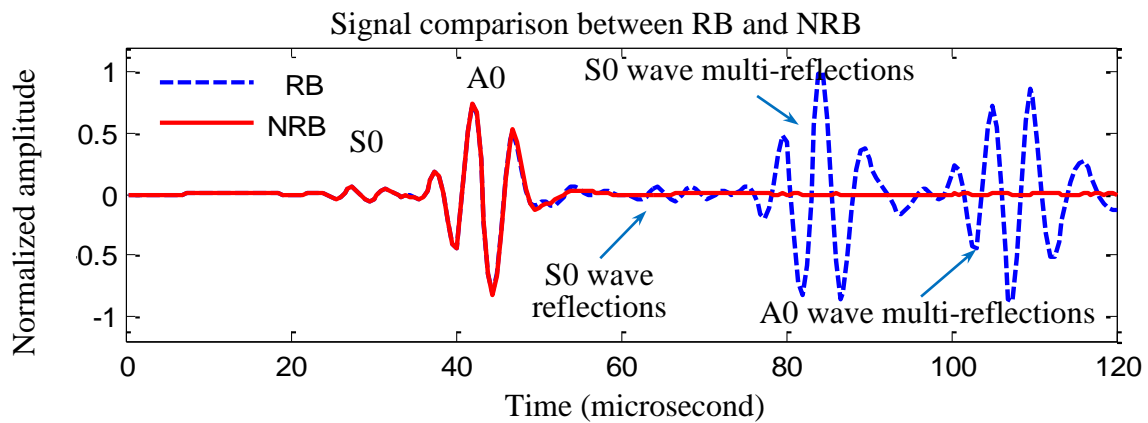


Figure 4.7: Comparison of sensing signals between RB and NRB simulation.

## 4.6    EXTRACTION OF WDICS FROM LOCAL FEM

### 4.6.1    LOCAL FINITE ELEMENT MODEL

The development of NRB was shown in the previous section with an example of a transient analysis. This NRB application was extended to analyze harmonic responses, in order to calculate the steady-state response under sinusoidal loads. NRB are used in the FEM harmonic analysis to simulate continuous harmonic waves which are incident to a region of interest, as well as waves scattering from an arbitrary damage. This analysis can be performed for any specific frequency of interest. The steady-state amplitude and phase information facilitate the extraction of WDICs $C_{AB}(\omega,\theta)e^{-i\varphi_{AB}(\omega,\theta)}$. In order to extract WDICs for a certain Lamb mode, a pair of harmonic analyses needs to be conducted: a pristine case and a damaged case. Since this study focused on fundamental S0 and A0 wave interaction with damage, two pairs of (a total of four) harmonic analyses need to be performed. Figure 4.8 shows the small-size FEM pair designed for a 2.032-mm thick 2024-T3 aluminum plate. Each model is 100mm long, 100 mm wide, and 2.032 mm thick, with a 30 mm wide NRB covering each boundary.

Figure 4.8 also shows the loading nodes and the sensing nodes. The loading nodes are aligned to create a straight crested harmonic incident wave field, which is a good approximation when the damage is located far away from the excitation source. In the pristine model, a circle of sensing nodes and one center sensing point are designed to collect the structural harmonic response. The center sensing point records the incident waves arriving at the damage location. In the damaged case, only a circle of sensing nodes, with the same location as the pristine model, are used to collect the response data.

The design of the circular positioned sensing nodes allows us to extract information for all the directions of interest.
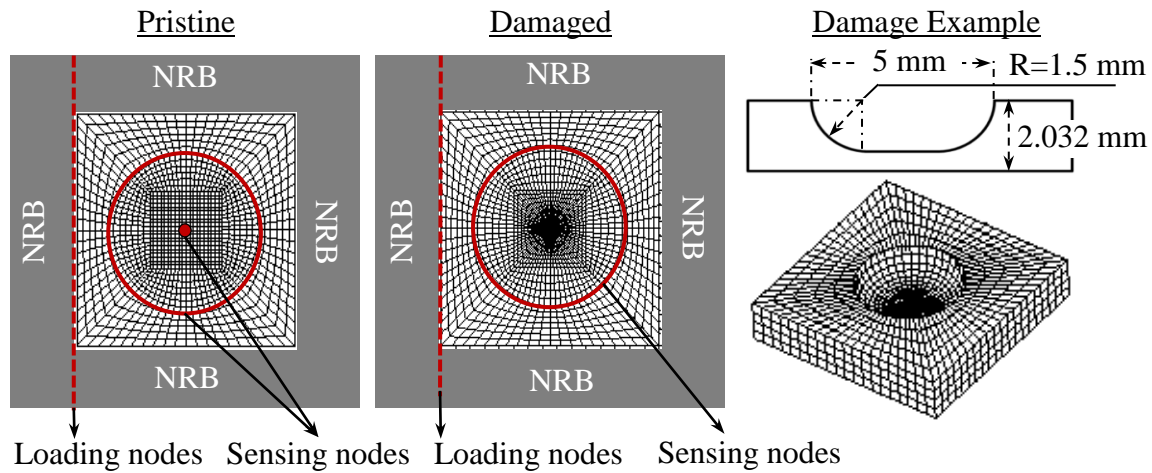


Figure 4.8: Small-size local FEM pair for WDICs extraction.

A damage example is shown in Figure 4.8. The geometry of damage is kept simple to ensure consistent FEM and experimental models, but complex enough to represent general wave-damage interaction phenomena, which have many mode conversion possibilities in the given frequency range. It should be noted that different types of damage will have different scattering characteristics; this will require a corresponding local damage model for WDIC extraction.

4.6.2  IMPOSING EXACT LAMB MODE EXCITATION

In this study, we imposed Lamb mode excitation through nodal forces by evaluating integrals of stress mode shape components on the loading nodes. The stress mode shapes are calculated analytically from Eq. (4.21) and Eq. (4.22).

For symmetric modes:

$$\sigma_{xx}^S(x,y,t) = C^S 2\mu\xi\eta_S \left[ \left(\xi^2 + \eta_S^2 - 2\eta_P^2\right)\cos\eta_S d \cos\eta_P y - (\xi^2 - \eta_S^2)\cos\eta_P d \cos\eta_S y \right] e^{i(\xi x - \omega t)}$$

$$\sigma_{yy}^S(x,y,t) = -C^S 2\mu\xi\eta_S \left(\xi^2 - \eta_S^2\right)\left(\cos\eta_S d \cos\eta_P y - \cos\eta_P d \cos\eta_S y\right) e^{i(\xi x - \omega t)}$$

$$\sigma_{xy}^S(x,y,t) = iC^S \mu \left[ 4\xi^2\eta_P\eta_S \cos\eta_S d \sin\eta_P y + \left(\xi^2 - \eta_S^2\right)^2 \cos\eta_P d \sin\eta_S y \right] e^{i(\xi x - \omega t)}$$

(4.21)

For antisymmetric modes:

$$\sigma_{xx}^A(x,y,t) = -C^A 2\mu\xi\eta_S \left[ \left(\xi^2 + \eta_S^2 - 2\eta_P^2\right)\sin\eta_S d \sin\eta_P y - (\xi^2 - \eta_S^2)\sin\eta_P d \sin\eta_S y \right] e^{i(\xi x - \omega t)}$$

$$\sigma_{yy}^A(x,y,t) = C^A 2\mu\xi\eta_S \left(\xi^2 - \eta_S^2\right)\left(\sin\eta_S d \sin\eta_P y - \sin\eta_P d \sin\eta_S y\right) e^{i(\xi x - \omega t)}$$

$$\sigma_{xy}^A(x,y,t) = iC^A \mu \left[ 4\xi^2\eta_P\eta_S \sin\eta_S d \cos\eta_P y + \left(\xi^2 - \eta_S^2\right)^2 \sin\eta_P d \cos\eta_S y \right] e^{i(\xi x - \omega t)}$$

(4.22)
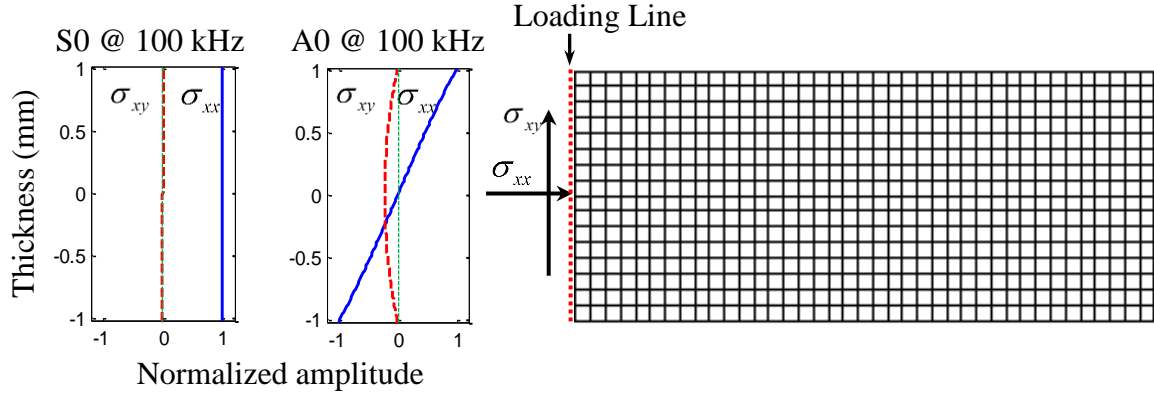


Figure 4.9: Imposing Lamb mode excitation.

Figure 4.9 shows the process of imposing Lamb mode excitation on the model. The stress mode shapes were obtained for each calculation frequency analytically. Then, the stress mode shapes were converted to nodal forces through boundary integration on each element along the loading line. The element nodal force can be evaluated according to Reddy 2005:

$$F_{ix}^e = \int_0^{L_{element}} \sigma_{xx}^e(s) N_i^e(s) \, ds; \quad F_{iy}^e = \int_0^{L_{element}} \sigma_{xy}^e(s) N_i^e(s) \, ds \qquad (4.23)$$

where $F_{ix}^e$ and $F_{iy}^e$ are nodal forces in $x$ and $y$ direction evaluated on element $e$; $i$ is the element node number; $\sigma_{xx}^e(s)$ and $\sigma_{xy}^e(s)$ are the normal and shear stress field acting on this element; $N_i^e(s)$ is the shape function of selected element type. In this study, we used SOLID45 3-D eight-node structure element, which utilizes linear shape function $N_i^e(x, y, z)$. Along the thickness direction, it becomes $N_i^e(s)$, which is 1-D interpolation function along the line.

$$N_1^e(s) = 1 - \frac{s}{L_{element}}; \quad N_2^e(s) = \frac{s}{L_{element}} \qquad (4.24)$$

After all the nodal forces were obtained, an assembly process was carried out to obtain the global nodal forces. Then the nodal forces were updated for each calculation step, imposing Lamb mode excitation for each excitation frequency.

### 4.6.3 WDICs EXTRACTION PROCEDURE

When Lamb waves arrive at damage, they will be scattered and mode converted. The scattered wave field, by its nature, can be regarded as the superposition of waves irradiating from distributed point sources around the damage contour. The constructive or destructive interference among these waves is the cause of scattered wave field directionality and phase lead or delay. We used frequency and direction dependent complex-valued WDICs to represent the wave scattering phenomena. It has been shown in Eq. (4.11) that Lamb waves irradiating from a point source follows a Hankel function of order one ($H_1^{(1)}(\xi_n r)$) propagation pattern. Shear horizontal (SH) waves irradiating from a point source can be derived starting from the governing equation.

$$\nabla^2 u = \frac{1}{c_S^2} \frac{\partial^2 u}{\partial t^2} \tag{4.25}$$

In polar coordinate system, considering an axisymmetric condition, Eq. (4.25) becomes

$$\frac{\partial^2 u_\theta}{\partial r^2} + \frac{1}{r} \frac{\partial u_\theta}{\partial r} + \frac{1}{r^2} \cancel{\frac{\partial^2 u_\theta}{\partial \theta^2}} = \frac{1}{c_S^2} \frac{\partial^2 u_\theta}{\partial t^2} \tag{4.26}$$

Assuming a harmonic wave field

$$u_\theta = U e^{-i\omega t}; \quad \frac{\partial^2 u_\theta}{\partial t^2} = -\omega^2 u_\theta \tag{4.27}$$

Substitution of Eq. (4.27) into Eq. (4.26) yields

$$\left( \xi^{SH} r \right)^2 \frac{\partial^2 u_\theta}{\partial \left( \xi^{SH} r \right)^2} + \left( \xi^{SH} r \right) \frac{\partial u_\theta}{\partial \left( \xi^{SH} r \right)} + \left( \xi^{SH} r \right)^2 u_\theta = 0 \tag{4.28}$$

where $\xi^{SH} = \dfrac{\omega}{c_s}$ is the wavenumber of SH waves. Recall the Bessel equation of order $\nu$.

$$x^2 \frac{d^2 y}{dx^2} + x \frac{dy}{dx} + \left( x^2 - \nu^2 \right) y = 0 \tag{4.29}$$

Eq. (4.28) can be immediately recognized as the Bessel equation of order zero and accepts the following solution for outward propagating waves.

$$u_\theta = \sum_{n=1}^{\infty} b_n(z) H_0^{(1)} \left( \xi_n^{SH} r \right) e^{-i\omega t} \tag{4.30}$$

where $b_n(z)$ is the modeshape of the $n^{\text{th}}$ SH mode, and $H_0^{(1)}$ is the first kind Hankel function of order zero.

Figure 4.10 shows the schematic of the sensing region from the small-size FEM for the extraction of WDICs. The in-plane displacements at the sensing nodes are used. According to Eq.(4.1), the scattered wave field can be obtained by the subtraction of the incident waves from the total waves.
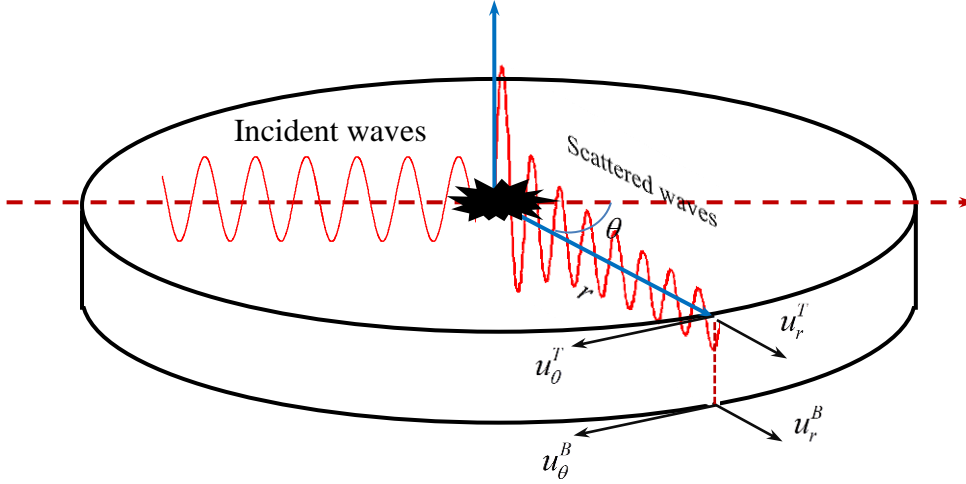
Figure 4.10: Extraction of WDICs from small-size FEM.

$$W_{SC} = W_{TOTAL} - W_{IN} \tag{4.31}$$

The sensing nodes data in the pristine model is the incident wave field, while the data from damaged model represents the total wave field containing both incident and scattered waves. Thus, the subtraction of the data between these two models provides the scattered wave field in all directions. Using Eq. (4.31) and a transformation from Cartesian to polar coordinate system, we calculated the scattered wave displacements at the top and bottom surface sensing nodes in both radial ($u_r^T$ and $u_r^B$) and tangential ($u_\theta^T$ and $u_\theta^B$) directions. Using Eq. (4.32), we can separate and selectively represent each wave mode.

$$u_{SC}^{S0} = \frac{u_r^T + u_r^B}{2}; \quad u_{SC}^{A0} = \frac{u_r^T - u_r^B}{2}; \quad u_{SC}^{SH0} = \frac{u_\theta^T + u_\theta^B}{2}; \tag{4.32}$$

The incident wave arriving at the damage location is recorded by the center sensing point and denoted as $u_{IN}$. The relationship between the incident wave arriving at the damage and the scattered wave picked up on the sensing boundary can be formulated as Eq. (4.33).

$$u_{IN}^{A} e^{-i\varphi_{IN}^{A}} C_{AB}(\omega,\theta) e^{-i\varphi_{AB}(\omega,\theta)} H_m^{(1)}(\xi^B r) = u_{SC}^{B}(\theta) e^{-i\varphi_{SC}^{B}(\theta)} \tag{4.33}$$

where $u_{IN}^{A} e^{-i\varphi_{IN}^{A}}$ is the $A$ mode incident wave recorded by the center sensing node with amplitude and phase information; $C_{AB}(\omega,\theta) e^{-i\varphi_{AB}(\omega,\theta)}$ is the WDIC, containing mode conversion ($A$ mode to $B$ mode), direction dependency, amplitude ratio, and phase relationship information; $H_m^{(1)}(\xi^B r)$ represents the outward propagating 2-D wave field of the resulting scattered wave mode $B$, with $m=1$ for Lamb waves and $m=0$ for SH waves. $u_{SC}^{B}(\theta) e^{-i\varphi_{SC}^{B}(\theta)}$ is the resulting scattered waves recorded on the sensing circle with scatter angle, amplitude and phase information.

The harmonic analysis of the small-size FEM can provide the incident and scattered wave amplitude-phase information in Eq. (4.33), with $C_{AB}(\omega,\theta) e^{-i\varphi_{AB}(\omega,\theta)}$ left as the only unknown term. Upon rearrangement, Eq. (4.33) becomes

$$C_{AB}(\omega,\theta) e^{-i\varphi_{AB}(\omega,\theta)} = \frac{u_{SC}^{B}(\theta)}{u_{IN}^{A}} \frac{1}{H_m^{(1)}(\xi^B r)} e^{-\Delta\varphi_{AB}(\theta)}; \quad \Delta\varphi_{AB}(\theta) = \varphi_{SC}^{B}(\theta) - \varphi_{IN}^{A} \tag{4.34}$$

By identification, the amplitude coefficient and phase coefficient can be extracted.

$$C_{AB}(\omega,\theta) = \left| \frac{u_{SC}^{B}(\theta)}{u_{IN}^{A}} \frac{1}{H_m^{(1)}(\xi^B r)} \right|$$

$$\varphi_{AB}(\omega,\theta) = \Delta\varphi_{AB}(\theta) - \left[ \angle \frac{1}{H_m^{(1)}(\xi^B r)} - \angle \frac{1}{H_m^{(1)}(0^+)} \right] \tag{4.35}$$

### 4.6.4   EXAMPLES OF WDICS

Figure 4.11 shows an example of S0 wave interaction with damage at 200 kHz. The first row shows the amplitude coefficients and the second row shows the phase coefficients. It can be observed that the interaction between the incident S0 wave and the

damage not only involves scattered S0 wave, but also involves mode converted A0 and SH0 waves. Also, the amplitude and phase coefficients are different for each scattering direction, i.e., they are heavily direction-dependent. The calculation of amplitude coefficients has been investigated in many literatures with various methods, but the estimation of phase coefficients has been ignored by previous researchers. The phase coefficients are of great significance in simulating wave-damage interaction, because they represent the constructive or destructive superposition of incident and scattered wave fields. Figure 4.12 shows the $C_{SA}$ amplitude coefficient and $\varphi_{SA}$ phase coefficient under various frequencies. It can be observed that WDICs are frequency dependent.
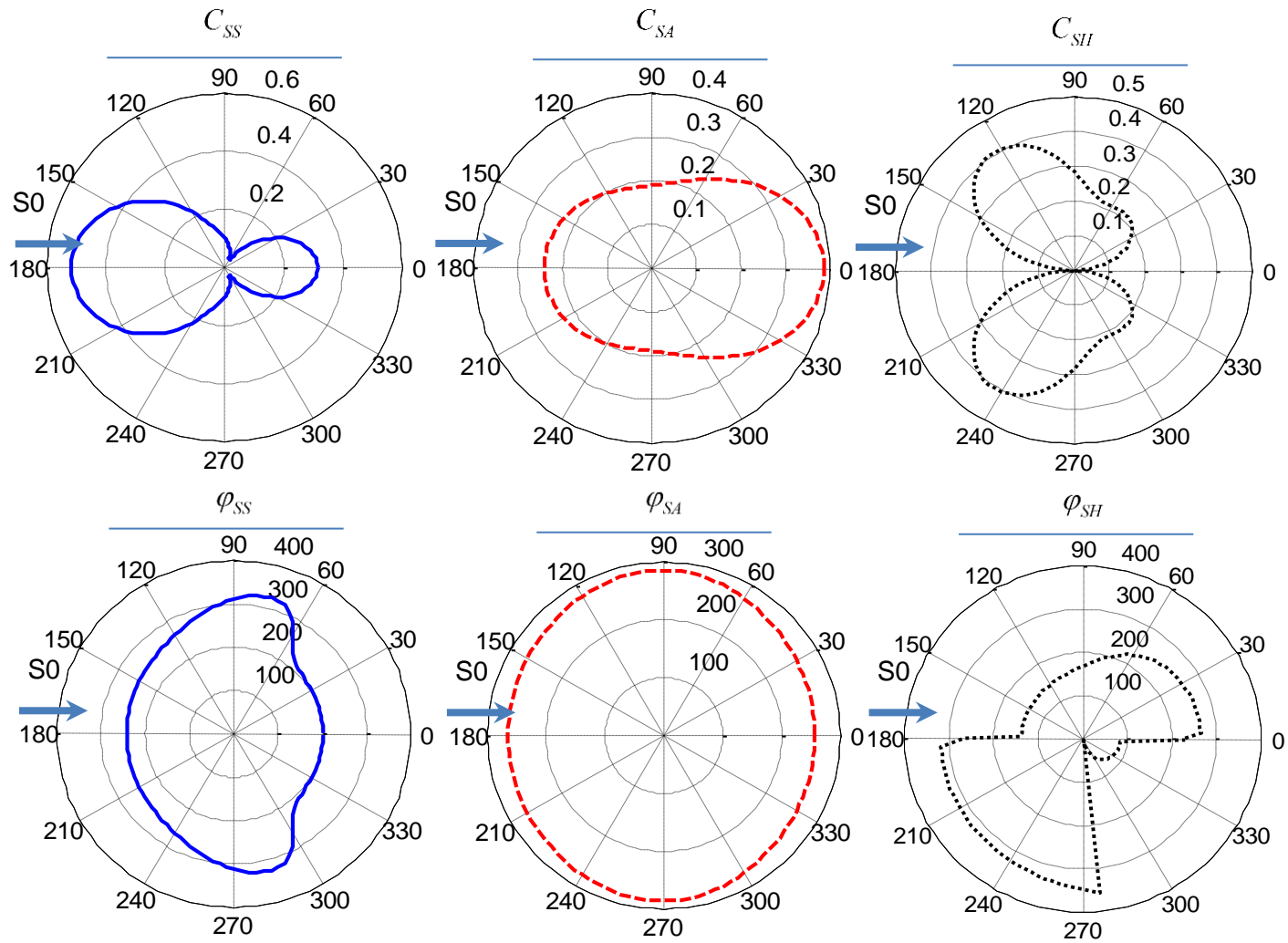
Figure 4.11: WDICs example of S0 wave interaction with damage at 200 kHz.
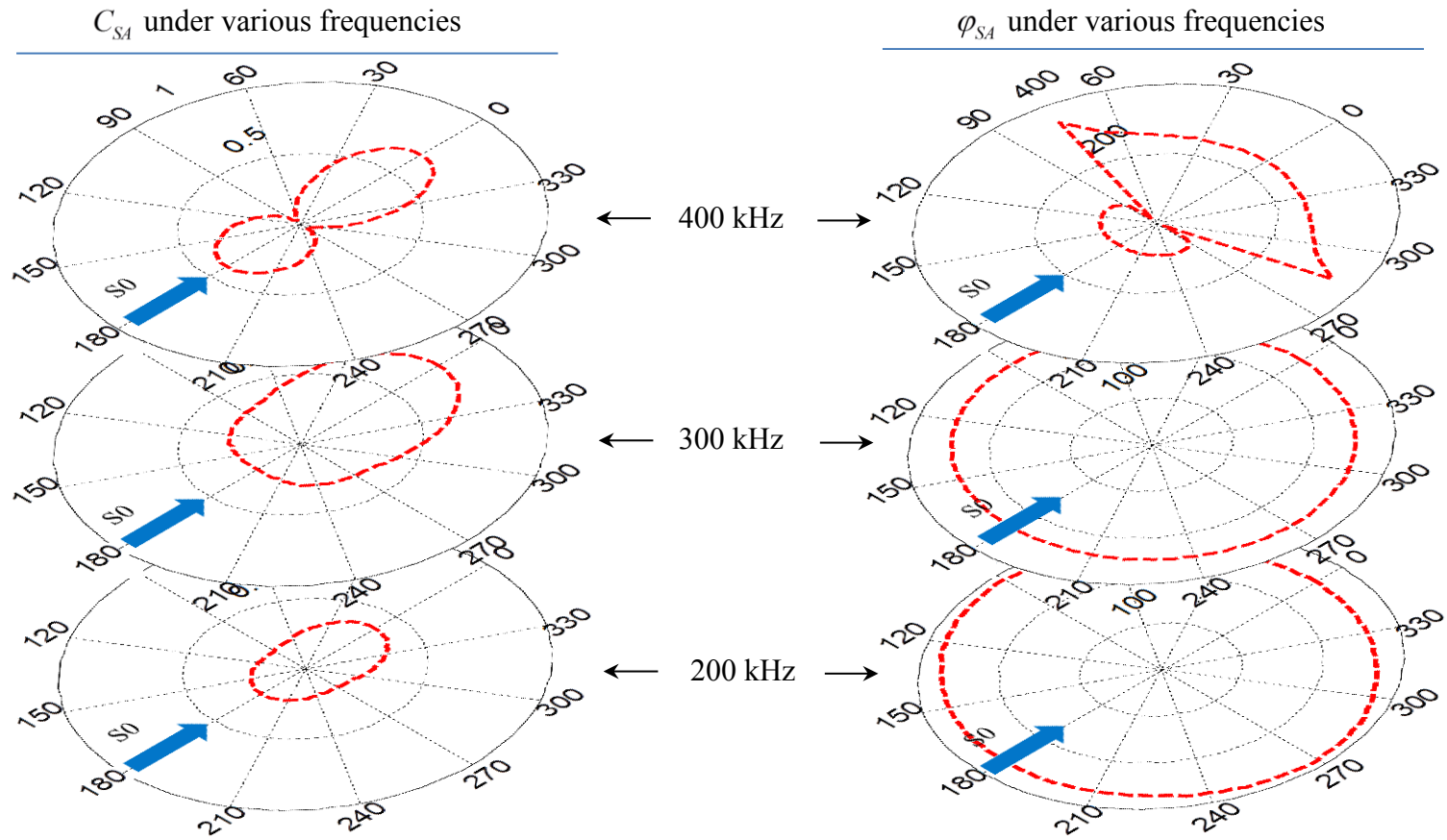
Figure 4.12: WDICs under various frequencies.
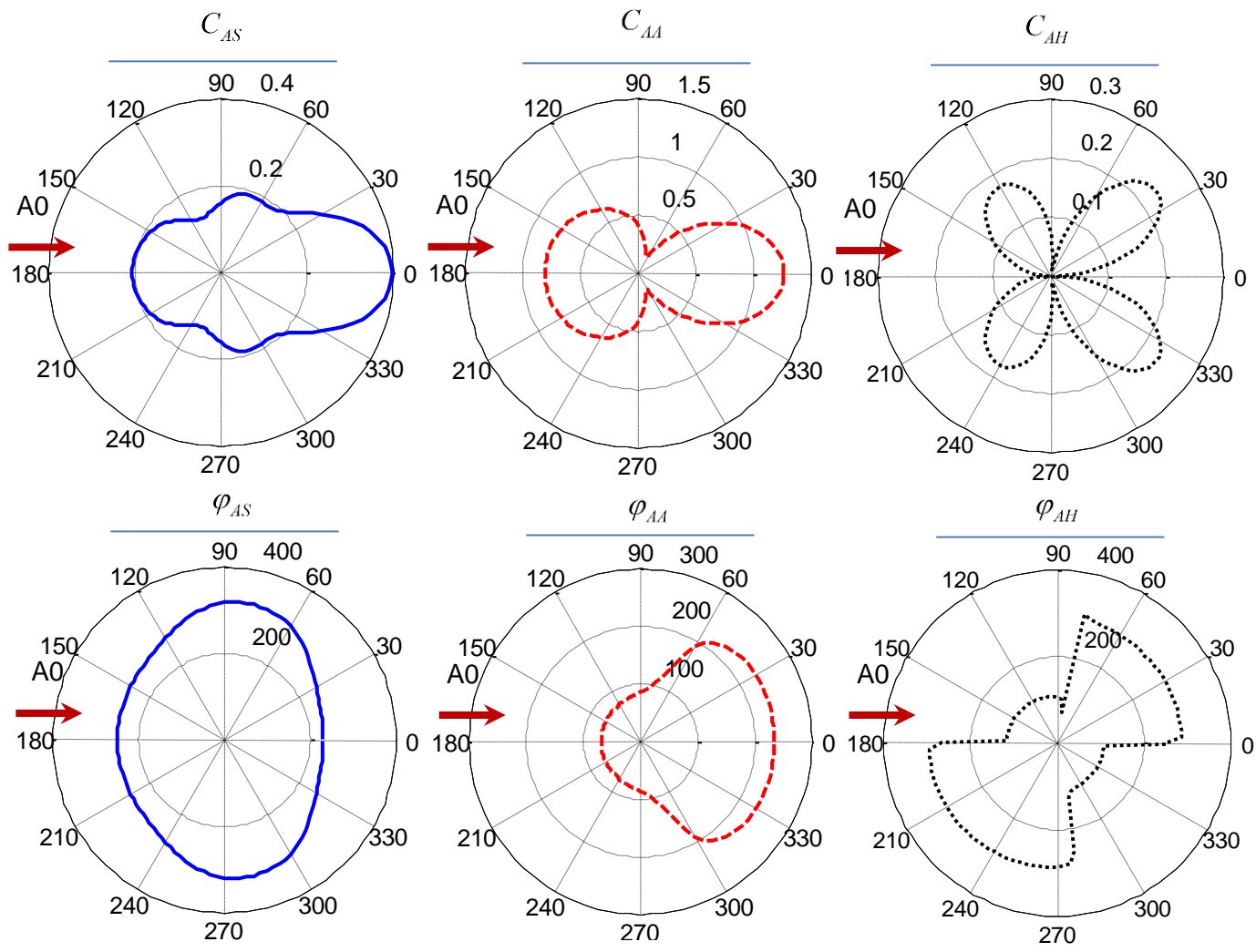
Figure 4.13: WDICs example of A0 wave interaction with damage at 200 kHz.

Figure 4.13 shows the WDICs for the incident A0 wave at 200 kHz. Similar scattering, mode conversion and direction-dependency phenomena can also be noticed in the coefficient patterns.

## 4.7 NUMERICAL AND EXPERIMENTAL VERIFICATIONS

In this section, we will present the multiphysics finite element models and experiments for CAFA verification. The comparison results are shown for wave propagation in a pristine plate and a damaged plate.

### 4.7.1 MULTI-PHYSICS FINITE ELEMENT MODEL

Figure 4.14 shows the finite element model. The specimen is a 2.032 mm thick aluminum plate. To minimize the calculation burden, NRB were implemented around the model. We used SOLID5 coupled field elements to simulate the piezoelectric effect of T-PWAS, SOLID45 eight node structure element to mesh the plate, and COMBIN14 spring-damper element to construct the NRB. The mesh size adopted in this study is 1 mm for in-plane direction and 0.5 mm for thickness direction. The T-PWAS and damage regions were meshed with even smaller elements to accommodate the high stress gradient. A total of 423,468 elements were used. The time step was set to 0.25 μs.
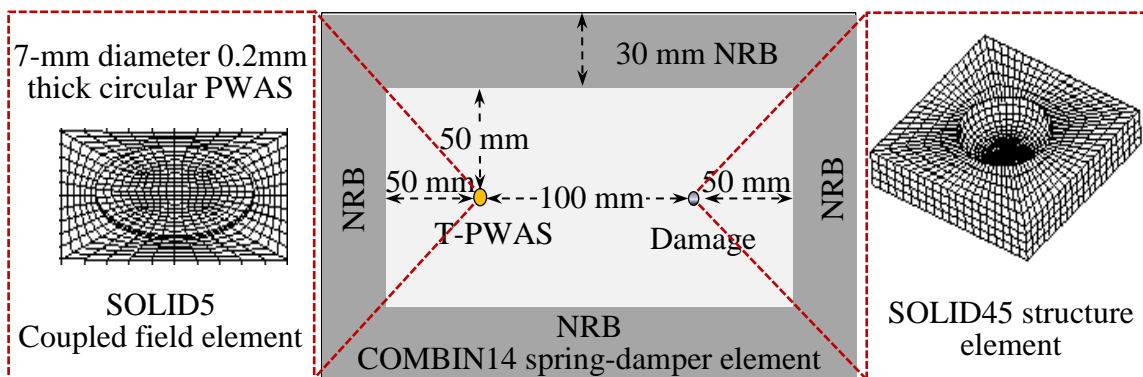


Figure 4.14: Multi-physics finite element model.

Two sets of simulations were carried out: (1) 2-D Lamb wave propagation in a pristine plate; (2) 2-D Lamb wave propagation in a damaged plate. The location and geometry information of the T-PWAS, damage and specimen are shown in Figure 4.14.

4.7.2    EXPERIMENTS WITH SCANNING LASER VIBROMETER

Figure 4.15 shows the experimental setup. The function generator was used to generate a 3-count Hanning window modulated tone burst which was amplified to 50 vpp by the amplifier and applied to the T-PWAS. Lamb waves generated by the T-PWAS propagated along the structure, interacted with the damage, and were measured by a Polytec PSV-400 scanning laser vibrometer. The quantity measured by the scanning laser vibrometer is the out-of-plane velocity of surface particle motion. Reflective tape was used to enhance the surface reflections and improve visualization quality. A C-scan of the specimen surface was carried out for both the pristine and the damaged plates. The locations of the T-PWAS, damage, and special recording points are illustrated.
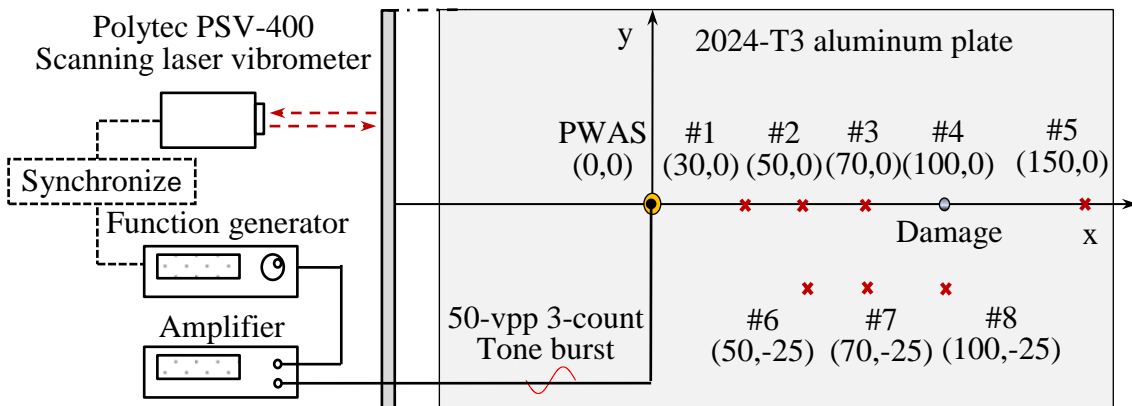


Figure 4.15: Experimental setup with scanning laser vibrometer.

## 4.8    RESULTS AND DISCUSSION

### 4.8.1    WAVE PROPAGATION IN A PRISTINE PLATE

Figure 4.16 shows the comparison of the transient spatial wave field among CAFA, FEM simulation, and experimental measurement in a pristine plate.
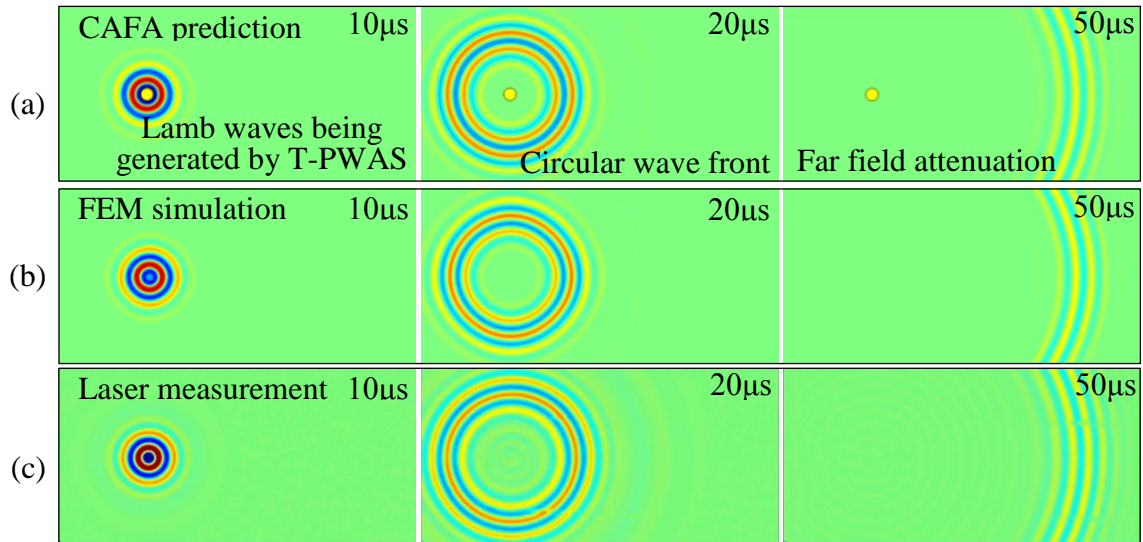


Figure 4.16: Comparison of 200 kHz wave field in the pristine plate: (a) CAFA prediction; (b) FEM simulation; (3) experiment.

It can be observed that CAFA predictions have good agreement with both FEM and experiment. A circular wave front was generated by the T-PWAS, strong near the wave source, and weak at far field due to the outward propagation pattern.

Figure 4.17 shows the waveform validation results at various sensing locations for a 200 kHz excitation. It can be observed that CAFA predictions have good agreement with both FEM simulation and experiments. At the near field (location #2), S0 and A0 waves are mixed together. The FEM result shows a shift from the CAFA prediction, while CAFA prediction agrees well with the laser measurement. The FEM mesh adopted in this study does not capture the near field waves as accurate as CAFA. Of course, we can improve the accuracy of FEM simulation by further discretizing the analyzed domain

with smaller time marching step, but this increase in accuracy requires additional computation resources and a much longer computation time. For higher frequency simulations, full scale FEM becomes prohibitive. It can also be observed that CAFA prediction of the far field waveform agrees well with both FEM and experiments for a pristine plate.
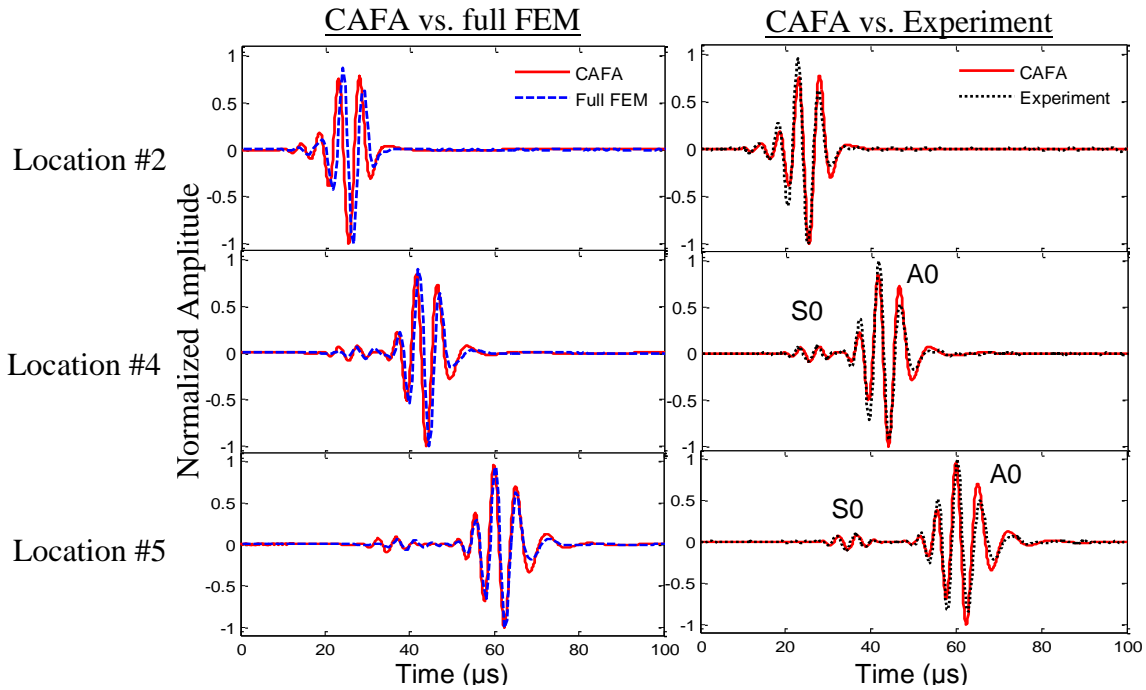


Figure 4.17: CAFA (solid line) validation with full FEM (dashed line) and experiments (dotted line). 200 kHz signals of pristine plate at various sensing locations shown in Figure 4.15.

### 4.8.2 WAVE PROPAGATION IN A DAMAGED PLATE

Figure 4.18 shows the comparison of a transient spatial wave field among CAFA, full FEM simulation and experiment in a damaged plate. It can be observed that the CAFA results agree well with FEM simulation and experimental measurement. At 30 μs, the fast propagating S0 mode with a long wavelength and the slowly propagating A0 mode with short wavelength can be clearly identified. The mode converted A0 waves can

be noticed, propagating with a short wavelength from S0 interaction with the damage. At 50 μs, after A0 waves interact with damage, the scattered A0 mode can be observed as well as the shading left behind the damage. This shading effect is caused by the destructive superposition between the incident A0 waves and the scattered A0 waves. This also illustrates the importance of obtaining phase information in the WDICs. It should be noted that measurement discontinuities were found in the experimental data, which were caused by the reflective tape boundaries.
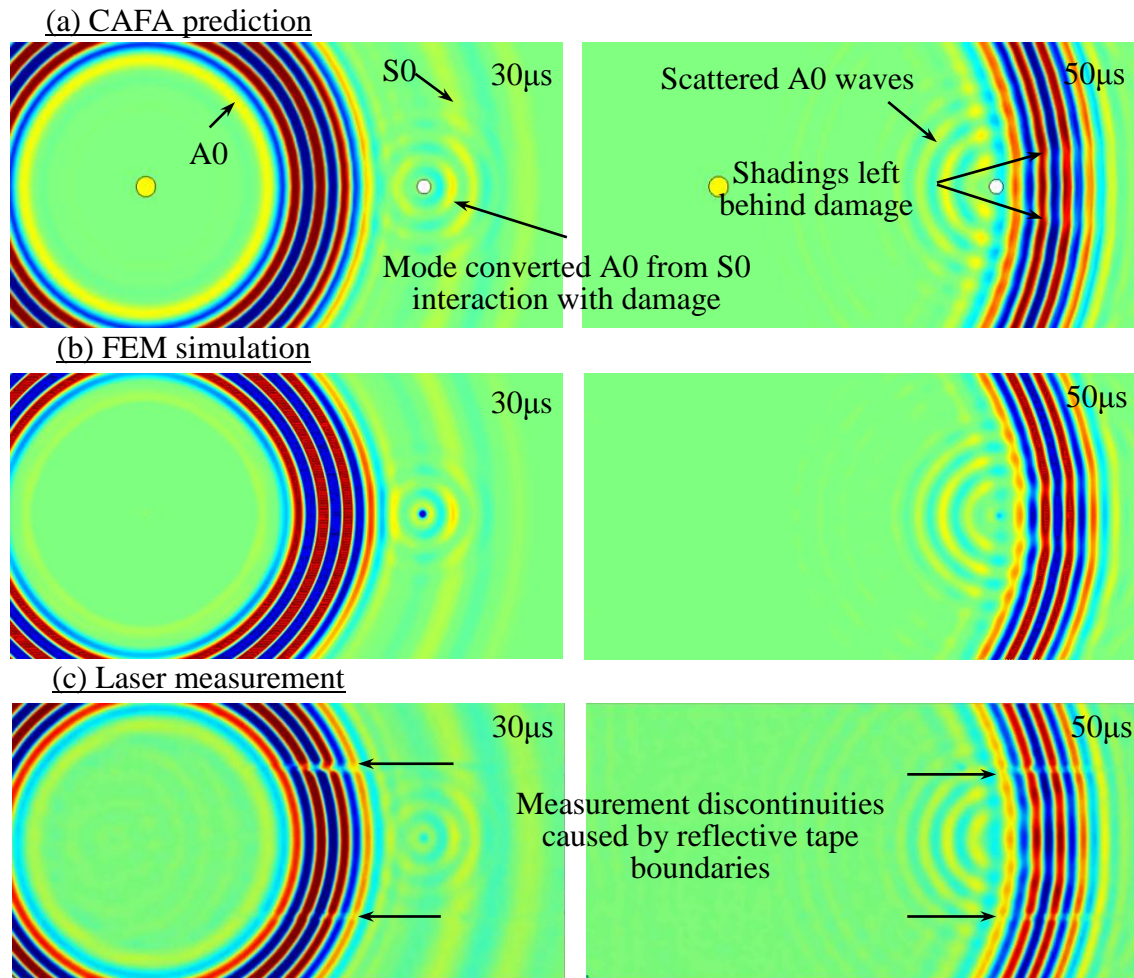


Figure 4.18: Comparison of wave field in damaged plate, showing S0 and A0 Lamb modes interacting with damage: (a) CAFA prediction; (b) FEM simulation; (c) experiment.

Figure 4.19 shows the waveform validation results at various sensing locations for a 200 kHz excitation. It can be observed that WFR predictions match well with FEM simulation and experiments. The signals at location #1, #2, and #3 show that the scattered A0 wave amplitude increases when the sensing location moves closer to the damage. The signal at location #5 shows the mode converted A0 wave packet from the S0 interaction with damage.
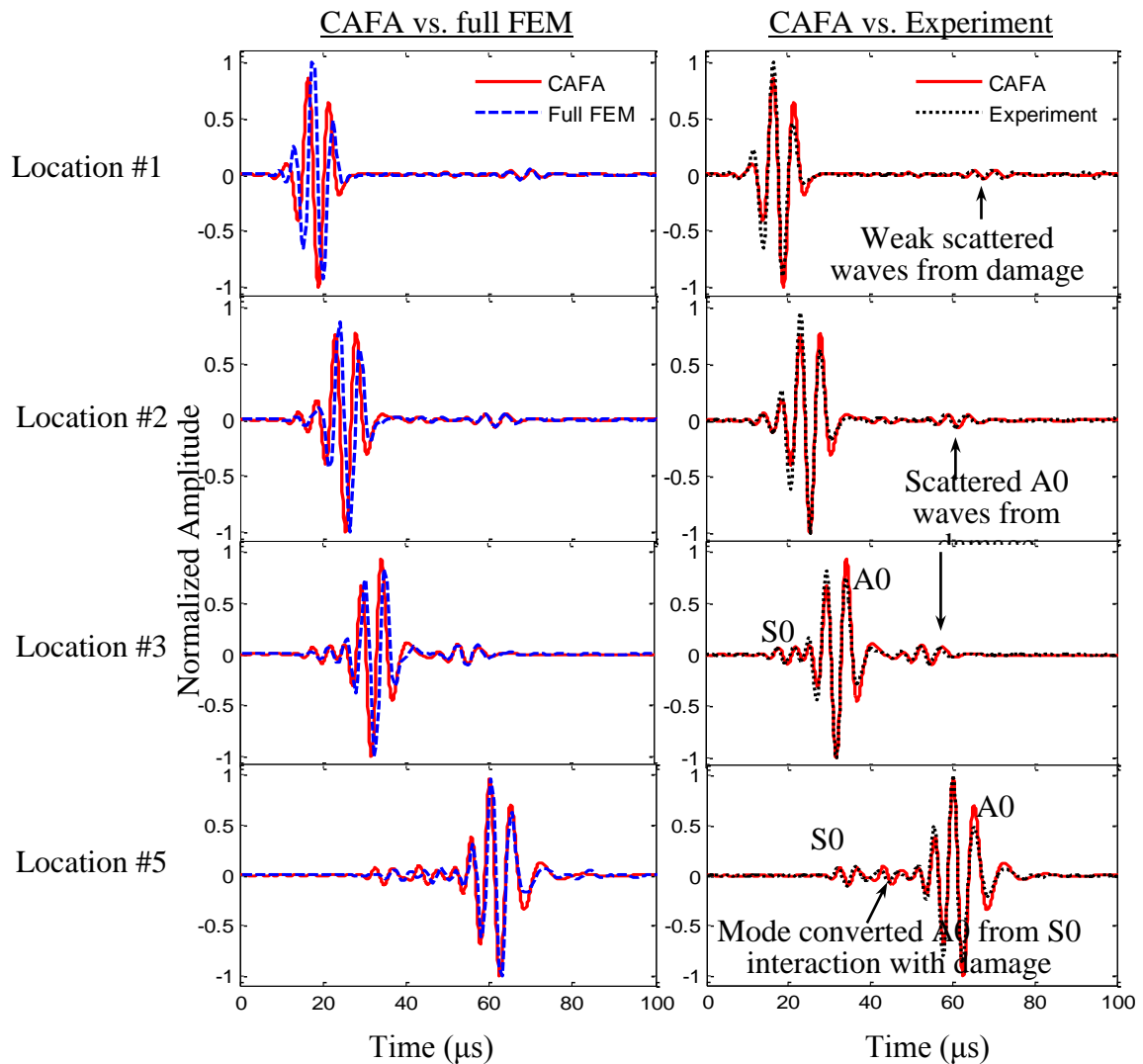


Figure 4.19: CAFA prediction (solid line) validation with full FEM (dashed line) and experiments (dotted line). 200 kHz signals of damaged plate at locations #1 through #5 shown in Figure 4.15.

Figure 4.20 shows the comparison of the sensing signals at locations #6, #7, and #8, which are in certain directions with respect to the incident waves and the damage. It should be noted that at location # 6 and #7, damage scattered waves are clearly observed, but at location #8, no damage effect can be seen. Recall the WDICs pattern in Figure 4.13, the scattered A0 amplitude coefficient reaches a minimum value near 90 degrees with respect to the incident waves. This fact illustrates that at certain sensing locations, the damage cannot be effectively detected. Using CAFA and WFR-2D, the waveform can be predicted at arbitrary sensing locations, and the users can determine whether these locations are sensitive points or blind zones, optimizing the design of a sensor network for damage detection.
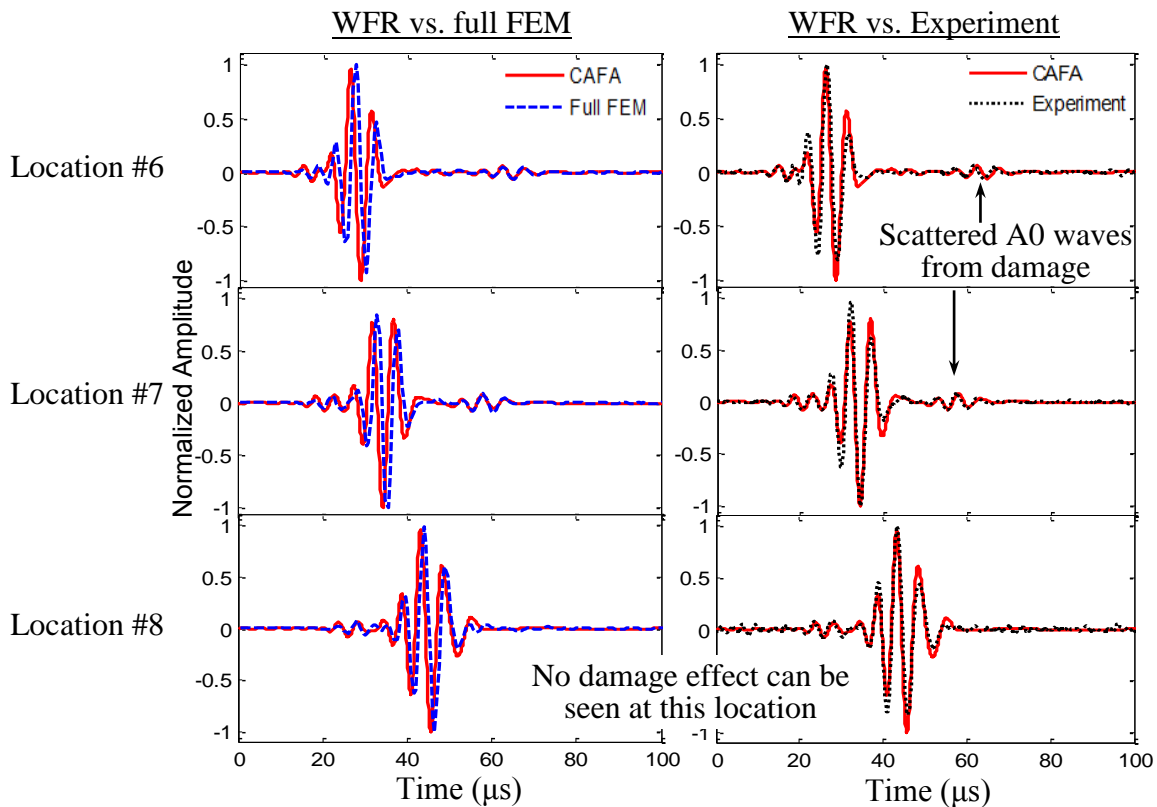


Figure 4.20: CAFA prediction (solid line) validation with full FEM (dashed line) and experiments (dotted line). 200 kHz signals of damaged plate at locations #6 through #8 shown in Figure 4.15.

4.8.3    TEST AT VARIOUS FREQUENCIES

The results demonstrated in the previous sections are from examples of a 200 kHz excitation. To illustrate the accuracy of CAFA for various frequencies, we compared CAFA predictions with experimental results for 150 kHz, 200 kHz, and 250 kHz excitations. The results of sensing signals at location #5 are shown for both the pristine plate case and the damaged plate case.
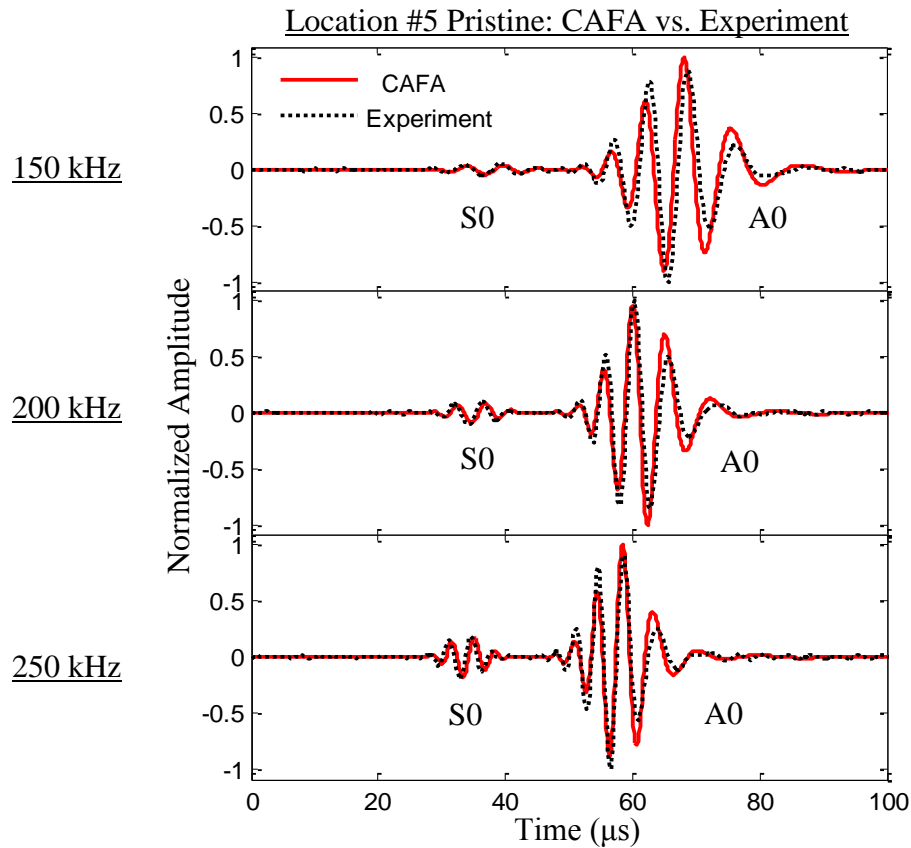


Figure 4.21: Test for various frequencies in the pristine plate.

Figure 4.21 shows the signal comparison in the pristine plate under 150 kHz, 200 kHz, and 250 kHz. It can be observed that the CAFA predictions agree well with experimental measurements. The relative amplitude ratio between S0 and A0 waves matches well. At low frequency, i.e. 150 kHz, the S0 wave is weak and the A0 wave is

dominant. As the excitation frequency goes up, the amplitude of the S0 wave grows and its participation in the wave signal increases.

Figure 4.22 shows the signal comparison in the damaged plate under 150 kHz, 200 kHz, and 250 kHz. The CAFA predictions for the test frequencies compare well with experimental measurements. By comparing with Figure 4.21, it can be observed that beside S0 and A0 wave packet, damage effects showed up in the sensing signal as an additional wave packet between the S0 and A0 waves. At low frequencies, i.e. 150 kHz, the damage effect is not clear, but at higher excitation frequencies, the damage effect can be distinguished clearly. This illustrates the importance of choosing the right interrogation frequency.
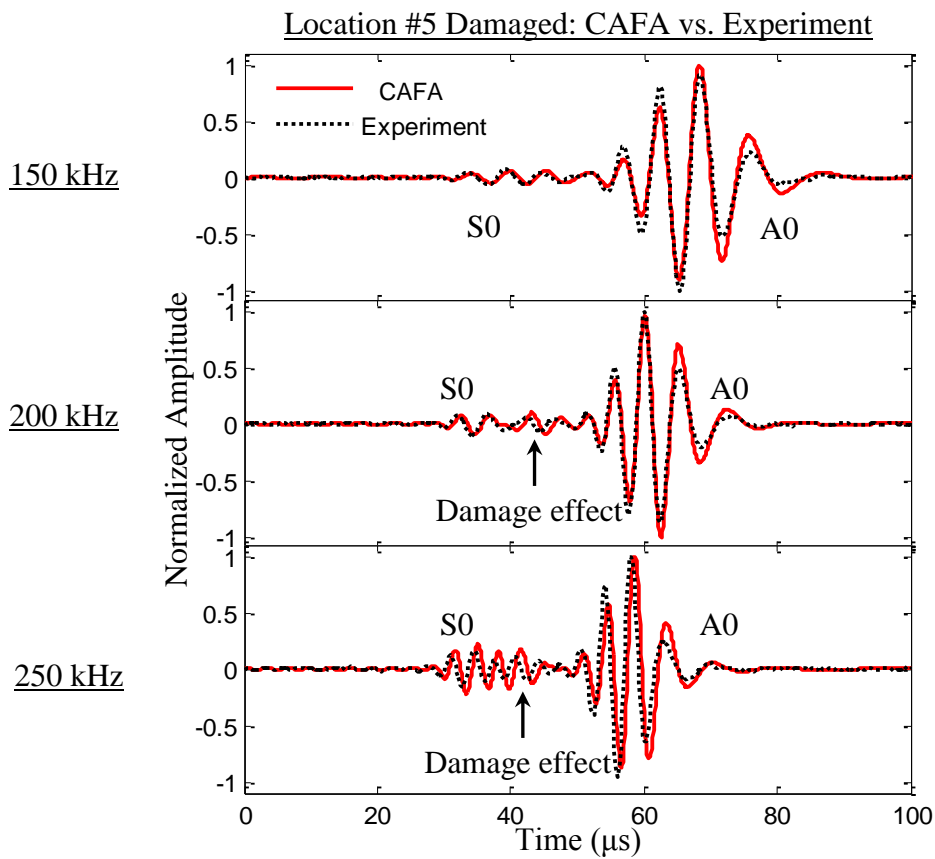


Figure 4.22: Test for various frequencies in the damaged plate.

### 4.8.4 ADVANTAGE OF CAFA OVER CONVENTIONAL FEM

For the simulation of guided wave active sensing, conventional transient FEM simulation is widely used (also shown in our comparative study). CAFA's advantage over conventional FEM comes from its highly efficient computation algorithm. Conventional transient FEM simulation requires the dense discretization of the entire analysis domain, and extremely small time marching step to ensure the accuracy for high frequency, short wavelength, and long propagation distance waves. Such kind of computation may become prohibitive for high frequency and large scale problems. CAFA only requires the discretization of the local damage region, where the numerical model size is minimized. Instead of transient analysis, the damage interaction phenomena are calculated through harmonic analysis, which is the most efficient way of extracting wave damage interaction characteristics under all the frequencies of interest. The frequency domain global analytical formulation, using Fourier and inverse Fourier transform, facilitates the high efficiency of transient wave field calculation. The analytical formulation also enables the exploration of a wide range of parameters. Besides, the conventional FEM needs to save all the nodal solutions for each time marching step, which is a memory consuming procedure and requires large hard drive space for storing the big size of data. However, CAFA generates a 2-D wave field data with much less computer resource consumption.

Taking the examples in this study, we used the multi-physics (with coupled-field elements for piezoelectric effect simulation) implicit solver of ANSYS to conduct the conventional FEM simulation. For each test frequency, it takes more than 20 hours. CAFA contains two steps: (1) local FEM calculation; (2) sensing signal calculation using analytical predictive tool WFR-2D. The local FEM takes only two to three hours. The

WFR-2D takes only 1 minute in addition to the local FEM calculation time. Conventional FEM requires re-model and re-run for the exploration of design parameters such as PWAS transducer size, sensor-damage relative location, interrogating wave frequency, and excitation waveform; however, CAFA only requires the modification of the corresponding calculation parameter and the exploration for each parameter only takes several minutes. Thus, CAFA can achieve orders of magnitude greater design efficiency when compared with conventional FEM. The data size of conventional 3-D FEM simulation can reach several hundreds of Gigabytes, while the 2-D time space wave field only consumes several hundreds of Megabytes. Therefore, CAFA can achieve orders of magnitude saving of computer resources.

# CHAPTER 5
## SEMI-ANALYTICAL FINITE ELEMENT METHOD FOR MODELING GUIDED WAVES IN COMPOSITE STRUCTURES

This chapter presents the semi-analytical finite element (SAFE) method for modeling guided waves in composite structures. The theoretical foundation for calculating guided waves in plate structures using the 1-D quadratic element is illustrated. The SAFE formulation forms a stable eigenvalue problem for solving wavenumbers and mode shapes in a given frequency range. Based on SAFE method, we developed the predictive tool SAFE-DISPERSION for calculating of dispersion curves, mode shapes, and directivity information of isotropic and composite plate structures. Case studies on various materials were carried out to verify SAFE solutions. First, dispersion curves and mode shapes were obtained for isotropic materials, which were then compared with the exact analytical solutions. Second, dispersion curves and modes shapes in composite structures were calculated and compared with commercially available software, DISPERSE$^{TM}$, which is based on the global matrix method. Several cases were investigated, including unidirectional carbon fiber reinforced polymer (CFRP) plate, 0/90 CFRP cross plies, and quasi-isotropic CFRP plates.

## 5.1 INTRODUCTION AND STATE OF THE ART

Composite materials are currently widely used in aerospace, automotive, and civil structures due to their light weight and high strength properties. However, composite materials are generally anisotropic and the damage developed in them is hard to be

observed from the structural surface. Thus, their wide application raises new challenges for the Structural Health Monitoring (SHM) community (Rose 2012). Ultrasonic guided wave technique provides a promising solution for damage detection and health monitoring of composite structures. However, due to the anisotropic material properties, the guided waves excited in composites exhibit directivity behaviors. These complicated behaviors include direction dependent dispersion curves and mode shapes.

To solve wave propagation problems in composite structures, many methods have been developed. Transfer matrix method (TMM) is used to solve wave propagation in layered media (Thomson 1950; Haskell 1953). It is computational efficient for its condensed equation system, but numerical instability has been reported at large frequency-thickness ($fd$) products (Lowe 1995). The TM formulation itself has no deficiency, but numerical value of the real exponential fluctuates at high frequency and cause the instability problem. A number of researches have been carried out to propose reformulation of the TMM equations to avoid instability (Wang and Rokhlin 2001). The method is based on Stiffness matrix method (SMM) instead of TMM. At large $fd$ values, the SMM turned out to be stable, but for small $fd$ values, it suffers root finding problems. Kamal and Giurgiutiu (2014) proposed a stable Stiffness Transfer matrix method (STMM), aiming at combining the virtues of TMM and SMM. Steady stability was found for all the $fd$ values. However, the transition between small $fd$ TMM region and large $fd$ SMM region needs to be determined for each calculation setup. The Global matrix method (GMM) was first developed by Knopoff (1964). It combines stress and displacement components at the boundaries of each layer with boundary conditions. All these quantities are assembled in one single matrix. Compared with TMM technique, the

107

GMM has the advantage that it remains stable throughout the *fd* range. The disadvantage of GMM is that the global matrix assembled to be a large matrix for laminates with a large number of layers, resulting in heavy computation burden and long computation time.

This chapter focuses the semi-analytical finite element (SAFE) method. Different from the analytical approaches, the SAFE method discretizes the cross section of the waveguide (plate, rod, or cylinder) with finite elements and uses analytical formulation along the wave propagation direction (Gavric 1995). The finite element discretization makes SAFE capable of modeling waveguides with arbitrary cross section and material properties (Bartoli et al. 2006). Promising results have been reported using SAFE for calculation of dispersion curves and mode shapes in pipe and rail structures (Hayashi et al. 2004). The application of SAFE method to composite structures showed very good results with the straight forward manner in material property definition (Rose 2012; Ahmad et al. 2013). Besides, the SAFE method does not require a root searching procedure like most of the analytical method. Instead, the formulation reaches a stable eigenvalue problem, which is efficient and easy in terms of numerical computation.

## 5.2    SEMI-ANALYTICAL FINITE ELEMENT METHOD FORMULATION

This section illustrates the SAFE formulation for plate structures. Details of the mathematical derivation and finite element implementation are shown.

### 5.2.1    PROBLEM DESCRIPTION

To model wave propagation in plate structures, we only need 1-D elements to discretize the cross section and describe the mode shapes of guided waves. The SAFE setup in an infinitely wide plate is shown in Figure 5.1. The waves propagates along $x$ direction with wavenumber $\xi$ at frequency $\omega$. The cross section lies in the $y-z$ plane.

The harmonic displacement, stress, and strain field components at each point of the waveguide are expressed by

$$\mathbf{u} = \begin{bmatrix} u_x & u_y & u_z \end{bmatrix}$$

$$\boldsymbol{\sigma} = \begin{bmatrix} \sigma_x & \sigma_y & \sigma_z & \sigma_{yz} & \sigma_{xz} & \sigma_{xy} \end{bmatrix}, \quad \boldsymbol{\varepsilon} = \begin{bmatrix} \varepsilon_x & \varepsilon_y & \varepsilon_z & \varepsilon_{yz} & \varepsilon_{xz} & \varepsilon_{xy} \end{bmatrix}$$

(5.1)
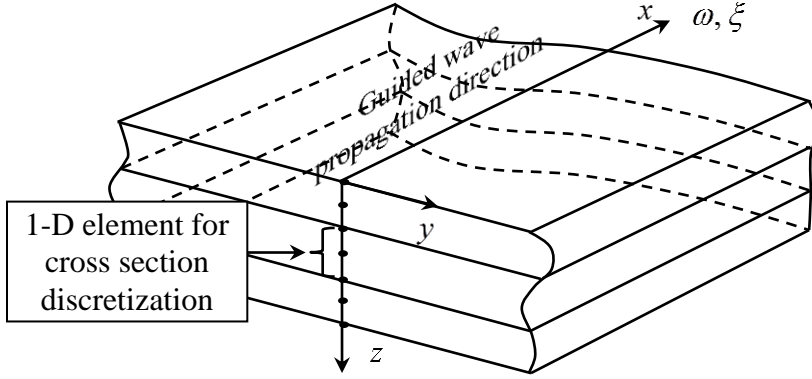


Figure 5.1: SAFE model of wave propagation in plate structures.

The constitutive equation at a point is given by $\boldsymbol{\sigma} = \tilde{C}\boldsymbol{\varepsilon}$, where $\tilde{C}$ is complex valued stiffness matrix. This complex stiffness matrix contributes to complex valued wavenumbers for the modeling of damped guided wave propagation. The stress-displacement relation can be written in matrix form as

$$\boldsymbol{\varepsilon} = \left[ \mathbf{L}_x \frac{\partial}{\partial x} + \mathbf{L}_y \frac{\partial}{\partial y} + \mathbf{L}_z \frac{\partial}{\partial z} \right] \mathbf{u}$$

(5.2)

where

$$\mathbf{L}_x = \begin{bmatrix} 1 & 0 & 0 \\ 0 & 0 & 0 \\ 0 & 0 & 0 \\ 0 & 0 & 0 \\ 0 & 0 & 1 \\ 0 & 1 & 0 \end{bmatrix}, \quad \mathbf{L}_y = \begin{bmatrix} 0 & 0 & 0 \\ 0 & 1 & 0 \\ 0 & 0 & 0 \\ 0 & 0 & 1 \\ 0 & 0 & 0 \\ 1 & 0 & 0 \end{bmatrix}, \quad \mathbf{L}_z = \begin{bmatrix} 0 & 0 & 0 \\ 0 & 0 & 0 \\ 0 & 0 & 1 \\ 0 & 1 & 0 \\ 1 & 0 & 0 \\ 0 & 0 & 0 \end{bmatrix}$$

(5.3)

5.2.2   COORDINATE TRANSFORM FOR STIFFNESS MATRIX OF LAMINATED COMPOSITES

The stiffness matrix is usually defined in a coordinate system according to fiber orientation, with the 1-axis long the fiber direction, the 2-axis in the laminate plane and perpendicular to the fiber direction, and the 3-axis perpendicular to the laminate plane. Figure 5.2 shows two situations of lamina stacking angle.
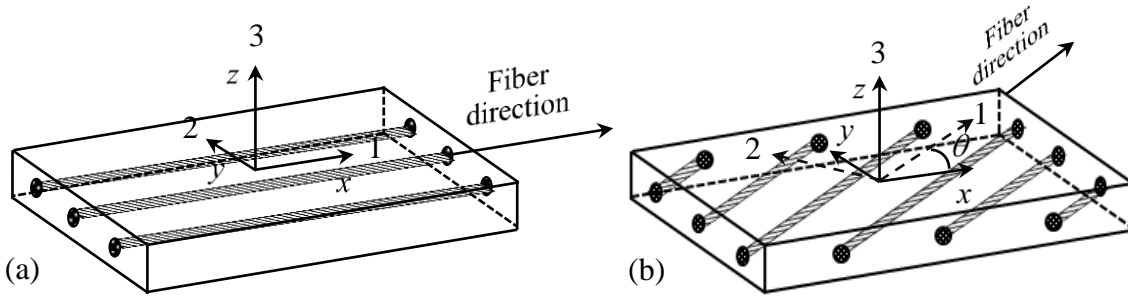


Figure 5.2: Coordinate transformation for different stacking angle.

Figure 5.2a shows the 1-2-3 axis coincides with the $x$-$y$-$z$ global coordinate system, which refers to a situation where the stacking angle $\theta$ is zero. Since the stiffness matrix $\tilde{C}_{local}$ is defined in 1-2-3 systems, in this case, the stiffness matrix $\tilde{C}$ in global coordinate equals $\tilde{C}_{local}$, i.e., $\tilde{C} = \tilde{C}_{local}$. Figure 5.2b shows the 1-2-3 axis no longer coincides with the $x - y - z$ global coordinate system, which refers to a situation where the stacking angle $\theta$ is nonzero. The stiffness matrix $\tilde{C}$ in global coordinate is calculated from $\tilde{C}_{local}$ by the coordinate transform

$$\tilde{C} = \mathbf{T}^{-1} \tilde{C}_{local} \mathbf{T}^{-T} \tag{5.4}$$

where -1 means the inverse of a matrix, and the superscript $T$ means the transpose of a matrix. $\mathbf{T}$ is the transformation matrix defined as

$$\mathbf{T} = \begin{bmatrix} m^2 & n^2 & 0 & 0 & 0 & 2mn \\ n^2 & m^2 & 0 & 0 & 0 & -2mn \\ 0 & 0 & 1 & 0 & 0 & 0 \\ 0 & 0 & 0 & m & -n & 0 \\ 0 & 0 & 0 & n & m & 0 \\ -mn & mn & 0 & 0 & 0 & m^2-n^2 \end{bmatrix} \qquad (5.5)$$

where $m = \cos(\theta)$ and $n = \sin(\theta)$. In this way, we can define the stiffness matrix for implementation in the finite element procedure for each layer of lamina with a certain stacking angle.

5.2.3   GOVERNING EQUATION

The governing equation is obtained by inserting the kinetic and potential energies into Hamilton's equation; its variation form is expressed in Eq. (5.6) (see Bartoli et al. 2006).

$$\delta H = \int_{t_1}^{t_2} \delta(\Phi - K)\,dt = 0 \qquad (5.6)$$

where $\Phi$ is the strain energy and $K$ is the kinetic energy. The strain energy and kinetic energy are given by

$$\Phi = \frac{1}{2}\int_V \boldsymbol{\varepsilon}^T \tilde{C} \boldsymbol{\varepsilon}\,dV, \quad K = \frac{1}{2}\int_V \dot{\mathbf{u}}^T \rho \dot{\mathbf{u}}\,dV \qquad (5.7)$$

where $V$ is the volume, $\rho$ is the material density, and the dot represent a time derivative. After integrating by parts, Eq. (5.6) can be written as

$$\int_{t_1}^{t_2} \left[ \int_V \delta(\boldsymbol{\varepsilon}^T)\tilde{C}\boldsymbol{\varepsilon}\,dV + \int_V \delta(\mathbf{u}^T)\rho\ddot{\mathbf{u}}\,dV \right]dt = 0 \qquad (5.8)$$

In general, the displacement filed can be described as

111

$$\mathbf{u}(x,y,z,t) = \begin{bmatrix} u_x(x,y,z,t) \\ u_y(x,y,z,t) \\ u_z(x,y,z,t) \end{bmatrix} = \begin{bmatrix} U_x(y,z) \\ U_y(y,z) \\ U_z(y,z) \end{bmatrix} e^{i(\xi x - \omega t)} \tag{5.9}$$

where $i$ is the imaginary unit, $\xi$ is the wavenumber, and $\omega$ is the angular frequency. It can be noticed in Eq. (5.9) that at each point, there are three degrees of freedom corresponding to $x$, $y$, and $z$ direction. The displacement field is assumed to be harmonic along the $x$ propagation direction. And, the displacement amplitude is a function of space. The $y$-$z$ plane amplitude describes the mode shape of guided waves. For a plate waveguide, considering a straight crested wave field propagating in $x$ direction, the problem is y-invariant for the given setup in Figure 5.1. Thus the displacement field is independent of the $y$ coordinate and can be simplified as

$$\mathbf{u}(x,z,t) = \begin{bmatrix} U_x(z) \\ U_y(z) \\ U_z(z) \end{bmatrix} e^{i(\xi x - \omega t)} \tag{5.10}$$

### 5.2.4 FINITE ELEMENT PROCEDURE

The finite element formulation uses shape functions to describe the displacements. In this study, we used the 1-D quadratic isoparametric element. Figure 5.3 shows the quadratic isoparametric element, the local coordinates, and its shape functions. The 1-D quadratic element is comprised of three nodes. The shape functions are evaluated at each node, so that the function value reaches one at the corresponding node and vanishes at the other two nodes. In this way, the displacement at a certain node is described exactly by the nodal solution, while the displacement at arbitrary location is approximated by the weighted contribution from the nodal solutions, with the weight being the shape function.

| Node number | Local coordinate | Shape function |
|---|---|---|
| Node 1 | $\zeta = -1$ | $N_1 = \dfrac{1}{2}\zeta(\zeta - 1)$ |
| Node 2 | $\zeta = 0$ | $N_2 = (1-\zeta)(1+\zeta)$ |
| Node 3 | $\zeta = 1$ | $N_3 = \dfrac{1}{2}\zeta(\zeta + 1)$ |

Figure 5.3: 1-D quadratic isoparametric element, local coordinate, and shape function.

The global coordinate $z$ can be expressed with local coordinates $z_1, z_2, z_3$ with the interpolation functions $N_1, N_2, N_3$, i.e.,

$$z = \begin{bmatrix} N_1 & N_2 & N_3 \end{bmatrix} \begin{bmatrix} z_1 \\ z_2 \\ z_3 \end{bmatrix} \tag{5.11}$$

where $z$ is an arbitrary location in the global coordinate. $z$ is described by the shape functions and nodal coordinates.

The displacements over the element domain are expressed in terms of the shape functions $N_k(z)$ and the nodal unknown displacements $U_{kx}$, $U_{ky}$, and $U_{kz}$ of node $k$ in $x$, $y$, and $z$ direction in Eq. (5.12). For the quadratic element, there are totally three nodes in each element, so $k$ takes the value from one to three ($N = 3$).

$$\mathbf{u}^{(e)}(x, z, t) = \begin{bmatrix} \displaystyle\sum_{k=1}^{N} N_k(z)U_{kx} \\ \displaystyle\sum_{k=1}^{N} N_k(z)U_{ky} \\ \displaystyle\sum_{k=1}^{N} N_k(z)U_{kz} \end{bmatrix}^{(e)} e^{i(\xi x - \omega t)} = \mathbf{N}(z)\mathbf{q}^{(e)} e^{i(\xi x - \omega t)} \tag{5.12}$$

where

$$\mathbf{N}(z) = \begin{bmatrix} N_1 & & N_2 & & N_3 & \\ & N_1 & & N_2 & & N_3 & \\ & & N_1 & & N_2 & & N_3 \end{bmatrix} \qquad (5.13)$$

$$\mathbf{q}^{(e)} = \begin{bmatrix} U_{1x} & U_{1y} & U_{1z} & U_{2x} & U_{2y} & U_{2z} & U_{3x} & U_{3y} & U_{3z} \end{bmatrix}^T \qquad (5.14)$$

The symbol $(e)$ means the elemental expression. Recall Eq. (5.2) and Eq. (5.12), the strain vector can also be expressed in terms of nodal displacement and shape functions.

$$\boldsymbol{\varepsilon}^{(e)} = \left[ \mathbf{L}_x \frac{\partial}{\partial x} + \mathbf{L}_y \frac{\partial}{\partial y} + \mathbf{L}_y \frac{\partial}{\partial y} \right] \mathbf{N}(z) \mathbf{q}^{(e)} e^{i(\xi x - \omega t)} = \left( \mathbf{B}_1 + i\xi \mathbf{B}_2 \right) \mathbf{q}^{(e)} e^{i(\xi x - \omega t)} \qquad (5.15)$$

where

$$\mathbf{B}_1 = \mathbf{L}_y \frac{\partial \mathbf{N}}{\partial y} + \mathbf{L}_z \frac{\partial \mathbf{N}}{\partial z}; \quad \mathbf{B}_2 = \mathbf{L}_x \mathbf{N} \qquad (5.16)$$

It should be noted that for this y-invariant problem, the first term in $\mathbf{B}_1$ vanishes. It should also be noted that the derivatives of shape functions are with respect to the global coordinate $z$, while the shape functions are given in local coordinate $\zeta$ of the isoparametric element.

In general, a Jacobian matrix is used to convert the derivatives from global coordinate to the local isoparametric coordinate. For the 1-D quadratic element, the Jacobian becomes a constant, and the derivative in global coordinate can be expressed as

$$\frac{d\mathbf{N}}{dz} = \frac{d\mathbf{N}}{d\zeta} \frac{d\zeta}{dz} = \frac{1}{J} \frac{d\mathbf{N}}{d\zeta} \qquad (5.17)$$

where the Jacobian, according to Eq. (5.11), is evaluated as

$$J = \frac{dz}{d\zeta} = \begin{bmatrix} \zeta - \dfrac{1}{2} & -2\zeta & \zeta + \dfrac{1}{2} \end{bmatrix} \begin{bmatrix} z_1 \\ z_2 \\ z_3 \end{bmatrix} \tag{5.18}$$

Let $n_e$ being the total number of elements along the plate thickness, the discrete form of the governing equation from Eq. (5.8) is

$$\int_{t_1}^{t_2} \left\{ \bigcup_{e=1}^{n_e} \left[ \int_{V_e} \delta\left(\boldsymbol{\varepsilon}^{(e)T}\right) \tilde{C}_e \boldsymbol{\varepsilon}^{(e)} \, dV_e + \int_{V_e} \delta\left(\mathbf{u}^{(e)T}\right) \rho_e \ddot{\mathbf{u}}^{(e)} \, dV_e \right] \right\} dt = 0 \tag{5.19}$$

where $\tilde{C}_e$ and $\rho_e$ are the stiffness matrix and density of the corresponding element. For multilayer laminated composites, these material properties need to be defined for the elements in each layer. The symbol $\bigcup$ denotes the assembling procedure.

The substitution of Eq. (5.15) into the strain energy term in Eq. (5.19) yields

$$\int_{V_e} \delta\left(\boldsymbol{\varepsilon}^{(e)T}\right) \tilde{C}_e \boldsymbol{\varepsilon}^{(e)} \, dV_e = \delta\mathbf{q}^{(e)T} \int_{\Omega_e} \left[ \mathbf{B}_1^T \tilde{C}_e \mathbf{B}_1 - i\xi \mathbf{B}_2^T \tilde{C}_e \mathbf{B}_1 + i\xi \mathbf{B}_1^T \tilde{C}_e \mathbf{B}_2 + \xi^2 \mathbf{B}_2^T \tilde{C}_e \mathbf{B}_2 \right] d\Omega_e \mathbf{q}^{(e)}$$

$$\tag{5.20}$$

where $\Omega_e$ is the elemental domain.

The substitution of the displacement expression in Eq. (5.12) into the kinetic energy term in Eq. (5.19) yields

$$\int_{V_e} \delta\left(\mathbf{u}^{(e)T}\right) \rho_e \ddot{\mathbf{u}}^{(e)} \, dV_e = -\omega^2 \delta\mathbf{q}^{(e)T} \int_{\Omega_e} \mathbf{N}^T \rho_e \mathbf{N} \, d\Omega_e \mathbf{q}^{(e)} \tag{5.21}$$

Substituting Eq. (5.20) and Eq. (5.21) into Eq. (5.19) yields

$$\int_{t_1}^{t_2} \left\{ \bigcup_{e=1}^{n_e} \delta\mathbf{q}^{(e)} \left[ \mathbf{k}_1^{(e)} + i\xi \mathbf{k}_2^{(e)} + \xi^2 \mathbf{k}_3^{(e)} - \omega^2 \mathbf{m}^{(e)} \right] \mathbf{q}^{(e)} \right\} dt = 0 \tag{5.22}$$

where

$$\mathbf{k}_1^{(e)} = \int_{\Omega_e} \left[ \mathbf{B}_1^T \tilde{C}_e \mathbf{B}_1 \right] d\Omega_e, \quad \mathbf{k}_2^{(e)} = \int_{\Omega_e} \left[ \mathbf{B}_1^T \tilde{C}_e \mathbf{B}_2 - \mathbf{B}_2^T \tilde{C}_e \mathbf{B}_1 \right] d\Omega_e$$

$$\mathbf{k}_3^{(e)} = \int_{\Omega_e} \left[ \mathbf{B}_2^T \tilde{C}_e \mathbf{B}_2 \right] d\Omega_e, \quad \mathbf{m}^{(e)} = \int_{\Omega_e} \left[ \mathbf{N}^T \rho_e \mathbf{N} \right] d\Omega_e \tag{5.23}$$

It should be noted that the integration in Eq. (5.23) is carried out with the Gaussian quadrature method in the master element under local coordinate, and then converted to global coordinate with the Jacobian. For the given 1-D, three node quadratic elements, a two-point Gaussian quadrature can accurately evaluate the integration. The Gaussian quadrature integration points locations $\zeta_i$ and weights $w_i$ are shown in Table 5.1. A typical numerical integration example is illustrated for the $\mathbf{k}_1^{(e)}$ term of Eq. (5.23) in Eq. (5.24).

$$\mathbf{k}_1^{(e)} = \frac{1}{2} \sum_{i=1}^{2} \mathbf{B}_{1G}^T \tilde{C}_e \mathbf{B}_{1G} J w_i \tag{5.24}$$

where $\mathbf{B}_{1G}$ denotes the $\mathbf{B}_1$ term in the global coordinate. According to Eq. (5.17), $\mathbf{B}_{1G}$ can be expressed in the local coordinate as $\mathbf{B}_{1L}$

$$\mathbf{B}_{1G} = J^{-1} \mathbf{B}_{1L} = \frac{1}{J} \mathbf{B}_{1L} \tag{5.25}$$

Table 5.1: Gaussian quadrature points locations and weights.

| Point number $i$ | Location $\zeta_i$ | Weight $w_i$ |
| --- | --- | --- |
| 1 | -0.5773502691896257 | 1.00 |
| 2 | 0.5773502691896257 | 1.00 |

Upon applying the standard finite element assembling procedure, Eq. (5.22) becomes

$$\int_{t_1}^{t_2} \left\{ \delta \mathbf{U}^T \left[ \mathbf{K}_1 + i\xi \mathbf{K}_2 + \xi^2 \mathbf{K}_3 - \omega^2 \mathbf{M} \right] \mathbf{U} \right\} dt = 0 \tag{5.26}$$

where $\mathbf{U}$ is the global vector of unknown nodal displacements, and

$$\mathbf{K}_1 = \bigcup_{e=1}^{n_e} \mathbf{k}_1^{(e)}, \quad \mathbf{K}_2 = \bigcup_{e=1}^{n_e} \mathbf{k}_2^{(e)}, \quad \mathbf{K}_3 = \bigcup_{e=1}^{n_e} \mathbf{k}_3^{(e)}, \quad \mathbf{M} = \bigcup_{e=1}^{n_e} \mathbf{m}^{(e)} \tag{5.27}$$

Since Eq. (5.26) is true for an arbitrary $\delta\mathbf{U}$, the following homogeneous general wave equation is finally obtained

$$\left[ \mathbf{K}_1 + i\xi\mathbf{K}_2 + \xi^2\mathbf{K}_3 - \omega^2\mathbf{M} \right] \mathbf{U} = 0 \tag{5.28}$$

Eq. (5.28) can be written in an equivalent equation system

$$\left( \begin{bmatrix} \mathbf{0} & \mathbf{K}_1 - \omega^2\mathbf{M} \\ \mathbf{K}_1 - \omega^2\mathbf{M} & i\mathbf{K}_2 \end{bmatrix} - \xi \begin{bmatrix} \mathbf{K}_1 - \omega^2\mathbf{M} & \mathbf{0} \\ \mathbf{0} & -\mathbf{K}_3 \end{bmatrix} \right) \begin{bmatrix} \mathbf{U} \\ \xi\mathbf{U} \end{bmatrix} = 0 \tag{5.29}$$

Eq. (5.29) is an eigenvalue problem. If we let $M$ equals the dimension of vector $\mathbf{U}$, then at each frequency $\omega$, $2M$ eigenvalues and consequently, $2M$ eigenvectors are obtained. The eigenvectors are the $M$ forward and the corresponding $M$ backward wave mode shapes. The eigenvalues occur as pairs of real numbers ($\pm\xi_{\text{Re}}$), representing propagative waves in the $\pm x$ directions, or as pairs of complex conjugate numbers ($\pm\xi_{\text{Re}} \pm i\xi_{\text{Im}}$), representing damped propagative waves decaying in the $\pm x$ directions, or as pairs of purely imaginary numbers ($\pm i\xi_{\text{Im}}$), representing the evanescent waves in the $\pm x$ directions. The phase velocity can be calculated by $c_{ph} = \omega/\xi_{\text{Re}}$, and the attenuation, in Nepers per meter, by $\xi_{\text{Im}}$.

## 5.2.5   POSTPROCESSING OF SAFE DATA

Although the eigenvalue SAFE solution is easy and straight forward, the data processing, however, is very complicated. The wavenumber solutions are discrete points of pure real numbers, pure imaginary number, or complex numbers. These discrete solutions also do not provide information on which wave mode they belong to. In

117

practical applications, it is very important to distinguish the wavenumber solution for each wave mode. In addition, although the nodal displacement solution can describe the displacement mode shape, the strain solutions are only available at Gaussian quadrature points. Furthermore, the stress mode shapes for composites are generally discontinuous due to the sudden change of the material properties for each lamina. All these factors bring difficulties to the data post processing.

5.2.5.1 Auto-tracing and mode separation of wavenumber solutions

In this study, we focus on the propagative wave modes which are used as interrogating field for SHM systems. The general wave expression $Ae^{i(\xi x - \omega t)}$ represents a wave field propagating in the positive direction with the amplitude $A$. The wavenumber solution in the first octant of the solution domain ($\xi_{\mathrm{Re}} - \xi_{\mathrm{Im}} - f$ shown in Figure 5.4a) can be expressed as $\xi = \xi_{\mathrm{Re}} + i\xi_{\mathrm{Im}}$. Substituting this wavenumber solution into the general wave expression yields

$$Ae^{i(\xi x - \omega t)} = Ae^{i\left[\left(\xi_{\mathrm{Re}} + i\xi_{\mathrm{Im}}\right)x - \omega t\right]} = \left(Ae^{-\xi_{\mathrm{Im}}x}\right)e^{i(\xi_{\mathrm{Re}}x - \omega t)} \tag{5.30}$$

Eq. (5.30) shows that the general complex valued wavenumber solution in the first octant of the solution domain is physically meaningful for SHM application. The $e^{i(\xi_{\mathrm{Re}}x - \omega t)}$ term represents the propagative wave in the positive direction, and the $Ae^{-\xi_{\mathrm{Im}}x}$ represents the decaying amplitude with propagation distance $x$ due to damping.

Figure 5.4b shows the auto-tracing algorithm to connect the discrete solutions and separate the wave modes. The solution tracing starts from high frequency wavenumbers, where the solution experiences fewer crossings among various wave modes. Thus, the first few solution points are treated as separated solutions for each wave mode. Then, extrapolation was used to predict the solution for the next frequency as a guess value.

Finally, the solution set at that frequency is compared with the guess value, and the nearest solution in the set is regarded as the target solution. There are two specific scenarios in the auto-tracing procedure: (1) forward tracing like mode one in Figure 5.4b; (2) forward-backward tracing like mode seven in Figure 5.4b. The scenario of mode one is easy, while we need to set a threshold value for the scenario of mode seven. It should be noted that the default tracing direction is from high frequency to low frequency. When all the values of the next frequency solution set exceed a threshold limit from the guess value, the frequency tracing direction will change to a backward one, i.e., instead of searching in the lower frequency solution set, we turn to search in the higher frequency set (described as backward tracing in Figure 5.4b). The results show that this auto-tracing algorithm can effectively connect the discrete solution points and distinguish the wave modes.
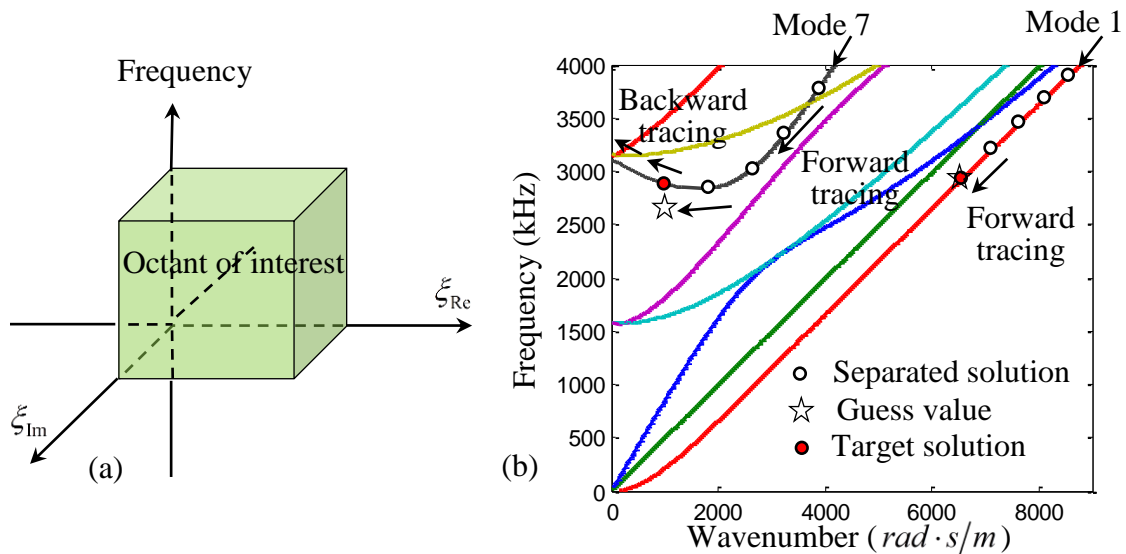


Figure 5.4: (a) Octant of propagative modes; (b) wavenumber solution tracing algorithm.

5.2.5.2 Displacement, strain, and stress mode shapes

The SAFE eigenvalue problem provides the displacement mode shape directly by the eigenvectors which are the displacement components at each element node. The strain mode shape solution is obtained from Eq. (5.15), and is only evaluated at the Gaussian quadrature points. It should be noted that the strain mode shape should be continuous across the thickness. Thus, we used the interpolation and extrapolation to obtain the strain solution at an arbitrary location. Since strain is the derivative of displacement, the finite element procedure states that strain solution, in general, is one order less accurate than that of displacement. The accuracy of strain mode shape can be achieved by a denser discretization of the waveguide cross section. For laminate composite structures, although the strain mode shapes are continuous across the thickness, the stress mode shapes are not. We used the continuous strain mode shapes $\boldsymbol{\varepsilon}$ to evaluate the stress mode shapes $\boldsymbol{\sigma}$ through the stress-strain relationship

$$\boldsymbol{\sigma} = \tilde{C}_k \, \boldsymbol{\varepsilon} \tag{5.31}$$

where $\tilde{C}_k$ is the stiffness matrix of the corresponding $k^{th}$ lamina.

5.3    SOFTWARE DEVELOPMENT: SAFE-DISPERSION

The SAFE procedure was coded in a MATLAB graphical user interface (GUI), and the software SAFE-DISPERSION was developed. SAFE-DISPERSION aims at providing dispersion curves (phase velocity, group velocity, and frequency-wavenumber), mode shapes (displacement, strain, and stress), and directivity plots for isotropic plates, laminate composite plates, and sandwich composite plates.

Figure 5.5 shows the main interface of SAFE-DISPERSION. It is comprised of several function panels: the material properties input panel, the parameter control panel,

the dispersion curve plot panel, the mode shape plot panel, and the directivity plot panel. The material input panel allows users to define three kinds of plate waveguides: isotropic materials, laminated composites, and sandwich composites. The parameter control panel is used to define the frequency range of interest, the frequency resolution for the solution, and the single/all direction calculation scenario. For the single direction calculation, users can specify which wave propagation direction solution is desired. For the omnidirectional calculation, users can define the angular step for the calculation setup. The frequency and direction slider, as well as the text input, allows users to specify the result display for the dispersion curves and mode shapes. The dispersion curve plot panel has three options: phase velocity dispersion curves, group velocity dispersion curves, and frequency-wavenumber dispersion curves. The mode shape plot panel can display displacement mode shape, strain mode shape, and stress mode shape. The dispersion plot and the mode shape plot are inter connected, i.e., by clicking a wave mode on the dispersion curve, the corresponding mode shape at the selected frequency will be shown in the mode shape plot panel. The directivity plot panel can display direction-dependent wave properties.
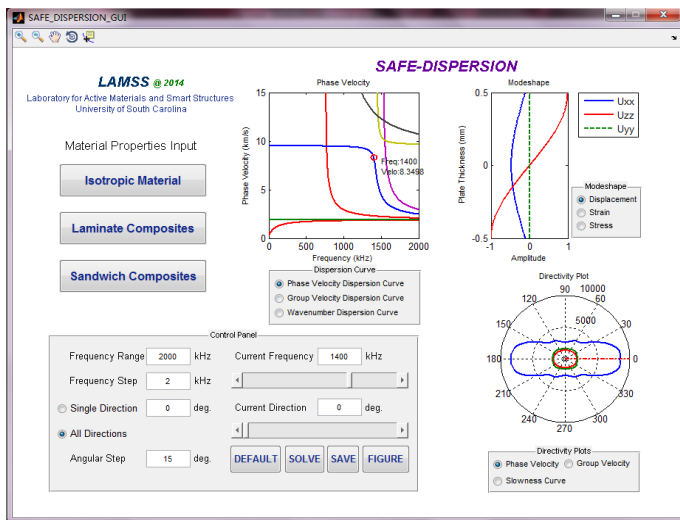


Figure 5.5: Main interface of SAFE-DISPERSION.

Figure 5.6 shows the material properties input panel sub-GUIs for: (a) isotropic material; (b) laminated composites; (c) sandwich composites. For isotropic materials, the properties are defined through Young's modulus, Poisson's ratio, density, damping ratio. Users need to specify the plate thickness and how many elements are used for the calculation. For laminated composites, each lamina is considered to have the same material properties, but the thickness and stacking angle of each lamina can vary. The material properties are defined by the stiffness matrix, density, and damping ratio of the lamina. Users need to specify how many elements will be used for each lamina for the calculation. At least one element per lamina is required. The thickness and stacking angle of each lamina are also defined in this panel. The sandwich composites material input panel is similar to that of laminated composites. The difference is that users need to define the properties of each layer one by one through clicking the "NEXT LAYER".
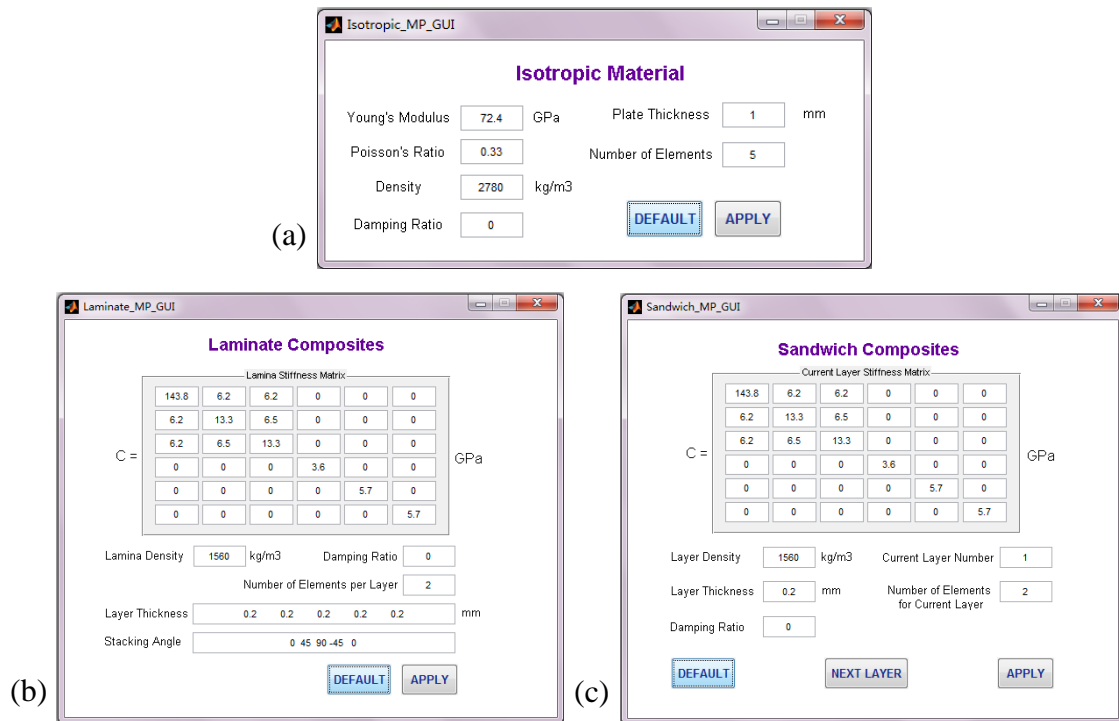


Figure 5.6: Material properties input panel.

122

On the SAFE-DISPERSION main interface and sub-GUIs, users can use the "DEFAULT" button to load default parameters. The "SAVE" button allows users to export the calculation results to Excel files. The "FIGURE" button can float the figures which are displayed, so that users can use them for documentation.

## 5.4 CASE STUDY OF GUIDED WAVES IN ISOTROPIC MATERIALS

To verify the SAFE-DISPERSION solution, we first conducted a case study of wave propagation in isotropic materials, where, the exact analytical solution for dispersion curves and mode shapes exist. In this section, the comparison between SAFE-DISPERSION and analytical solution is shown for aluminum 2024-T3 plate. The material properties of aluminum 2024-T3 are given in Table 5.2.

Table 5.2: Material properties of aluminum 2024-T3.

| Young's modulus ($E$) | Poisson's ratio ($\nu$) | Density ($\rho$) |
| --- | --- | --- |
| 73.1 GPa | 0.33 | 2780 kg/m$^3$ |

### 5.4.1 SAFE-DISPERSION VS EXACT ANALYTICAL SOLUTION: DISPERSION CURVES

Figure 5.7 shows the comparison between exact analytical solution and SAFE-DISPERSION solution of phase velocity dispersion curve for a 1-mm thick aluminum 2024-T3 plate. It can be observed that the result from SAFE method match well the analytical solution. The number of Lamb modes, the cut-off frequencies, and the phase velocity values all agree very well. It should be pointed out that the accuracy of SAFE solution depends on the number of elements to mesh the waveguide cross section for describing the mode shapes. For high frequency-thickness products, more elements are required to obtain an accurate solution, which also means with certain number of

elements, the high frequency solutions are less accurate. For the simulation of 1-mm thick plate up to 10,000 kHz, we used 10 quadratic elements across the thickness. At very high frequency, a slight deviation of SAFE solution from exact analytical solution can be observed, but the overall accuracy is excellent, considering that SHM techniques usually adopt frequencies within hundreds of kilohertz. It should be noted that SAFE also provides shear horizontal modes. In Figure 5.7, we only selected the Lamb modes to compare with the solutions from the Rayleigh-Lamb equation.
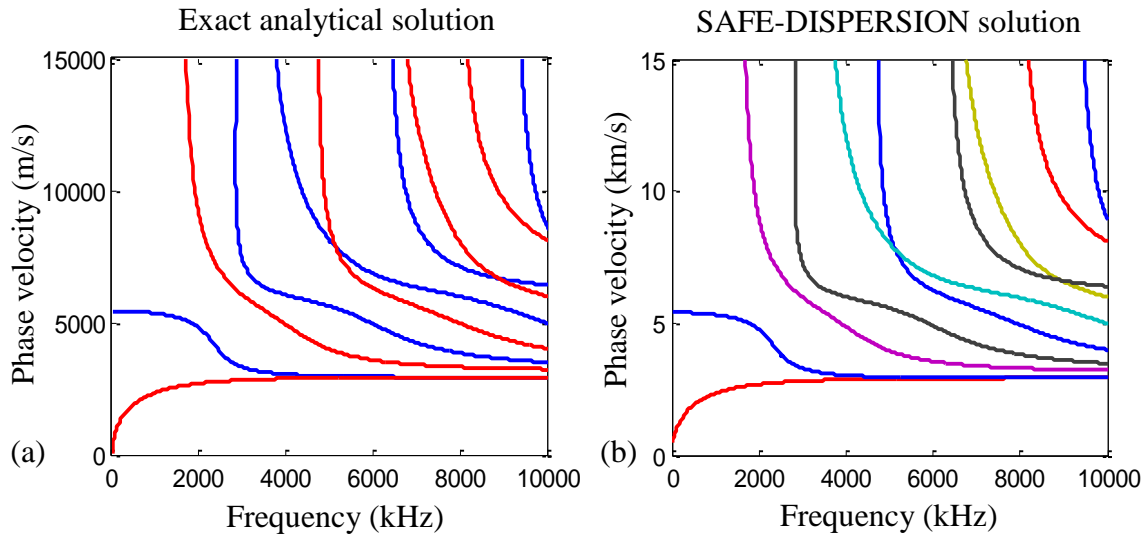


Figure 5.7: Phase velocity dispersion curve comparison between (a) exact analytical solution and (b) SAFE-DISPERSION solution.

SAFE-DISPERSION can also provide group velocity dispersion curves and wavenumber dispersion curves. Figure 5.8 shows the group velocity and wavenumber dispersion curves calculated by SAFE-DISPERSION. Figure 5.9 shows the directivity plots of phase velocity, group velocity, and slowness curve for the aluminum plate at 100 kHz, with blue line standing for the fundamental symmetric (S0) mode, green line standing for the fundamental shear horizontal (SH0) mode, and red line standing for the fundamental antisymmetric (A0) mode. It can be noticed that the calculated quantities are

124

the same in all the directions. This is because aluminum is an isotropic material which

possesses the same material properties in all the directions.
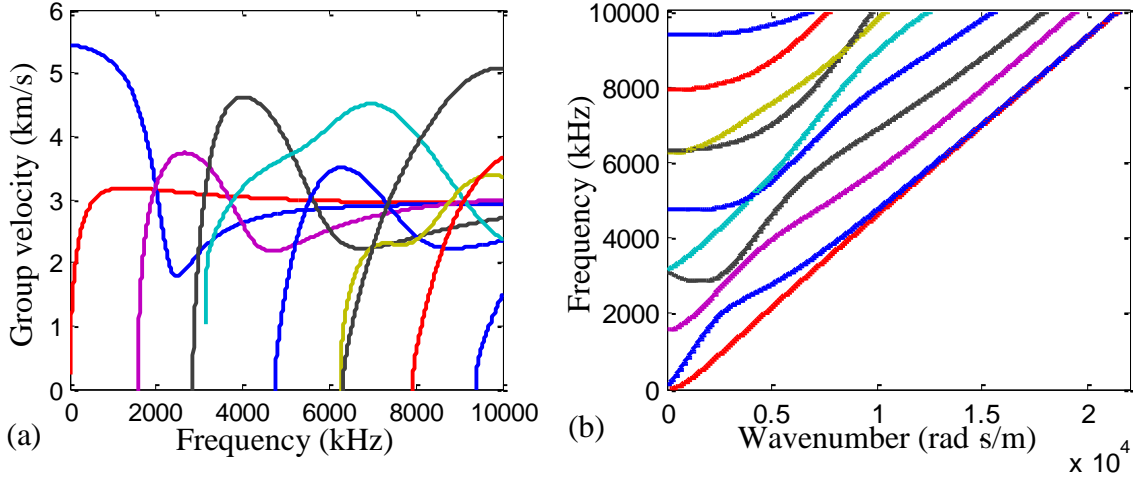


Figure 5.8: (a) Group velocity dispersion curve; (b) wavenumber dispersion curve.
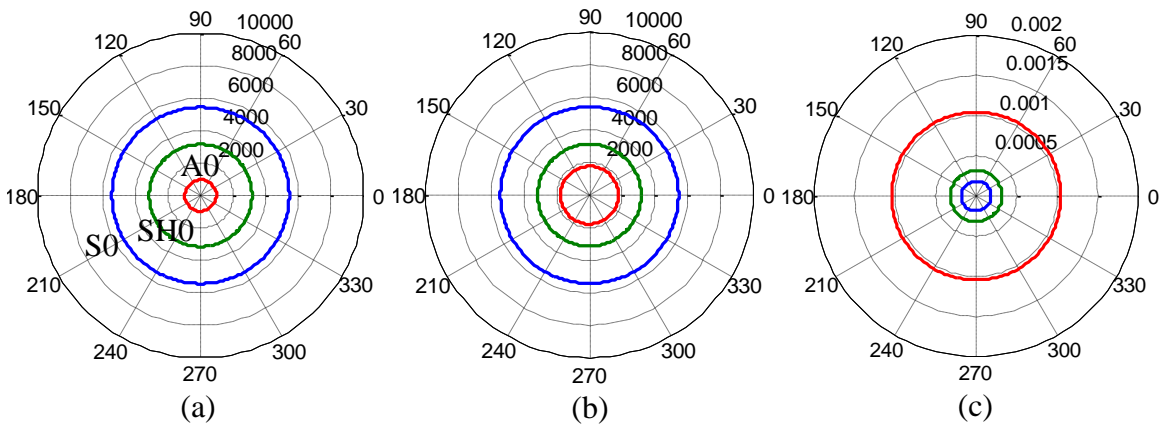


For 1-mm thick aluminum 2324-T3 plate at 100 kHz

Figure 5.9: Directivity plots of (a) phase velocity, (b) group velocity, and (c) slowness curve(blue line: S0; green line: SH0; red line: A0).

5.4.2    SAFE-DISPERSION vs EXACT ANALYTICAL SOLUTION: MODE SHAPES

Figure 5.10 shows the comparison of displacement mode shapes between exact analytical

results and SAFE solutions. The $x-y-z$ coordinate system has the same definition as

Figure 5.1, with $x$ along wave propagation direction and $z$ denoting the plate thickness

direction. It can be observed that the SAFE solutions have very good accuracy compared

with the analytical results for both S0 and A0 mode even at high frequency values such as 5 MHz. It should also be noted that SAFE-DISPERSION also provides the $u_y$ displacement component, which represents a shear horizontal motion. For isotropic materials, such as aluminum, the Lamb modes are decoupled from shear horizontal motion. Thus, the $u_y$ displacement always equals to zero for Lamb waves.
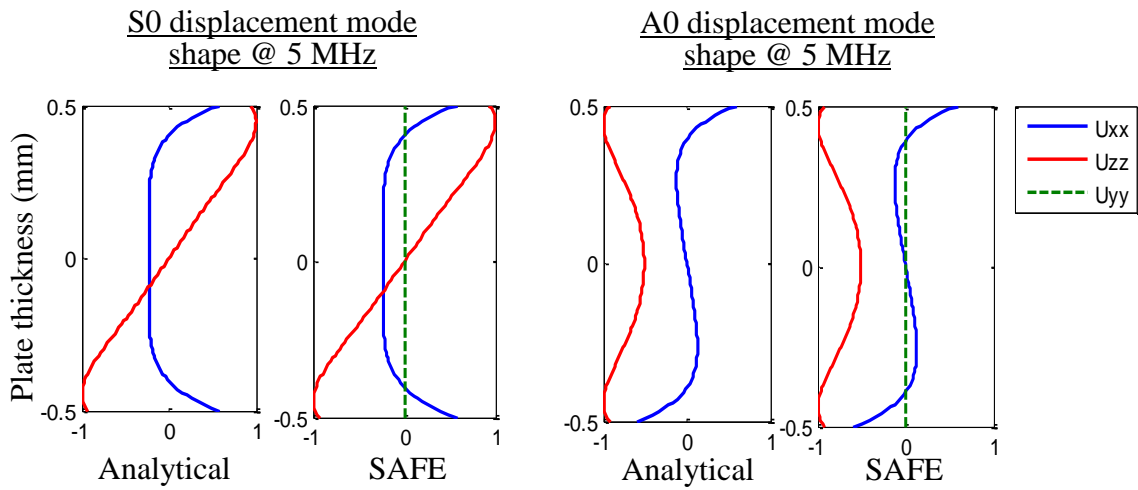


Figure 5.10: Comparison of displacement mode shapes between analytical and SAFE solution.
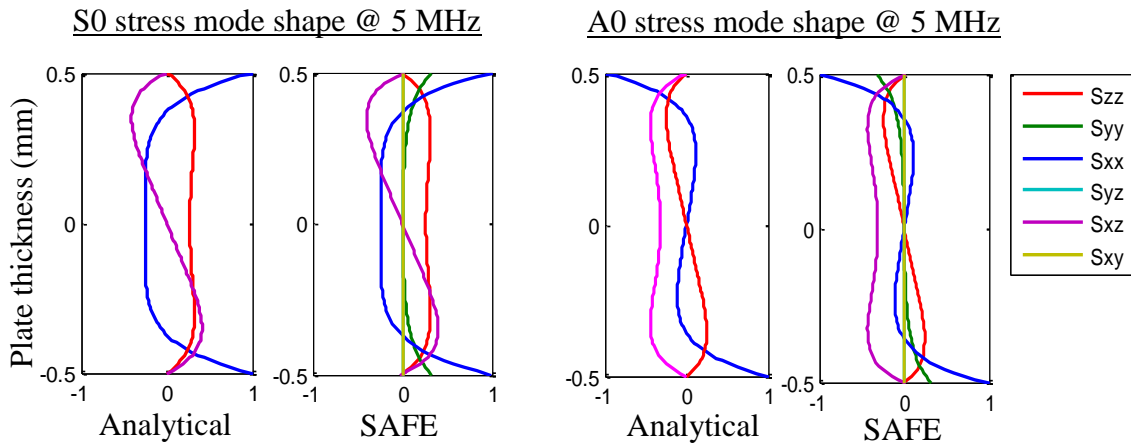


Figure 5.11: Comparison of stress mode shapes between analytical and SAFE solution.

Figure 5.11 shows the comparison of stress mode shapes between the exact analytical and SAFE solution. It can be observed that the results agree very well with each other for both S0 and A0 modes even at high frequency values such as 5 MHz. The stress boundary condition can further verify the SAFE simulation results. According to the stress free boundary condition of Lamb waves, the $\sigma_{zz}$ and $\sigma_{xz}$ stress components should vanish at the plate surfaces. This phenomenon can be clearly noticed in the SAFE results. It should also be noticed, since we used a 3-D elasticity formulation for SAFE-DISPERSION, we can obtain all the stress components.

## 5.5    CASE STUDY OF GUIDED WAVES IN COMPOSITE STRUCTURES

The second phase of case study in this chapter focuses on the guided wave modeling in laminate composite plates. We selected carbon fiber reinforced polymer (CFRP) plates as our subject, which have a wide application in aerospace and automotive structures. The stiffness of the CFRP lamina is given in Eq. (5.32). The material density is 1560 $kg/m^3$.

$$C_{CFRP} = \begin{bmatrix} 143.8 & 6.2 & 6.2 & 0 & 0 & 0 \\ 6.2 & 13.3 & 6.5 & 0 & 0 & 0 \\ 6.2 & 6.5 & 13.3 & 0 & 0 & 0 \\ 0 & 0 & 0 & 3.6 & 0 & 0 \\ 0 & 0 & 0 & 0 & 5.7 & 0 \\ 0 & 0 & 0 & 0 & 0 & 5.7 \end{bmatrix} GPa \tag{5.32}$$

### 5.5.1    SAFE-DISPERSION VS GLOBAL MATRIX METHOD: DISPERSION CURVES

Three cases were investigated: (1) wave propagation in various directions in unidirectional CFRP plates, (2) guided waves in cross ply CFRP plates, and (3) guided waves in quasi-isotropic CFRP plates. The global matrix method (GMM) solutions were obtained from the software DISPERSE[TM] (Lowe 1995). Both phase velocity results and

group velocity plots were compared between GMM solution obtained from DISPERSE[TM] and SAFE solution obtained from SAFE-DISPERSION.

5.5.1.3 Unidirectional CFRP plates: wave propagation in various directions

Figure 5.12 shows the dispersion curve comparison between GMM and SAFE for wave propagation in 0 degree direction (along the fiber) in a 1-mm unidirectional CFRP plate. In the SAFE simulation, we used 10 elements across the thickness. The SAFE-DISPERSION solution matches well with GMM result. It should be noted that SAFE method provides the SH0 mode, which is not present in DISPERSE[TM] solution.

Global matrix method (GMM) from DISPERSE[TM]



Semi-analytical finite element (SAFE) method from SAFE-DISPERSION
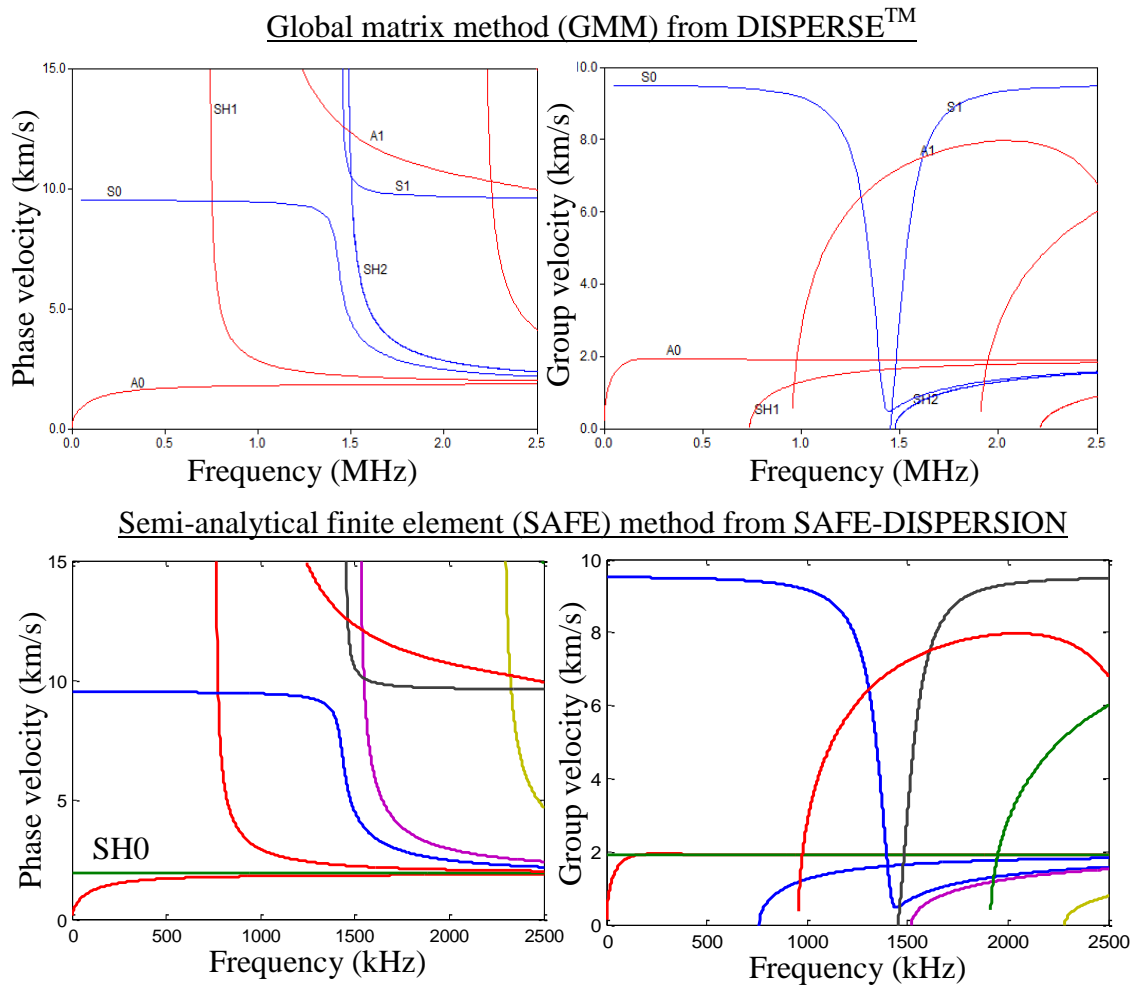


Figure 5.12: Dispersion curves along fiber (0 degree) direction in a 1-mm unidirectional CFRP plate.

Figure 5.13 shows the comparison of dispersion curves for wave propagation in 30 degree direction with respect fiber orientation. The results from GMM and SAFE-DISPERSION match well with each other. Compared with the results in Figure 5.12, one significant change is that the phase velocity of the fundamental symmetric mode decreases. This is because this value is directly related to the stiffness in the propagation direction.

Global matrix method (GMM) from DISPERSE$^{TM}$



Semi-analytical finite element (SAFE) method from SAFE-DISPERSION
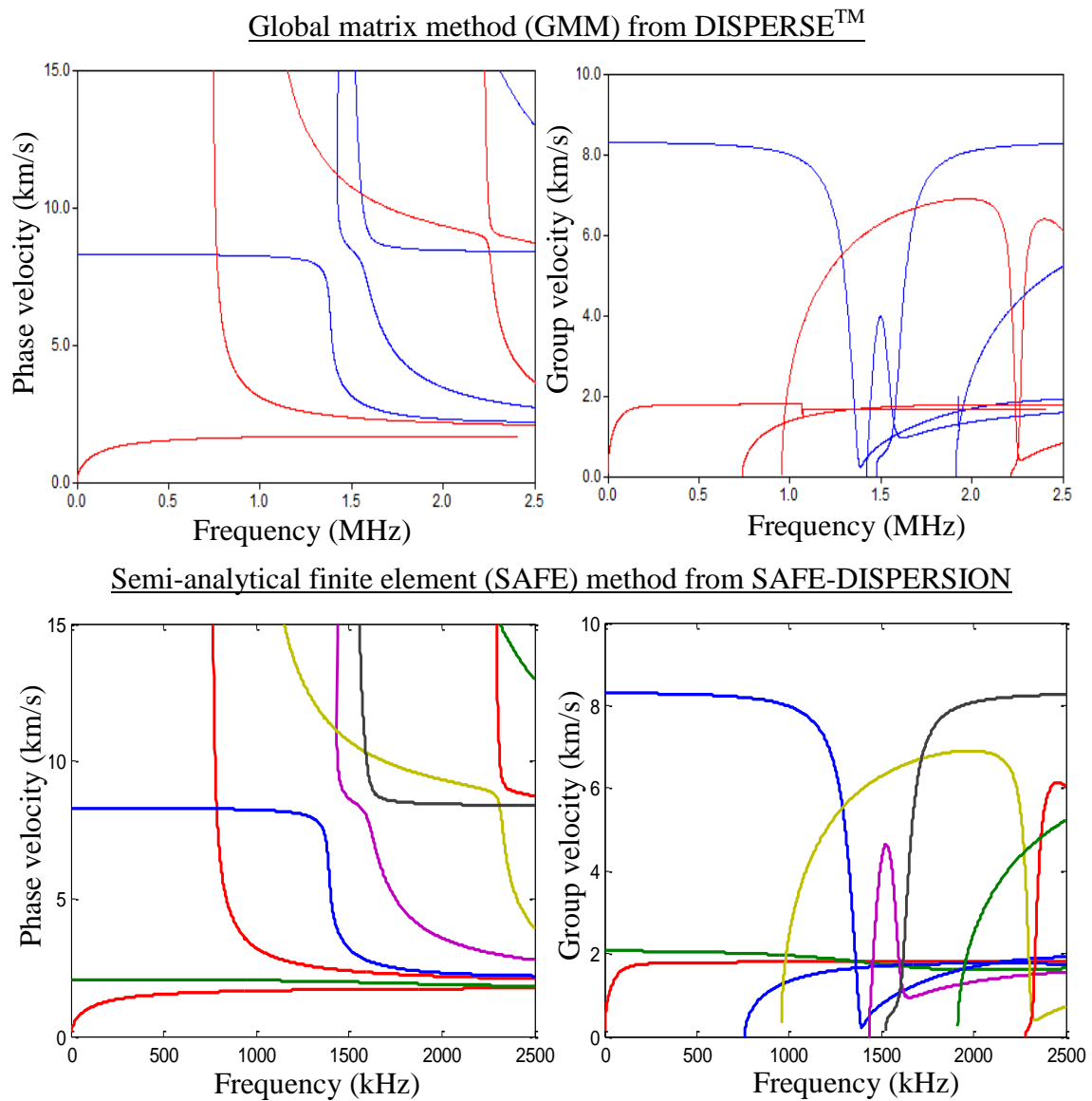


Figure 5.13: Dispersion curves in 30 degree direction in a 1-mm unidirectional CFRP plate.

Figure 5.14 shows the comparison of dispersion curves for wave propagation in 45 degree direction with respect to fiber orientation. The SAFE-DISPERSION solutions also match well with those from GMM. Again, the velocity of the fundamental mode further drops due to the decreased stiffness in the 45 degree direction.

Global matrix method (GMM) from DISPERSE$^{TM}$
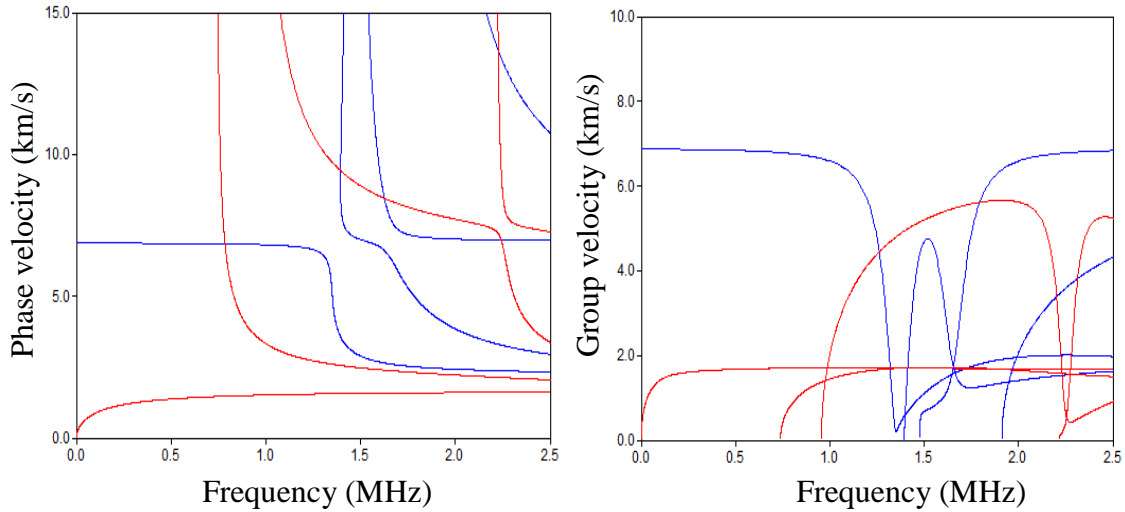
Semi-analytical finite element (SAFE) method from SAFE-DISPERSION
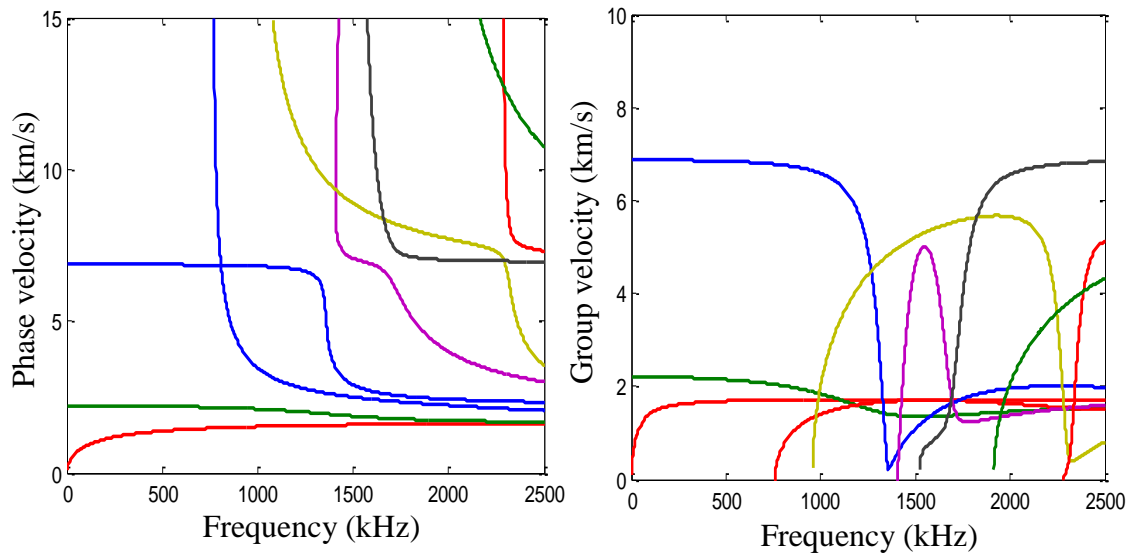
Figure 5.14: Dispersion curves in 45 degree direction in a 1-mm unidirectional CFRP plate.

Figure 5.15 shows the comparison of dispersion curves for wave propagation in 90 degree direction with respect to fiber orientation. The solutions from both methods agree very well. It should be noted that the S0 mode is missing from GMM solution, while the S0 mode in SAFE-DISPERSION solution shows a very small value due to the fact that the stiffness in the 90 degree direction is small.
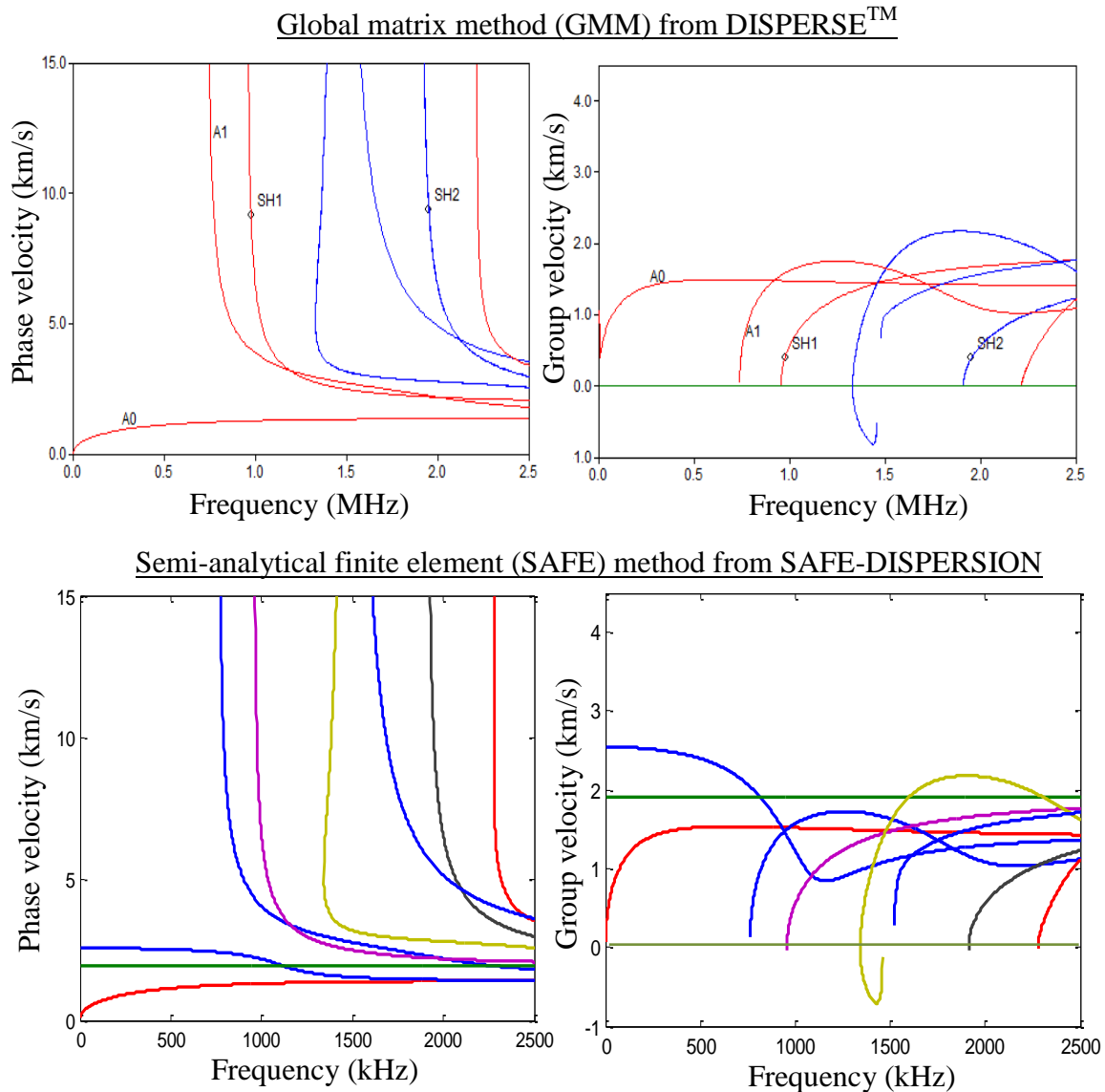


Figure 5.15: Dispersion curves in 90 degree direction in a 1-mm unidirectional CFRP plate.

Figure 5.16 shows the directivity plots, showing the heavy dependence of dispersion quantities on wave propagation directions. Since unidirectional CFRP plates have big differences in the stiffness for various directions, a drastic change in phase velocity, group velocity, and slowness curve can be observed. The fundamental symmetric and antisymmetric motion wave velocities are highest along fiber direction, and lowest in the perpendicular direction with fiber orientation. However, the shear motion wave has highest velocity in the direction between 0 and 90 degree. This effect of anisotropic composite material is completely different from that of aluminum shown in Figure 5.9.



(a)  (b)  (c)

For 1-mm thick unidirectional CFRP plate at 100 kHz
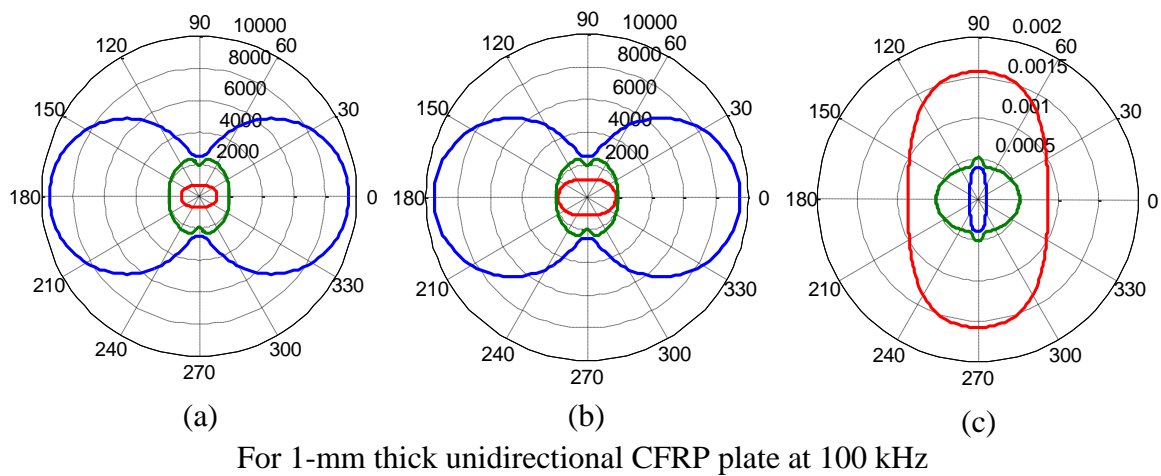
Figure 5.16: Directivity plots of (a) phase velocity, (b) group velocity, and (c) slowness curve.

5.5.1.4 Cross ply CFRP plates

For cross ply CFRP plates case, we studied two specific examples: (1) 1-mm thick two layer 0/90 cross ply and (2) 1-mm thick four layer $[0/90]_s$ cross ply.

Figure 5.17 shows the comparison between GMM solutions and SAFE-DISPERSION results with 10 elements. The results compare very well each other for the 1-mm 0/90 cross ply CFRP plate.

Global matrix method (GMM) from DISPERSE[TM]
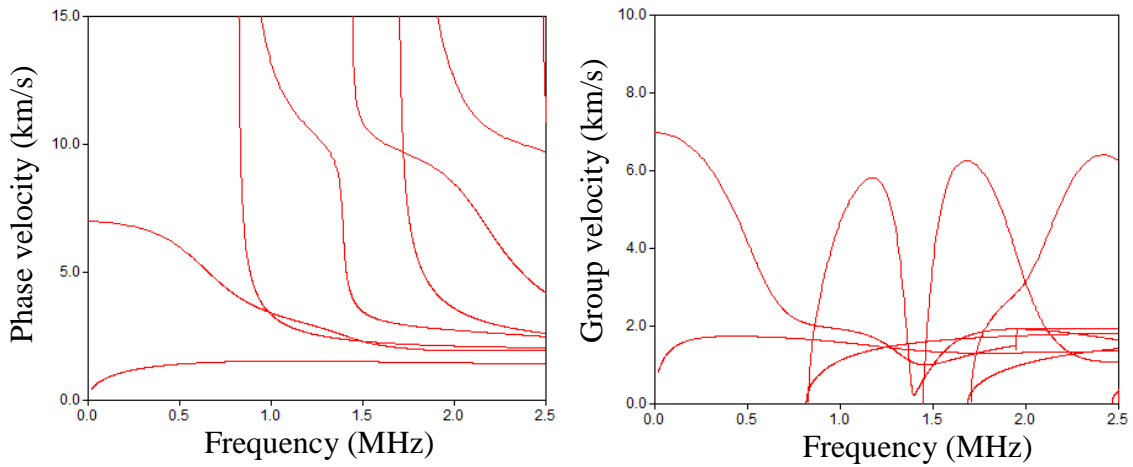


Semi-analytical finite element (SAFE) method from SAFE-DISPERSION
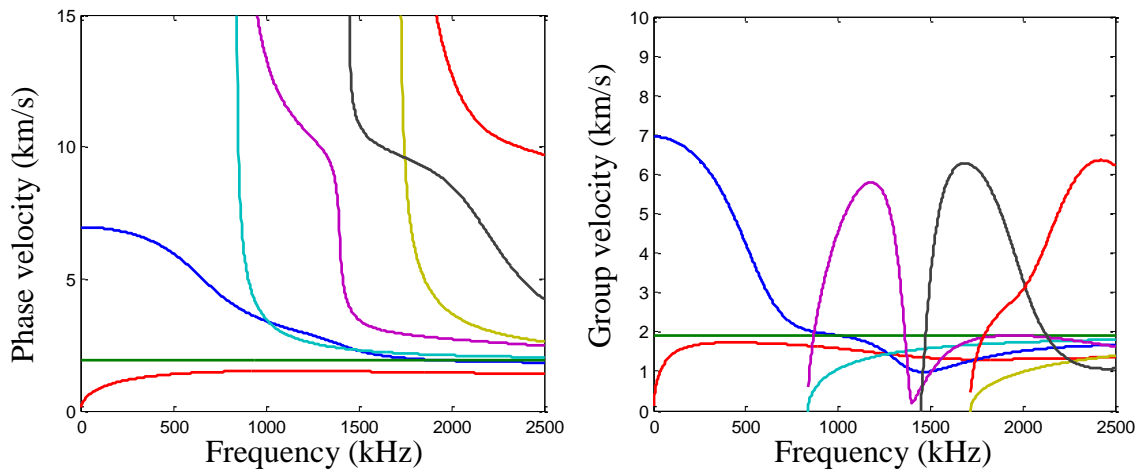


Figure 5.17: Dispersion curves for 1-mm thick 0/90 cross ply CFRP plate.



(a)        (b)        (c)

For 1-mm thick 0/90 cross ply CFRP plate at 100 kHz
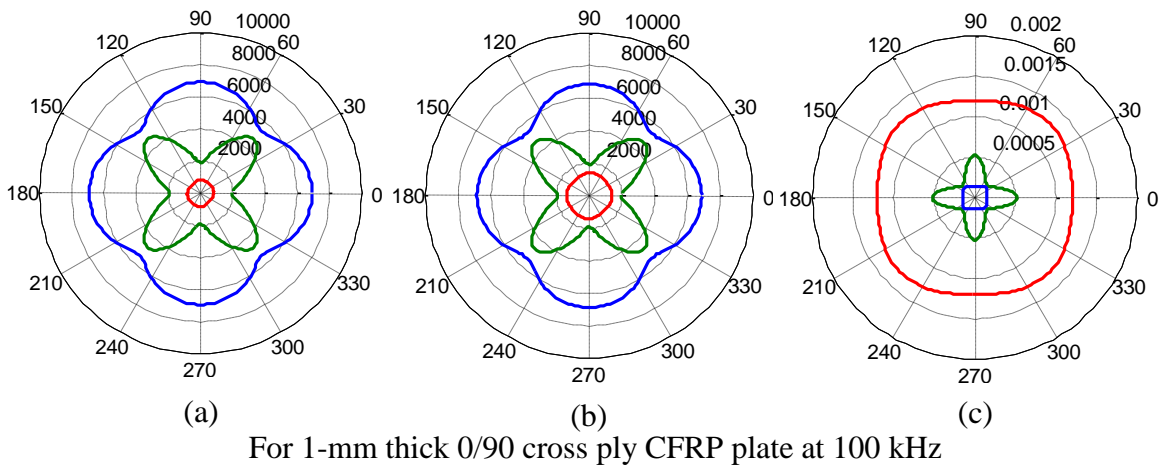
Figure 5.18: Directivity plots of (a) phase velocity, (b) group velocity, and (c) slowness curve.

Figure 5.18 shows the directivity plots for this test case. Since the 0/90 cross ply plate has the material properties in the 0 degree and 90 degree directions, the dispersion quantities are also the same in 0 and 90 degree directions. The symmetric and antisymmetric waves reach their highest velocity in the 0 and 90 directions, while the shear motion wave reaches the maximum velocity in its 40 degree direction.

Global matrix method (GMM) from DISPERSE[TM]



Semi-analytical finite element (SAFE) method from SAFE-DISPERSION
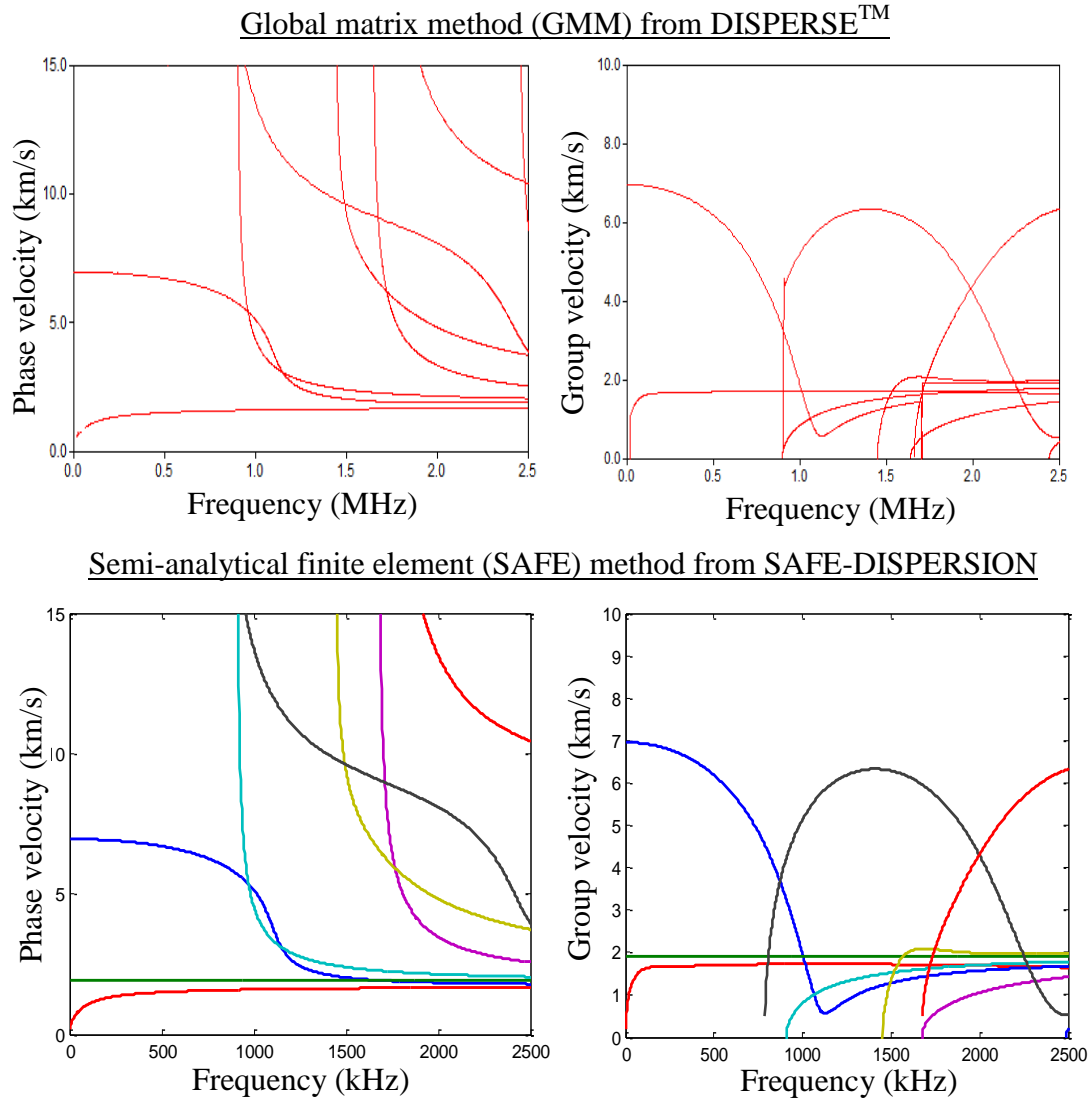


Figure 5.19: Dispersion curves for 1-mm thick [0/90]$_s$ cross ply CFRP plate.

Figure 5.19 shows the comparison results for 1-mm thick [0/90]$_s$ cross ply CFRP plate. It can be observed that the solutions from SAFE-DISPERSION (12 elements)

match well with GMM. It should be noted that, for all the results presented, SAFE-DISPERSION provides stable solutions for all the possible wave modes including shear horizontal waves. But fine training is required to get satisfying results using DISPERSE$^{TM}$ based on the GMM. The group velocity calculated from GMM in Figure 5.19 shows numerical discontinuities, while SAFE-DISPERSION result shows smooth solutions.

Figure 5.20 shows the directivity plots for the case of 1-mm [0/90]$_s$ cross ply CFRP plate. Similar effects to those in Figure 5.18 can be observed. However, the material properties are no longer the same for anti-symmetric waves. For 0 degree propagation antisymmetric waves, the 0 degree lamina is at the very outside, which make the effective "bending stiffness" bigger, while, for 90 degree propagating antisymmetric waves, the 90 degree lamina is at the very outside, which make the effective "bending stiffness" smaller. Thus, antisymmetric waves will have a higher velocity along 0 degree propagation direction, and will have a relatively lower velocity along 90 direction propagation direction.
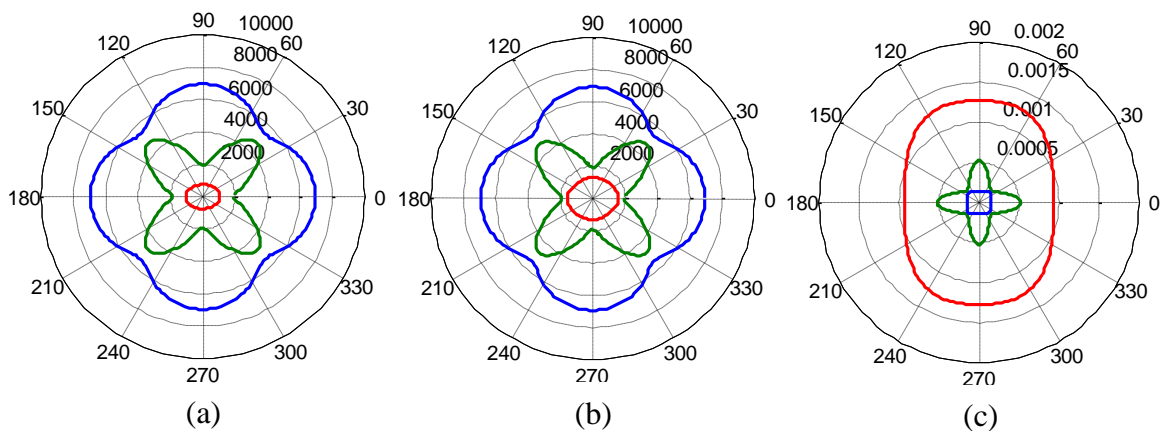


For 1-mm thick [0/90]s cross ply CFRP plate at 100 kHz

Figure 5.20: Directivity plots of (a) phase velocity, (b) group velocity, and (c) slowness curve.

5.5.1.5 Quasi-isotropic CFRP plates

A 1-mm eight layer quasi-isotropic CFRP plate is considered in this case study. The stacking sequence is [+45/-45/0/90]$_s$. For SAFE-DISPERSION, we used two elements for each layer, i.e., 16 elements were used to discretize the cross section of the plate and describe the mode shapes.

Global matrix method (GMM) from DISPERSE$^{TM}$



Semi-analytical finite element (SAFE) method from SAFE-DISPERSION
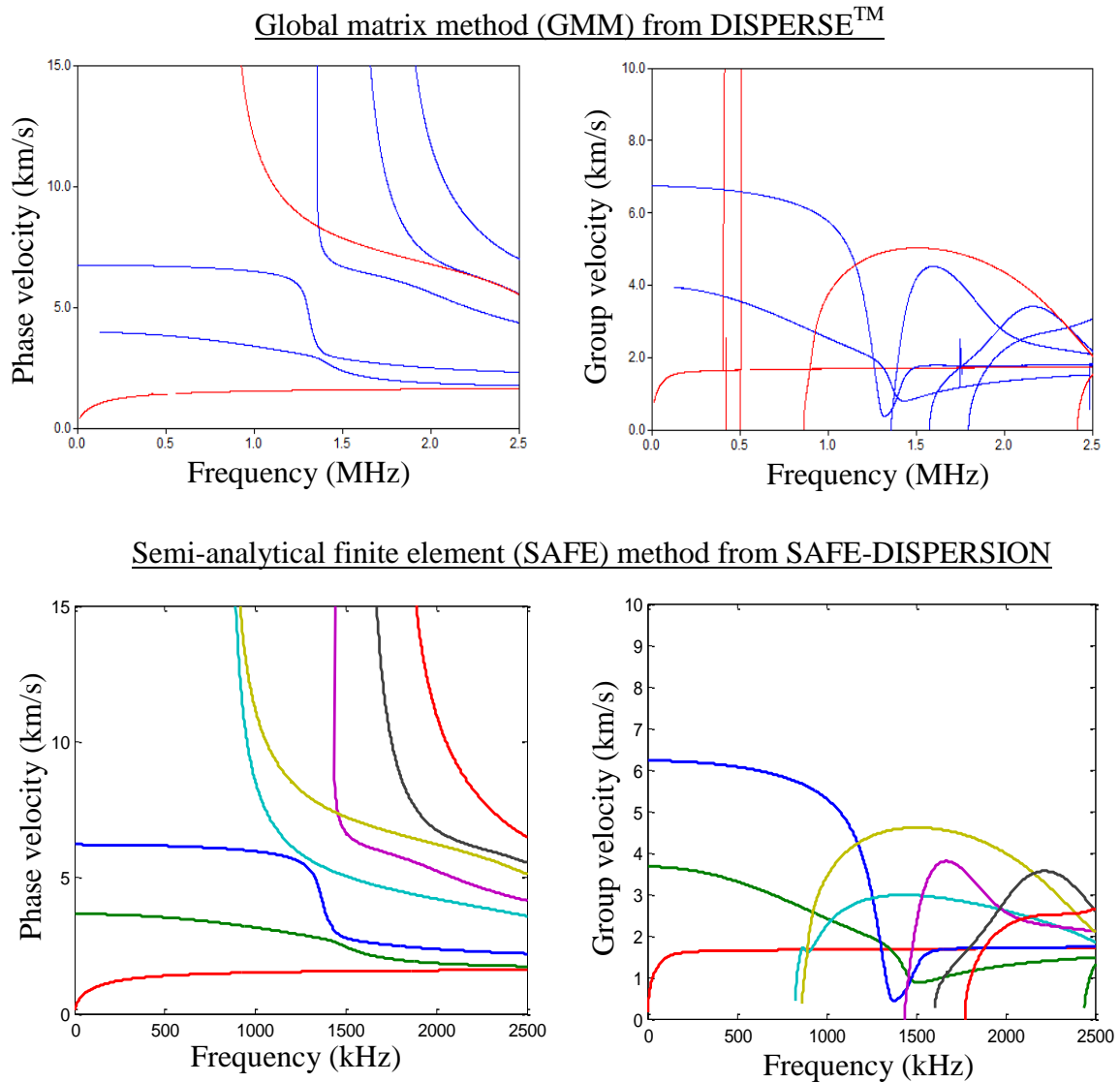


Figure 5.21: Dispersion curves for 1-mm thick [+45/-45/0/90]$_s$ quasi-isotropic CFRP plate.

Figure 5.21 shows that the dispersion curves for this 1-mm 8 layer quasi-isotropic CFRP plate match well with each other. Beyond 2000 kHz, slight differences are noticed. This is because the quasi-isotropic plate has 8 layers of lamina, which makes the cross section more complicated than the previous cases. Thus, the accurate modeling of mode shapes across the thickness requires more elements. Numerical discontinuities can be observed from DISPERSE$^{TM}$ solution. Smooth results are obtained from SAFE-DISPERSION.



(a)          (b)          (c)
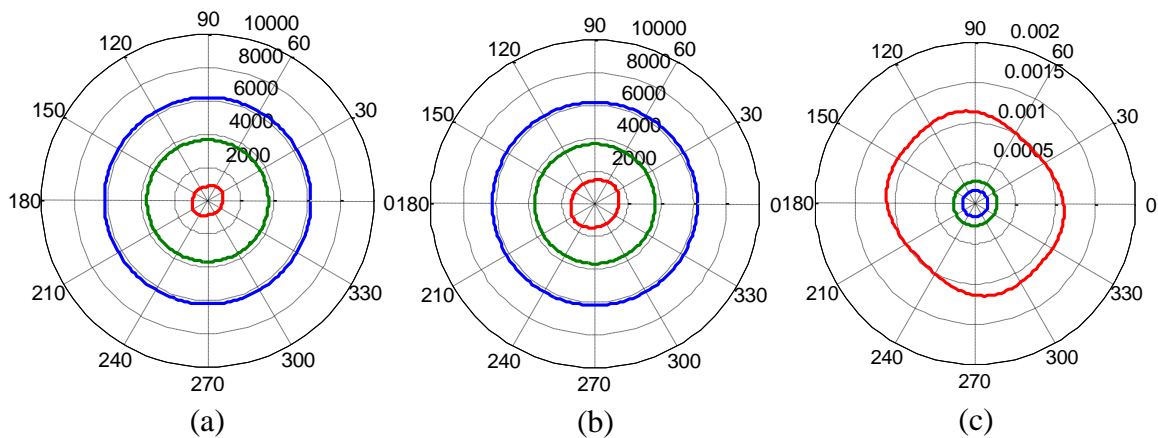
For 1-mm thick [+45/-45/0/90]s quasi-isotropic CFRP plate at 100 kHz

Figure 5.22: Directivity plots of (a) phase velocity, (b) group velocity, and (c) slowness curve.

Figure 5.22 shows the directivity plots of this quasi-isotropic CFRP plate. Due to the multi-directional stacking of the plate, the material properties are very similar in all the wave propagation directions. It can be noticed that the fundamental symmetric mode and shear horizontal mode show an axisymmetric velocity pattern as wave propagation in an isotropic material. However the fundamental antisymmetric mode shows certain dependency on propagation direction. The 45 degree wave propagation direction presents the largest phase, the largest group velocity, and the smallest slowness. This is because

the outermost two laminate on top and bottom surfaces have the stacking angle of +45 degree, and these outermost layers have the biggest contribution to the bending stiffness of the plate, which will result in the largest antisymmetric mode velocity.

### 5.5.2 SAFE-DISPERSION VS GLOBAL MATRIX METHOD: MODE SHAPES

The mode shapes of composite material are more complicated than those of isotropic materials. The DISPERSE[TM] software is based on the GMM, and provides a mode shape display option. The SAFE-DISPERSION, developed in this study using SAFE method, also has a mode shape display function. To verify our SAFE-DISPERSION results for mode shapes in composites, we conducted the case study on a 1-mm 0/90 cross ply CFRP plate and compared the results with DISPERSE[TM] (GMM). We choose this two layer laminate, because it is very representative with drastic stiffness change between the two layers.
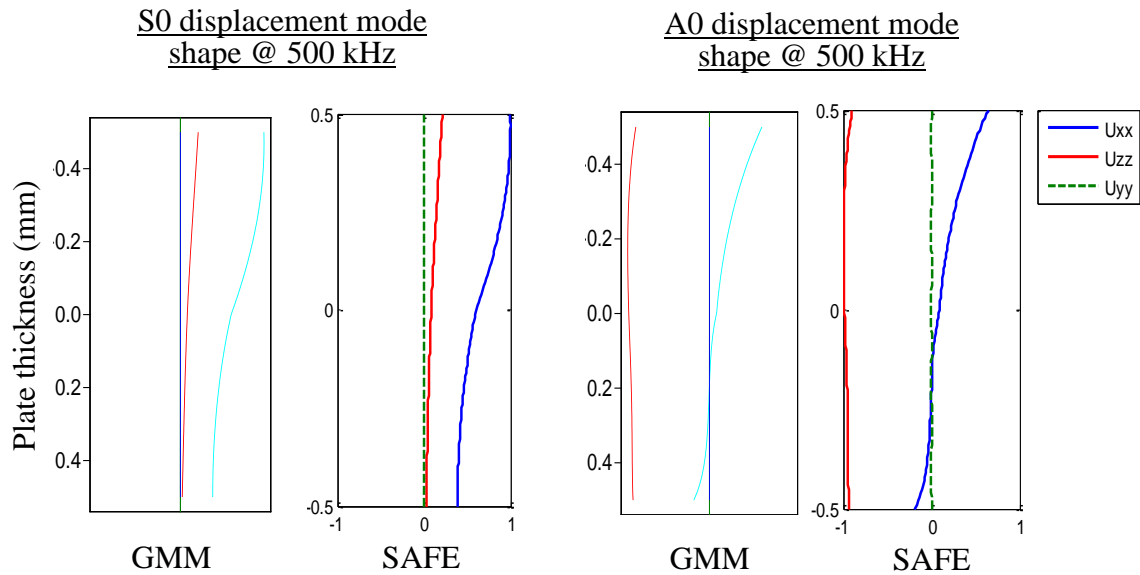


Figure 5.23: Comparison of displacement mode shapes between GMM and SAFE at 500 kHz.

138

Figure 5.23 shows the comparison of displacement mode shapes between GMM and SAFE method at 500 kHz. It should be noted that the figure captured from DISPERSE$^{TM}$ software has slightly different figure margins and line colors. But it can be observed that the SAFE-DISPERSION solutions match very well for both fundamental symmetric and antisymmetric wave mode. Compared with the mode shapes in isotropic materials (Figure 5.10), the fundamental symmetric and antisymmetric mode displacement components are no longer purely symmetric or antisymmetric to the mid-plane of the plate. The 90 degree layer with lower stiffness undergoes greater motion than the 0 degree layer with higher stiffness.
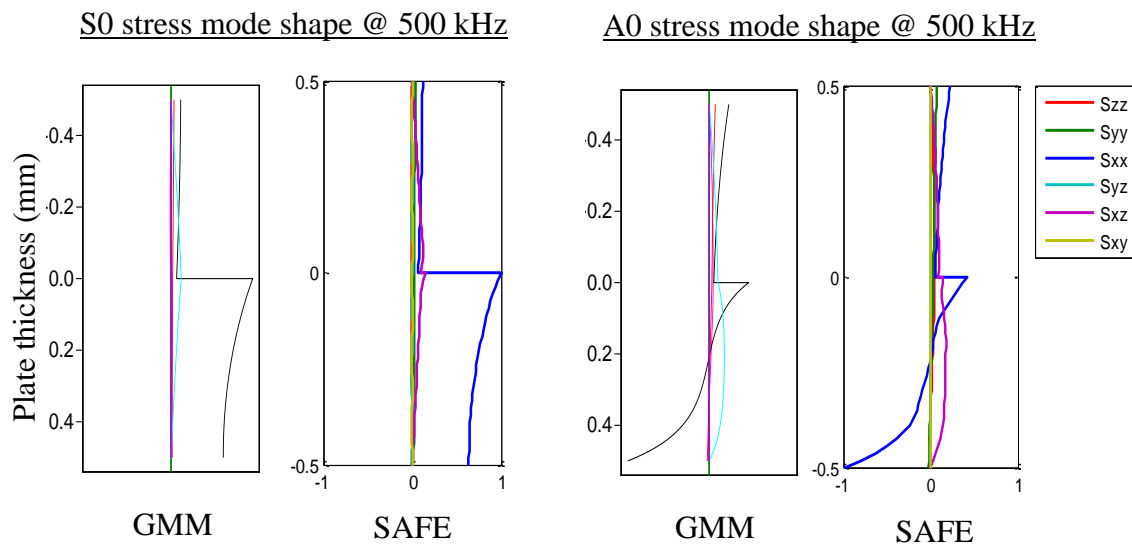


Figure 5.24: Comparison of stress mode shapes between GMM and SAFE at 500 kHz.

Figure 5.24 shows the comparison of stress mode shapes between GMM and SAFE method. It can be observed that the results from both methods agree very well with each other. The stress mode shapes are even more complicated, because the stress components are no longer continuous across the thickness, which is quite different from the case of isotropic materials (Figure 5.11). The stress components have a drastic change

at the interface between the two layers. This is because the deformation (displacement and strain) is continuous across the thickness considering the compatibility of elastic solid, but the stiffness varies a lot between the 0 degree lamina and the 90 degree lamina. According to Eq. (5.31), the discontinuity in stiffness will result in the drastic change in the stress across the plate thickness. The 0 degree layer with higher stiffness carries higher stress than the 90 degree layer with lower stiffness. Another aspect which serves as an additional proof of the correctness is the free surface boundary condition. It can be observed that the $\sigma_{zz}$ and $\sigma_{xz}$ stress components vanishes at the top and bottom surfaces, which satisfies the stress free boundary condition.
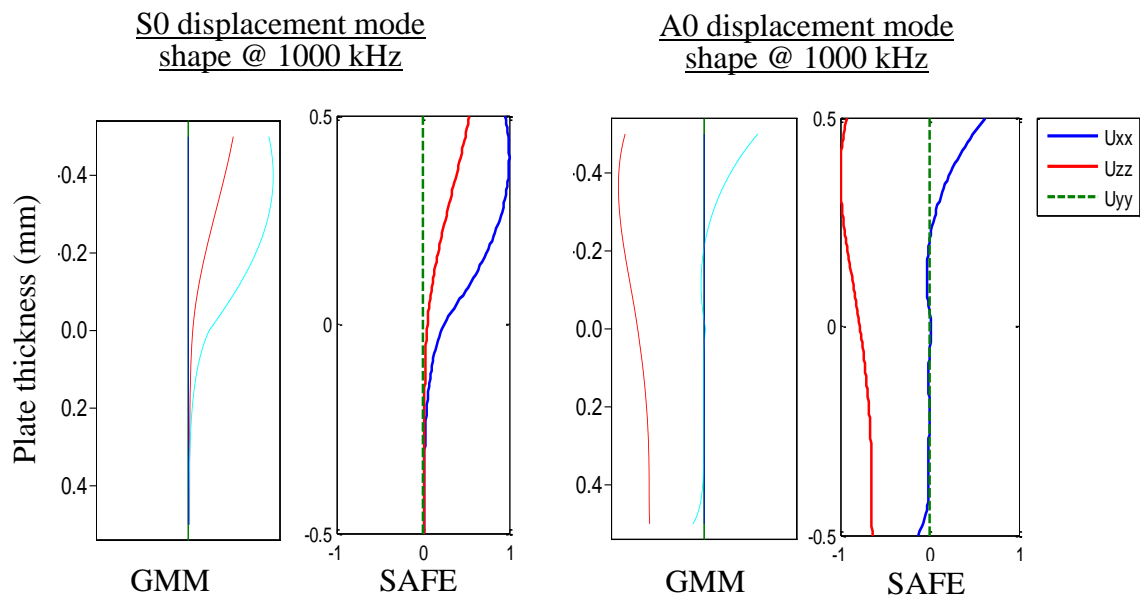


Figure 5.25: Comparison of displacement mode shapes between GMM and SAFE at 10000 kHz.

Figure 5.25 and Figure 5.26 shows the displacement and stress mode shapes comparison for a higher frequency value at 1000 kHz. It can be noticed that the solution from SAFE-DISPERSION still match well with the results from DISPERSE$^{TM}$ (GMM).

140

Compared with Figure 5.23 and Figure 5.24, the mode shapes become more complicated.

For even higher frequency, more elements are required to accurately model the waves.
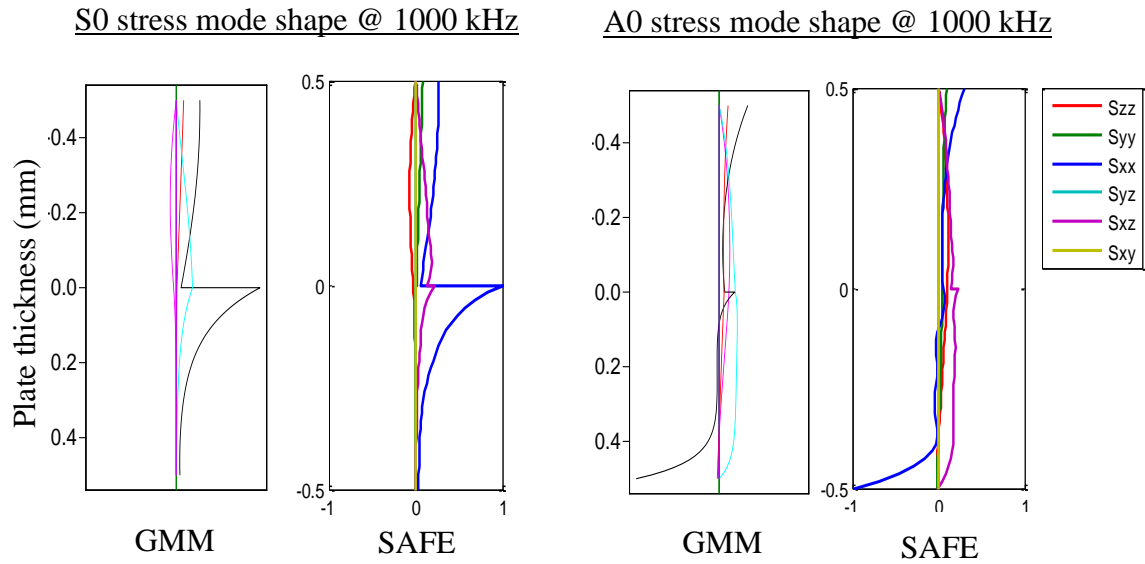


Figure 5.26: Comparison of stress mode shapes between GMM and SAFE at 1000 kHz.

# CHAPTER 6
## Nonlinear Oscillation Theory and Techniques for Structural Health Monitoring

This chapter introduces the fundamentals of nonlinear oscillation theory and its application to Structural Health Monitoring (SHM). Three nonlinear mechanisms, with promising application potentials, are discussed, including the classical nonlinear elasticity, contact and clapping nonlinearity, and material hysteresis behavior. To illustration the contact and clapping nonlinearity, we conducted a parameter study with a bi-linear stiffness model using MATLAB SIMULINK. The most prevailing nonlinear ultrasonic techniques are introduced and discussed, including higher harmonics technique, subharmonic and DC response technique, nonlinear resonant ultrasound spectroscopy technique, and mixed frequency response (nonlinear modulation) technique.

## 6.1    INTRODUCTION

Conventional ultrasonic NDE and SHM techniques are developed based on linear elastic theory, and they normally rely on measuring some particular parameter, such as wave speed, attenuation, and transmission/reflection coefficients, to detect damage. The logic behind these conventional ultrasonic techniques is that the presence of damage will bring changes to the above measuring quantities. Practical applications have shown that the linear theory is sensitive to gross damage or open cracks, where there exists an effective scatterer for wave propagation. However, they are found to be less sensitive to incipient structural damage such as micro cracks, fatigue zone, or close cracks.

Nonlinear techniques, on the other hand, have shown great potential for detecting such incipient changes at their early stage, using features that are distinctive from nonlinear frequency responses (Jhang 2009).

6.2    NONLINEAR ULTRASONIC MECHANISMS

For various physical situations, the nonlinear ultrasonic mechanisms are very complicated. This section discusses three physics of nonlinear ultrasonics: (1) classical nonlinear elasticity, (2) contact and clapping nonlinearity, and (3) material hysteresis behavior.

6.2.1    CLASSICAL NONLINEAR ELASTICITY

The classical nonlinear elasticity model describes a nonlinear relationship between stress and strain, which is associated with material change at a mesoscopic level, such as accumulation of dislocations in metallic structures (Nagy 1998; Cantrell 2009; Jhang 2009; Broda et al. 2014).

A fundamental representation of the classical nonlinear elasticity is the nonlinear Hooke's law which accounts for higher-order elastic terms. There are two basic nonlinear types which are considered and distinguished due to their distinctively different forced responses: (1) quadratic nonlinearity and (2) cubic nonlinearity. Considering a general nonlinear dynamic system, the quadratic nonlinearity can be expressed using Eq. (6.1).

$$U_Q = Ax\left(1 + \beta x + \gamma x^2 + \cdots\right) \tag{6.1}$$

where $U_Q$ is the output of the quadratic nonlinear system, $A$ is the scale factor, and $\beta$ and $\gamma$ are the second and third nonlinear coefficients. It should be noted that Eq. (6.1) contains all the higher-order terms. A single frequency forced response of the quadratic

nonlinear system will bring in nonlinear higher harmonics. This effect can be illustrated by considering a harmonic input in the form of Eq. (6.2).

$$X(\omega) = \hat{x}e^{i\omega t} \tag{6.2}$$

By substituting Eq. (6.2) in to Eq. (6.1), the output of the nonlinear system takes the form

$$
\begin{aligned}
U_Q &= A\hat{x}e^{i\omega t} + A\beta(\hat{x}e^{i\omega t})^2 + A\gamma(\hat{x}e^{i\omega t})^3 + \cdots \\
&= A\hat{x}e^{i\omega t} + A\beta\hat{x}\hat{x}e^{i2\omega t} + A\gamma\hat{x}^2\hat{x}e^{i3\omega t} + \cdots \\
&= AX(\omega) + A\beta\hat{x}X(2\omega) + A\gamma\hat{x}^2X(3\omega) + \cdots
\end{aligned}
\tag{6.3}
$$

Eq. (6.3) shows that the output of the quadratic nonlinear system contains all the higher harmonics $2\omega, 3\omega \cdots$, while the input to the system contains only one frequency component $\omega$. This distinctive feature allows us to detect material degradation, fatigue, or accumulated dislocations which may introduce nonlinearity into the materials.

Similar to quadratic nonlinearity, the cubic nonlinearity can be expressed using Eq. (6.4). It can be noticed that compared with Eq. (6.1), the cubic expression is an odd function, which only keeps the odd higher-order terms.

$$U_C = Ax\left(1 + \gamma x^2 + \eta x^4 \cdots\right) \tag{6.4}$$

where $U_C$ is the output of a cubic nonlinear system, and $\gamma$ and $\eta$ are the third and fifth nonlinear coefficients. The single frequency forced response of cubic nonlinear system will only generate odd higher harmonics shown in Eq. (6.5).

$$U_C = AX(\omega) + A\gamma\hat{x}^2X(3\omega) + A\eta\hat{x}^4X(5\omega) + \cdots \tag{6.5}$$

Figure 6.1 shows the quadratic and cubic nonlinear elasticity relationship between input $X$ and output terms $U_Q$ and $U_C$, as well as their frequency response to a single frequency excitation centered at $f_c$. The first vertical line stands for the fundamental response at the excitation frequency, and the rest represent the nonlinear higher

harmonics response. The difference in the response spectrum can be clearly identified: the quadratic nonlinearity response contains all the higher order harmonics, whereas the cubic nonlinearity response contains only the odd higher order harmonics.
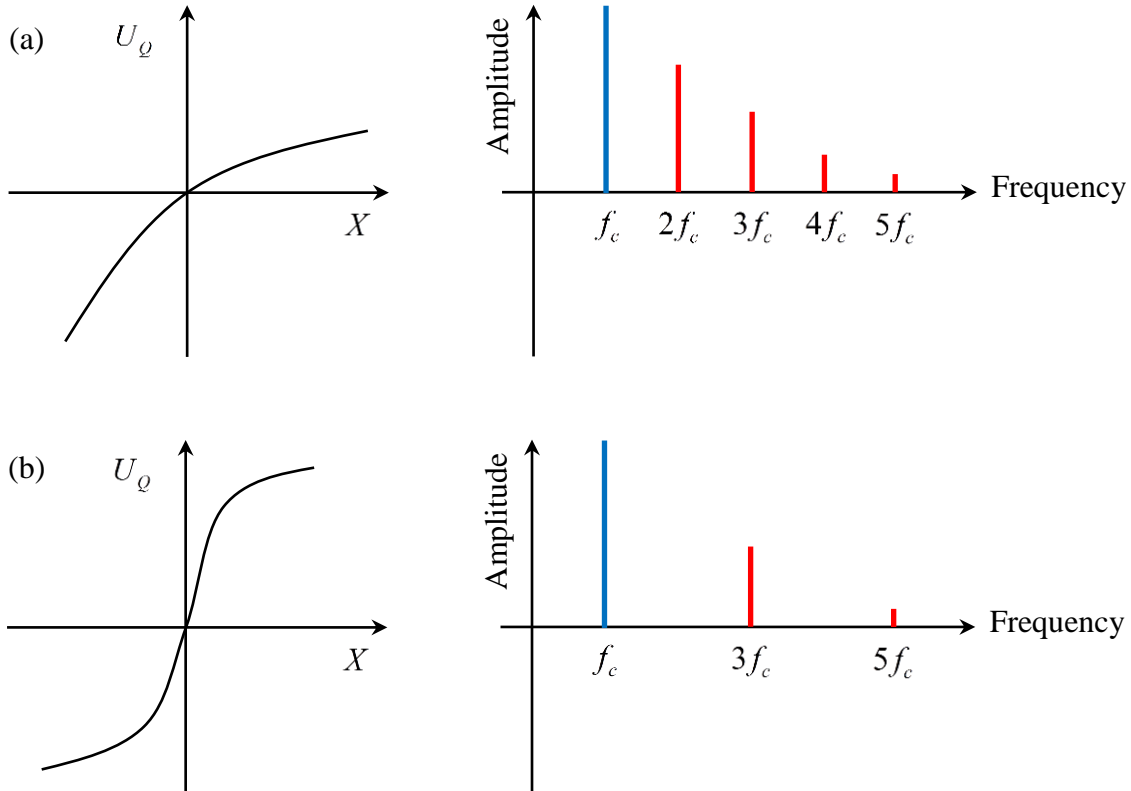


Figure 6.1: (a) Quadratic nonlinear system and its response to single frequency forced excitation; (b) cubic nonlinear system and its response to single frequency forced excitation (modified after Broda et al. 2014).

Other explanations of the higher order harmonic generation due to material nonlinear elasticity are found using perturbation theory (Nayfeh and Mook 1995). An example of such problem is longitudinal wave propagation through a thin circular rod with quadratic nonlinear material. The formulation starts from the nonlinear wave equation considering one higher order nonlinear term with nonlinear coefficient $\beta$ (Jhang 2009).

$$\rho \frac{\partial^2 u}{\partial t^2} = E \frac{\partial^2 u}{\partial x^2} + 2E\beta \frac{\partial^2 u}{\partial x^2} \tag{6.6}$$

where $\rho$ is the material density, $x$ is the propagation direction coordinate, $\sigma$ is the stress, and $u$ is the displacement. The perturbation theory is then applied by assuming the displacement as

$$u = u_0 + u' \tag{6.7}$$

where $u_0$ represents the initially excited wave and $u'$ represents the first order perturbation solution. If we set $u_0$ to a sinusoidal single frequency wave at $\omega$ with the wavenumber $\xi$ expressed in Eq. (6.8),

$$u_0 = A_1 \cos(\xi x - \omega t) \tag{6.8}$$

then, we can obtain the perturbation solution up to the second order as follows (Brillouin 1964; Mumaghan 1951)

$$u = u_0 + u' = A_1 \cos(\xi x - \omega t) - A_2 \sin 2(\xi x - \omega t) \tag{6.9}$$

$$A_2 = \frac{\beta}{8} A_1^2 \xi^2 x \tag{6.10}$$

The second term in Eq. (6.9) represents the second harmonic frequency component. Eq. (6.10) gives the relationship between the fundamental component amplitude $A_1$ and the second harmonic component amplitude $A_2$. It can be observed that the participation of second harmonic component depends on the nonlinear elasticity parameter $\beta$. It can also be noted that the second harmonic is cumulative with propagation distance $x$. This dependency of higher harmonic amplitude to nonlinear parameters makes it possible to evaluate the degradation of elastic properties by monitoring the magnitude of the higher harmonic wave component in the transmitted wave.

More complicated cases, such as the cumulative second-harmonic generation of Lamb waves in plate structures, have also been studied theoretically (Deng 1999 and 2003). Experimental observations of such material nonlinear effects on Lamb waves have been reported (Bermes 2007). Srivastava and Lanza di Scalea (2009) further discussed the existence of antisymmetric nonlinear Lamb modes due to material nonlinear elasticity. The same authors (Srivastava and Lanza di Scalea 2010) also investigated the nonlinear guided wave generation in arbitrary cross section waveguides using the semi-analytical finite element (SAFE) method. All the theoretical and numerical studies mentioned here also started from the nonlinear form of wave equations. The derivation proved to be mathematically complicated and hard to attain.

6.2.2  CONTACT AND CLAPPING NONLINEARITY

All the models in the nonlinear elasticity section consider the nonlinear elastic behavior exhibited over the whole material domain, which may correspond to the case of material degradation and mesoscopic accumulated dislocations. More practical applications of nonlinear techniques should focus on the detection of fatigue cracks, breathing cracks, or closed cracks, which are local damage and exhibit totally different nonlinear behaviors. The widely accepted approach to understanding this nonlinear mechanism is the contact and clapping model. In this section, a bi-linear stiffness model is introduced and programed using MATLAB SIMULINK. This model is constructed based on the mechanical behavior of micro cracks: the presence of tension and compression leads to crack opening and closing (Worden and Tomlinson 2001; Friswell and Penny 2002; Giurgiutiu 2002). Parameter studies on damage severity and excitation

frequency were carried out to demonstrate the capability of nonlinear techniques for detection and quantification of structural damage.

6.2.2.1 Bi-linear stiffness model for contact nonlinearity

Fatigue cracks or micro cracks may cause structures to behave nonlinearly under dynamic load. Figure 6.2 shows the contact bi-linear behavior of cracks in structures. When the crack zone is stretched, the crack opens, and the structure is discontinuous with a lower effective stiffness $k_s$. However, when the crack zone is under compression, the crack closes, and the structure behaves like a continuum with the original structural stiffness $k_c$, which is greater than $k_s$. Therefore, the structure has a changing effective stiffness related with the size and status of the "breathing crack".
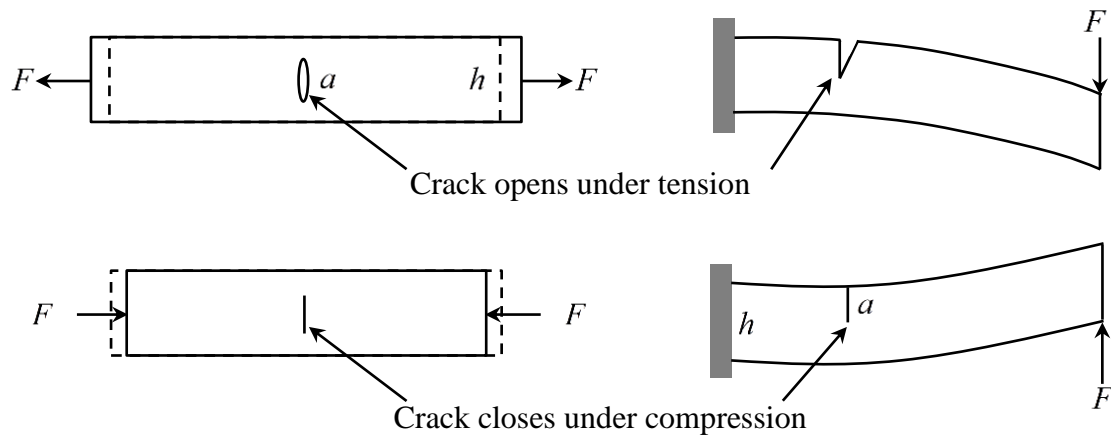


Figure 6.2: Bi-linear contact behavior of cracks in structures (Giurgiutiu 2002).

A reduced order model was built to approximate a general contact nonlinear behavior for parameter study. Figure 6.3a shows the bi-linear stiffness effect under compression and tension. Figure 6.3b shows the reduced order model with changing spring coefficient. The spring coefficient is higher under compression than that under tension.
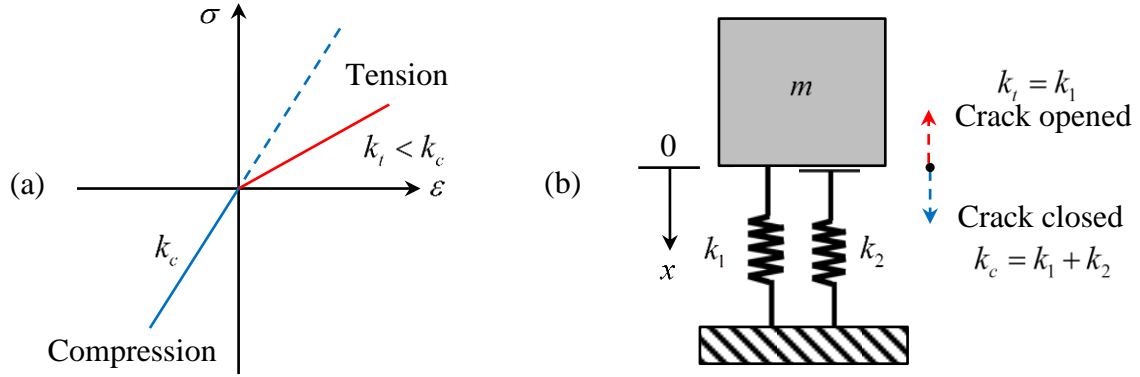
Figure 6.3: Bi-linear stiffness model for contact nonlinearity of cracks.

A piecewise-linear nonlinear equation was used to model the contact nonlinear system (after Giurgiutiu 2002).

$$\begin{cases} \ddot{X} + 2\zeta_t\omega_t\dot{X} + \omega_t^2 X = A\sin(\omega t + \varphi), X \geq 0 \\ \ddot{X} + 2\zeta_c\omega_c\dot{X} + \omega_c^2 X = A\sin(\omega t + \varphi), X < 0 \end{cases} \tag{6.11}$$

where the subscripts $C$ and $T$ denote "compression" and "tension" of the crack status. Under compression, the structure behaves like a continuum, so $\omega_c = \omega_n$ which is the natural frequency of the component in pristine condition. At stretching, the crack opens, the component becomes discontinuous, and the effective stiffness decreases. Hence, it is apparent that $\omega_t < \omega_n$. $\omega_t$ is directly related to the severity of the damage in the structure. The more severe the damage, the more $\omega_t$ deviates from $\omega_n$. Assuming $\omega_t = \omega_n\sqrt{1-r}$, $\omega_c = \omega_n$, where $r$ is the relative crack size, $r = a/h$, the severity index of the damage.

The piecewise-linear equation was solved numerically by MATLAB SIMULINK. Figure 6.4 shows the SIMULINK program to solve Eq. (6.11). The natural frequency of the pristine system is set to 200 Hz. The damping ratios for both stretching and compression are considered as 0.02.

149
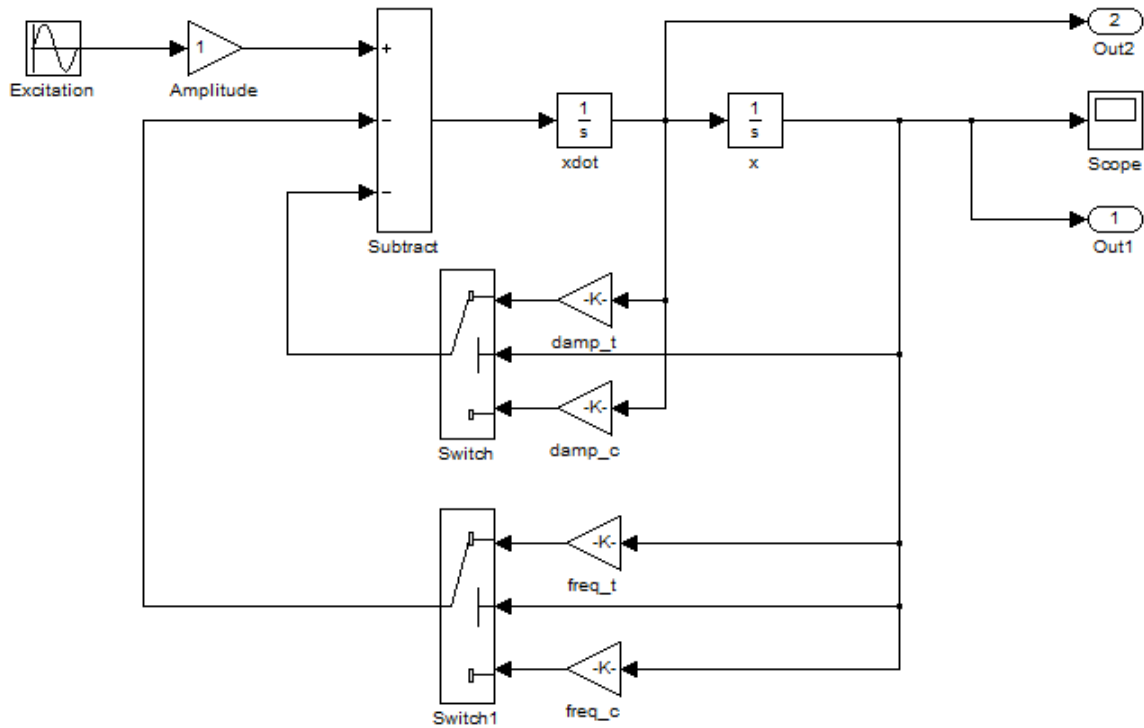
Figure 6.4: SIMULINK for solving the piecewise-linear nonlinear equation.

6.2.2.2 Parameter study on damage severity

A parameter study was carried out to investigate the influence of the damage severity on the sensing signal. Figure 6.5 shows the parameter study plots. Each row of the plots corresponds to one damage situation. Four degrees of damage severity was investigated, with r = 0.0, 0.1, 0.4, 0.6, standing for respectively pristine, small damage, medium damage, and severe damage cases. The first column shows the time domain displacement signal. The second column shows the phase plane including the information from both displacement and velocity. A phase plane is the representation of oscillations showing the variation of velocity $\dot{u}$ with displacement $u$ (Nayfeh and Mook 1995). The third column shows the frequency spectrum of the displacement signals. It should be noted that SIMULINK provided a transient response. The excitation is at 50 Hz. The signals shown in Figure 6.5 are selected when the response reaches steady state.

150
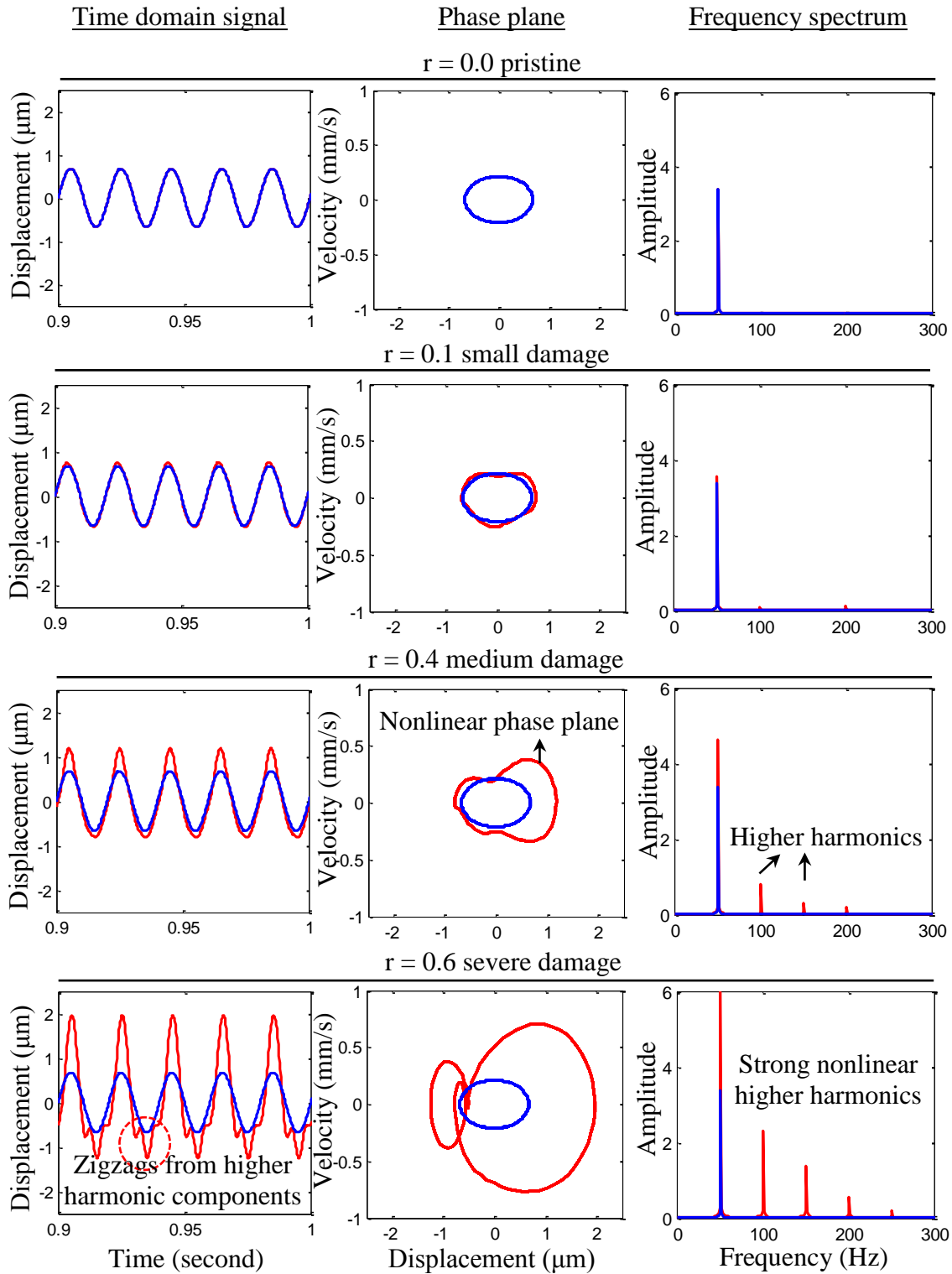
Figure 6.5: Parameter study on damage severity. Time domain signal, phase plane signal, and frequency domain spectrum (blue line: pristine case; red line: damaged case).

The time domain displacement signals in the first column show that with higher degree of damage severity, more distortion is introduced into the signal. When the structure is pristine, the displacement oscillation takes a perfect sine waveform. When damage appears in the structure, the signal deviates from the sine waveform. One significant phenomenon is that the amplitude is no longer equal with respect to the origin. When the damage is severe, obvious zigzags can be noticed, denoting the participation from higher harmonic frequency components.

The phase planes can also show the effects from the nonlinear damage. It has been shown that the displacement takes a sine waveform. The velocity is the derivative of displacement with respect to time and takes a cosine waveform.

$$u = A\sin(\omega t); \quad \dot{u} = \frac{\partial u}{\partial t} = (A\omega)\cos(\omega t) \tag{6.12}$$

Squaring both sides of displacement and velocity formulae in Eq. (6.12) yields

$$u^2 = A^2 \sin^2(\omega t)$$
$$\dot{u}^2 = (A\omega)^2 \cos^2(\omega t) = (A\omega)^2 \left[1 - \sin^2(\omega t)\right] \tag{6.13}$$

The phase plane showing the variation of velocity $\dot{u}$ with displacement $u$ can be obtained from Eq. (6.13) as

$$\left(\frac{u}{A}\right)^2 + \left(\frac{\dot{u}}{A\omega}\right)^2 = 1 \tag{6.14}$$

Thus, when the structure is pristine, the phase plane is a regular elliptic as shown in Figure 6.5. When damage appears, the phase plane starts to deviate from the elliptic shape, and takes an irregular form, unbalanced with respect to the origin and axis in an asymmetric shape. When the damage is severe, obvious deviation from the elliptic can be

152

noticed with additional complete cyclic motions, which indicate the appearance of zigzags in the time domain signal and strong participation of other harmonic components.

The frequency spectrum shows even more distinctive features of nonlinear oscillations. It can be observed, for the pristine case, there is only one frequency component at the excitation frequency $f_e$, and no other frequency components are noticed. When damage appears, beside the fundamental excitation component at $f_e$, small amplitude higher harmonic components are present at $2f_e$, $3f_e$, and $4f_e$, etc.. When the severity of damage goes up, the nonlinear higher harmonics become much stronger. This distinctive feature can be used for detecting nonlinear damage and further identify the severity of damage.

6.2.2.3 Parameter study on excitation frequency

Another special feature of nonlinear systems is that their response is sensitive to the excitation frequency, and can be totally different for certain special frequencies. To illustrate this important aspect, a parameter study was conducted on the bi-linear stiffness model. We kept the damage severity the same at r = 0.6 for a severe damage case. The natural frequency of the pristine structure is set to 200 Hz. By using $\omega_t = \omega_n \sqrt{1-r}$, the crack open status natural frequency is 126.5 Hz. We tested four excitation frequencies: 50 Hz, 100 Hz, 250 Hz, and 334.67 Hz. Figure 6.6 shows the parameter study plots. Each row contains the results for an excitation frequency case. The first column shows the time domain displacement signal. The second row shows the phase plane containing both the displacement and velocity relationship information. The third column shows the frequency spectrum of the displacement signal. The steady state response was used to generate these plots.

153
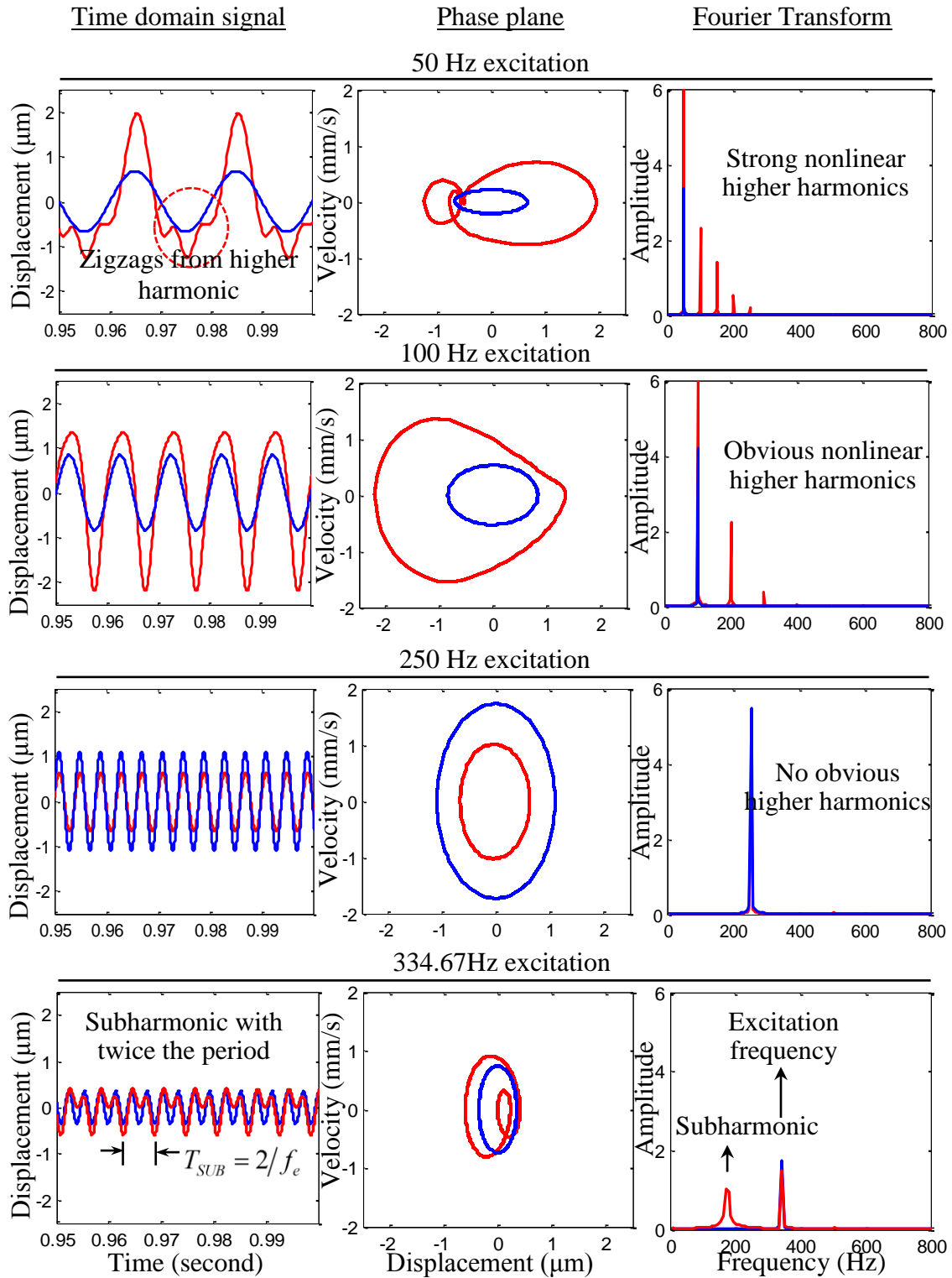
Figure 6.6: Parameter study on excitation frequency. Time domain signal, phase plane signal, and frequency domain spectrum (blue line: pristine case; red line: damaged case).

It can be observed that at 50 Hz, obvious nonlinear effects can be identified from time domain signal which shows zigzags, the phase plane showing asymmetric deviation from the elliptic shape, and the frequency spectrum with strong higher harmonics. When we apply 100 Hz excitation to the nonlinear system, the time domain signal and the phase plane look totally different. The time domain oscillation gains higher amplitude toward the negative direction, which also appears in the phase plane as the asymmetry to the left hand side, instead of to the right hand side as in the 50 Hz case. The frequency spectrum still shows obvious nonlinear higher harmonics. At a certain frequency, such as 250 Hz, the nonlinear effects are not obvious. The 250 Hz time domain signal approaches a perfect sine waveform, and the phase plane shows a nice and smooth symmetric elliptic. The only difference is the amplitude. The frequency spectrum also shows no obvious higher harmonic components. There is a special excitation frequency, around which a distinctive subharmonic may be excited. This frequency is identified as twice the natural frequency of the linearized damaged system. The natural frequency of the linearized damaged system is given by Johnson et al. (2010) in Eq. (6.15).

$$f_0 = \sqrt{\left(f_c^2 + f_t^2\right)/2} \tag{6.15}$$

which is 167.335 Hz for this case study. The bottom row of Figure 6.6 shows the unique subharmonic phenomenon for a 334.67 Hz excitation, which is twice the natural frequency of the linearized damaged system. The time domain signal shows a waveform component with a period twice as much as the pristine case signal. This means the corresponding frequency of this component is half of the excitation. A component at half the excitation frequency is referred to as subharmonic. The phase plane shows obvious nonlinearity with an asymmetric deviation from the elliptic shape, and the additional

complete cyclic motion indicates the zigzags in time domain signal and the strong participation of other harmonic components. The frequency spectrum shows that, besides the fundamental frequency at 326.5 Hz, an obvious subharmonic component at 163.25 Hz appears. This subharmonic effect can help us identify nonlinear damage and avoid influence from electronic devices with inherent nonlinearity; this is because electronic devices can generate higher harmonics but not subharmonics.

### 6.2.3 MATERIAL HYSTERESIS BEHAVIOR

Another nonlinear material behavior is stress strain hysteresis. This aspect of the nonlinear model will only be briefly introduced here. Hysteresis in metals and rocks was observed experimentally as early as the end of 19th and the beginning of 20th century (Love 1944). Experimental results show that hysteresis nonlinearity is stronger under rapid loading/unloading, and weaker in the case of slow deformation. Many factors have been suggested to cause this phenomenon, such as plasticity, viscosity, and the presence of cracks.
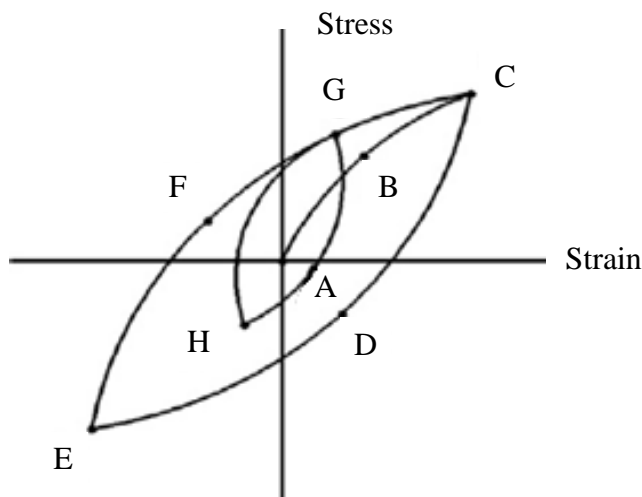


Figure 6.7: Stress strain hysteresis (Broda 2014).

156

Figure 6.7 shows a typical stress strain hysteresis loop, which is different from the classical nonlinear elasticity model described in Figure 6.1. In the classical nonlinear model, the loading and unloading will go through the same path. The hysteresis behavior, however, shows different paths of stress strain relation under loading and unloading. During the initial loading, the material behavior is described by the curve ABC. When the material is unloaded, instead of going back along the path CBA, the material behavior follows the path CDE. When reloaded again, the material will move along the path EFC. Additionally, the hysteresis path can be totally different under various loading levels, i.e., under smaller loading, the path can be GHG. The integration of stress over strain provides strain energy. It can be noticed that the loop area is the energy dissipated during cyclic loading. Most of the models describing the hysteresis behavior are phenomenological, the theoretical explanation of the cause is still not clear.

## 6.3    NONLINEAR TECHNIQUES FOR STRUCTURAL HEALTH MONITORING

Nonlinear ultrasonic techniques for structural health monitoring are attracting more and more interest in recent years for their remarkable sensitivity to incipient damage. In this section, four prevailing nonlinear techniques are introduced.

### 6.3.1    HIGHER HARMONICS TECHNIQUE

Higher harmonic generation is a classical phenomenon where the waveform of an incident wave is distorted by the nonlinear elastic response of the medium to the incident wave; therefore, higher harmonics are generated in the transmitted wave. Figure 6.8 shows the higher harmonic technique. Figure 6.8a shows that when the structure is pristine, if we input an excitation at a certain frequency, the output waveform will not be distorted and contains only the frequency component of the excitation. Figure 6.8b shows

that when the structure is damaged, wave distortion will occur at the damage and the frequency spectrum will not only contain the excitation frequency, but also the distinctive nonlinear higher harmonics.
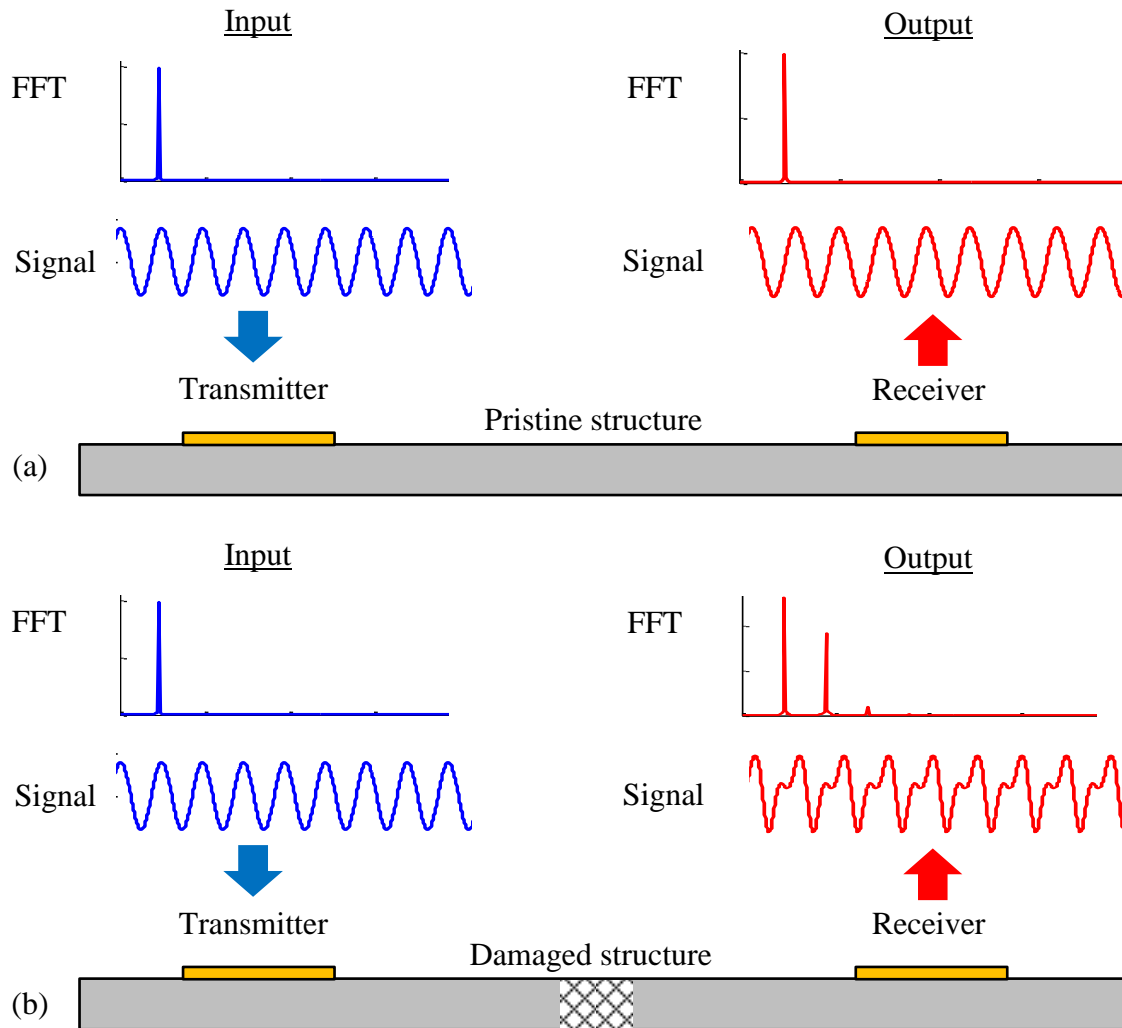


Figure 6.8: Nonlinear higher harmonic technique: (a) response of pristine structure shows no waveform distortion or nonlinear higher harmonics; (b) response of damaged structure shows waveform distortion and distinctive nonlinear higher harmonics.

This technique has been used to detect fatigue damage in various metals (Cantrell and Yost 1994; Hurley et al. 1998). A direct correlation between dislocation density within the fatigued material and an increase in harmonic ultrasonic signals has been reported (Kim et al. 2006). Since the experimental observation and theoretical analysis of

the generation of the second harmonic from interfaces and cracks, there have been numerous investigations due to its potential application to the ultrasonic inspection of imperfect interfaces and cracks (Buck et al. 1978; Richardson 1979; Donskoy et al. 2001; Biwa et al. 2004).

Although super harmonic generation is the classic and straight forward nonlinear technique, there is still great potential for research. First, most of the previous research work focuses on nonlinear non-dispersive bulk waves, but the amount of research on dispersive guided nonlinear waves is still limited. Further, inherent electronic nonlinearity from experimental device is unavoidable, which will greatly influence the judgment of the final results based on the generation of super harmonics. However, few solutions were found or mentioned in literatures.

6.3.2 SUBHARMONIC AND DC RESPONSE TECHNIQUE

Sub-harmonic and DC responses have been extensively studied recently (Korshak et al. 2002; Solodov et al. 2002). Sub-harmonics is a nonlinear wave distortion where the amplitude of adjacent carriers becomes different, resulting in a doubling of the period and a halving of the excitation frequency, i.e., $f_c/2$. A DC response is a nonlinear rectifying effect resulting in amplitude demodulation (Yamanaka et al. 1994), which the present authors also discovered in the cantilever of an atomic force microscope (Kolosov and Yamanaka 1993). Sub-harmonic and DC responses have a common feature of having a frequency range lower than that of the input wave. Sub-harmonic response of structures can help us avoid inherent electronic nonlinearity because the nonlinearity from electronic device can only generate higher harmonics, but the generation of subharmonics has two main requirements. First, the amplitude of the interrogating waves must be large

enough to overcome a certain threshold in order to excite the structure. Second, the excitation frequency must be tuned to meet the sweet spot for such subharmonic phenomenon to occur, which was identified as twice the natural frequency of the linearized damaged system (Johnson et al. 2010). Figure 6.9 shows the model for the generation of sub-harmonic and DC responses at a closed crack.
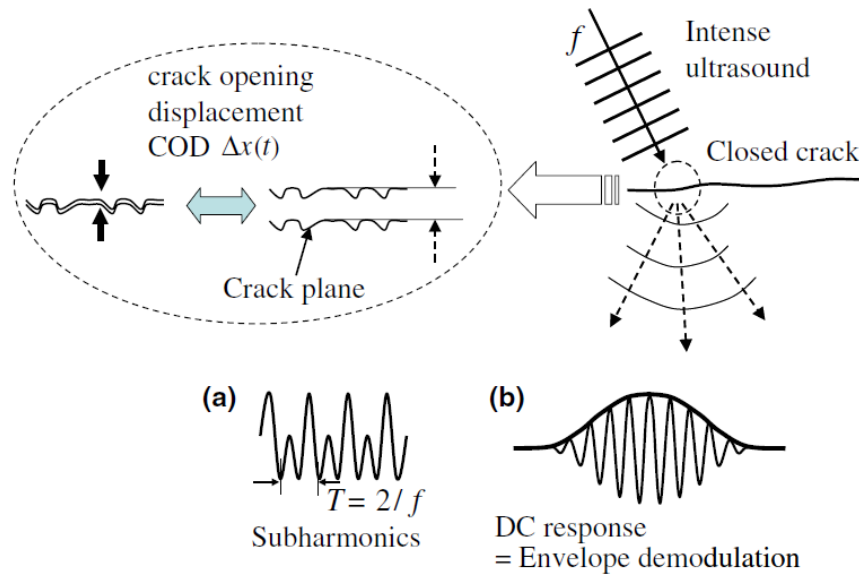


Figure 6.9: Model for subharmonic and DC responses (Ohara et al 2006).

### 6.3.3   NONLINEAR RESONANT ULTRASOUND SPECTROSCOPY TECHNIQUE

It has been shown in previous discussion that the response of nonlinear systems is sensitive to excitation frequency. Another important aspect of nonlinear responses is that they are also sensitive to excitation amplitude. This distinctive phenomenon has been used in a Nonlinear Resonant Ultrasound Spectroscopy (NRUS) technique (Abeele et al. 2000). This method measures the resonant frequency under various excitation amplitudes. By observing the relative frequency shift, it is possible to measure the internal degradation of the micro structure properties of the material (Johnson 2001; Windels and

Abeele 2004). The principle behind this method is that the nonlinear effects are different under different excitation amplitudes, usually stronger under higher amplitude excitation.

### 6.3.4 MIXED FREQUENCY RESPONSE: NONLINEAR MODULATION TECHNIQUE

One of the simplest ways to evaluate nonlinear acoustic properties of a material is to measure the modulation of an ultrasonic wave by low-frequency vibration. This method is known as Nonlinear Wave Modulation Spectroscopy (NWMS). Figure 6.10 shows the the principle of this technique. Two frequencies are usually used to excite the structure. The low frequency input is usually referred to as the pumping wave, and the high frequency input is usually referred to as the probing wave (Yoder and Adams 2010). When the structure is pristine, the frequency spectrum of the received signal only contains the original input frequency components. When nonlinear damage appears, the modulation frequency components will be present. The advantage of this method is that one does not need baseline data of the pristine specimen for the detection of nonlinear damage. Thus, it is regarded as a baseline free technique (Lim et al. 2014).
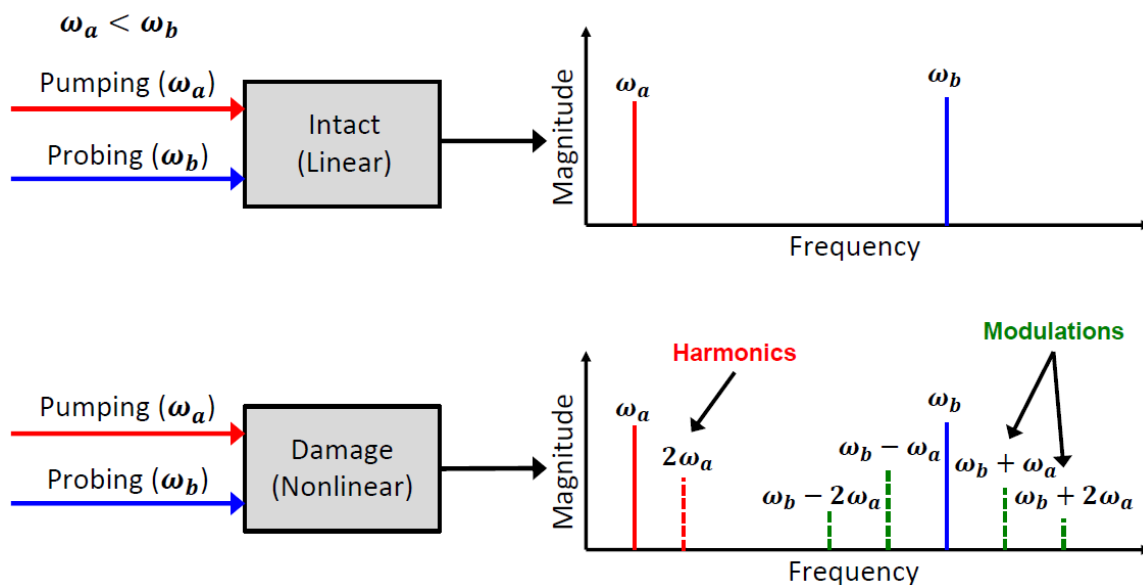


Figure 6.10: Nonlinear wave modulation technique (Sohn et al. 2013).

The physical nature of this modulation can be explained simplistically as shown in Figure 6.11, with a single crack shown as a slit. The crack opens and closes under the pumping excitation, while the probing signal pass through the cracked area.
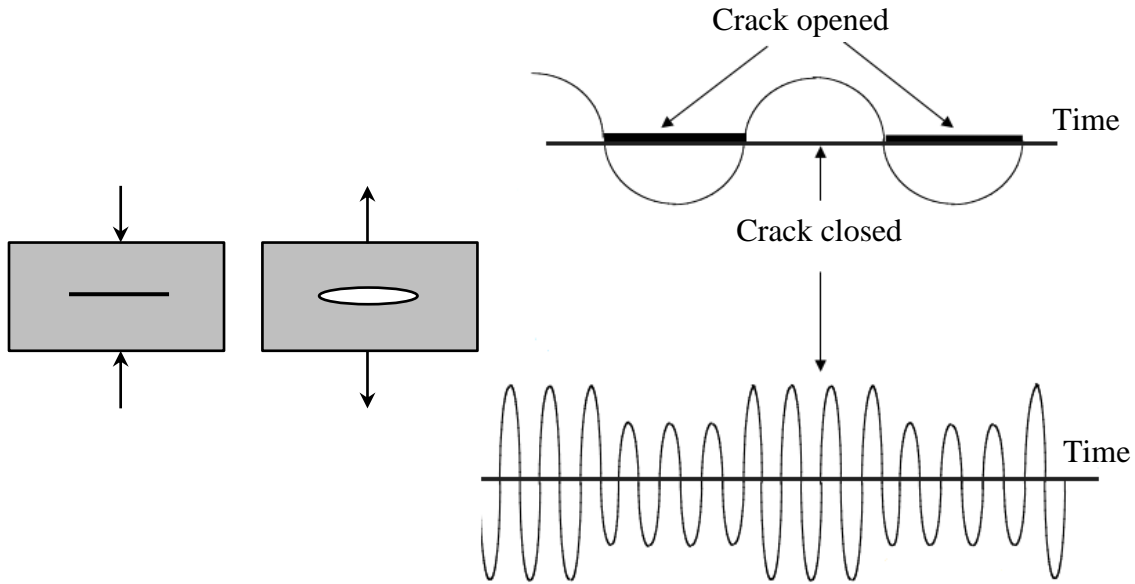


Figure 6.11: Mechanism of nonlinear modulation (Sutin and Johnson 2005).

An applied low-frequency vibration signal changes the width of the slit depending on the phase of the vibration. Consider that the sample is under sufficient vibration amplitude such that the compression phase completely closes the crack, whereas the subsequent dilation opens the crack. A high-frequency signal is simultaneously applied to the crack. During the dilation phase of the low-frequency cycle, the high frequency signal is partially decoupled by the open crack. This reduces the amplitude of the high-frequency signal passing through the crack. In the other half of the low-frequency cycle, the closed crack does not interrupt the ultrasonic signal and the amplitude of the transmitted signal amplitude increases. This results in an amplitude modulation of the ultrasonic signal. Fourier transformation of this signal reveals sideband frequencies that

are the sum and difference of the frequencies of the ultrasonic probe and vibration signals. These new frequency components may indicate that a flaw or crack is present. Research based on this nonlinear technique has been reported recently for fatigue crack detection and monitoring of composite delamination (Sohn et al. 2013; Giurgiutiu and Soutis 2012).

Although a considerable amount of research has been carried out on the nonlinear ultrasonic techniques for nondestructive evaluation and structural health monitoring, there are still phenomena that are unclear, mechanisms that are unknown, and new approaches that are uninvestigated, leaving great potential for future research and applications.

CHAPTER 7

# PREDICTIVE MODELING OF NONLINEAR GUIDED WAVES INTRODUCED BY BREATHING CRACKS FOR STRUCTURAL HEALTH MONITORING

This chapter presents predictive modeling of nonlinear guided waves for structural health monitoring using finite element method (FEM). The nonlinearity of guided waves may serve as an indication for the presence and severity of small size incipient fatigue cracks. Under dynamic loading, the surfaces of these cracks may come into contact under compression and depart from each other under tension. Such cracks, where the surfaces close and open under cyclic loading, are usually referred to as breathing cracks. In our study, the nonlinearity of the guided waves is generated by the interaction with a nonlinear breathing crack. Two nonlinear FEM techniques are used to simulate the breathing crack: (a) element activation/deactivation method; (b) contact analysis. Both techniques are available in the ANSYS software package. The solutions obtained by these two FEM techniques compare quite well. The relationship between the nonlinearity of guided waves and damage severity (crack depth) was shown using a damage index.

## 7.1 INTRODUCTION AND STATE OF THE ART

The nonlinear ultrasonic technique, which uses distinctive higher harmonics and sub harmonics features, has proven to be a promising approach to detect incipient changes which are precursors to structural damage (Jhang 2009; Kruse and Zagrai 2009). The combined use of guided Lamb waves and nonlinear methods is drawing increasing

164

interest because the nonlinear Lamb waves have the advantage of both the sensitivity of nonlinear methods and the large inspection ranges of guided waves.

To date, most studies on nonlinear ultrasonics have been experimental, demonstrating the capability of nonlinear Lamb waves to detect structural damage (Bermes et al. 2007; Jumar et al. 2009; Cantrell 2009; Nagy 1998; Dutta 2009). However, few theoretical predictive studies exist, especially for nonlinear Lamb waves. Generation of the higher harmonics of Lamb waves have been investigated theoretically (Deng 1999; 2003), and the existence of antisymmetric or symmetric Lamb waves at nonlinear higher harmonics has been discussed via the modal analysis approach and the method of perturbation (Srivastava and Lanza Di Scalea 2009). However, these theoretical studies considered only the situations where nonlinearity are present over the whole domain of wave propagation in the material (mesoscopic nonlinearity); other cases of nonlinear wave propagation, such as wave propagation through localized breathing cracks, are also possible.
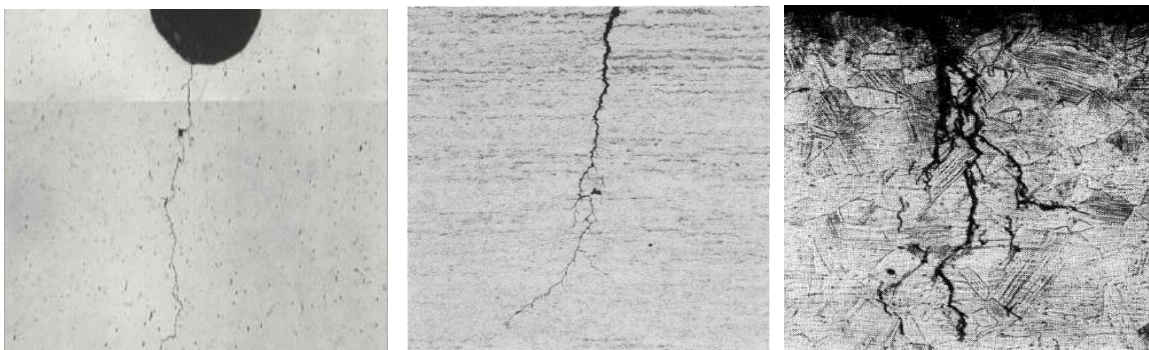


Figure 7.1: Microscopic cracks nucleated at structural surface (Corrosion Testing Lab 2007, www.corrosionlab.com).

When structures are under cyclic fatigue loading, microscopic cracks will begin to form at the structure surface, shown in Figure 7.1. They need to be found before they

grow to the critical size and cause catastrophic failures. In our study, we investigated the characteristics of the inspection waves interacting with this kind of microscopic cracks, especially when they behave as nonlinear breathing cracks under wave cycles.

Figure 7.2 shows the typical breathing crack behavior when ultrasonic waves propagate through it. When ultrasonic waves reach a microscopic crack, the crack can be closed and opened under compression and tension; the compression part of the waves can penetrate the crack, while the tension part cannot. The nonlinear phenomenon lies in the fact that the apparent local stiffness of the crack region changes under tension and compression.
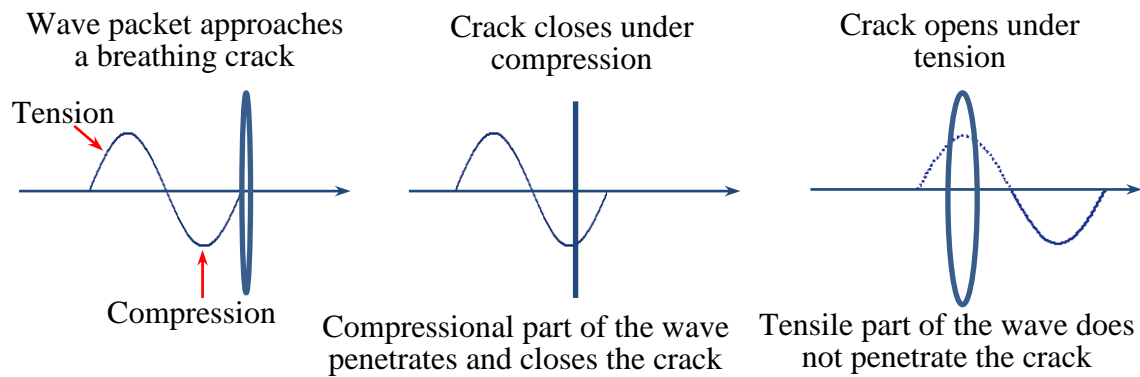
Figure 7.2: Ultrasonic waves propagating through a breathing crack (Shen and Giurgiutiu 2012).

The interaction of elastic waves with clapping mechanisms has been studied in the past. Research on clapping-induced nonlinearities and higher harmonics has been carried out (Richardson 1979; Biwa et al. 2004; 2006); however, most of these investigations aim at the nonlinearity of elastic bulk waves. Our study focuses on the modeling aspect of contact acoustic nonlinearity (CAN) of Lamb waves, which is a localized nonlinear phenomenon of dispersive guided plate waves, and it is different from the previous

theoretical studies of nonlinear Lamb waves (Deng 1999; 2003; Srivastava and Lanza di Scalea 2009).

## 7.2 FINITE ELEMENT SIMULATION OF LAMB WAVES INTERACTION WITH NONLINEAR BREATHING CRACKS

A pitch-catch method may be used to interrogate a plate with a breathing crack which opens and closes under tension and compression. The ultrasonic waves generated by the piezoelectric wafer active sensor (PWAS) propagate into the structure, interact with the breathing crack, acquire nonlinear features, and are picked up by the receiver PWAS. This process is shown in Figure 7.3.
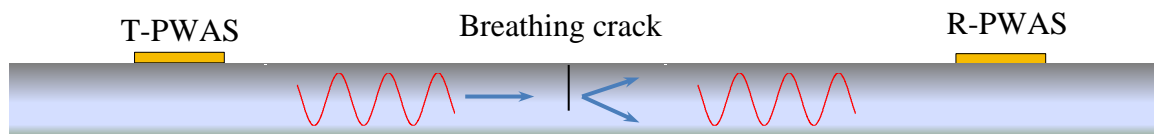


Figure 7.3: Pitch-catch method for the detection of a breathing crack; the mode conversion at the crack is illustrated by the two arrows.

Two methods are used to model the breathing crack: (a) the element activation/deactivation method; (b) contact analysis. The solving scheme and results from both methods are discussed and compared.

### 7.2.1 ELEMENT ACTIVATION/DEACTIVATION METHOD

The element activation/deactivation technique can be described as deactivating and reactivating selected elements according to certain criteria. To deactivate elements, the stiffness matrices of the elements are multiplied by a severely small reduction factor, $\eta$ (usually 1E-6 or smaller), while mass, damping, loads and other such effects are set to zero. Thus, upon deactivation, the element stiffness matrix, mass matrix and associated loads will no longer contribute to the assembled global matrices. It should be noted that the deactivated elements are not removed from the model, but left in place in a dormant

state with a greatly diminished participation. Similarly, when elements are activated, they are not added to the model. Instead, the dormant elements are simply reactivated, recovering their original stiffness, mass, damping, element loads, etc. The assembled global equation will take the following form

Original global equation

$$
\begin{pmatrix} M_{11} & \cdots & 0 \\ \vdots & +M^e & \vdots \\ 0 & \cdots & M_{nn} \end{pmatrix} \begin{Bmatrix} \ddot{u}_1 \\ \vdots \\ \ddot{u}_n \end{Bmatrix} + \begin{pmatrix} C_{11} & \cdots & 0 \\ \vdots & +C^e & \vdots \\ 0 & \cdots & C_{nn} \end{pmatrix} \begin{Bmatrix} \dot{u}_1 \\ \vdots \\ \dot{u}_n \end{Bmatrix} + \begin{pmatrix} K_{11} & \cdots & 0 \\ \vdots & +K^e & \vdots \\ 0 & \cdots & K_{nn} \end{pmatrix} \begin{Bmatrix} u_1 \\ \vdots \\ u_n \end{Bmatrix} = \begin{Bmatrix} Q_1 \\ \vdots + Q^e \\ Q_n \end{Bmatrix}
$$

(7.1)

Deactivated global equation

$$
\begin{pmatrix} M_{11} & \cdots & 0 \\ \vdots & +\Phi & \vdots \\ 0 & \cdots & M_{nn} \end{pmatrix} \begin{Bmatrix} \ddot{u}_1 \\ \vdots \\ \ddot{u}_n \end{Bmatrix} + \begin{pmatrix} C_{11} & \cdots & 0 \\ \vdots & +\Phi & \vdots \\ 0 & \cdots & C_{nn} \end{pmatrix} \begin{Bmatrix} \dot{u}_1 \\ \vdots \\ \dot{u}_n \end{Bmatrix} + \begin{pmatrix} K_{11} & \cdots & 0 \\ \vdots & +\eta K^e & \vdots \\ 0 & \cdots & K_{nn} \end{pmatrix} \begin{Bmatrix} u_1 \\ \vdots \\ u_n \end{Bmatrix} = \begin{Bmatrix} Q_1 \\ \vdots + \Phi \\ Q_n \end{Bmatrix}
$$

(7.2)

where $M^e, C^e, K^e, Q^e$ are the elemental mass matrix, damping matrix, stiffness matrix, and external loads. The reduction factor $\eta$ is very small ($\eta \ll 1$, typically $\eta < 1E-6$). The symbol $\Phi$ denotes a zero matrix or vector. Comparing Eq. (7.2) with Eq. (7.1), it is apparent that the elements, after deactivation, will no longer contribute to the structure, because $\eta K^e \approx [\Phi]$ with $\eta \ll 1$. The nonlinear effect is imparted by the periodical change of matrices $M, C$ and $K$.

The solving scheme for this transient dynamic problem using the element activation/deactivation method is shown in Figure 7.4. The crack status, open or closed, is judged for each calculation step in the transient analysis; calculation configuration of the current step is based on the results of the previous step.

The crack open/close criterion is based on the tension and compression status of the thin layer of nonlinear elements which simulate the breathing crack. When these elements are under tension, the crack is considered open. The criterion is shown in the following equation

$$(U2 - U1 < 0) \cap (\bar{\varepsilon} = \frac{\sum_{1}^{n} \varepsilon_n}{n} < 0) \tag{7.3}$$

where $U1$ and $U2$ are the displacements of the two nodes located on the two edges of the selected element in the crack opening direction. $\bar{\varepsilon}$ is the average strain of the selected elements in the crack opening direction. This criterion is developed based the contact behavior of the breathing crack and through numerical experiments. Details of this criterion can be found in Shen and Giurgiutiu (2012). It should be noted that for mode shapes at high frequency and plate thickness combination (high $fd$ value), the criterion needs to be modified by taking into account more nodes across the crack surface in order to consider the more complicated contact behavior.
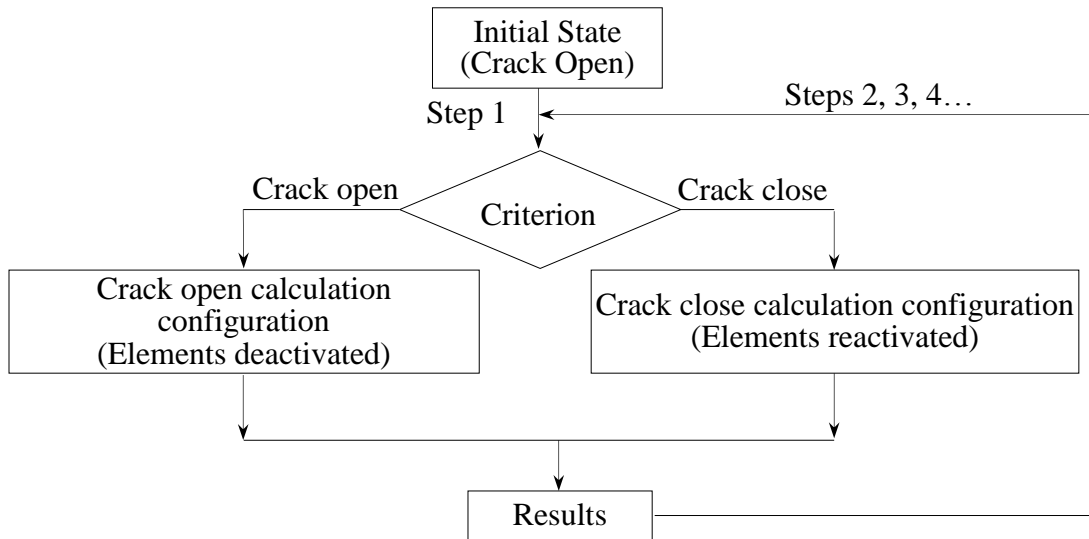


Figure 7.4: Solving scheme of element activation/deactivation method.

### 7.2.2 CONTACT ANALYSIS WITH FINITE ELEMENT METHOD

In the physical world, no penetration will happen between contact surfaces; however, in finite element analysis, hypothetical penetration is allowed to ensure equilibrium. The contact parameters are determined by either (a) Lagrange multiplier or (b) penalty methods. In this research, the penalty method is adopted. The relationship of penetration and contact tractions is illustrated in Figure 7.5, where $k$ is the contact stiffness, $\Delta_N$ and $\Delta_T$ are the normal and tangential penetrations.
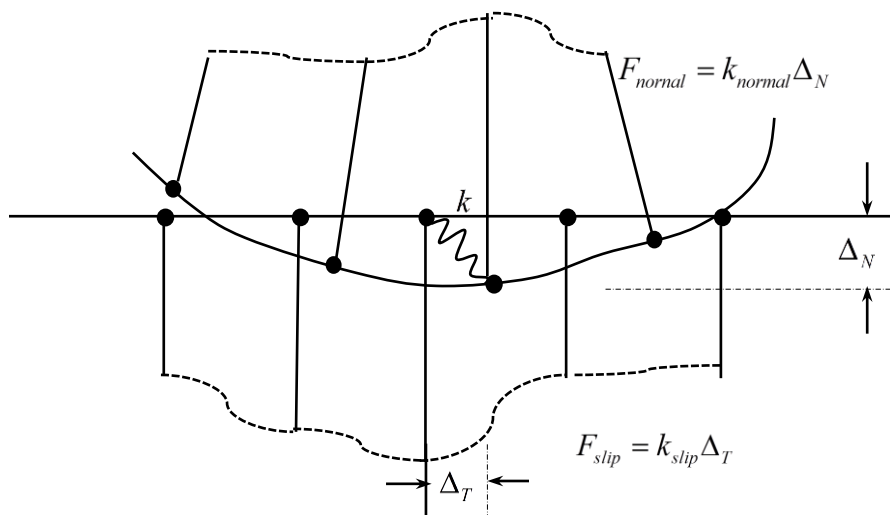


Figure 7.5: Penetration between contact surfaces and contact tractions (Hughes et al. 1975).

The choice of contact stiffness is an important part of contact analysis, because it influences both the accuracy and convergence of the solution, and usually calls for previous experience. When analyzing a contact problem, there is a dilemma: a small amount of penetration will render more accurate results, so we should chose large contact stiffness; however, this may lead to ill-conditioning of the global stiffness matrix and to convergence difficulties. Lower stiffness values can lead to a certain amount of penetration/slip and make the solution easier to converge, but this gives a less accurate

solution. Thus, we are searching for a high enough stiffness that the penetration/slip is acceptably small and render a relatively accurate result, but a low enough stiffness that the problem will be well-behaved in terms of convergence. ANSYS provides a suggested value of contact stiffness, which will be modified by the penalty coefficient to achieve both convergence and accuracy. A common practice is to start from a low contact stiffness which ensures convergence, check if the penetration of the contact surfaces is reasonable, and then increase the penalty coefficient until the surface penetration is reasonably small and ensure solutions between two sequent penalty coefficients do not change. The final contact stiffness used in this study is $7.051 \times 10^{15}$ Pa.

## 7.3 FINITE ELEMENT MODEL FOR PITCH-CATCH ANALYSIS

Figure 7.6 shows the finite element model of a pitch-catch method for detection of a nonlinear breathing crack.
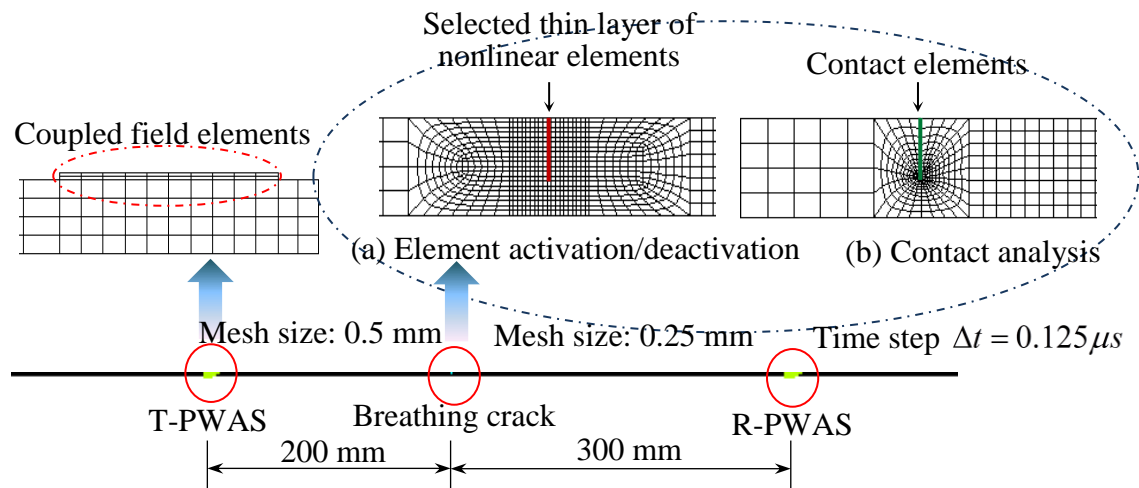


Figure 7.6: Nonlinear finite element model of pitch-catch method for detection of a breathing crack.

Two $7mm \times 7mm \times 0.2mm$ PWAS are considered ideally bonded on a 2 mm thick aluminum plate. The plate is long enough to ensure the received signals are not influenced by boundary reflections. The crack is located 200 mm from the transmitter,

such that the S0 and A0 wave packets will have already separated by the time they arrive at the crack location, therefore the S0 and A0 wave packets interact with the breathing crack individually, which allows us to see how the crack interacts with S0 and A0 waves.

The plate is made of aluminum 2024-T3 with a Young's modulus of 72.4 GPa, a density of 2700 kg/m$^3$, and Poisson's Ratio of 0.33. The APC-850 material properties are assigned to the PWAS as follows

$$\left[ C_p \right] = \begin{bmatrix} 97 & 49 & 49 & 0 & 0 & 0 \\ 49 & 84 & 49 & 0 & 0 & 0 \\ 49 & 49 & 97 & 0 & 0 & 0 \\ 0 & 0 & 0 & 24 & 0 & 0 \\ 0 & 0 & 0 & 0 & 22 & 0 \\ 0 & 0 & 0 & 0 & 0 & 22 \end{bmatrix} GPa \qquad (7.4)$$

$$\left[ \varepsilon_p \right] = \begin{bmatrix} 947 & 0 & 0 \\ 0 & 605 & 0 \\ 0 & 0 & 947 \end{bmatrix} \times 10^{-8} \, F/m \qquad (7.5)$$

$$\left[ e_p \right] = \begin{bmatrix} 0 & 0 & 0 & 12.84 & 0 & 0 \\ -8.02 & 18.31 & -8.02 & 0 & 0 & 0 \\ 0 & 0 & 0 & 0 & 12.84 & 0 \end{bmatrix} C/m^2 \qquad (7.6)$$

where $\left[ C_p \right]$ is the stiffness matrix, $\left[ \varepsilon_p \right]$ is the dielectric matrix, and $\left[ e_p \right]$ is the piezoelectric matrix. The density of the PWAS material is assumed to be $\rho = 7600$ kg/m$^3$.

The finite element model is built under the plane strain assumption. PWAS transducers are modeled with coupled field elements (PLANE13) which couple the electrical and mechanical variables (ANSYS 13.0 Multi-Physics). The plate is modeled with the four node structure element PLANE182 with "element birth and death" capability. A 20 vpp 5-count Hanning window modulated sine tone burst signal centered

at 100 kHz is applied on the top electrode of the transmitter PWAS. The plate is under free boundary condition.

To solve this problem with good accuracy and high efficiency, a meshing strategy of varying density needs to be performed. The maximum acceptable element size and time step to ensure accuracy is shown in the following equations (Moser et al. 1999).

$$l_e = \frac{\lambda_{\min}}{20} \tag{7.7}$$

$$\Delta t = \frac{1}{20 f_{\max}} \tag{7.8}$$

For the excitation centered at 100 kHz, we considered the maximum frequency of interest up to 400 kHz, containing up to the third higher harmonic. The dispersion curve is calculated by solving the Rayleigh-Lamb equation and shown in Figure 7.7(a). The frequency wavelength relationship is obtained using Eq. (7.9) from the dispersion data, and plotted in Figure 7.7(b). The minimum wavelength at 400 kHz appears in A0 mode at 5.478 mm. According to Eq. (7.7), the maximum element size should be 0.275 mm. According to Eq. (7.8), for 400 kHz, the maximum time step is 0.125 microsecond.

$$\lambda = c/f \tag{7.9}$$

Since the mechanical response at the crack zone is very complicated, the crack zone is more densely meshed. The region between the breathing crack and the receiver has a mesh size of 0.25 mm (smaller than 0.275) to accurately depict up to the third higher harmonic. A time step of 0.125 microseconds is adopted. In the element activation/deactivation method, a very thin layer of nonlinear elements (0.1 mm thick) at the crack zone are selected to be deactivated and reactivated. For the contact analysis, the contact pair is constructed using contact elements (CONTA172 and TARGE169).
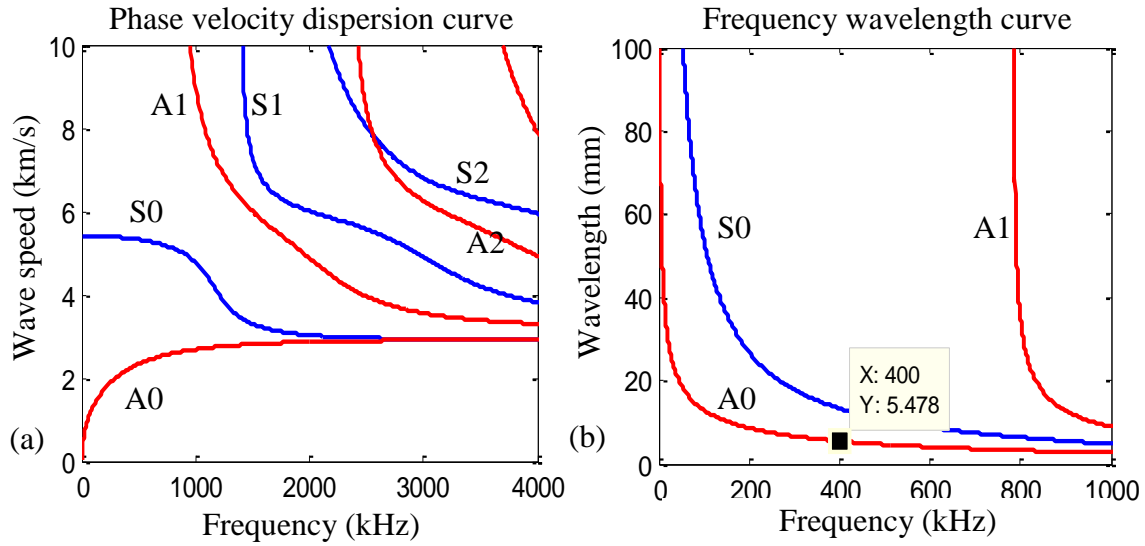
Figure 7.7: (a) Dispersion curve; (b) frequency wavelength curve.

The severity of damage is represented by the number of elements selected to be deactivated and reactivated. We define the damage severity $r = a/h$ ($a$ and $h$ are the crack size and plate thickness respectively). An index of $r = 0.0$ corresponds to a pristine condition, where there is no crack in the plate. In our simulation, we used 20 elements across the thickness at the crack zone. Different damage severities $r = 0.6, 0.5, 0.4, 0.3, 0.2, 0.1$ and $0.0$ are generated by selecting 12, 10, 8, 6, 4, 2 and 0 elements. ANSYS uses an average nodal solution for data post-processing. Hence, the deactivated elements must be excluded from the average process to avoid result contamination.

To highlight the effect of nonlinear wave propagation through a breathing crack, the linear wave propagation through the crack is also investigated.

7.4    FINITE ELEMENT SIMULATION RESULTS AND DISCUSSION

The $r = 0.6$ case is used as a representative for demonstrating Lamb wave interaction with a breathing crack and is shown in Figure 7.8. The same crack behavior

could be observed for both the element activation/deactivation method and contact analysis. It is shown that the tension part of the Lamb waves opens the crack, and the waves do not penetrate through it. On the other hand, the compression part of the Lamb waves closes the crack with collision between crack surfaces; hence, the compression part of the Lamb wave can penetrate into the crack.
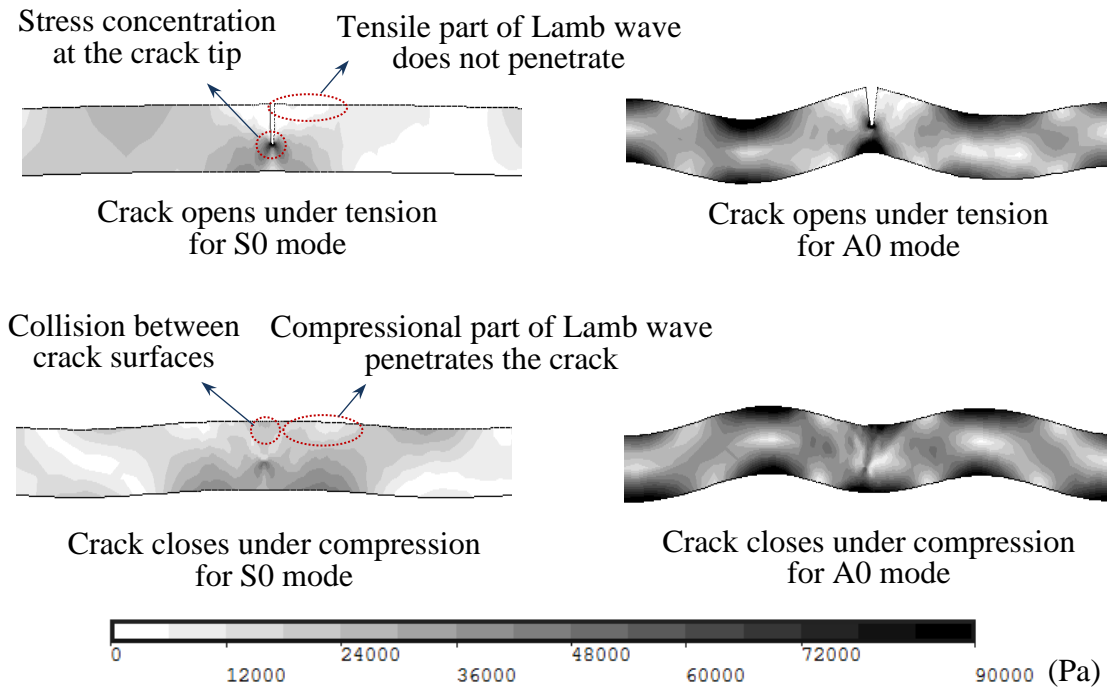


Figure 7.8: FEM simulation of Lamb waves interacting with breathing crack.

Figure 7.9 shows the waveforms of Lamb waves after linear interaction with the crack (Figure 7.9a) and the waveforms of Lamb waves after nonlinear interaction with a breathing crack (Figure 7.9b).

It can be observed that compared with pristine condition, the cracked plate signal has a slight amplitude drop and phase shift in both S0 and A0 packets. Another difference is that a new wave packet appears due to the presence of the crack. This new packet is introduced by mode conversion and contains both S0 packet converted A0 mode, and A0

packet converted S0 mode. The linear crack signal is smooth, but the nonlinear breathing crack signal has small zigzags.
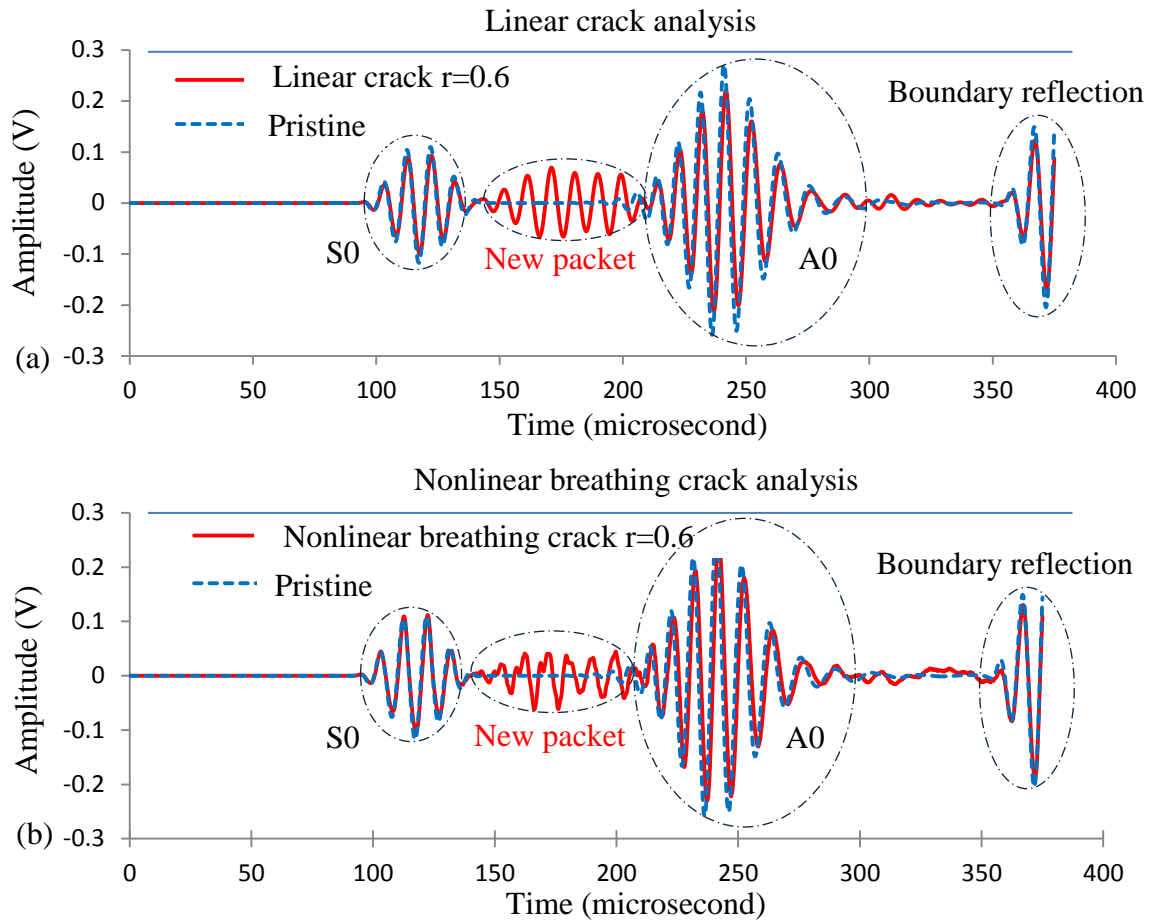


Figure 7.9: Superposed time domain simulation signals at receiver PWAS for pristine (r = 0) and cracked (r = 0.6) cases: (a) linear crack; (b) nonlinear breathing crack.

The S0, A0, and new wave packets were extracted from the whole time-history using a Hanning window and then Fourier transformed. Frequency spectrums of S0, A0, and the new wave packets, with r = 0.6 case for linear crack signal and nonlinear breathing crack signal, are carried out and plotted in Figure 7.10 and Figure 7.11 respectively. For all the wave packets, the pristine signal does not show any higher frequency components. Figure 7.10 shows, for the linear crack case, all the wave packets

show only the fundamental excitation frequency at 100 kHz. It should be noted there are no higher harmonics for linear interaction between Lamb waves and cracks.
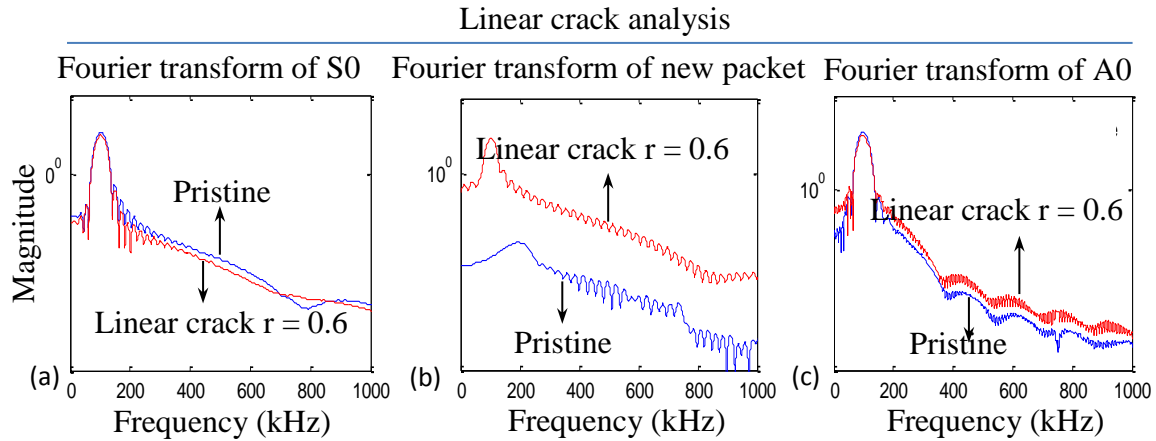


Figure 7.10: Frequency spectrum of the Lamb wave signals after linear interaction with a crack: (a) S0 mode; (b) new packet; (c) A0 mode. Note the absence of higher harmonics.

However, the signal from the breathing crack plate shows distinctive nonlinear higher harmonics. Figure 7.11a shows nonlinear higher harmonics in the S0 wave packet. Since the excitation frequency is centered at 100 kHz, the 102.8 kHz peak corresponds to the excitation frequency, and the 203.1 kHz and 300.5 kHz correspond to 2nd and 3rd higher harmonics respectively. It should be noted that the higher harmonics below 400 kHz can be accurately simulated according to the discussions on the mesh size and time step. The frequency components calculated beyond 400 kHz cannot be correctly described and predicted by the finite element mesh employed. For the A0 wave packet (Figure 7.11c), the first peak corresponds to the excitation frequency, and the 2nd higher harmonic could be clearly observed at 198.2 kHz, but the 3rd harmonic is somehow missing. This phenomenon is due to the tuning effect of PWAS and plate structure combination (Giurgiutiu 2005). The tuning curve shown in Figure 7.11d indicates that at around 300 kHz, where the 3rd harmonic should appear, the A0 mode reaches its rejection

177

point; in other words, for the given PWAS and plate structure, this frequency could not be detected due to the rejection effect at the receiver PWAS. Analysis of the observed "new packet" (Figure 7.11b) also reveals the nonlinear higher harmonics pattern. In this new packet, the feature of nonlinear higher harmonics seems to be more obvious than in the S0 and A0 packets, and the spectral amplitudes of the higher harmonics are closer to that of the excitation.
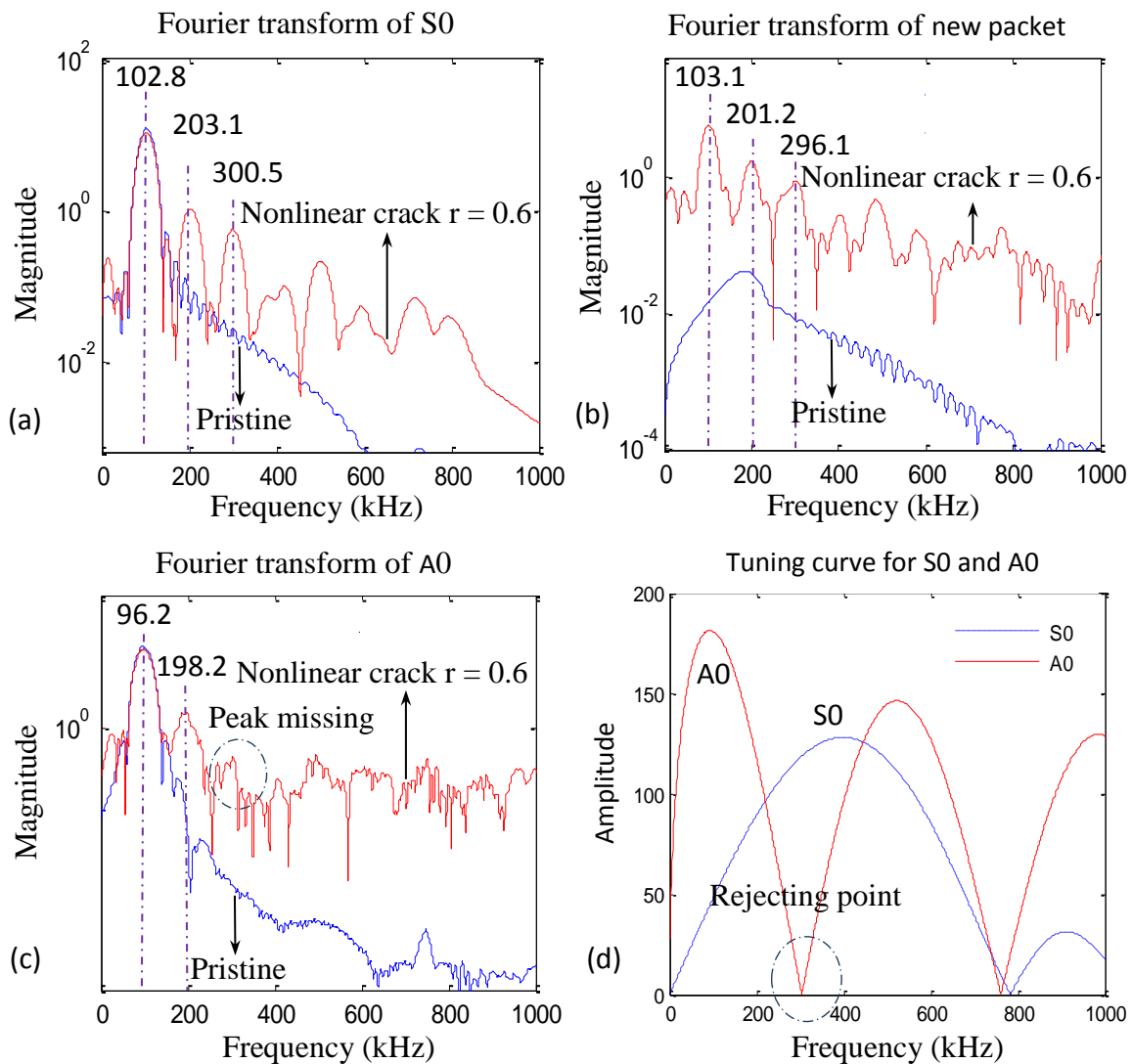


Figure 7.11: Frequency spectrum of the Lamb wave signals after nonlinear interaction with a crack: (a) S0 mode; (b) new packet; (c) A0 mode; (d) tuning curves for A0 and S0

modes explaining the missing A0 peak in (c). Note the presence of distinctive nonlinear higher harmonics.

To diagnose the severity of this nonlinear damage, the results of all the damage severities are compared. The square root of the spectral amplitude ratio of the second harmonic to the excitation frequency is adopted to show the degree of signal nonlinearity, which may serve as a damage index, i.e.

$$DI = \sqrt{\frac{A(2f_c)}{A(f_c)}} \tag{7.10}$$

where $A(f_c)$ and $A(2f_c)$ denote the spectral amplitude at the excitation frequency and at the second higher harmonic.
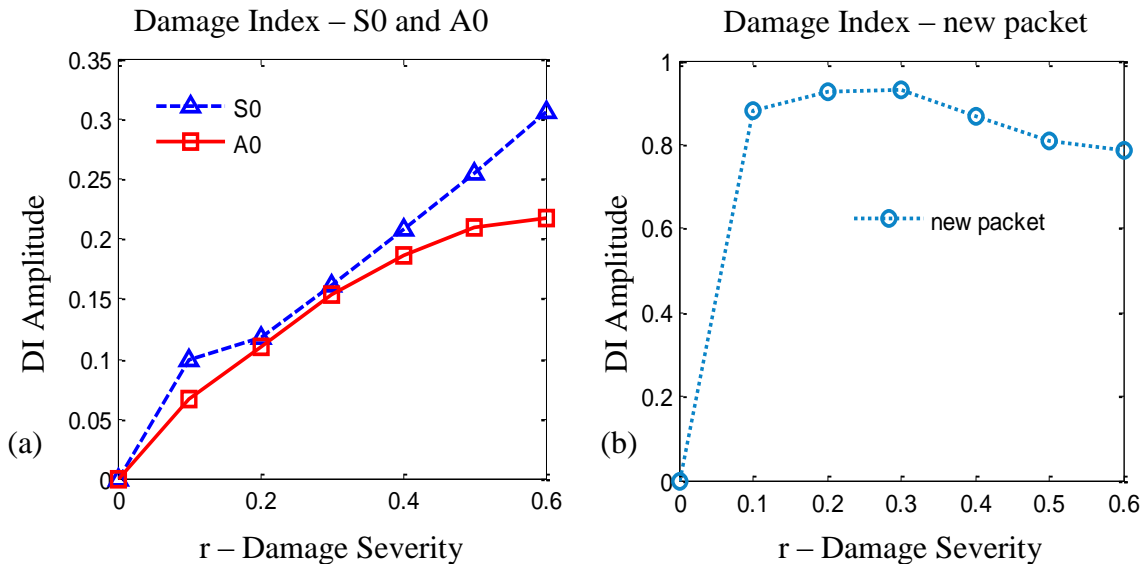


Figure 7.12: Damage severity index.

The variation of DI with crack damage intensity is shown for S0 and A0 packets in Figure 7.12a and for the new packet in Figure 7.12b. It can be observed that the amplitude ratio DI is relatively small for both S0 and A0 packets, but it is quite big for the new wave packet even at small damage severity. The DI for S0 and A0 has a

179

monotonically increasing relationship with the crack damage intensity. So the DI from the new packet could serve as an early indicator for the presence of a breathing crack, and the DI for the S0 and A0 packets can serve as an indicator of damage severity.

7.5 COMPARISON OF NUMERICAL RESULTS BETWEEN THE TWO NONLINEAR FEM ANALYSIS METHODS

The numerical results from the element activation/deactivation method and the contact analysis are compared. The superposed time domain simulation signals and frequency spectrum from the two finite element methods, for $r = 0.6$ case, are shown in Figure 7.13a and Figure 7.13b.

It can be observed that the solutions from these two methods agree well with each other. The S0 packets match well; however, the A0 and the new packet have slight phase and amplitude difference. In the frequency spectrum, it could be noticed that at a lower frequency range (within two harmonics range) the two methods have a good match, but at higher frequency they deviate from each other.

The difference between the two solutions are measured and presented by the non-dimensional $L_2$ norm

$$\|u_e - u_c\| = \sqrt{\frac{\sum_1^N (u_e - u_c)^2}{\sum_1^N u_c^2}} \tag{7.11}$$

where $u_e$ and $u_c$ are the solutions from the element activation/deactivation method and contact analysis; $N$ is the number of solution points in the time domain signal. The L2 norm values for $r = 0.1, 0.2, 0.3, 0.4, 0.5, 0.6$ are plotted in Figure 7.14. It can be observed

that for all the damage severity cases, both methods match consistently well with each other.
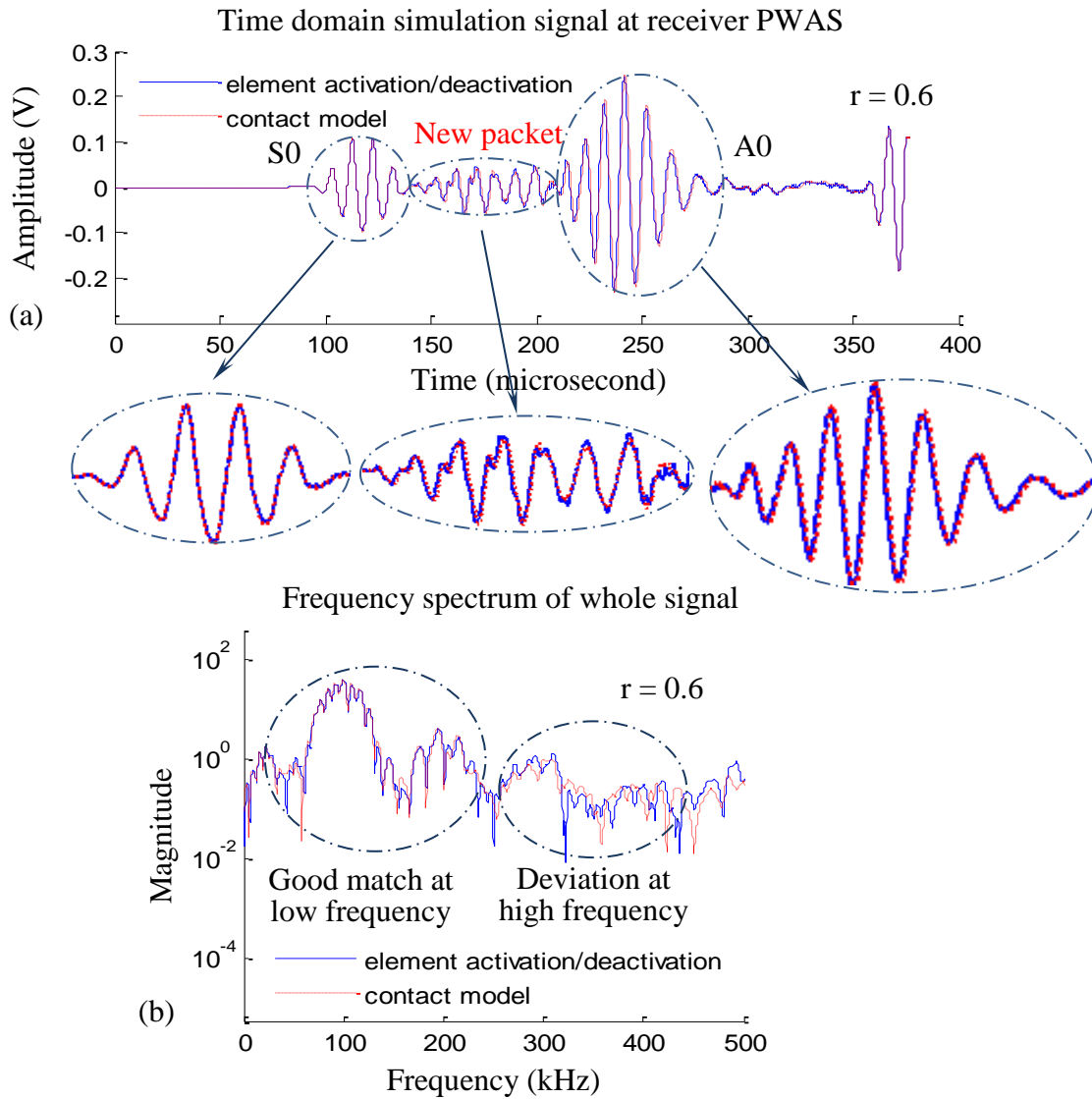


Figure 7.13: Comparison between signals from element activation/deactivation method and contact analysis (a) time domain signal; (b) frequency spectrum.
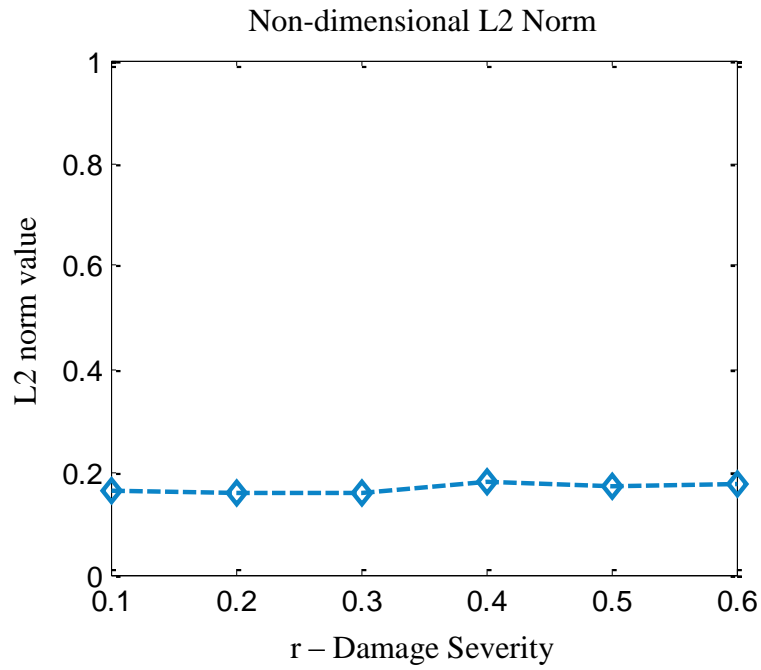
Figure 7.14: Difference between two solutions for various damage severities.

# CHAPTER 8
## HEALTH MONITORING OF BOLTED LAP JOINTS USING NONLINEAR ULTRASONICS

This chapter presents a theoretical and experimental study of nonlinear ultrasonic spectroscopy method for health monitoring of bolted lap joints. This study is aimed at the monitoring of bolt load status through nonlinear features of ultrasonic guided waves. The interrogating waves generated by a transmitter piezoelectric wafer active sensor (T-PWAS) propagate along the structure, interact with the lap joint contact surfaces, carry the information of bolt load and are picked up by a receiver PWAS (R-PWAS). The contact acoustic nonlinearity (CAN) introduced by the interaction between guided waves and contact surfaces serves as an index for the assessment of bolt load status. Contact finite element models (FEM) are built to simulate the contact behavior of the lap joint surfaces under ultrasonic cyclical loading. The relationship between the bolt load and the CAN is investigated. Experiments on a bolted lap joint are carried out to verify the FEM predictions. The inherent nonlinearity of the electronic equipment (function generator, amplifier, etc.) is addressed. Scanning Laser Doppler Vibrometry (SLDV) is used to visualize the wave propagation through the lap joint, and the results are compared with FEM simulations. Nonlinear effects such as higher harmonics are observed from the FEM predictions and the experimental results.

8.1     INTRODUCTION AND STATE OF THE ART

Bolted lap joints are widely used to connect structural components. The loosening of a bolt may result in instant structural failure or a progressive level of fatigue on neighboring fasteners. Thus, a structural health monitoring (SHM) strategy is desired for bolt load condition monitoring.

A significant amount of research has been carried out aimed at developing SHM techniques for bolt load monitoring using ultrasonic waves. An attenuation based method relates the transmitted wave energy with the bolt preload level (Yang and Chang 2006). A wave propagation delay method relates the relative delay of waves with the applied torque (Zagrai et al. 2008). Numerical studies have been done to establish computational setup for SHM of bolted lap joints (Doyle et al. 2011). Linear and nonlinear finite element models were proposed to investigate Lamb wave interaction with bolted lap joints (Bao et al. 2013). Nonlinear ultrasonic techniques when compared with traditional linear methods are found to be more sensitive to incipient changes with distinctive sub and higher harmonics and side band effects (Amerini and Meo 2011); however, the nonlinear techniques still leave many aspects to be investigated before they can be implemented in an SHM system. This chapter discusses the nonlinear ultrasonic spectroscopy method, both theoretically and experimentally, for the application of bolted lap joints load status monitoring.

8.2     MODELING OF WAVE PROPAGATION THROUGH BOLTED LAP JOINTS

In this section, a static to transient finite element solving scheme was put forward to simulate wave propagation through bolted lap joints under various bolt loads. We studied the mechanism of contact acoustic nonlinearity and its dependence on bolt load

pressure using a simplified 2-D finite element model. Then a 3-D finite element simulation was carried out to predict the experimental wave signals.

## 8.2.1 A STATIC TO TRANSIENT FINITE ELEMENT SOLVING SCHEME

Doyle et al. (23011) investigated the finite element setup of wave propagation through bolted lap joints. They adopted the conventional transient analysis in their simulation and found a pulse wave generated by the bolt load applied to the lap joints. This is because the transient analysis regards the bolt load as an instant pressure which will cause transient effects by deforming the loading area which propagates into the structure. To avoid the influence of the initial pulse wave, the authors reported that they need to wait for the pulse wave to damp out and then apply the interrogating signal. This conventional solving scheme for such specific problems has two main disadvantages: (1) the calculation time is long due to the delay from the pulse wave; (2) the simulation deviates from the actual situation where the bolt load is a static pressure.

To better approximate the real situation and avoid the long delay time between the application of the bolt load and the signal generation, we put forward the static to transient solving scheme. Figure 8.1 shows the flow chart of conventional transient finite element analysis and our static to transient solving scheme (Shen et al. 2013).

It can be observed that in conventional transient analysis (Figure 8.1a) the time integration is always on, which will take the pressure as an initial loading. In contrast, the static to transient solving scheme (Figure 8.1b) turns off the time integration on the first step when the pressure is applied on the structure. Thus, the first step is calculated in the transient solver as a static problem and serves as an initial condition for the later steps. On the second step, the time integration is turned on and a full transient analysis is started

185

with the initial condition from the first step. Then PWAS excitation is applied. By switching off and on the time integration in the transient analysis, we achieved the static to transient solving scheme. This allows us to treat the pressure loading from the bolt as an initial condition similar to the real situation; we also do not need the redundant waiting time for PWAS excitation.

(a) Conventional Transient Analysis

| Time Integration On | → | Pressure Loading | → | Pulse Wave |

| Sensing Signal | ← | PWAS excitation |

(b) Static to Transient Solving Scheme

| 1st Step: Time Integration Off (Static Analysis) | → | Pressure Loading | → | Initial Condition |

| 2nd – Nth Step: Time Integration On (Full Transient Analysis) |

| Sensing Signal | ← | PWAS excitation |
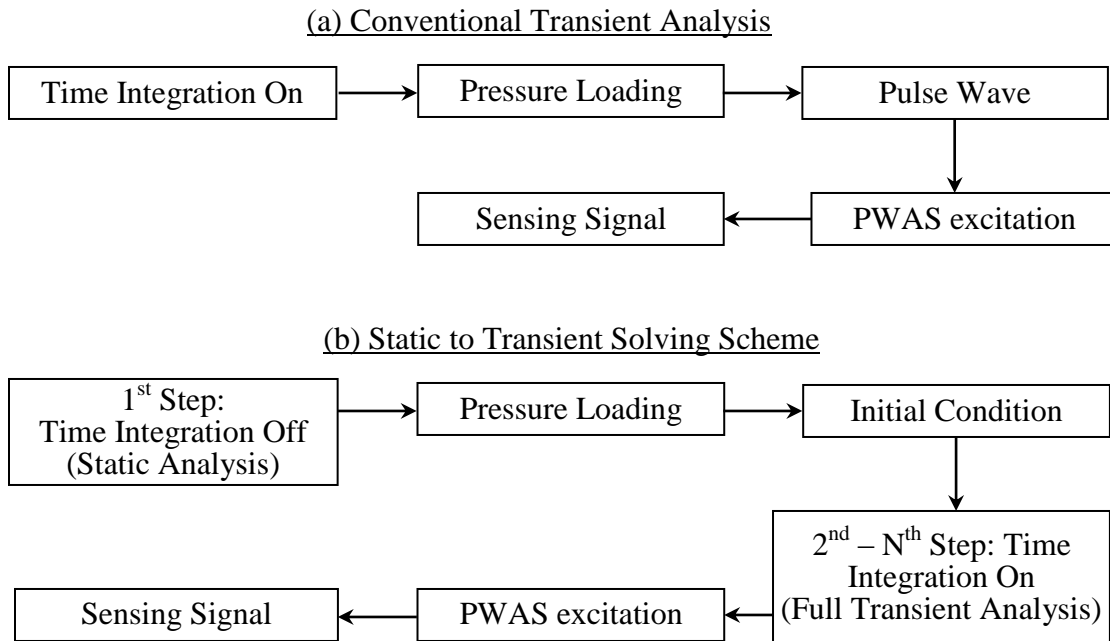
Figure 8.1: (a) conventional transient analysis; (b) static to transient solving scheme.

8.2.2  2-D FEM FOR STUDYING NONLINEARITY GENERATION MECHANISM

To understand the mechanism of nonlinearity generation and its relationship with normal pressure on the contact surfaces, 2-D finite element models were built to simulate: (1) pressure wave propagation through contact surfaces subjected to normal clamping pressure; (2) 1-D Lamb wave propagation through a bolted lap joint under various bolt loads.

8.2.2.1 Contact Acoustic Nonlinearity under Various Contact Surface Pressures

Figure 8.2 shows the 2-D finite element model of bulk wave propagation through contact surfaces. The excitation was a 5-count 1 MHz Hanning window modulated pressure tone burst. The maximum pressure of the excitation was set to 1 MPa peak to peak. The uniformly distributed pressure was applied on top of the model to create normal contact pressure between the contact surfaces. The static pressure was increased from 0 to 500 kPa by 50 kPa steps to see the relationship between transmitted wave nonlinearity and normal contact or clamping pressure between contact surfaces. As shown in Figure 8.2, the contact surfaces under pressure presented two wave transmission modes: (1) breathing surfaces where the pressure wave is strong enough to open and close the contact surfaces; this wave transmission behavior will introduce contact acoustic nonlinearity (CAN); (2) closed surfaces where the contact surfaces stay closed under the applied normal pressure, where wave transmission will not exhibit nonlinearity.
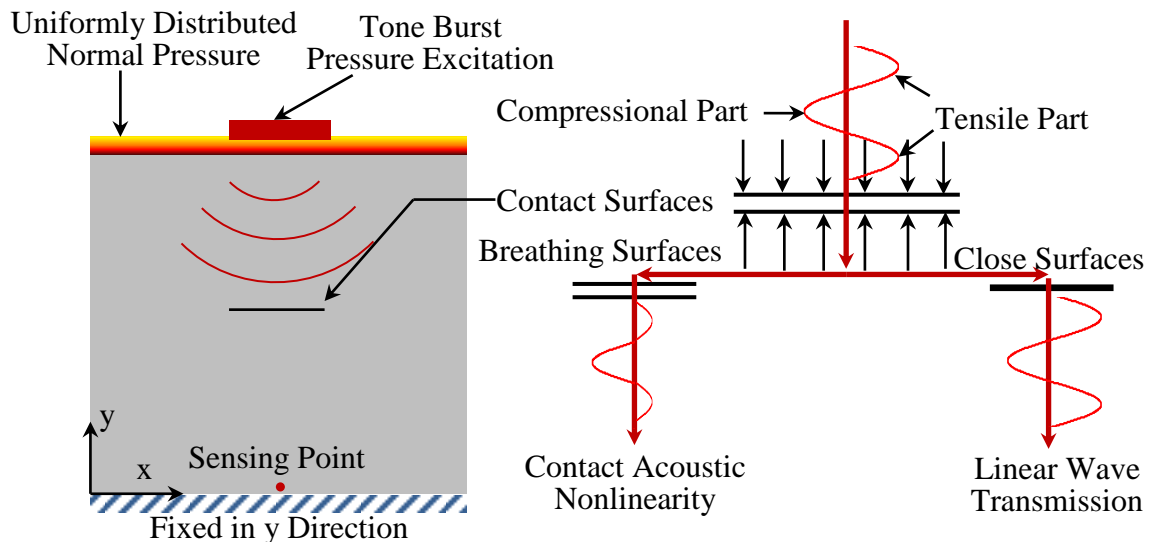


Figure 8.2: Finite element model for CAN mechanism study.

Figure 8.3 shows that the pressure excitation generated two wave packets: (1) a pressure wave which travels with a faster speed; (2) a shear vertical wave which travels more slowly. When the pressure wave arrived at the contact surface, it interacted with the surfaces, after this interaction a clear nonlinear wave pattern could be observed in the transmitted wave packet.
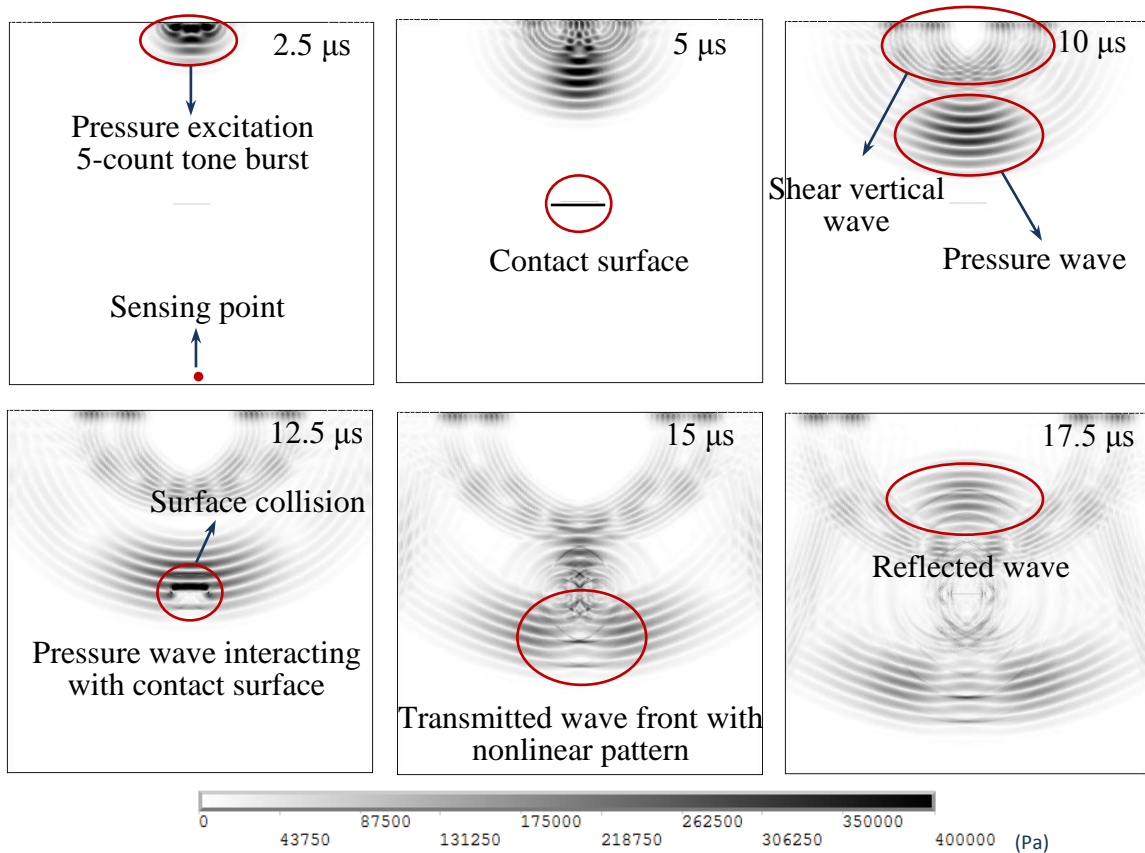


Figure 8.3: Simulation of bulk wave propagation through contact surfaces.

Figure 8.4 shows the sensing signal from simulation. It can be observed that the waveform is heavily distorted, the compressional part presented high amplitude pressure from surface collision. The maximum pressure is 733 kPa, which is higher than the excitation amplitude of 500 kPa, and the tensile amplitude decreased significantly.
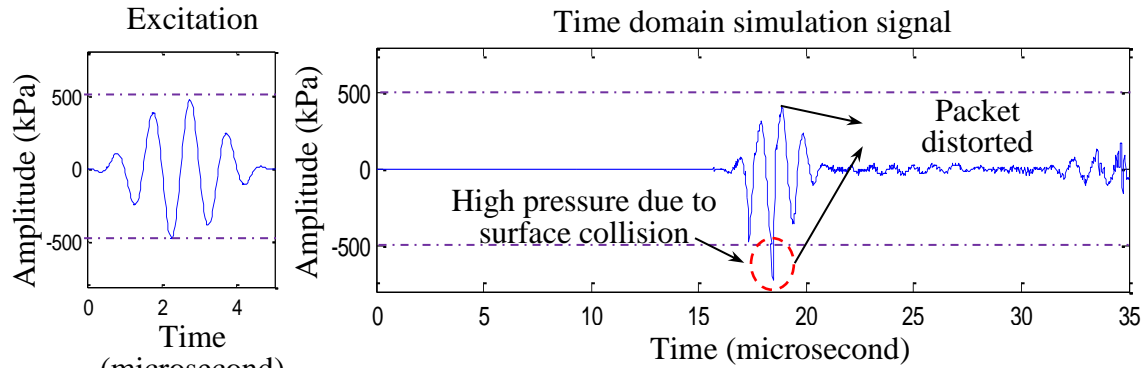
Figure 8.4: Time domain signal of bulk wave propagation through contact surfaces.
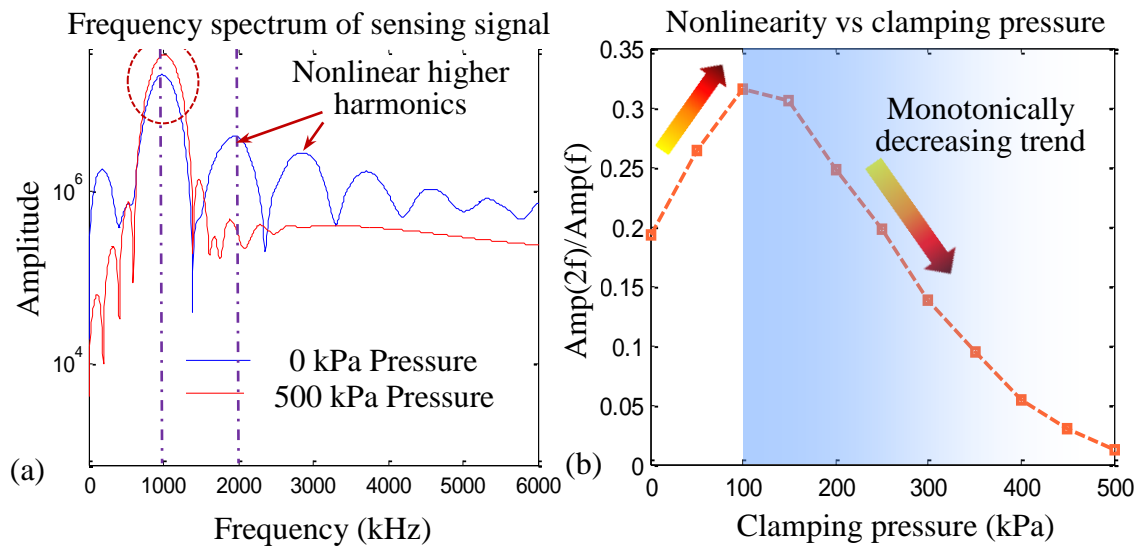


Figure 8.5: (a) frequency spectrum of simulation signals; (b) nonlinearity index vs clamping pressure.

The frequency spectrum of the received pressure wave signal is shown in Figure 8.5a. The nonlinearity is presented by the spectral amplitude ratio of the second harmonic to the excitation. The second higher harmonic can be clearly observed for the 0 kPa clamping pressure case, but for the 500 kPa case, where the clamping pressure equals the amplitude of the excitation wave, no nonlinearity is shown. It can also be noticed that with higher clamping pressure the transmitted wave power presented by the spectrum

amplitude is higher than the lower clamping pressure level cases. Figure 8.5b shows that the nonlinearity goes up with the clamping pressure first for a short range, then decreases monotonically from 100 kPa to 500 kPa reaching 0. Thus, we can deduce that when the lap joint becomes loose, the clamping pressure lies in the monotonic region. An increasing nonlinearity index may indicate the loosening of the bolt load.

8.2.2.2 2-D FEM of Bolted Lap Joint

After investigating the bulk wave and clamping surface interaction, we continued our study with a simplified 2-D contact finite element model in order to understand the nonlinearity from the interaction between guided Lamb waves with bolted lap joints. Figure 8.6 shows the simplified 2-D model of a bolted lap joint.
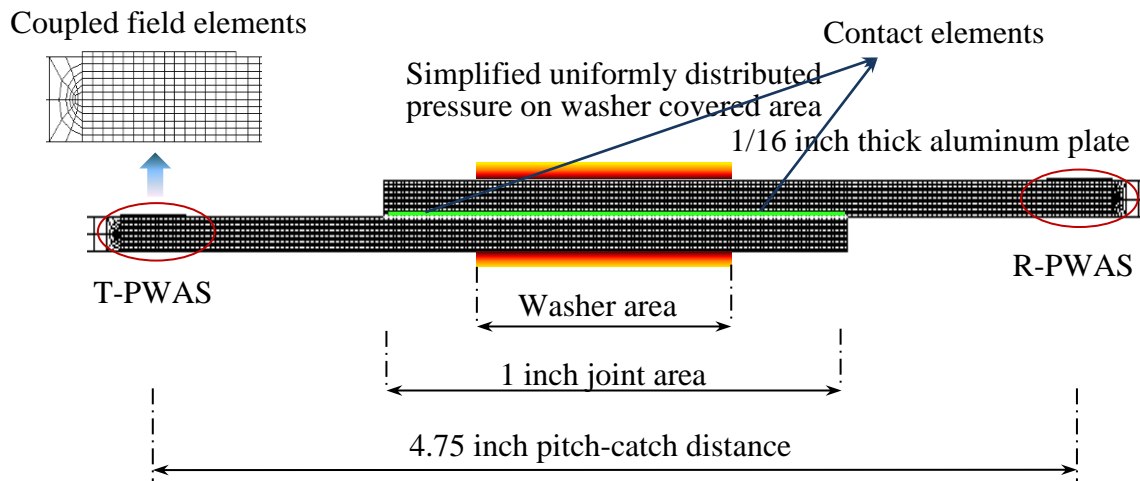


Figure 8.6: Simplified 2-D finite element model for nonlinear mechanism study.

PLANE13 coupled field elements were used to simulate the piezoelectric wafer active sensors. The PLANE182 solid structural elements were used to model the bolted lap joint. The bolt load was converted to pressure from the washer. Contact elements CONTA172 and TARGE169 were used to construct the contact pair to simulate the contactor and target of the contact surface.

To introduce nonlinearity, the wave power must be strong enough to interact with the contact surface; therefore, a 100 vpp tone burst is used as the excitation signal. From the experiments on lap joint monitoring, it was determined that the A0 mode has better sensitivity in this application. In addition, a narrow-band excitation and response is desired to show clear frequency component peaks. Thus, a 20 count Hanning window modulated tone burst centered at 25 kHz was used to send a strong A0 mode Lamb wave through the lap joint. Figure 8.7a shows the excitation signal used in this study; Figure 8.7b shows the typical sensing signal at the R-PWAS.

The frequency spectrum of the sensing signal is shown in Figure 8.8a; the nonlinear index and bolt load relationship is shown in Figure 8.8b. It can be observed that at low torque values (low clamping pressure) there are nonlinear higher, while at high torque levels (high clamping pressure) the nonlinearity disappears. The nonlinear index or nonlinearity of the signal goes down with an increasing torque load; at high torque values, the nonlinearity disappears.
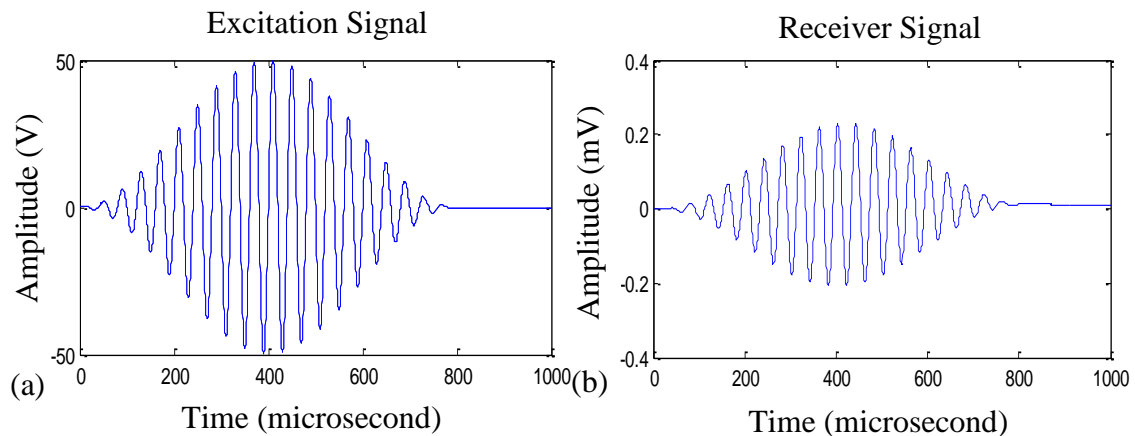


Figure 8.7: (a) Excitation Signal; (b) Receiver Signal.
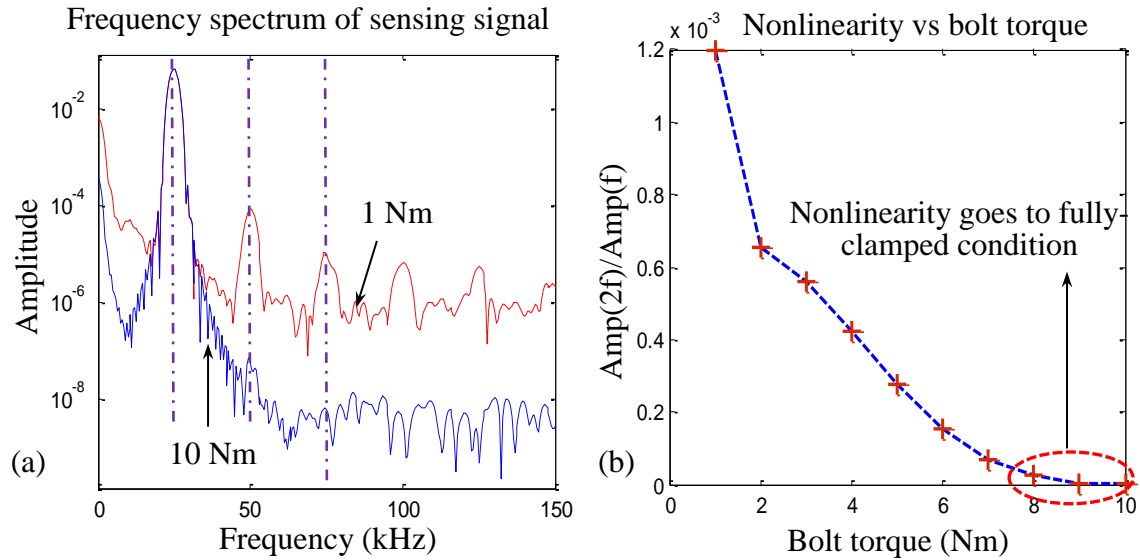
Figure 8.8: (a) Frequency spectrum of sensing signal; (b) Nonlinear index vs torque load.

### 8.2.3    3-D FEM FOR COMPARISON WITH EXPERIMENTS

The real bolted lap joint geometry is more complicated than what a 2-D FEM can capture. For the purpose of comparing with experiments, we conducted 3-D FEM simulations. Figure 8.9 shows the 3-D finite element model for studying the wave interaction with a bolted lap joint. The structure is made of two 11 inches long, 2 inches wide and 1/16 inch thick aluminum 6061 plates. The lap joint has an overlap of 1 inch, so that the total overlap area is 2 square inches. Two PWAS transducers are placed symmetric to the bolt line. The distance between the two PWAS transducers is 4.75 inches.

PWAS transducers are modeled with coupled field elements (SOLID5) which couple the electrical and mechanical properties to simulate piezoelectric material. The contact surfaces are modeled with a contact pair (CONTA174 and TARGE170). The transmitter PWAS (T-PWAS) is excited with a Hanning window modulated sine tone

burst (36 kHz 20 counts 50 Vpp). The bolt load is applied through the pressure loading on the washer area. The pressure is calculated from Eq. (8.1)

$$P = \frac{T}{kdA} \tag{8.1}$$

where $P$ is the pressure, $T$ is the applied torque, $k$ represents the torque coefficient which depends on a variety of parameters including but not limited to geometry and friction of the threads, $d$ is the nominal diameter of the bolt, and $A$ is the washer area.
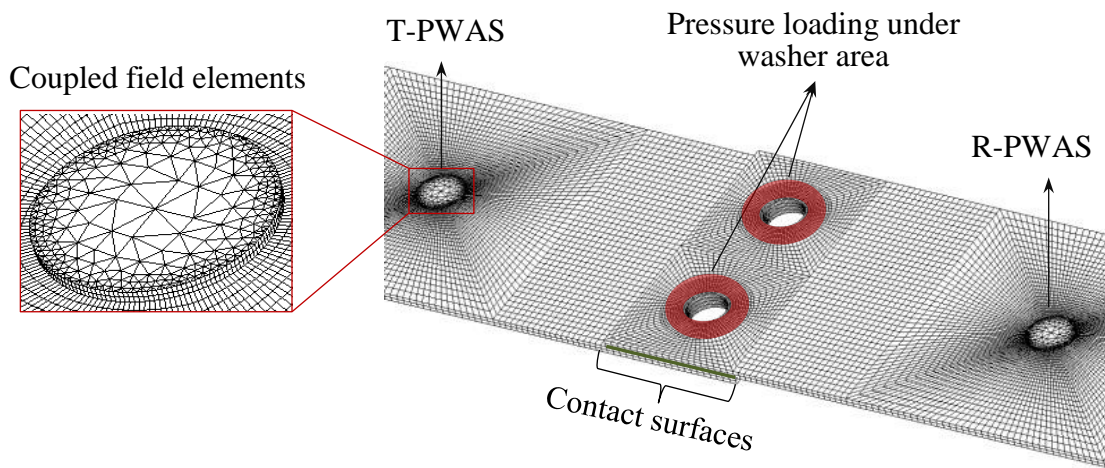


Figure 8.9: 3-D finite element model of the bolted lap joint.

The applied torque is changed from 5 lb-in up to 50 lb-in by steps of 5 lb-in to simulate different situations of bolt load. The ultrasonic waves generated by the T-PWAS propagate along the lap joint, interact with the joint contact surfaces and are picked up by the R-PWAS. The wave signals are recorded, analyzed and then compared with experimental results.

8.3    ACTIVE SENSING EXPERIMENTS FOR BOLT LOAD MONITORING

In this section, we will introduce the experimental procedure. The linear relationship between the applied torque and the washer pressure were verified. A pitch-

catch active sensing method was used to interrogate the bolted lap joint. A Scanning Laser Doppler Vibrometer (SLDV) was used to visualize the field of wave propagation through the bolted lap joint and compare with the 3-D FEM simulation.

## 8.3.1 RELATIONSHIP BETWEEN APPLIED TORQUE AND BOLT LOAD

A torque wrench (Check-line DTL-100i) is used to apply specific torque to the bolts. The torque range measures the applied torque with a resolution of 0.1 lb-in, and the maximum torque load is rated at 106 lb-in. We also use two bolt sensors (Omega LC901) to directly measure the clamping force from the bolt. The bolt sensors are capable of measuring force up to 2000 lb force, with an accuracy of +/-3.5% full scale output. A calibration experiment was performed to evaluate the relation between the applied torque and the actual load in the bolted joint. Figure 8.10 shows the torque wrench and bolt load sensor used in this study. Figure 8.11 shows the linear relationship between the applied torque and the bolt load, which can be described by Eq. (8.1).

Check-line DTL-100i torque wrench

Omega LC901 bolt load sensor



Figure 8.10: Check-line DTL-100i torque wrench and Omega LC901 bolt load sensor.

## 8.3.2 PWAS PITCH-CATCH MONITORING OF BOLT LOAD

The experimental setup for a pitch-catch nonlinear ultrasonic experiment is shown in Figure 8.12. A Hanning window modulated sine tone burst signal (36 kHz 20 counts)

194

is generated by the HP 33120A function generator. This signal is then amplified by an HAS 4014 amplifier to 50 Vpp and applied to the T-PWAS. The T-PWAS converts the electrical energy into mechanical energy and generates ultrasonic guided waves which interact with the bolted lap joint. The interrogating waves are finally picked up by the R-PWAS, where the mechanical energy is converted back into an electrical signal and recorded by the Tektronix TDS5034B oscilloscope.

Linear relationship between applied torque and bolt load

$$y = 0.0088x + 0.0722$$
$$R^2 = 0.997$$
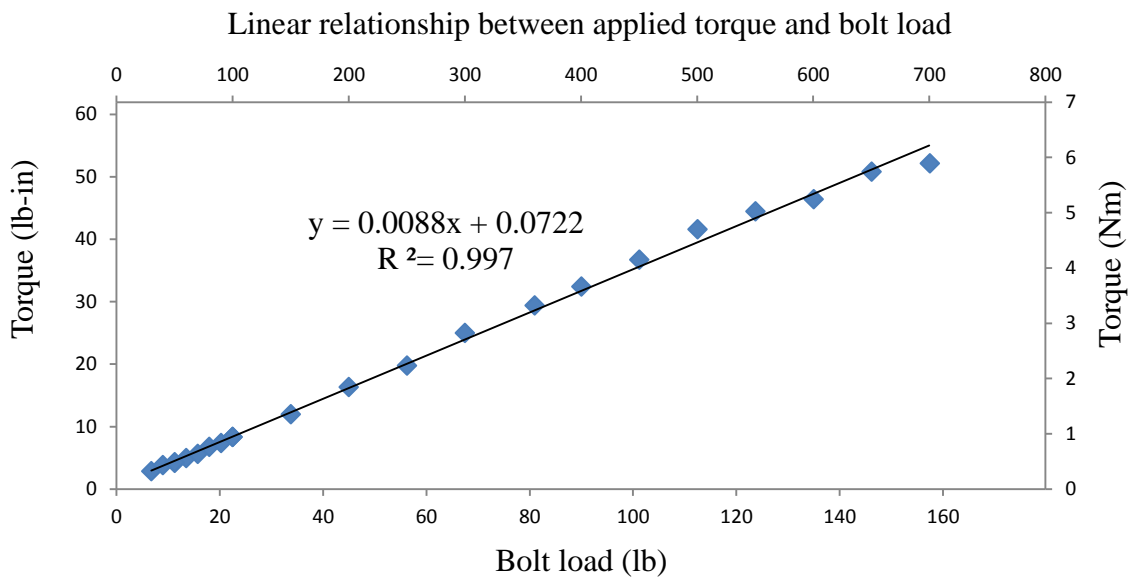
Figure 8.11: Linear relationship between applied torque and bolt load.
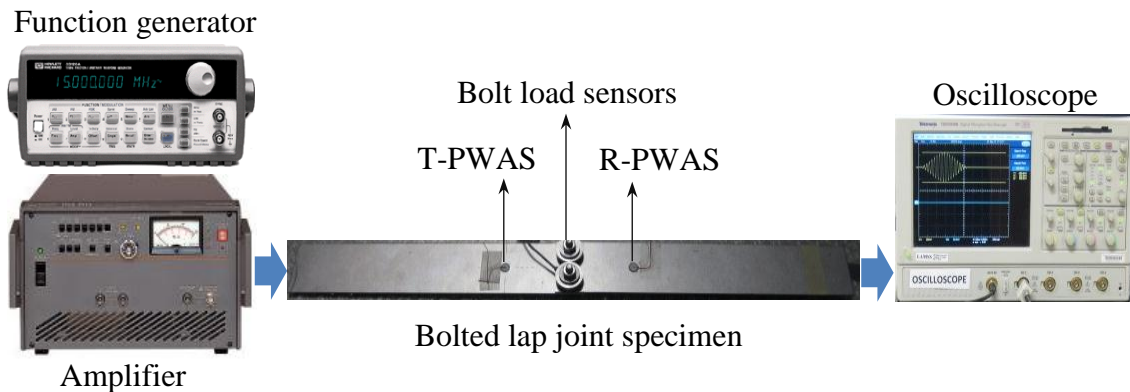
Figure 8.12: Experiment setup for pitch-catch active sensing of the bolted lap joint.

### 8.3.3 WAVE FILED VISUALIZATION WITH SCANNING LASER DOPPLER VIBROMETER

To visualize the wave propagation through the bolted lap joint structure and compare with 3-D FEM predictions, the Polytec PSV-400 Scanning Laser Doppler Vibrometer is used to capture the propagating wave field. The experimental setup is shown in Figure 8.13. The excitation signal generated by the HP 33120A function generator and HAS 4014 amplifier is applied to the T-PWAS. The SLDV scans the specimen surface, and measures the out-of-plane vibration velocity during wave propagation. The out-of-plane wave field is then visualized by post processing of the scanning data. The reflective tape is used to enhance the surface reflection and improve the visualization quality.
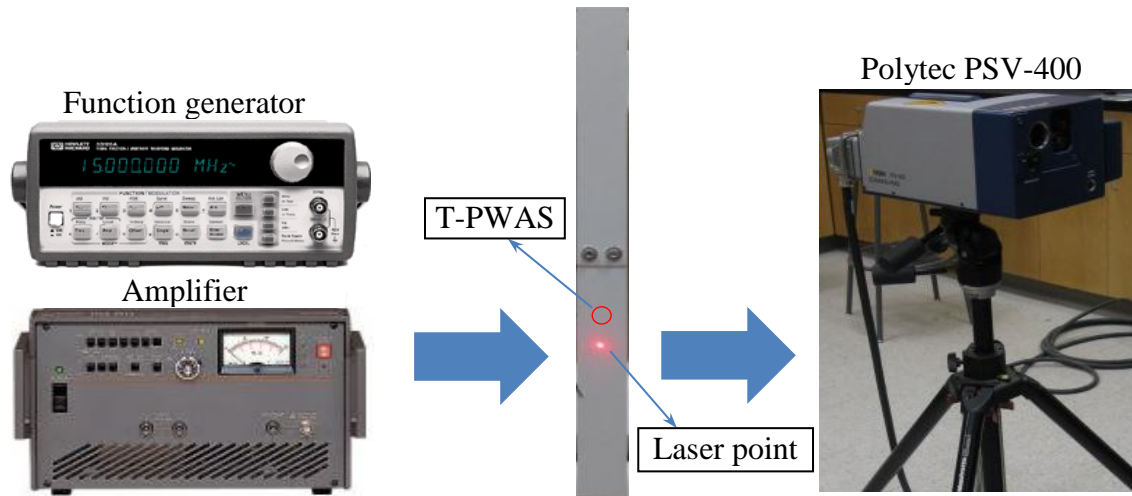


Figure 8.13: Experiment setup for wave propagation visualization.

### 8.4 RESULTS AND DISCUSSION

### 8.4.1 WAVEFORM AND WAVE FIELD COMPARISON BETWEEN FEM AND EXPERIMENTS

Figure 8.14 shows the snap shots of simulation results. It can be observed that the washer loading areas are subjected to a high level of stress. Guided ultrasonic waves generated by the T-PWAS interact with the lap joint, and the contact surfaces are closed

196

and opened under the cyclic wave excitation. The total area of contact surface changes while the interrogating waves pass through the lap joint. When contact surfaces are closed, the lap joint reacts with the waves like a continuous medium. However, when contact surfaces are partially opened, the non-contact area cannot let the waves pass through, and the lap joint acts as a discontinuous medium. The nonlinearity of the received wave signal lies in the fact that the apparent local stiffness of the lap joint changes under cyclic wave excitation. It is important to note that under a higher torque level, the contact surface clapping phenomenon will degrade.
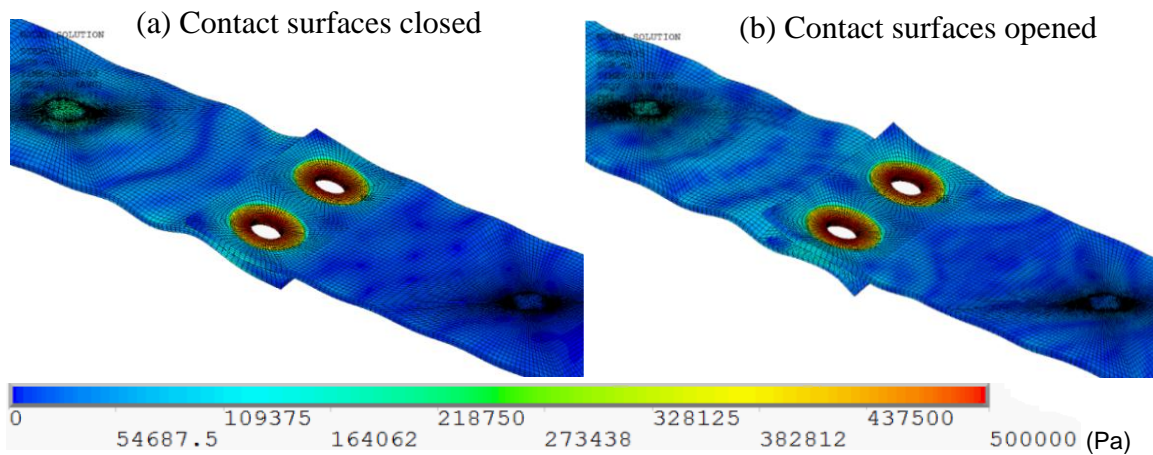


Figure 8.14: Wave interaction with the lap joint for 10 lb-in loading condition: (a) contact surfaces closed; (b) contact surfaces opened.

Figure 8.15 presents the comparison between simulation and experimental waveforms for a torque load of 10 lb-in. It can be observed that the waveforms are in good agreement with each other. It should be noted that the experimental waveform is found to be very sensitive to the lap joint condition. Fine tuning of the plate and bolt placement were used to achieve the results shown in Figure 8.15. The wave amplitudes of the multi-physics FEM simulation and the experiment differ from each other by a factor

around 50. Normalization to the maximum amplitude is used to compare the waveforms from the experiment and simulation.

Comparison between simulation and experiment waveforms
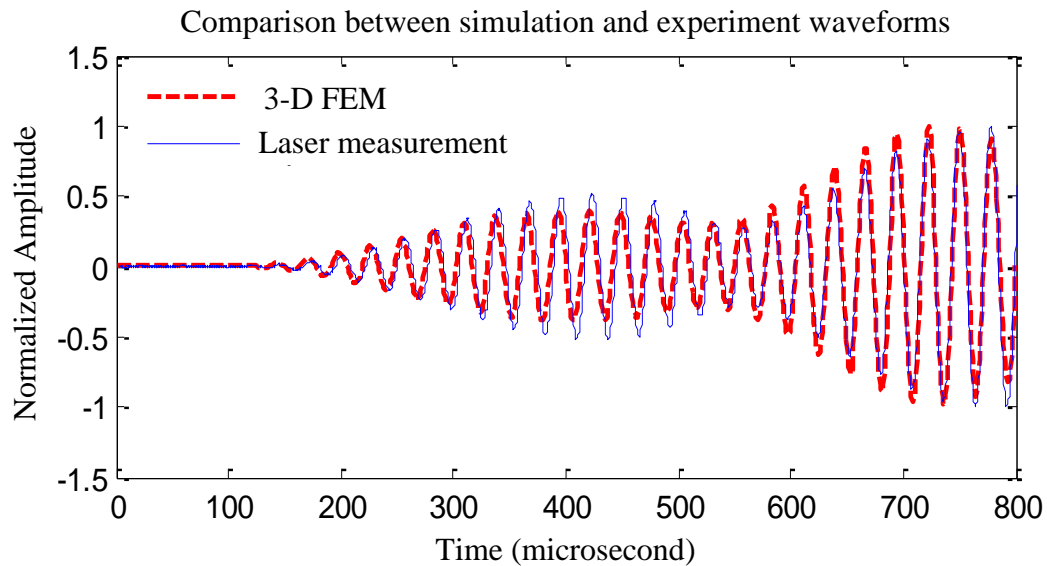


Figure 8.15: Comparison between simulation and experiment waveforms for 10 lb-in loading condition.

Figure 8.16 shows the wave fields captured by the scanning laser vibrometer and calculated by FEM. The wave fields at 10 μs clearly display the waves being generated by the T-PWAS, and propagating into the lap joint structure. At 20 μs, the reflections from the edges can be observed, and the interaction between the interrogating waves and the bolted area can be noticed. The wave field at 30 μs shows the interference between forward propagating waves and reflections from boundaries. The wave field at 40 μs shows the phenomenon of wave interference and the pattern of local resonance. It should be noted that the finite element simulation represents ideal manufacturing and loading conditions of the bolted lap joint, while the real specimen has manufacturing tolerance and uncertainties in loading conditions. For instance, the numerically calculated wave field is symmetric, but the laser measurement is not, especially after the interaction with

the lap joint area. The finite element model is artificially restricted at three different nodes at the end to constrain structural rigid body motion, which will also result in differences between the experimental wave field and the numerical simulation.

(a) Laser measurement                    (b) FEM simulation



10 μs    20 μs    30 μs    40 μs            10 μs    20 μs    30 μs    40 μs
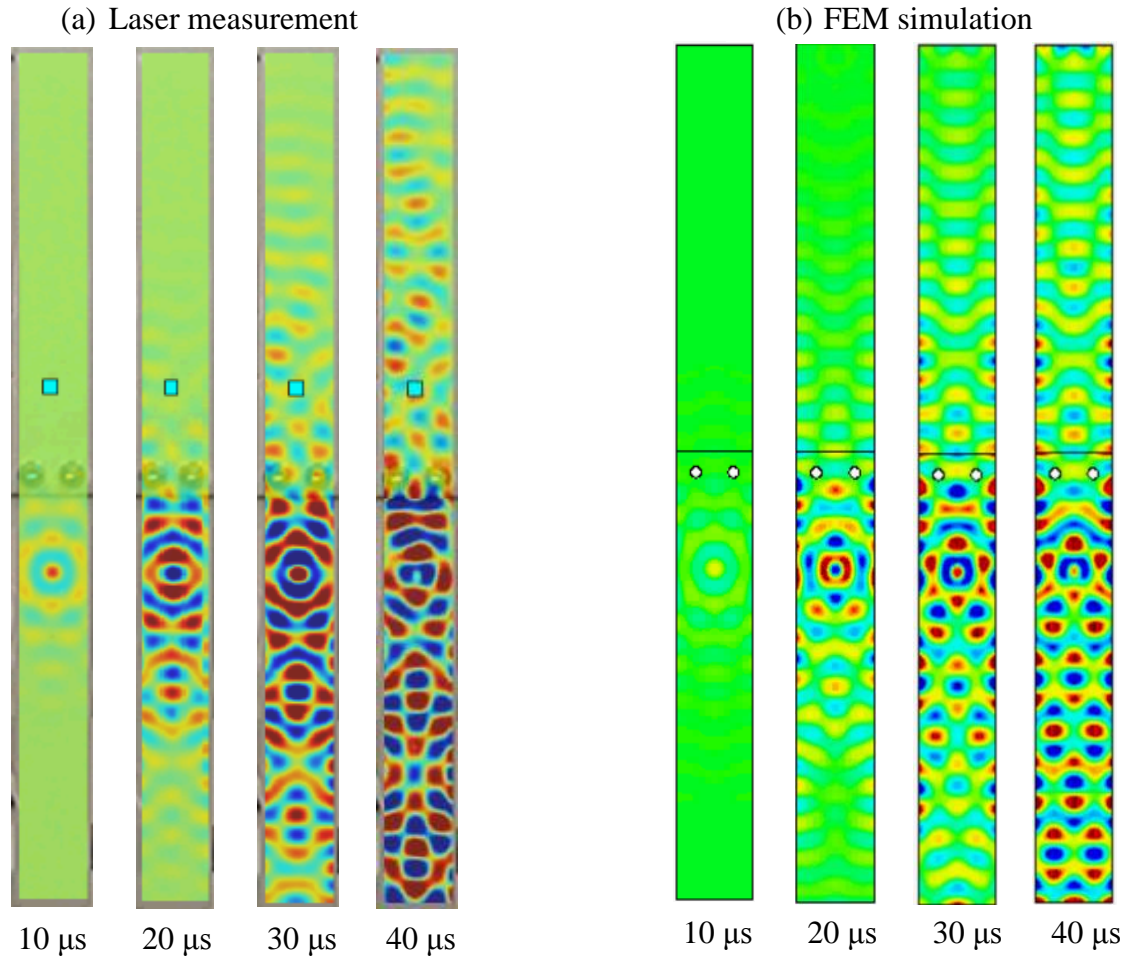
Figure 8.16: Comparison between wave fields: (a) Laser measurement; (b) FEM simulation.

8.4.2   SPECTRAL ANALYSIS OF SENSING SIGNALS

Figure 8.17 shows the frequency spectrum of the simulation signal and the experimental data. It can be noticed that besides the fundamental excitation frequency at $f_c$, distinctive nonlinear higher harmonics at $2f_c$ and $3f_c$ are also present in both simulation

signal and experimental data. This shows the contact model can simulate the nonlinear phenomena of wave interaction with the bolted lap joint.
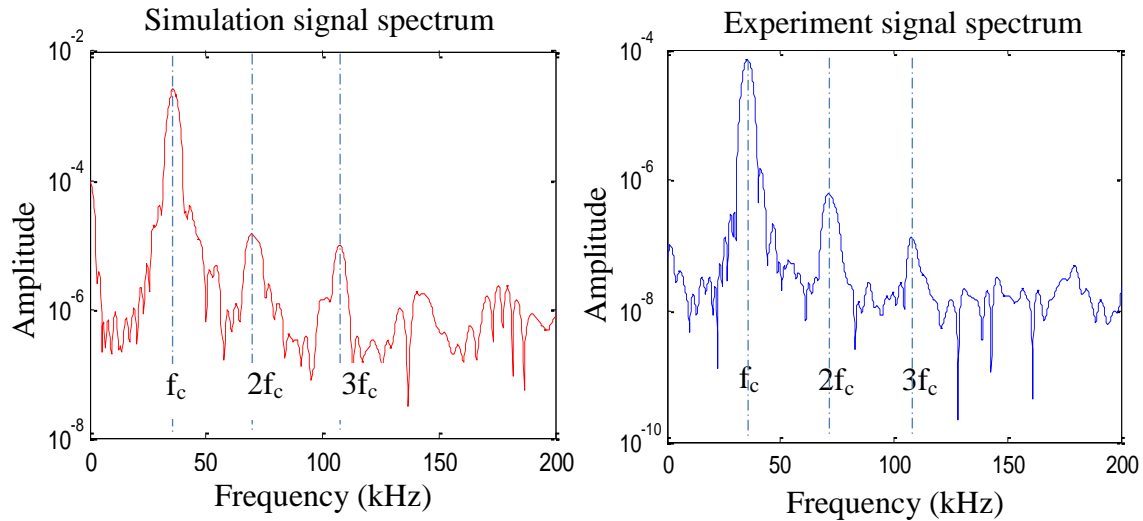


Figure 8.17: Spectrum of simulation and experimental signal.

The degree of nonlinearity is expressed by Eq. (8.2), and serves as the index of the bolt load status of the bolted lap joint.

$$DI = \sqrt{\frac{A(2f_c)}{A(f_c)}} \tag{8.2}$$

where $A(f_c)$ and $A(2f_c)$ denote the spectral amplitude at the excitation frequency and at the second harmonic. The nonlinearity indexes of various torque values are calculated for both the simulation and five independent sets of experiments.

Figure 8.18 shows the nonlinearity index results. It could be observed from Figure 8.18(a) that the numerical simulation result shows a clear decaying trend of nonlinearity with increasing applied torque, which indicates that a tighter joint approaches a linear system with contact surfaces firmly clamped together. However, the experimental data in Figure 8.18(b) shows a much more complicated pattern. In general, under low applied

200

torque values, the nonlinearity index of the signal is high, and then with increased torque, the index fluctuates around certain values.
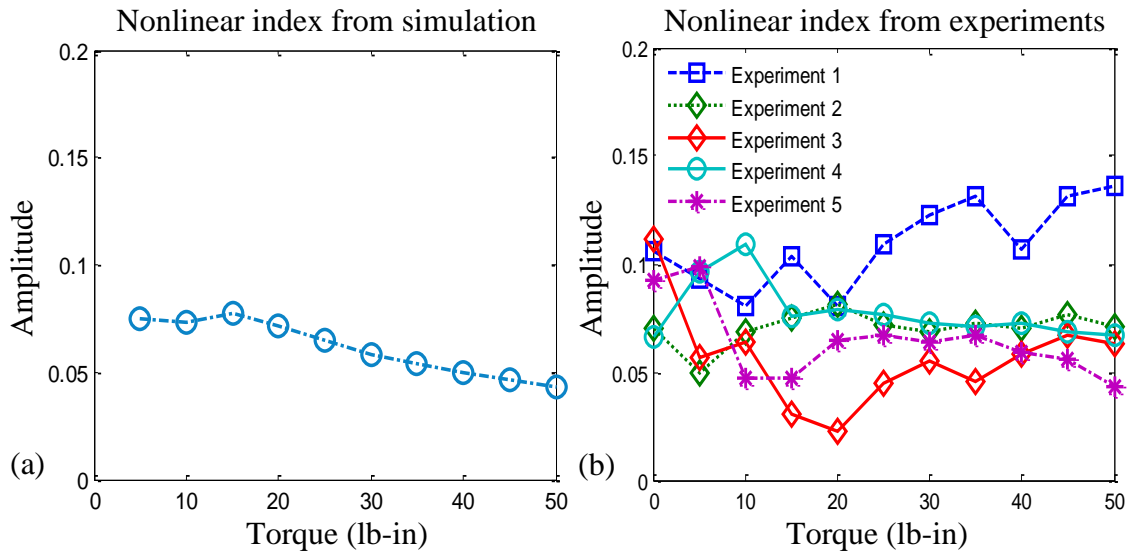


Figure 8.18: Nonlinear index plots: (a) FEM simulation results; (b) experimental data.
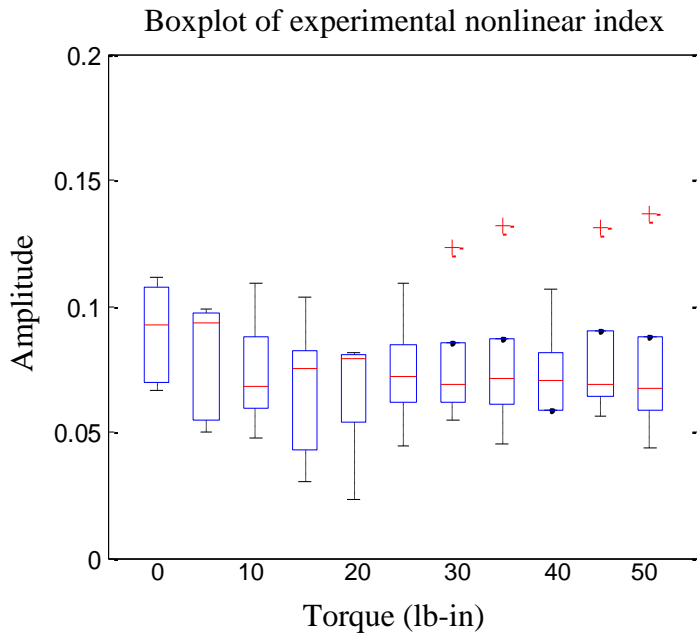


Figure 8.19: Statistical boxplot of experimental data.

Statistically, Figure 8.19 shows at low value of applied torque, an increment of nonlinearity index could indicate the loosening of bolts. A possible cause of the complicated nonlinearity index pattern is the inherent nonlinearity from the excitation signal constructed by the function generator and amplifier. In addition, the nonlinearity of the bolted lap joint structure is found to be very sensitive to the initial relative positioning of the two strips of the lap joint and the load difference between the two bolts. Due to the wide spread of the nonlinear index, the practical application of this higher harmonic method requires further investigation.

8.4.3    INHERENT NONLINEARITY FROM ELECTRONIC EQUIPMENT

Figure 8.20 shows the excitation signal constructed by the function generator and amplifier, and directly recorded by the oscilloscope. The frequency spectrum of the excitation signal shows higher harmonic frequency components generated by the electronic equipment, which will influence the experimental results. These inherent higher harmonic frequency components will also be converted by the T-PWAS and contribute to the R-PWAS received signal. It is difficult to distinguish between the inherent nonlinearity from electronic equipment and the nonlinearity from wave-structure interaction. The transmission coefficients for different frequency components may vary with the bolt loading conditions, resulting in the complicated nonlinearity index change patterns.

The inherent electronic nonlinearity generally exists as a considerable negative influence in structural health monitoring using nonlinear ultrasonic guide waves. Future work will focus on minimizing the influence of the inherent electronic nonlinearity, and

understanding how to use sub-harmonic characteristics for damage identification and detection.
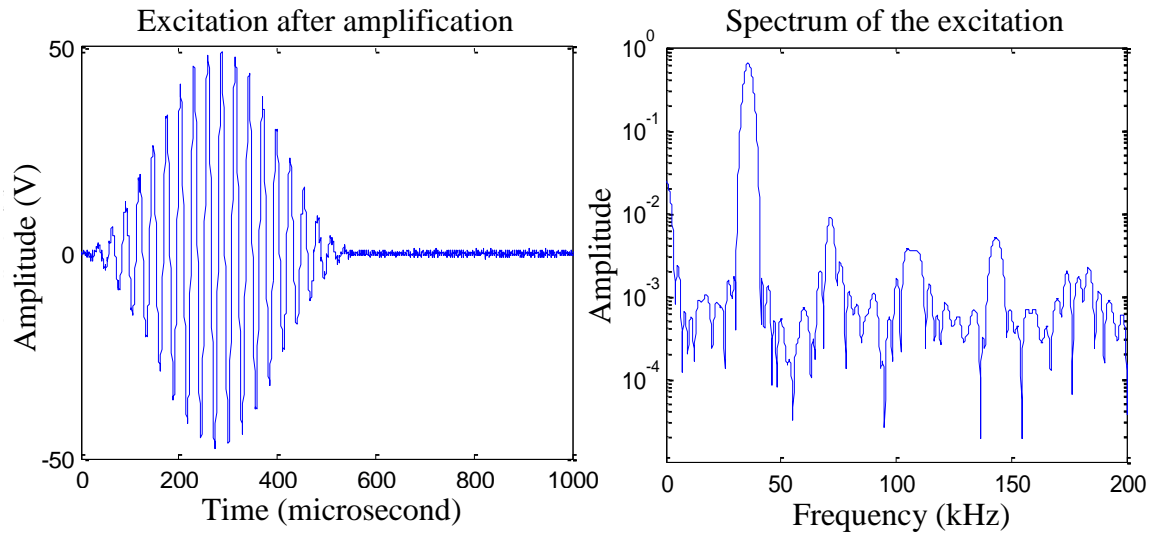


Figure 8.20: Excitation signal and inherent nonlinearity from electronic equipment.

# CHAPTER 9
## CONCLUSIONS AND FUTURE WORK

This dissertation has presented Structural Health Monitoring (SHM) using linear and nonlinear ultrasonic guided waves, with a focus on the development of accurate, efficient, and versatile modeling techniques for guided wave based active sensing procedures.

The dissertation started with an introduction to guided waves, SHM concepts, and piezoelectric wafer active sensors (PWAS). A 1-D analytical framework was constructed based on the exact Lamb wave solution for the simulation of 1-D multimode Lamb wave propagation and interaction with linear/nonlinear structural damage. Case studies were carried out and verified with experiments and finite element simulations. Then, the analytical framework was extended to 2-D wave problems, and the combined analytical/FEM approach (CAFA) was developed for the efficient simulation of 2-D Lamb wave propagation and damage interaction. The wave damage interaction information was extracted from a local finite element model (FEM) with non-reflective boundaries (NRB). The analytical framework was coded with MATLAB into the user friendly software WaveFormRevealer (WFR). CAFA results were compared and verified with full scale FEM simulations and experiments utilizing Scanning Laser Doppler Vibrometry (SLDV). To study guided wave propagation in composite structures, the semi-analytical finite element (SAFE) method was adopted to calculate the dispersion curves, mode shapes, and directivity plots of guided waves in composites. The SAFE procedure was coded with MATLAB, and the software SAFE-DISPERSOIN was

developed. Case studies on an aluminum plate and various kinds of composite plates were carried out. The SAFE-DISPERSION results were compared and verified with analytical solutions and the global matrix method (GMM).

The dissertation continued with an introduction to nonlinear ultrasonic techniques. The classical nonlinear theory and phenomena were discussed. Two nonlinear FEM techniques were investigated for the simulation of nonlinear interaction between guided waves and a breathing crack. These two techniques are (1) the element activation/deactivation approach and (2) contact analysis. The simulation results from both methods were compared. The characteristics of the nonlinear interaction were studied. A damage index was proposed for the detection of breathing cracks and further diagnosing the severity of the nonlinear damage. Then, the higher harmonic technique was applied for bolt load monitoring of an aerospace bolted lap joint. The relationship between the nonlinearity of the sensing signal and the contact pressure was investigated. 2-D and 3-D FEM simulations were carried out to study wave propagation through bolted lap joints. Experiments using SLDV and the PWAS pitch-catch method were conducted and compared with FEM simulations. A review of the main results of this research is given next.

## 9.1    RESEARCH CONCLUSIONS

### 9.1.1    1-D WAVE MODELING AND WFR

The complex valued wave damage interaction coefficients (WDICs) successfully inserted damage effects into the analytical model, and can describe complicated interaction phenomena, such as wave transmission, reflection, mode conversion and nonlinear higher harmonics components. The analytical model was coded into MATLAB,

and the WFR software was developed to obtain fast predictive waveforms for arbitrary combinations of sensors, structural properties, and damage. It can be used to obtain time-space domain waveforms with damage effects, and frequency-wavenumber analysis. WFR can provide fast predictive solutions for multi-mode Lamb wave propagation and interaction with linear/nonlinear damage. The solutions compared well with experiments and finite element simulations. It was also found that computational time savings of several orders of magnitude are obtained by using the analytical WFR instead of FEM methods. WFR allowed users to conduct fast parametric studies with their own designed materials, geometries, and excitations.

### 9.1.2    2-D WAVE MODELING AND CAFA

CAFA was developed to obtain accurate, efficient, and versatile simulation of 2-D guided wave propagation and interaction with damage. WFR-2D was developed as the analytical framework which uses the exact 2-D Bessel and Hankel function solution to calculate Lamb wave propagation excited by a piezoelectric wafer and WDICs for scattered field prediction. A non-reflective boundary (NRB) condition for Lamb waves was developed for the construction of a local FEM. The WDICs are calculated from the efficient local area FEM analysis. The CAFA results compared well with full-scale multi-physics FEM simulations and scanning laser vibrometer experiments.

CAFA has the following advantages over other SHM simulation tools:

1. CAFA can deal with transient wave interaction with complicated damage type and geometries in an easier and more user-friendly way, than other analytical or semi-analytical formulations such as distributed point source method (DPSM) and semi-analytical finite element (SAFE) method.

2. CAFA does not require meshing of the entire structure, thus it minimizes the computation burden; the analytical framework is constructed in the frequency domain, and does not require a time marching procedure, thus it saves considerable computation time, compared with conventional numerical methods such as finite element method (FEM), spectral element method (SEM), or finite difference method (LISA).

3. The harmonic analysis of small-size FEM with NRB is faster and more target-oriented compared with conventional transient analysis. The use of NRB minimizes the model size. Also, harmonic analysis does not require the results of the previous calculation step to solve the current step, as is the case in conventional transient analysis.

4. Because it is fast and efficient, CAFA can be used for parameter studies of various engineering scenarios. It enables researchers to define transducer size, structure material and thickness, sensor-damage locations, and arbitrary excitations by interacting with the graphical user interface of WFR. This user-friendly feature and parameter definition freedom allows users to explore the best sensor arrangement for damage detection in a highly efficient manner, whereas any of these parameter changes will result in re-built/re-mesh/re-run of the whole model in the case of conventional FEM simulation.

### 9.1.3 GUIDED WAVES IN COMPOSITES

The SAFE formulation for layered plate structures was derived. The SAFE method can calculate guided wave dispersion curves and mode shapes through an eigenvalue problem instead of conducting root searching procedure as other matrix

methods. The post processing methodology was presented, including auto mode tracing and mode shape formation. The SAFE procedure was coded with MATLAB into a user friendly software SAFE-DISPERSION for the calculation of dispersion curves, mode shapes, and directivity plots.

Case studies were conducted to verify SAFE-DISPERSION solutions. First, the dispersion curves and mode shapes in an aluminum plate were calculated and compared with the exact analytical solution. The results compare well with each other. Then, the guided waves in various composites were calculated, including a unidirectional CFRP plate with different propagation directions, cross ply CFRP plates, and quasi-isotropic CFRP plates. The dispersion curves, displacement mode shapes, and stress mode shapes all compared well with those obtained from the global matrix method (GMM) using the commercial software DISPERSE$^{TM}$. It was found that SAFE-DISPERSION can generate a more stable solution when compared with DISPERSE$^{TM}$ which requires fine training for the users. The stress mode shapes in composite structures are no longer continuous across the plate thickness.

9.1.4  NONLINEAR ULTRASONIC THEORY

The classical nonlinear mechanisms were reviewed. The contact acoustic nonlinearity (CAN) was investigated with a reduced order bi-linear stiffness model. A parameter study on damage severity was conducted to illustrate the potential of nonlinear ultrasonic techniques to detect nonlinear damage and further diagnose the severity of the damage. A parameter study on the excitation frequency was carried out to show the frequency dependence of the distinctive nonlinear phenomena, such as super harmonic and sub harmonic generation. The nonlinear response was found to be sensitive to the

appearance of incipient damage and the excitation frequency. A review of prevalent nonlinear ultrasonic techniques was presented, including higher harmonic technique, subharmonic and DC response technique, nonlinear resonant ultrasound spectroscopy technique, and nonlinear modulation technique.

9.1.5   BREATHING CRACK DETECTION USING NONLINEAR ULTRASONICS

The nonlinear ultrasonic technique was investigated to detect breathing cracks in plate structures. Two nonlinear finite element methods were proposed to simulate the nonlinear interaction between guided waves and the breathing crack: (1) the element activation/deactivation technique; (2) contact analysis. The solutions obtained by these two FEM techniques compared quite well. A linear FEM analysis of this situation was also performed.

It was found that the two FEM methods considered in this study can simulate equally well the nonlinear behavior of the breathing crack. Also, it was found that the nonlinear interaction between guided waves and the breathing crack generates higher harmonics, which were not found in the linear FEM simulation. A damage index (DI) was proposed based on the amplitude ratio of the signal spectral harmonics to relate the signal nonlinearity with damage severity. This DI was applied to the S0 and A0 wave packets as well as to a new packet resulting from the interaction between the guided waves and the damage. It was found that the DI of the new packet is more sensitive to the presence of the crack, while the DIs of the S0 and A0 packets can provide monitoring information on the damage severity.

### 9.1.6   BOLT LOAD MONITORING OF BOLTED LAP JOINTS

First, he relationship between CAN and contact pressure was investigated. The nonlinearity of the transmitted waves showed a monotonic decaying trend with increasing contact pressure beyond a contact pressure threshold. This correlation between contact pressure and signal nonlinearity shows great potential for monitoring the change of contact pressure. This phenomenon was applied for monitoring the bolt load status of a bolted lap joint.

We proposed a static to transient finite element solving scheme to simulate guided wave propagation through a bolted lap joint. It was found that the contact finite element model can describe the interaction between guided ultrasonic waves and bolted lap joints. The waveforms and wave fields from the FEM simulation agree well with the experimental data from PWAS pitch-catch and scanning laser vibrometer measurements. Distinctive nonlinear higher harmonics are found in both the numerical simulation and experimental results. The theoretical study shows a decaying trend of nonlinearity with increasing applied bolt load level, which could be used as a correlating quantity for monitoring bolt tight/loose status. However, the experimental data shows more complicated patterns. Two sources of nonlinearity are found in the experiments: (1) inherent nonlinearity from electronic equipment; (2) nonlinearity from wave-structure interaction. The final nonlinearity has a contribution from both sources.

### 9.2   MAJOR CONTRIBUTIONS

This dissertation has contributed to the SHM community in a variety of ways. The major contributions of this dissertation to the state of the art are listed below:

1. A novel methodology was proposed for inserting damage effects into an analytical model. We have introduced the complex-valued WDICs which are capable of describing mode conversion, amplitude, phase, directionality information, and nonlinear higher harmonic components during wave damage interaction. We have found that the phase information is very important, although it was ignored by previous researchers.

2. The effective non-reflective boundary (NRB) was developed for Lamb wave problems. It was found to work well for both the symmetric and antisymmetric modes.

3. A novel approach has been developed for coupling analytical model with local FEM models for simulation of 2-D interaction between guided waves and damage.

4. The methodology of using small-size local FEM harmonic analysis with NRB to determine the WDICs over the frequency band required for analytical simulation has been presented.

5. We not only developed the analytical framework and derived the semi-analytical finite element formulation, but also developed corresponding software which can benefit the SHM community. The software packages are: (1) WaveFormRevealer 1-D (WFR-1D); (2) WaveFormRevealer 2-D (WFR-2D); (3) SAFE-DISPERSION. These graphical user interfaces provide a versatile user-friendly method for studying a large family of SHM problems.

6. The element activation/deactivation approach was used to simulate the contact nonlinearity of a breathing crack, which has not been attempted in existing literatures.

7. The damage index based on nonlinear spectral amplitude was developed for detection of nonlinear damage and diagnosis of damage severity.

8. The static to transient finite element solving scheme was proposed to simulate the transient response of wave interaction with pre-loaded structures, which has not been reported elsewhere.

## 9.3 RECOMMENDATION FOR FUTURE WORK

This dissertation has presented various modeling techniques for the simulation of guided wave propagation and interaction with linear/nonlinear damage. This work has laid the foundation for future investigations to extend the methodologies to more complicated structures. The suggestions for future work are listed below:

1. CAFA verification with other types of damage should be performed.

2. Extension to more than the basic S0, A0, and SH0 modes should be made.

3. Inclusion of nonlinear effects in CAFA should be attempted.

4. WFR concept should be developed to simulate wave propagation in composite structures.

5. The small-size FEM with NRB should be further explored to obtain characteristics of waves excited by arbitrary shaped PWAS transducers on various kinds of structures.

6. CAFA should be explored to solve wave propagation in structures with more complicated geometries and should include boundary reflections.

7. The analytical framework should be further investigated to include thermal and loading effects to consider wave generation, propagation, damage interaction, and detection under various temperature and loading conditions.

8. The behavior of a breathing crack under different interrogating wave amplitude should be studied, as well as the transition requirement from an initially opened or closed crack into a breathing crack. Experiments should be performed to verify these theoretical predictions.

9. Nonlinear ultrasonic techniques should be further studied. The possibility of separating inherent nonlinearity and wave-structure interaction nonlinearity should be explored.

10. Design of the bolted lap joint test specimen should be improved to represent a real structure, for example, two plates joint by multiple bolts or rivets. The case of loosening only one of the multiple bolts should also be explored by this nonlinear spectroscopy method using PWAS transducers.

REFERENCES


Abeele, V,; Carmeliet, K,; Ten Cate, J,; and Johnson, P. (2000). Nonlinear Elastic Wave Spectroscopy (NEWS) Techniques to Discern Material Damage, Part II: Single-Mode Nonlinear Resonance Acoutic Spectroscopy. *Research in Nondestructive Evalucation, 12*(1), 31-42.

Ahmad, Z,; Vivar-Perez, J,; and Gabbert, U. (2013). Semi-analytical finite element method for modeling of Lamb wave propagation. *CEAS Aeronaut Journal, 4*, 21-33.

Alleyne, D,; and Cawley, P. ((1992)). The interaction fo Lamb waves with defects. *IEEE Transactions on Ultrasonics Ferroelectrics and Frequency Control, 39*(3), 381-397.

Alleyne, D,; Pavlakovic, B,; Lowe, M,; and Cawley, P. (2001). Rapid, Long Range Inspection of Chenical Plant Pipework Using Guided Waves. *Review of Progress in QNDE*, (pp. 180-187).

Amerini, F,; and Meo, M. (2011). Structural health monitoring of bolted joints using linear and nonlinear acoustic/ultrasound methods. *Structural Health Monitoring*, 659-672.

ANSYS. (n.d.). *ANSYS User's Manual Version 12.0.*

Bao, J,; Shen, Y,; and Giurgiutiu, V. (2013). Linear and Nonlinear Finite Element Simulation of Wave Propagation through Bolted Lap Joint. *54th AIAA/ASME/ASCE/AHS/ASC Structures, Structural Dynamics, and Materials Conference.*

Bartoli, I,; Marzani, A,; Lanza de Scalea, F,; and Viola, E. (2006). Modeling wave propagation in damped waveguides of arbitrary cross-section. *Journal of Sound and Vibration, 295*, 685-707.

Bermes, C,; Kim, J,; and Qu, J. (2007). Experimental characterization of material nonlinearity using Lamb waves. *Applied physics letters*, 021901.

Biwa, S,; Hiraiwa, S,; and Matsumoto, E. (2006). Experimental and Theoretical Study of Harmonic Generation at Contacting Interface. *Ultrasonics*, 44, e1319-e1322.

Biwa, S,; Nakajima, S,; and Ohno, N. (2004). On the Acoustic Nonlinearity of Solid-Solid Contact with Pressure-Dependent Interface Stiffness. *Trans. ASME Journal of Applied Mechanics, 71*, 508-515.

Bottger, W,; Schneider, H,; and Weingarten, W. (1987). Prototype EMAT system for tube inspection with guided ultrasonic waves. *Nuclear Eng. and Design*, 356-376.

Brillouin, L. (1964). *Tensors in Mechanics and Elasticity.* Academic Press.

Broda, D,; Staszewski, W,; Martowicz, A,; Uhl, T,; and Silberschmidt, V. (2014). Modeling of nonlinear carck-wave interactions for damage detection based on ultrasound - A review. *Journal of Sound and Vibration, 333*, 1097-1118.

Buck, O,; Morris, W,; and Richardson, J. (1978). Acoustic Harmonic Generation at Unbonded Interaces and Fatigue Cracks. *Applied Physics Letters, 33*(5), 371-373.

Cantrell, J. (2009). Nondestructive Evaluation of Metal Fatigue Using Nonlinear Acoustics. *CP1096 Review of Quantitative Nondestructive Evaluation*, 19-32.

Cantrell, J,; and Yost, W. (1994). Acoustice harmonic generation from fatigue-induced dislocation dipoles. *Philosophical Magazine A, 120*(2), 315-326.

Chang, Z,; and Mal, A. ((1999)). Scattering of Lamb waves from a rivet hole with edge cracks. *Mechanics of Materials*, 197-204.

Cho, Y,; Hongerholt, D,; and Rose, J. ((2000)). Estimation of ultrasonic guided wave mode conversion in a plate with thickness variation. *IEEE Transaction on Ultrasonics, Ferroelectrics, and Frequency Control, 47*(3).

Corrosion Testing Laboratories, I. (2007). *Fatigue Cracking of Steam Line Expansion Bellow.*

Deng, M. (1999). Cumulative second-harmonic generation of Lamb-modes propagation in a solid plate. *Journal of applied physics*, 3051-3058 .

Deng, M. (2003). Analysis of second-harmonic generation of Lamb modes using a modal analysis approach. *Journal of applied physics*, 4152-4159.

Donskoy, D,; Sutin, A,; and Ekimov, A. (2001). Nonlinear Acoustic Interaction on Contact Interfaces and its Use for Nondestructive Testing. *NDTandE International, 34*(4), 231-238.

Doyle, D,; Reynolds, W,; Arritt, B,; and Taft, B. (n.d.). Computational Setup of Structural Health Monitoring for Real-Time Thermal Verification. *SMASIS*, (pp. 447-453). 2011.

Dutta, D,; Sohn, H,; and Harries, K. (2009). A nonlinear acoustic technique for crack detection in metallic structures. *Structural Health Monitoring-an international journal*, 573-573.

Farrar, C,; and Worden, K. (2012). *Structural Health Monitoring: A Machine Learning Perspective.* John Wiley and Sons, Ltd.

Fink, M. (1992). Time Reversal of Ultrasonic Fields -- Part 1: Basic Principles. *IEEE Trans. Ultrasonics, Ferroelectrics, and Frequency Control*, 555-566.

Friswell, M,; and Penny, J. (2002). Crack modeling for structural health monitoring. *Structural Health Monitoring, 1*(2), 139-148.

Galan, J,; and Abascal, R. (2005). Boundary element solution for the bidimensional scattering of guided waves in laminated plates. *Computers and Structures, 83*, 740-757.

Gavric, L. (1995). Computation of propagative waves in free rail using a finite element technique. *Journal of Sound and Vibration, 185*(3), 531-543.

Gazis, D. (1959). Three Dimentional Investication of the Propgation of Waves in Hollow Circular Cylinders. *Journal of the Acoustical Society of America*, 568-578.

Giurgiutiu, V. ((2007)). *[Structural healthing monitoring with piezoelectric wafer active sensors].* Elsevier Academic Press.

Giurgiutiu, V. ((2014)). *[Structural Health Monitoring with Piezoelectric Wafer Active Sensors].* Second Edition, Elsevier Academic Press.

Giurgiutiu, V. (2003). Embedded Ultrasonics NDE with Piezoelectric Wafer Active Sensors. *Journal Instrumentation, Mesure, Metrologie, RS series 12M, 3*, 149-180.

Giurgiutiu, V. (2005). Tuned Lamb wave excitation and detection with piezoelectric wafer active sensors for structural health monitoring. *Journal of intelligent material systems and structures*, 291-306.

Giurgiutiu, V. (2007). *Structural Health Monitoring with Piezoelectric Wafer Active Sensors.* Academic Press.

Giurgiutiu, V. (2010). Structural Health Monitoring with Piezoelectric Wafer Active Sensors – Predictive Modeling and Simulation. *INCAS Bulletin, 2*, 31-44.

Giurgiutiu, V. (2014). *Structural Healthing Monitoring with Piezoelectric Wafer Active Sensors (Second Edition).* Elsevier Academic Press.

Giurgiutiu, V,; and Lyshevski, S. (2003). *Micromechatronics Modeling, Analysis, and Desgin with MATLAB.* New York: CRC Press.

Giurgiutiu, V,; and Soutis, C. (2012). Enhanced Composite Integrity through Structural Health Monitoring. *Applied Composite Materials*, DOI 10.1007/s10443-011-9247-2.

Giurgiutiu, V,; Gresil, M,; Lin, B,; Cuc, A,; Shen, Y,; and Roman, C. (2012). Predictive Modeling of Piezoelectric Wafer Active Sensors Interaction with High-frequency Structural Waves and Vibration. *Acta Mechanica*, 1681-1691.

Giurgiutiu, V,; Reynolds, A,; and Rogers, C. (1999). Experimental Investigation of E/M Impedance Health Monitoring of Spot-Welded Structural Joints. *Journal of Intelligent Material Systems and Structures*, 802-812.

Giurgiutiu, V,; Zagrai, A,; and Bao, J. (2002). Piezoelectric Wafer Embeded Active Sensors for Aging Aircraft Structural Health Monitoring. *Structural Health Monitoring -- An International Journal*, 41-61.

Glushkov, E,; Glushkova, N,; Lammering, R,; Eremin, A,; and Neumann, M. ((2011)). Lamb wave excitation and propagation in elastic plates with surface obstacles: proper choice of central frequency. *Smart Materials and Structures*, 11pp.

Graff, K. (1991). *Wave motion in elastic solids.* New York: Dover publications, INC.

Grahn, T. ((2002)). Lamb wave scattering from a circular partly through-thickness hole in a plate. *Wave Motion*.

Gresil, M,; and Giurgiutiu, V. (2013a). Time-Domain Hybrid Global-Local Concept for Guided-Wave Propagation with Piezoelectric Wafer Active Sensor. *Journal of Intelligent Material Systems and Structures, 24*(15), 1897-1911.

Gresil, M,; and Giurgiutiu, V. (2013b). Time-Domain Global-Local Prediction of Guided Waves Interaction with Damage. *Key Engineering Materials, 558*, 116-127 .

Gresil, M,; Shen, Y,; and Giurgiutiu, V. (2011). Predictive modeling of ultrasonics SHM with PWAS transducers. *8th International Workshop on Structural Health Monitoring.* Stanford, CA, USA.

Gresil, M,; Yu, L,; Shen, Y,; and Griugiutiu, V. (2013). Predictive model of fatigue crack detection in thick bridge steel structures with piezoelectric wafer active sensors. *Smart Structures and Systems*, 097-119.

Haskell, N. (1953). The dispersion of surface waves on multi-layered media. *Bulletin of the Seismological Society of America, 43*(1), 17-34.

Hayashi, T,; Kawashima, K,; and Rose, J. (2004). Calculation for Guided Waves in Pipes and Rails. *Key Engineering Materials*, 410-415.

Hinders, M. K. (1996). Lamb waves scattering from rivets. *Quantitative Nondestructive Evaluation, 15*.

Hosseini, S,; Duczek, S,; and Gabbert, U. (2013). Non-reflecting boundary condition for Lamb wave propagation problems in honeycomb and CFRP plates using dashpot elements. *Composites: Part B, 54*, 1-10.

Hughes, T,; Taylor, R,; Sackman, J,; Curnier, A,; and Kannoknukulchai, W. (1975). A finite element method for a class of contact-impact problems. *computer methods in applied mechanics and engineering*, 294-276.

Hurley, D,; Balzer, D,; Purtscher, P,; and Hollman, K. (1998). Nonlinear ultrasonic parameter in quenched martensitic steels. *Journal of Applied Physics, 83*, 4584-4588.

Ihn, J,; and Chang, F. (2008). Pitch-catch Active Sensing Methods in Structural Health Monitoring for Aircraft Structures. *Structural Health Monitoring An International Journal*, 5-15.

Jhang, K. Y. (2009). Nonlinear Ultrasonic Techniques for Nondestructive Assessment of Micro Damage in Material: A Review. *International journal of Materials*, 123-135.

Johnson, D,; Wang, K,; and Kim, J. (2010). Investigation of the threshold behaviorof subharmonics for damage detection of a structure with a breathing crack. *SPIE Smart Structures and NDE.* San Diego.

Johnson, P. (2001). *Patent No. No. 6330827.* US Patent.

Kabashima, S,; Ozaki, T,; and Takeda, N. (2001). Structural Health Monitoring Using FBG Sensor in Space Environment. *SPIE Smart Structures and Materials.* Newport Beach.

Kamal, A,; and Giurgiutiu, V. (2014). Stiffness transfer matrix method (STMM) for stable dispersion curves solution in anisotropic composites. *SPIE Smart Structures and NDE.* San Diego.

Kamal, A,; Gresil, M,; and Giurgiutiu, V. (2013). Shear Horizontal Guided Waves in Laminated Composite Plates Using SH-PWAS. *NDT of Composites.* Seattle WA.

Kim, J,; Jacobs, L,; and Qu, J. (2006). Experimetnal characterization of fatigue damage in a nickel-based superalloy using nonlinear ultrasonic waves. *Journal of the Acoustical Society of America, 120*(3), 1266-1273.

Knopoff, L. (1964). Matrix method for elastic wave problems. *Bulletin of the Seismological Society of America, 54*, 431-438.

Kolosov, O,; and Yamanaka, K. (1993). Nonlinear Detection of Ultrasonic Vibrations in an Atomic Force Microscope. *Japanese Journal of Applied Physics Part 2 Letters, 32*(8A), L1095-L1098.

Korshak, B,; Solodov, I,; and Ballad, E. (2002). DC Effects, Sub-Harmonics, Stochasticity and "Memory" for Contact Acoustic Nonlinearity. *Ultrasonics, 40*(1), 707-713.

Kruse, W,; and Zagrai, A. (2009). Investigation of Linear and Nonlinear Electromechanical Impedance Techniques for Detection of Fatigue Damage in Aerospace Materials. *7th International Workshop on Structural Health Monitoring.*

Kumar, A,; Torbert, C,; Jones, J,; and Pollock, T. (2009). Nonlinear Ultrasonics for In Situ Damage Detection during High Frequency Fatigue. *Journal of Applied Physics*, 024904_1-9.

Lee, B,; and Staszewski, W. (2007). Lamb wave propagation modelling for damage detection: I. Two-dimensional analysis. *Smart Materials and Structures*, 249-259.

Lim, H,; Sohn, H,; DeSimio, M,; and Brown, K. (2014). Reference-free fatigue crack detection using nonlinear ultrasonic modulation under various temperature and laoding conditions. *Mechanical Systems and Signal Processing, 45*, 468-478.

Lin, B,; Kamal, A,; Giurgiutiu, V,; and Kamas, T. ((2012)). Multimodal Lamb Waves Power and Transfer Function Analysis of Structurally-bounded PWAS. *ASME 2012 SMASIS.* Sone Mountain, Geogia, USA.

Liu, J. a. (2005). Three dimensional viscoelastic artificial boundaries in time domain for wave motion problems. *Engineering Mechanics, 20*(6), 46-51.

Love, A. (1944). *A Treatise on the Mathematical Theory of Elasticity.* NY: Dover Pub.

Lowe, M. (1995). Matrix techniques for modeling ultrosonic waves in multi-layered media. *Ultrasonics, Ferroelectrics and Frequency Control, IEEE Transactions, 42*(4), 525-542.

Lysmer, J,; and Kuhlemeryer, R. (1969). Finite-dynamic model for infinite media. *J. Eng. Mech. Div,; 95*(4), 859-877.

McKeon, J. P,; and Hinders, M. K. ((1999)). Lamb waves scattering from a through hole. *Journal of Sound and Vibration*, 843-862.

Meitzler, A. (1961). Mode Coupling Occuring in the Propagation of Elastic Pulses in Wires. *Journal of Acoustical Society of America*, 435-445.

Michaels, T,; Michaels, J,; and Ruzzene, M. (2011). Frequency-wavenumber domain analysis of guided wavefields. *Ultrasonics*, 452-466.

Moreau, L,; Caleap, M,; Velichko, A,; and Wilcox, P. D. ((2012)). Scattering of guided waves by flat-bottomed cavities with irregular shapes. *Wave Motion*, doi: 10.1016/j.wavemoti.2011.12.004.

Moreau, L,; Caleap, M,; Velichko, A,; and Wilcox, P. D. (2011). Scattering of guided waves by through-thickness cavities with irregular shapes. *Wave Motion, 48*, 586-602.

Moreau, L,; Velichko, A,; and Wilcox, P. ((2012)). Accurate finite element modeling of guided wave scattering from irregular defects. *NDTandE International, 45*, 46-54.

Moreau, L,; Velichko, A,; and Wilcox, P. (2012). Accurate finite element modelling of guided wave scattering from irregular defects. *NDTandE International, 45*, 46-54.

Moser, F,; Jacobs, L,; and Qu, J. (1999). Modeling elastic wave propagation in waveguides with the finite element method. *NDTandE International*, 225-234.

Mumaghan, F. (1951). *Finite deformation of an elastic solid.* Wiley Press.

Nadella, K,; and Cesnik, C. ((2013)). Local interaction simulation approach for modeling wave propagation in composite structures. *CEAS Aeronaut Journal, 4*, 35-48.

Nagy, B. (1998). Fatigue Damage Assessment by Nonlinear Ultrasonic Materials Characterization. *Ultrasonics*, 375-381.

Nayfeh, A,; and Mook, D. (1995). *Nonlinear oscillations.* New York: A Wiely-interscience pulicatoin.

Norris, A. N,; and Vemula, C. (1995). Scattering of flexual waves in thin plates. *Journal of Sound and Vibration*, 115-125.

Ostachowicz, W,; Kudela, P,; Krawczuk, M,; and Zak, A. ((2012)). *[Guided Waves in Structures for SHM: The Time-Domain Spectral Element Method].* West Sussex, UK: Wiley.

Raghavan, A,; and Cesnik, C. ((2005)). Finite-dimensional piezoelectric transducer modeling for guided wave based structural health monitoring. *Smart Materials and Structures, 14*, 1448-1461.

Rahani, E,; and Kundu, T. ((2011)). Modeling of Transient Ultrasonic Wave Propagation Using the Distributed Point Source Method. *IEEE Transactions on Ultrasonics, Ferroelectrics, and Frequency Control, 58*(10).

Richardson, J. (1979). Harmonic generation at an unbonded interface: I.planar interface between semi-infinite elastic media. *Int. J. Eng. Sci,; 17*, 73–85.

Rose, J. (2012). *Health Monitoring of Composite Structures Using Guided Waves.*

Rose, J. L. (1999). *Ultrasonic Waves in Solid Media.* Cambridge: Cambridge University Press.

Rose, J,; Ditri, J,; Pilarski, A,; Rajana, K,; and Carr, F. (1994). A Guided Wave Inspection Technique for Nuclear Steam Generator Tubing. *NDTandE International*, 307-310.

Ruzzene, M. (2007). Frequency-wavenumber domain filtering for improved damage visualization. *Smart Materials and Structures, 16*, 2116-2129.

Shen, Y,; and Giurgiutiu, V. (2012). Predictive simulation of nonlinear ultrasonics. *SPIE Smart Structures and Materials + Nondestructive Evaluation and Health Monitoring.* San Diego, California, USA.

Shen, Y,; and Giurgiutiu, V. (2012). Predictive Simulation of Nonlinear Ultrasonics. *SPIE 2012 Smart Structures and NDE.* San Diego.

Shen, Y,; and Giurgiutiu, V. (2012). Simulation of interaction between Lamb waves and cracks for structural health monitoring with piezoelectric wafer active sensors. *ASME 2012 Conference on Smart Materials, Adaptive Structures and Intelligent Systems.* Stone Moutain, Georgia, USA.

Shen, Y,; and Giurgiutiu, V. (2013). Modeling of Guided Waves for Detection of Linear and Nonlinear Structural Damage. *SPIE Smart Materials and Structure/NDE.* San Diego.

Shen, Y,; and Giurgiutiu, V. (2014). WaveFormRevealer: An Ananlytical Framework and Predictive Tool for the Simulation of Multi-modal Guided Wave Propagation and Interaction with Damage. *Structural Health Monitoring -- An International Journal*, DOI: 10.1177/1475921714552986.

Shen, Y,; and Giurgiutiu, V. (2014). WFR-2D: an analytical model for PWAS-generated 2D ultrasonic guided wave propagation. *SPIE Smart Structures and NDE.* San Diego.

Shen, Y,; Bao, J,; and Giurgiutiu, V. (2013). Health Monitoring of Aerospace Bolted Lap Joints Using Nonlinear Ultrasonic Spectroscopy: Theory and Experiments. *9th International Workshop on Structural Health Monitoring.* San Francisco.

Silk, M,; and Bainton , K. (1979). The Propagation in Metal Tubing of Ultrasonic Wave Modes Equivalent to Lamb Waves. *Ultrasonics*, 11-19.

Sohn, H,; Lim, H,; DeSimio, M,; Brown, K,; and Derriso, M. (2013). Fatige crack detection using guided waves nonlinear modulation. *SPIE Smart Structures/NDE.* San Diego.

Solodov, I,; Krohn, N,; and Busse, G. (2002). CAN: An Example of Nonclassical Acoustic Nonlinearity in Solids. *Ultrasonics, 40*, 621-625.

Srivastava, A. ((2009)). *[Quantitative structural health monitoring using ultrasonic guided waves].* PhD Thesis, University of California, San Diego, CA.

Srivastava, A,; and di Scalea, F. (2009). On the existence of antisymmetric or symmetric Lamb waves at nonlinear higher harmonics. *JOURNAL OF SOUND AND VIBRATION , 323*(3-5), 932-943.

Thomson, W. (1950). Transmission of elastic waves through a stratified solid medium. *Journal of Applied Physics, 21*, 89-93.

Tuegel, E,; Ingraffea, A,; Eason , T,; and Spottswood, S. (2011). Reengineering Aircraft Sturctural Life Prediction Using a Ditial Twin. *International Journal of Aerospace Engineering*, ID 154798.

Velichko, A,; and Wilcox, P. (2011). Efficient finite elment modeling of elastodynamic scattering from near surface and surfacebreaking defects. *AIP Conf. Proc. 1335, 59 (2011); doi: 10.1063/1.3591840.*

Velichko, A,; and Wilcox, P. (2012). Efficient finite element modeling of elastodynamic scattering with non-reflective boundary conditions. *AIP Conf. Proc. 1430, 142 (2012); doi: 10.1063/1.4716224.*

Vemula, C,; and Norris, A. N. ((1997)). Flexual wave propagation and scattering on thin plates using Mindlin theory. *Wave Motion, 26*, 1-12.

Wang, C,; and Chang, F. ((2005)). Scattering of plate waves by a cylindrical inhomogeneity. *Journal of Sound and Vibration, 282*, 429-451.

Wang, C,; and Liu, Z. (2012). Realization of viscoelastic boundary condition in wave field simulation with ANSYS finite element software. *Journal of Geodesy and Geodynamics, 32*(2).

Wang, C,; Rose , J,; and Chang, F. (2004). A Synthetic Time-Reversal Imaging Method for Structural Health Monitoring. *Smart Material and Structures*, 415-423.

Wang, L,; and Rokhlin, S. (2001). Stable reformulation of transfer matrix method for wave propagation in layered anisotropic media. *Ultrasonics, 39*, 407-418.

Windels, F,; and Abeele, V. (2004). The Influence of Localized Damage in a Smaple on Its Resonance Spectrum. *Ultrasonics, 42*, 1025-1029.

Worden, K,; and Tomlinson, G. (2001). *Nonlinearity in structural dynamics: detection, identificiation and modeling.* Bristol: IOP Publishing.

Worden, K,; Farrar, C,; Manson, G,; and Park, G. (2007). The Fundamental Axioms of Structural Health Monitoring. *Philosophical Transactions of the Royal Society A*, 1639-1664.

Yamanaka, K,; Ogiso, H,; and Kolosov, O. (1994). Ultraonic Force Microsopy for Nanameter Resolution Subsrface Imaging. *Applied Physics Letters, 64*(2), 178-180.

Yang, J,; and Chang, F.-K. (2006). Detection of bolt loosening in CC composite thermal protection panels: II. Experimental verification. *Smart Materials and Structures*, 591-599.

Yoder, N,; and Adams, D. (2010). Vibro-Acoustic Modulation Utilizing a Swept Probing Signal for Robust Crack Detection. *Structural Health Monitoring An International Journal, 9*, 257-267.

Yu, L,; Momeni, S,; Godlinez, V,; Giurgiutiu, V,; Ziehl, P,; and Yu, J. (2012). Dual Mode Sensing with Low-Profile Piezoelectric Thin Wafer Sensors for Steel Bridge Crack Detection and Diagnosis. *Advances in Civil Engineering*, ID 402179.

Zagrai, A,; and Giurgiutiu, V. (2001). Electro-Mechanical Impedance Method for Crack Detection in Thin Plates. *Journal of Intelligent Material Systems and Structures*, 709-718.

Zagrai, A,; Doyle, D,; and Arritt, B. (2008). Embedded nonlinear ultrasonics for structural health monitoring of satellite joints. *Proc SPIE.*

Zemenek, J. (1972). An Experimental and Theoretical Investigation of Elastic Wave Propagation in a Cylinder. *Journal of the Acoustical Society of America*, 265-283.

Zhou, W,; Li, H,; and Yuan, F. (2014). Guided wave generation, sensing and damage detection using in-plane shear piezoelectric wafers. *Smart Materials and Structures*.